Analysis of the Immersed Boundary Method for Stokes Flow

by

Thomas T. Bringley

A dissertation submitted in partial fulfillment

of the requirements for the degree of

Doctor of Philosophy

Department of Mathematics

New York University

May, 2008

Charles S. Peskin—Advisor

© Thomas T. Bringley

All Rights Reserved, 2008

Abstract

The immersed boundary method is a numerical scheme for dynamical simulations of solid or elastic bodies immersed in a surrounding fluid. The method was originally introduced by Peskin to model the flow of blood in the human heart. It has since proven to be a general and robust method for diverse flow problems arising in biology and engineering. Recently, the immersed boundary method has been applied to biological problems at the micro-scale or smaller, including swimming microorganisms and biomolecular motors. At these scales, the Stokes equations govern the dynamics of the surrounding fluid, and it is particularly important to represent accurately the hydrodynamic interactions that govern the motion of immersed bodies. In this thesis, we construct a new version of the immersed boundary method for Stokes flow. Our analysis of this new method sheds light on several fundamental questions about the immersed boundary method. In the new method, the structures are immersed in an infinite three-dimensional fluid; no artificial boundaries are necessary. Although we start from a discrete representation of the fluid on an infinite grid, we are able to eliminate the fluid variables and reduce the dynamics to that of a finite collection of Lagrangian points. Asymptotic methods reduce the computational cost and reveal the magnitudes of the numerical errors, as well as the dependence of these errors on the approximate delta function used to regularize singular sources.

We discuss the properties and the construction of these delta functions. We then study representations of simple rigid bodies: spheres and cylinders, by simplest-possible configurations of Lagrangian points, an isolated point for a sphere and a linear array of points for a cylinder. We use numerical experimentation to find how the physical parameters of these immersed bodies are related to the numerical parameters of the method. We find that the errors in our method are small if parameters are chosen appropriately, and we give recipes for parameter choices that should be helpful to future users.

Contents

Abstract iv

List of Figures vii

List of Tables xxix

1 Introduction **1**

2 An immersed boundary method for Stokes flow **7**

2.1 The continuous immersed boundary method 7

2.2 The discrete immersed boundary method 16

2.3 Constraints on motion 25

3 Asymptotics **31**

3.1 Expansion for the discrete Stokeslet 32

3.2 Computing the derivatives of $\mathcal{T}$ 48

3.3 Expansion for the Lagrangian Green's function 52

3.4 Numerical experiments 72

3.4.1 Expansion for $\mathcal{S}$ 72

3.4.2 Expansion for $\mathcal{G}$ 93

4 The approximate delta function **125**

4.1 Form of the delta function 126

4.2 Conditions on the delta functions 129

4.3 Derivation of the delta functions 139

4.4 Conditions in Fourier space 152

5 Simple bodies **169**

5.1 Representing a sphere 174

5.2 Representing a cylinder 191

5.2.1 Computing the resistance matrix 191

5.2.2 Choosing the number of immersed boundary points . . 195

5.2.3 Comparing to the results for a cylinder 206

5.2.4 Comparing velocity fields 213

5.2.5 Results for very long cylinders 222

6 Conclusion **237**

6.1 Conclusion 237

7 Appendices **241**

7.1 Approximate delta functions 241

7.2 Quadrature method for the discrete stokeslet 249

7.3 Slender-body theory results 254

List of Figures

3.1 A two-dimensional representation of the two pieces into which we break the integration domain in equation (3.7). The first piece in this equation is shown in blue; the second is shown in green. Both pieces extend to infinity in the k direction. The green piece extends also in the l direction. The blue piece extends also from $-1/2$ to $1/2$ in the m direction, which is out of the page. The green piece extends from $-\infty$ to ∞ in the m direction when $|l| \geq 1/2$. It extends from $-\infty$ to $-1/2$ and also from $1/2$ to ∞ in the m direction when $|l| < 1/2$. 35

3.2 Plot showing convergence of the one-coordinate expansion for the discrete Stokeslet, $\mathcal{S}$. Shown are values of $E^M(\mathbf{x})$, the relative difference of the Stokeslet computed by quadrature and the Stokeslet computed by the one-coordinate expansion with M terms, for various values of M and for $\mathbf{x} = (x, 0, 0)$. Because $y = z = 0$, the odd terms in the expansion are identically zero, so we show only even values of M. Beyond $x = 10$, quadrature error begins to dominate for the expansions with larger M. 74

3.3 Same as previous plot, except on a log-log scale. The dashed line has slope -1. The dotted line has slope -11. 75

3.4 Plot showing $E^M(\mathbf{x})$ for the one-coordinate expansion for various M with $\mathbf{x} = (x, 1, 0)$. Now, the odd terms in the expansion are not zero, so we show both even and odd values of M. . . . 76

3.5 Same as previous plot, except on a log-log scale. The dashed line has slope 0. The dotted line has slope -5. 77

3.6 Plot showing $E^M(\mathbf{x})$ for the one-coordinate expansion for various M with $\mathbf{x} = (x, 1, 0)$. This plot shows larger values of M than the previous plot. 78

3.7 Plot showing $E^M(\mathbf{x})$ for the one-coordinate expansion for various M with $\mathbf{x} = (x, 7, 5)$. 79

3.8 Plot showing $E^M(\mathbf{x})$ for the one-coordinate expansion for various M with $\mathbf{x} = (x, 7, 5)$. This plot shows larger values of M than the previous plot, and quadrature error dominates almost immediately. 80

3.9 Plot showing convergence of the two-coordinate expansion for the discrete Stokeslet. Shown are values of $E^M(\mathbf{x})$, the relative difference of the Stokeslet computed by quadrature and the Stokeslet computed by the two-coordinate expansion with $2 \leq p + q \leq M$, for various values of M and for $\mathbf{x} = (x, x, 0)$. Because $z = 0$, the odd terms in the expansion are identically zero, so we show only even values of M. 84

3.10 Same as previous plot, except on a log-log scale. The dashed line has slope -1. The dotted line has slope -3. 85

3.11 Plot showing $E^M(\mathbf{x})$ for the two-coordinate expansion for various M with $\mathbf{x} = (x, x, 1)$. Now, the odd terms in the expansion are not zero, so we show even and odd values of M 86

3.12 Same as previous plot, except on a log-log scale. The dashed line has slope -1. The dotted line has slope -5. 87

3.13 Plot showing $E^M(\mathbf{x})$ for the two-coordinate expansion for various M with $\mathbf{x} = (x, x, 1)$. This plot shows larger values of M than the previous plot. Quadrature error begins to dominate almost immediately. 88

3.14 Plot showing convergence of the three-coordinate expansion for the discrete Stokeslet. Shown are values of $E^M(\mathbf{x})$, the relative difference of the Stokeslet computed by quadrature and the Stokeslet computed by the three-coordinate expansion with $3 \leq p+q+r \leq M$, for various values of M and for $\mathbf{x} = (x, x, x)$. The odd terms in the expansion are identically zero for any value of $\mathbf{x}$, so we show only even values of M. . . 90

3.15 Same as previous plot, except on a log-log scale. The dashed line has slope -3. The dotted line has slope -5. 91

3.16 Discrete moments, $M_n(X)$, and discrete alternating moments, $N_n(x)$, for the two representative delta functions. For both delta functions, $M_0 \equiv 1$ and $M_1 \equiv 0$. For δ_4^{IB}, we have additionally that $N_0 \equiv 0$. For δ_4^{M}, we have additionally that $M_2 \equiv M_3 \equiv 0$. 95

3.17 Plot showing $\mathcal{H}_p(X, X')$ for various values of p and for the delta function δ_4^{IB}. The quantity X varies while X' is fixed and $X' \in [0, 1)$. In actuality, $\mathcal{H}_p$ oscillates about zero as X increases with a period of approximately 2. Thus, we have plotted $|\mathcal{H}_p(X, X')|$ for those X such that $|\mathcal{H}(X, X')|$ has a local maximum. The dashed line has slope -3. The dotted line has slope -7. 96

3.18 Same plot as above except for the delta function δ_4^{M}. Again, X' is fixed in $[0,1)$, and we plot the local maxima of $|\mathcal{H}(X,X')|$. The dashed line has slope -1. The dotted line has slope -5. . 97

3.19 Plot comparing exact calculation of $\mathcal{H}_1(X,X')$ with the approximate calculation $\mathcal{H}_1^M(X,X')$. X' is fixed in $[0,1)$. We plot the local maxima of the error, E^M. The dashed line has slope -4. The dotted line has slope -8. 100

3.20 Same plot as above except for the delta function δ_4^{M}. The dashed line has slope -2. The dotted line has slope -6. Note that because we plot only the local maxima of E^M, the line segments connecting these maxima have no significance. The reason that some of the curves in this plot are jagged is that E^M sometimes has two local maxima with different magnitudes in a given period. 101

3.21 Plot showing, E^M, the error of $\mathcal{G}$ computed by the one-coordinate expansion for various values of M relative to $\mathcal{G}$ computed exactly. The delta function used is δ_4^{IB}. The coordinate X varies while Y, Z, X', Y', and Z' are all fixed in $[0,1)$. In actuality, E^M is oscillatory as X varies with period approximately equal to 1. We plot the local maxima of E^M. The dashed line has slope -2. The dotted line has slope -6. 103

3.22 Same plot as above except for the delta function δ_4^{M}. The dashed line has slope 0. The dotted line has slope -3. 104

3.23 Plot showing, E^M, the error of $\mathcal{G}$ computed by the two-coordinate expansion for various values of M relative to $\mathcal{G}$ computed exactly. We show only even values of M because for M even $E^M \approx E^{M+1}$. The delta function used is δ_4^{IB}. The coordinate X varies, and we set $Y = X$. Z, X', Y', and Z' are all fixed in $[0, 1)$. We plot the local maxima of E^M. The dashed line has slope -5. For large values of M and $X = Y$, the relative error is smaller than machine precision. 107

3.24 Same plot as above except for the delta function δ_4^{M}. The dashed line has slope -1. The dotted line has slope -5. The reason that some of the curves in this plot are jagged is that E^M sometimes has two local maxima with different magnitudes in a given period. 108

3.25 Plot showing, E^M, the error of $\mathcal{G}$ computed by the three-coordinate expansion for various values of M relative to $\mathcal{G}$ computed exactly. We show only even values of M because for M even $E^M = E^{M+1}$. Also E^2 is not pictured because it equals E^0. The delta function used is δ_4^{M}. The coordinate X varies, and we set $Y = X$ and $Z = X$. X', Y', and Z' are all fixed in $[0, 1)$. We plot the local maxima of E^M. The dashed line has slope -3. The dotted line has slope -5. 110

3.26 Plot showing $\mathcal{H}_p^0(X, X')$ for various values of p and for the delta function δ_4^{IB}. The quantity X varies while X' is fixed and $X' \in [0, 1)$. $\mathcal{H}_0^p$ is identically 1 when $p = 0$ and is identically 0 when $p = 1$. 113

3.27 Same plot as above except for the delta function δ_4^{M}. $\mathcal{H}_0^p$ is identically 1 when $p = 0$ and is identically 0 when $p = 1$, 2, or 3. 114

3.28 Plot showing, E_0^M, the error of $\mathcal{G}_0$ computed by the one-coordinate expansion for various values of M relative to $\mathcal{G}_0$ computed exactly. The delta function used is δ_4^{IB}. The coordinate X varies while Y, Z, X', Y', and Z' are all fixed in $[0, 1)$. Unlike the plots for E^M, this plot shows E_0^M for all values of X, not just those for which E_0^M is at a local maximum. We do not show the case $M = 1$ because E_0^1 is identically equal to E_0^0. The dashed line has slope -2. The dotted line has slope -6. 115

3.29 Same plot as above except for the delta function δ_4^{M}. Also, we now plot only the local maxima of E_0^M. We do not show the cases $M = 1$, 2, or 3 because E_0^M is identically equal to E_0^0 for these values of M. The dashed line has slope -4. The dotted line has slope -8. The reason that some of the curves in this plot are jagged is that E_0^M sometimes has two local maxima with different magnitudes in a given period. 116

3.30 Plot showing, E_0^M, the error of $\mathcal{G}_0$ computed by the two-coordinate expansion for various values of M relative to $\mathcal{G}_0$ computed exactly. The delta function used is δ_4^{IB}. The coordinate X varies, and we set $Y = X$. Z, X', Y', and Z' are all fixed in $[0, 1)$. This plot shows E_0^M for all values of X, not just those for which E_0^M is at a local maximum. We do not show the case $M = 1$ because E_0^1 is identically equal to E_0^0. The dashed line has slope -2. The dotted line has slope -6. . 117

3.31 Same plot as above except for the delta function δ_4^{M}. Also, we now plot only the local maxima of E_0^M. We do not show the cases $M = 1$, 2, or 3 because E_0^M is identically equal to E_0^0 for these values of M. The dashed line has slope -4. The dotted line has slope -8. The reason that some of the curves in this plot are jagged is that E_0^M sometimes has two local maxima with different magnitudes in a given period. 118

3.32 Plot showing, E_0^M, the error of $\mathcal{G}_0$ computed by the three-coordinate expansion for various values of M relative to $\mathcal{G}_0$ computed exactly. The delta function used is δ_4^{IB}. The coordinate X varies, and we set $Y = X$ and $Z = X$. X', Y', and Z' are all fixed in $[0, 1)$. This plot shows E_0^M for all values of X, not just those for which E_0^M is at a local maximum. We do not show the case $M = 1$ because E_0^1 is identically equal to E_0^0. The dashed line has slope -2. The dotted line has slope -6. 119

3.33 Same plot as above except for the delta function δ_4^{M}. Also, we now plot only the local maxima of E_0^M. We do not show the cases $M = 1$, 2, or 3 because E_0^M is identically equal to E_0^0 for these values of M. The dashed line has slope -4. The dotted line has slope -8. The reason that some of the curves in this plot are jagged is that E^M sometimes has two local maxima with different magnitudes in a given period. 120

4.1 Plot of ϕ_d^{M}, which have maximum moment order. 143

4.2 Plot of ϕ_d^{IB}, which are traditionally used in the immersed boundary method. Though these functions may appear to have derivative discontinuities, they are in fact C^1. 147

4.3 Plot of $\phi_d^{m,a,s}$, for various numbers of moment conditions, m, and alternating moment conditions, a, satisfied by ϕ, and for ϕ satisfying or not satisfying the sum of squares condition (respectively $s = 1$ and $s = 0$). 151

5.1 Histograms of the effective radii a obtained for various delta functions and discretization methods. Upper left: δ_4^{IB} and the finite difference discretization. Upper right: δ_4^{IB} and the spectral discretization. Lower left: δ_4^{M} and the finite difference discretization. Note the drastically different horizontal scale of this plot from those of the plots above (see also figure 5.2). Lower right: δ_6^{IB} and the finite difference discretization. For definitions of these functions, see chapter 4. 177

5.2 Comparison of the effective radii obtained for δ_4^{IB} (blue line) and δ_4^{M} (green line). The plot on the left shows the probability density function of the scaled effective radius $a/\overline{a}$ for the two delta functions, inferred from the a obtained from 10,000 randomly selected locations of the immersed boundary point. The plot on the right shows the cumulative distribution function. 178

5.3 Histograms of ϵ, the error in the computed resistance matrices relative the that of a sphere of radius $\overline{a}$, obtained for various delta functions and discretization methods. Upper left: δ_4^{IB} and the finite difference discretization. Upper right: δ_4^{IB} and the spectral discretization. Lower left: δ_4^{M} and the finite difference discretization. Note again the drastically different horizontal scale of this plot from those of the plots above. Lower right: δ_6^{IB} and the finite difference discretization. 181

5.4 Summary of results obtained with various delta functions and discretization methods. For the purpose of visual clarity, the legends omit the subscript d on the delta functions. The maximum relative error in the resistance matrix $\overline{\epsilon}$ is plotted on a logarithmic scale against the mean effective radius $\overline{a}$. Each data point corresponds to one particular choice of delta function. Points with the same symbol and color correspond to delta functions in the same family. Within each family, delta functions with larger support have *smaller* $\overline{a}$ and smaller $\overline{\epsilon}$. Left: results obtained with the finite difference discretization method. Right: results obtained with the spectral discretization method. These two sets of results are nearly indistinguishable. For definitions of these functions, see chapter 4. . . 182

5.5 Results obtained using δ_4^{IB} and the finite difference discretization. Two-dimensional slice of the three-dimensional vector field $\mathbf{u}$, for $\mathbf{F} = \hat{x}$. For clarity, the velocity field has been translated by $-\mathbf{U}$, so the immersed boundary point is at rest and there is a flow of $-\mathbf{U}$ at infinity. The red circle shows the effective surface of the sphere represented by the immersed boundary point. This sphere has radius $\overline{a}$, which we found earlier by measuring the drag on immersed boundary points at many locations. 189

5.6 Results obtained using δ_4^{IB} and the finite difference discretization. Relative error in $\mathbf{u}$ is plotted as a function of distance from the center of the sphere, averaged over cubic shells. Distance is measured in the infinity norm. The error decays rapidly with distance and is under 5 percent even at a distance of 2 grid cells. 190

5.7 Results for high densities of immersed boundary points. The solid lines show mean drag in the normal (shown in green) and tangential (shown in blue) directions as a function of immersed boundary point density ρ. $L = 20$, and we use the finite difference discretization. Dashed lines show the maximum and minimum drags in these directions. Upper left: results for δ_4^{IB}. Upper right: results for δ_4^{M}. Lower left: results for δ_6^{IB}. In all cases, as ρ becomes very large, the mean, maximum, and minimum drags seem to converge to a finite limit. At this limit, the drags depend significantly on the position and orientation of the pseudo-cylinder. 197

5.8 Results for low densities of immersed boundary points. Plots showing drags for δ_4^{IB} and the finite difference discretization as a function of immersed boundary point density. Solid lines show mean drags. Dashed lines show maximum and minimum drags. Results are shown for $L = 10$ (blue), 20 (green), 30 (red), 40 (yellow), and 50 (cyan). Upper left: tangential drag. Upper right: normal drag. Lower left: rotational drag. Lower right: off-diagonal element of $\mathcal{R}$ showing drag in one normal direction as a result of velocity in the orthogonal normal direction. We note that the qualitative behavior of the drags seems to depend only on ρ, and not on L and N independently. Moreover, there is a range of densities, $0.4 < \rho < 1.0$, where the drags are approximately constant, independent of position and orientation, and where there is little off-diagonal coupling. 198

5.9 Plots showing normal drags for different delta functions and discretization methods as a function of immersed boundary point density. Solid lines show mean drags. Dashed lines show maximum and minimum drags. Results are shown for $L =$ 10 (blue), 20 (green), 30 (rid), 40 (cyan), and 50 (magenta) with shorter lengths represented by darker lines. Upper left: δ_4^{IB} and the spectral discretization. The remaining plots use the finite difference discretization. Upper middle: δ_4^{M}. Upper right: δ_4^{D}. Lower left: δ_6^{IB}. Lower middle: δ_6^{M}. Lower right: δ_5^{IB}. The results are similar to those for δ_4^{IB} with the finite difference discretization shown in figure 5.8. 200

5.10 Position and orientation dependence of the pseudo-cylinder resistance matrices as a function of the density ρ. The quantity $\overline{\sigma}$ is a measure of maximum relative deviation (see equation (5.5)). For delta functions in the families δ_d^{IB} with d odd or even, $\overline{\sigma}$ is small when ρ is less than 1. Delta functions in the family δ_d^{M} never have $\overline{\sigma}$ below 10 percent, though $\overline{\sigma}$ still has a local minimum at a density of about 1. 202

5.11 Position and orientation dependence of the pseudo-cylinder resistance matrices as a function of the length L at the preferred immersed boundary point density. Solid lines show $\overline{\sigma}$ for the finite difference discretization. Dashed lines show $\overline{\sigma}$ for the spectral discretization. Blue lines show results for δ_4^{IB}, green lines show results for δ_6^{IB}, red lines show results for δ_4^{M}, and cyan lines show results for δ_6^{M}. Note the difference in vertical scale between the plots on the left and those on the right. The delta functions traditionally used in the immersed boundary method (left) result in deviations below 5 percent for the entire range of L. Deviations obtained with the delta functions in the family δ_d^{M} are much larger. 205

5.12 Mean drag on a pseudo-cylinder as a function of length compared to formulas from slender-body theory (equation (5.6)) for various delta functions and the finite difference discretization. The pseudo-cylinder results are shown by blue lines. The slender-body theory formulas are shown by green lines. The top row of plots shows drag in the tangential and normal directions. In all cases, normal drag is larger than tangential drag. (It is customary to say that the normal drag is twice the tangential drag, but this, in fact, is only true in the limit $\tilde{L} \to \infty$, and that limit is approached only slowly. See equation (5.6).) The bottom row shows drag in the rotational direction. Agreement is very good except at very small lengths, for which the slender-body theory formulas are not accurate. 210

5.13 Norm of the difference between the mean resistance matrix of a pseudo-cylinder and the resistance matrix obtained from the slender-body theory formulas as a function of length for various delta functions. The difference is small for all delta functions except at small lengths where slender-body theory is invalid. 212

5.14 Top: two-dimensional slice of the three-dimensional velocity field created by a pseudo-cylinder moving in the tangential direction. For clarity, the velocity has been translated so that the pseudo-cylinder is fixed and there is an incoming flow at infinity along the axis of the pseudo-cylinder. The red rectangle indicates the effective surface of the pseudo-cylinder. Note that the velocity is nearly zero on the effective surface of the pseudo-cylinder as dictated by the no-slip condition, and that the velocity is small inside the effective surface. Bottom: the slender-body theory approximation to the velocity field of a cylinder of radius r and length $\tilde{L}$ moving in the tangential direction. The velocity is defined to be identically zero inside the surface of the cylinder. The velocities near the endpoints of the cylinder may not be accurate. 215

5.15 The velocity field of a pseudo-cylinder (top) and the slender-body theory approximation to the velocity field of a cylinder (bottom) held fixed with an incoming flow in the normal direction from infinity. 216

5.16 The velocity field of a pseudo-cylinder (top) and the slender-body theory approximation to the velocity field of a cylinder (bottom) held fixed with an incoming linear shear flow from infinity. 217

5.17 This plot compares the velocity fields created by a pseudo-cylinder in the immersed boundary method and the slender-body approximation given in equation (5.7). Motion is in the tangential (blue), normal (green), and rotational (red) directions. We have used δ_4^{IB} and the finite difference discretization. Shown is the relative difference in these fields, plotted against distance from the axis of the cylinder in the infinity norm. These quantities have been averaged in the L_2 sense over rectangular shells of grid points. Even for the worst case, which is rotational motion, the relative difference is 11 percent at a distance of 1.5 grid cells from the axis of the cylinder, and quickly decays to 2 percent at a distance of twenty-five grid cells. For the translational cases, relative difference is small even inside the surface of the cylinder. 219

5.18 Position and orientation dependence of the pseudo-cylinder resistance matrices as a function of the length L at the preferred immersed boundary point density for very large values of L. The quantity $\overline{\sigma}$ is a measure of maximum relative deviation (see equation (5.5)). Results are shown for various delta functions and for the spectral discretization method. Those delta functions traditionally used in the immersed boundary method, shown on the left, generally perform better than those with maximum interpolation order, shown on the right. . . . 225

5.19 Same as the plot above, except the mean value of σ, the measure of position and orientation dependance, is shown instead of the maximum. Again, those delta functions traditionally used in the immersed boundary method, shown on the left, generally perform better than those with maximum interpolation order, shown on the right. 226

5.20 Position and orientation dependence of the pseudo-cylinder resistance matrices as a function of the length L for very large values of L. This plot compares $\overline{\sigma}$ for the preferred immersed boundary point density, with $\overline{\sigma}$ for double and triple the preferred density for various delta functions. Using a higher density of immersed boundary points results in greater position and orientation dependence. For the delta function δ_4^{IB}, σ was so large for some trials that we plot the maximum of σ excluding the largest 5 percent of trials. 227

5.21 Results for large values of L computed by asymptotic methods. Mean drag on a pseudo-cylinder as a function of length compared to formulas from slender-body theory (equation (5.6)) for various delta functions and the spectral discretization. The pseudo-cylinder results are shown by blue lines. The slender-body theory formulas are shown by green lines. The left column of plots shows drag in the tangential and normal directions. In all cases, normal drag is larger than tangential drag. The right column shows drag in the rotational direction. . . . 229

5.22 Norm of the difference between the mean resistance matrix of a pseudo-cylinder and the resistance matrix obtained from the slender-body theory formulas, ϵ, as a function of length for various delta functions and for very large values of L. . . 230

5.23 Best fit values of the pseduo-cylinder radius, r, and effective length correction, δL, for very large values of L and for various delta functions. 232

5.24 Norm of the difference between the mean resistance matrix of a pseudo-cylinder and the resistance matrix obtained from the slender-body theory formulas, ϵ, when the best fit values of r and δL are used as the parameters in the slender-body theory formulas. By best fit, we mean those values which minimize ϵ. The minimized value of ϵ is shown as a function of L for very large values of L. 233

7.1 Plot of ϕ with maximum moment order. 245

7.2 Plot of ϕ traditionally used in the immersed boundary method. 248

7.3 Relative errors in the quadrature method to compute $\mathcal{S}_1(\mathbf{x})$. The dashed line shows ϵ_1, the error obtained using a number of quadrature points characterized by $N_q = 16$ relative to $N_q = 64$. The solid line shows ϵ_2, the error obtained using $N_q = 32$ relative to $N_q = 64$. These errors are functions of $\mathbf{x}_1$, the distance from the origin in the x direction, and they are averaged over $\mathbf{x}_2$ and $\mathbf{x}_3$, the distances in the y and z directions. The vertical axis shows a logarithmic scale. The computations in this appendix were performed using $N_q = 32$, so the solid line shows the relative error in $\mathcal{S}_1(\mathbf{x})$ for these computations. The errors increase exponentially as $\mathbf{x}_1$ increases, but we still obtain six digits of accuracy at $\mathbf{x}_1 = 60$. 255

List of Tables

5.1 Reference table of results for the various delta functions and discretization methods used in this appendix. Shown are the computed effective radius of an immersed boundary point meant to represent a sphere, $\overline{a}$, and the maximum relative error in the resistance matrix of a point meant to represent a sphere, $\overline{\epsilon}$. These numbers are computed for the case $h = 1$. For general h, the radii should be multiplied by h. The delta functions are arranged by family with different families separated by horizontal lines. 185

Chapter 1

Introduction

In numerical computations it is tempting, but dangerous, to use numerical parameters (such as grid spacing) for the representation of physical quantities (such as the radius of an immersed elastic filament). In this thesis, we validate such a procedure for the immersed boundary method as applied to slender bodies and spheres in a Stokes fluid. Another contribution of the present thesis is that we solve the Stokes equations in the presence of immersed bodies on an *unbounded* domain. This is particularly important at zero Reynolds number because of the long-range character of interactions in Stokes flow.

The immersed boundary method has been used to simulate diverse systems involving the interaction of fluid and elastic structure [27, 24, 20, 26, 17, 25]. Recently the method has been used for modeling cellular and sub-cellular biological processes that occur at very low Reynolds number [9, 4, 8, 22]. Many such applications contain objects that might be represented as slender

bodies or particles immersed in fluid. Examples of slender bodies include the tails of spermatozoa, eukaryotic cilia, bacterial flagella, microtubules, chromosomes, and strands of DNA and RNA. Objects such as cells, cell organelles, and individual protein molecules might, at a low level of detail, be represented as spherical particles. Outside biology, the immersed boundary method has been used in studying particle and filament suspensions at low Reynolds number [12, 31, 30]. At larger scales, fibers are the basic constituents of many biological tissues, and many higher Reynolds number immersed boundary method computations involve elastic structures that are constructed of fibers [26].

Slender bodies in the immersed boundary method have often been represented in a particularly simple way. Instead of using a two or three-dimensional mesh of Lagrangian immersed boundary points to define the position of the body, a linear array of points is used [22, 11, 35]. In practice, this is what is meant when it is said that a body is constructed of fibers. Particles, in some applications, have been represented as a single immersed boundary point [12, 2]. Moreover, single immersed boundary points have often been used to visualize flow in the immersed boundary method.

There is a vast computational savings associated with using these simple representations of spheres and slender bodies. Many fewer immersed boundary points are needed to represent a body, the configuration of points is simple, and, for slender bodies, it is easy to specify arbitrary elastic behavior in response to stretching and bending. Also, the spacing of the Eulerian fluid

grid is typically on the order of the spacing of the Lagrangian mesh, so using a complicated mesh requires refining the fluid grid significantly. The time step must then be reduced accordingly. In three dimensions, this refinement is exceedingly costly. Moreover, a complicated Lagrangian mesh is likely to introduce extra stiffness constraints that require even a further reduction in the time step.

Some questions may arise about the approach of using these simple representations. If a single immersed boundary point is meant to represent a sphere, what is sphere's radius? What is the radius of a slender body represented by a one-dimensional array of immersed boundary points? How many points should be used? Finally, is this method accurate and consistent as the immersed boundary points change their position and, in the case of a slender body, their collective orientation relative to the Eulerian fluid grid?

In this thesis, we attempt to answer these questions. We focus on the case of zero Reynolds number because many interesting applications occur in this regime and because results from slender-body theory are available for comparison. We first develop a numerical method in chapter 2 to solve the Stokes equations on an infinite three-dimensional grid. We do this by calculating the Green's function for the discretized equations. Coupling this calculation to the immersed boundary method allows us to calculate the linear relationship between the forces that a given configuration of immersed boundary points apply to the fluid and the resulting velocities of those points. We formulate our method for rigid bodies, though it could be used for bodies

that can change shape. Rigid bodies pose the additional problem that a constraint force must arise to maintain the body's rigidity. We calculate the resistance matrix of the body, which gives the linear relationship between the translational and rotational velocities of the body and the forces and torques applied. We are also able to calculate the velocity at any point in the fluid grid created by the motion of the body.

In section 5.1, we use this method to study the interaction with the fluid of a single Lagrangian point to which an external force is applied. We compare the computed results to the exact solution for Stokes flow around a sphere. We show that, for certain choices of the approximate delta function used in the immersed boundary method, the resistance matrix is close to that of a sphere of some particular radius and is essentially independent of the location of the Lagrangian point with respect to the Eulerian grid. We call the radius of this sphere the effective radius of an immersed boundary point. We also calculate the velocity field generated by a translating point and show that it is close to that created by a translating sphere whose radius is the effective radius.

In section 5.2, we study the interaction with the fluid of a linear array of Lagrangian points that are constrained to move as a rigid body, and we compare results to those of slender-body theory for a rigid cylinder. We show that there is a range of preferred densities of immersed boundary points relative to the Eulerian grid spacing. At these densities the interactions of the Lagrangian array with the fluid are essentially independent of the

position and orientation of the array relative to the Eulerian grid. Also, the resistance matrix of such an array is close to that of the slender-body theory approximation for a rigid cylinder of some effective radius. Given the effective radius of a sphere represented by a single immersed boundary point, we determine the effective radius of the cylinder by a mathematical argument, and do so without fitting parameters. We show that the computed and slender-body velocity fields in the fluid are in good agreement as well.

We conclude that simple representations of spheres and rigid cylinders in the immersed boundary method can be used with only a small loss of accuracy and with large computational savings. Our results suggest that this conclusion will hold for slender bodies with curvature or which are non-rigid. Moreover, we identify values of the relevant parameters, such as the effective radius of an immersed boundary point and the effective radius and length of an array of points. The radii are proportional to the Eulerian grid spacing, so this grid spacing can be chosen so as to represent a sphere or cylinder of arbitrary radius. Spheres and cylinders of several different radii may be represented simultaneously if several different approximate delta functions are used.

In principle, our numerical method works for an arbitrary discretization of the Stokes equations, and we investigate both a second order finite difference discretization and a spectral discretization. We find that these two discretizations give nearly identical qualitative results and very similar quantitative results. Our method also makes sense for an arbitrary choice of the

approximate delta function. We investigate a variety of delta functions, and find that the delta functions conventionally used in the immersed boundary method give superior performance when compared to higher order delta functions of the same support. In particular, the sensitivity of results to position and orientation relative to the grid is much smaller when the conventional immersed boundary delta functions are used.

Chapter 2

An immersed boundary method for Stokes flow

2.1 The continuous immersed boundary method

We begin by formulating the immersed boundary method as a system of partial differential equations in continuous variables. Later, we discuss the discretization of these equations. We wish to describe the coupled dynamics of elastic or solid structure immersed in an infinite fluid. Together, the fluid and the structure occupy all of $\mathbb{R}^3$.

It is typical for the immersed boundary method to be formulated for a fluid occupying a finite domain. Doing so is necessary when the Reynolds number is finite and the Navier–Stokes equations for the fluid are used. We here focus on the case of zero Reynolds number and use the Stokes equations.

One goal of this work is to construct a solution method for the discretized equations on an infinite domain. There are several advantages to using an infinite domain for analysis of the immersed boundary method and for modeling problems where the nature of the true fluid boundaries is ambiguous or unknown. Because of the long-range nature of hydrodynamic interactions for the Stokes equations, fluid boundaries can have significant effects, even when they are far from the immersed structure. Eliminating boundaries isolates the fluid-structure interactions and so results in a simpler model. Existing exact solutions for Stokes flow around bodies assume an infinite fluid, and other Green's function based methods for bodies in Stokes flow typically require an infinite fluid. Accurate comparison with these results requires an immersed boundary method in an infinite domain. Finally, in an infinite domain we expect the hydrodynamics of immersed bodies to be invariant to translations and rotations. This reduces the dimensionality of the parameter space when considering flow past a body and also is something we can check to verify the accuracy of the discretized immersed boundary method.

The immersed boundary method uses both Eulerian and Lagrangian coordinates. The Eulerian variable $\mathbf{x}$ specifies a position in space, either in the fluid region or in the region occupied by the structure. A Lagrangian description is needed only for the structure. A material element of the structure is assigned the Lagrangian label $\mathbf{q}$ and we denote the set of all labels Ω. The function $\mathbf{X}(\mathbf{q}, t)$ maps the label to the corresponding element's position in space at time t. We let $\mathbf{U}(\mathbf{q}, t)$ be the velocity of the element with label

$\mathbf{q}$ at time t, then

$$\mathbf{U}(\mathbf{q},t) = \frac{\partial}{\partial t}\mathbf{X}(\mathbf{q},t). \tag{2.1}$$

Let $\mathbf{u}(\mathbf{x},t)$ be the Eulerian velocity at position $\mathbf{x}$ and time t, where $\mathbf{x}$ may be either in the fluid region or in $\Omega(t)$. We must have

$$\mathbf{U}(\mathbf{q},t) = \mathbf{u}(\mathbf{X}(\mathbf{q},t),t) \tag{2.2}$$

which, for later discretization, it is convenient to express as

$$\mathbf{U}(\mathbf{q},t) = \int_{\mathbb{R}^3} \mathbf{u}(\mathbf{x},t)\delta(\mathbf{X}(\mathbf{q},t) - \mathbf{x})\mathbf{dx} \tag{2.3}$$

where δ is the three-dimensional Dirac delta function.

We make several assumptions about the nature of the fluid and the solid structure. The fluid is assumed isotropic, homogeneous, Newtonian, and incompressible and is assumed to have uniform density ρ. The structure is also assumed to be incompressible with uniform density ρ. Shearing motions of the structure are assumed to induce viscous stresses with effective viscosity equivalent to that of the fluid. Other sorts of stresses may also be created by the structure, for instance by its elastic properties. This assumption allows us to use a single Eulerian equation with constant coefficients to describe momentum conservation in both the fluid region and in the region occupied by the structure. In the case of rigid bodies, there are no internal shears so this assumption is superfluous. For elastic bodies, this assumes the bodies have

viscoelastic properties similar to that of the surrounding fluid. The viscous forces, however, depend on Eulerian motions of the body, not Lagrangian, which is atypical for a viscoelastic solid. If elastic deformations are small, these will be approximately equivalent. Additionally, if one considers solid structure that is permeated by fluid, a typical situation for biological tissues, one might expect this structure to exhibit viscoelastic properties that can be represented as the sum of the viscous stresses produced by the fluid and additional viscous or elastic stresses created by the structure. The immersed boundary method uses exactly such a sum to represent the viscoelastic properties of the structure. Versions of the immersed boundary method have been constructed which relax some of these assumptions, for instance by allowing the fluid and structure to have different densities [35, 19]. Other assumptions could be relaxed in principle, though doing so may be difficult in practice.

We mentioned that the solid structure may create additional internal or surface stresses. In particular we suppose the structure produces Lagrangian force density $\mathbf{F}(\mathbf{q}, t)$, meaning that the total force produced by elements in a subset of Ω can be found by integrating $\mathbf{F}$ with respect to $\mathbf{q}$. We formally allow $\mathbf{F}$ to be infinite on the structure surface, provided it is in $L^1(\Omega)$. We can convert $\mathbf{F}$ to an equivalent Eulerian force density, $\mathbf{f}(\mathbf{x}, t)$ by multiplying by the appropriate Jacobian.

$$\mathbf{F}(\mathbf{q}, t) = \left| \frac{\partial \mathbf{X}}{\partial \mathbf{q}} \right| (\mathbf{q}, t)\, \mathbf{f}(\mathbf{X}(\mathbf{q}, t), t) \tag{2.4}$$

For later discretization, it is convenient to express this equality as

$$\mathbf{f}(\mathbf{x},t) = \int_\Omega \mathbf{F}(\mathbf{q},t)\delta(\mathbf{X}(\mathbf{q},t)-\mathbf{x})\mathbf{dq}. \tag{2.5}$$

This equation is taken to be valid for all $\mathbf{x} \in \mathbb{R}^3$. This makes $\mathbf{f}$ equal to zero in the region occupied by the fluid.

Because the fluid and structure are everywhere incompressible, we have for all values of $\mathbf{x} \in \mathbb{R}^3$

$$\nabla \cdot \mathbf{u} = 0. \tag{2.6}$$

The Eulerian equation of momentum conservation is

$$\rho(\mathbf{u}_t + \mathbf{u}\cdot\nabla\mathbf{u}) + \nabla p = \mu\Delta\mathbf{u} + \mathbf{f}. \tag{2.7}$$

Throughout this thesis, subscripts indicate partial differentiation. The variable p is pressure, which serves to enforce the incompressibility of both the fluid and the structure. The parameter μ is the viscosity which, we have assumed, is constant for all $\mathbf{x}$. Equations (2.7) and (2.6) together are the familiar Navier–Stokes equations with an applied force density. Our assumptions and our definition of $\mathbf{f}$ imply that these equations are valid for all $\mathbf{x}$ in the interiors of the regions occupied by the fluid or structure. We take the boundary condition at the interface of these two regions to be that $\mathbf{u}$ is continuous, which is the no-slip condition. Derivatives of $\mathbf{u}$ may be discontinuous if there are forces concentrated on the interface, so that $\mathbf{f}$ is singular on

the interface. If we assume that equation (2.7) is also valid at the interface of these two regions, this equation will automatically enforce the no-slip condition as well as the appropriate jump conditions for derivatives of the velocity generated by surface forces. We take the boundary condition at infinity to be that $\mathbf{u}$ and p decay to zero. For this condition to make sense, we insist that the structure at all times occupies a bounded region of $\mathbb{R}^3$.

The boundary condition at infinity, the kinematic equation, (2.1), the Eulerian equations of motion, (2.6) and (2.7), the equations connecting the Eulerian and Lagrangian variables, (2.3) and (2.5), along with a specification of how $\mathbf{F}$ is determined constitute a complete system of equations governing the fluid and structure. If the dynamics generated by these equations generate fluid motions with typical spatial scale L and typical velocity U, we can identify the Reynolds number, R, a non-dimensional parameter that characterizes the motion.

$$R = \frac{\rho U L}{\mu} \tag{2.8}$$

There may be more non-dimensional parameters of interest related to the elastic properties of the structure. For this thesis, we are interested in the case in which the Reynolds number is small and so the inertia of the fluid may be neglected and also in the case in which the inertia of the structure may also be neglected. This implies that any elastic vibrations of the structure are strongly overdamped. If these assumptions are true, we may replace the Navier–Stokes equations, in particular equation (2.7), by the Stokes equa-

tions, which are equation (2.6) along with

$$\nabla p = \mu \Delta \mathbf{u} + \mathbf{f}. \tag{2.9}$$

The Stokes equations have the advantage of being linear, so that Green's function techniques may be applied to them. Also, the Stokes equations contain no time derivates. Time appears only as a parameter. This means that solutions of the equations are determined instantaneously by the value of $\mathbf{f}$ and the boundary conditions. The biological systems we are interested in modeling have length scales on the order of 10^{-2} cm or smaller, velocity scales on the order of 10^{-1} cm/s or slower, and exist in fluids *at least* as viscous as water ($\mu \approx 0.01$ g/cm·s) and with roughly the same density as water ($\rho = 1.0$ g/cm^3). The Reynolds numbers of these problems are therefore at most 10^{-1} and often much smaller. Many other problems of scientific and practical interest occur at low Reynolds numbers, as described in detail in the introduction to this thesis.

We have a complete system of equations. We now describe their solution and some of their properties. The Stokes equations are linear and constant-coefficient, so they have a Green's function known as the Stokeslet, which we denote by $\mathcal{S}_0$.

$$\mathcal{S}_0(\mathbf{x}) = \frac{1}{8\pi\mu} \frac{\mathcal{I} + \hat{\mathbf{x}}\hat{\mathbf{x}}^{\mathrm{T}}}{|\mathbf{x}|} \tag{2.10}$$

The symbol $\mathcal{I}$ denotes the 3×3 identity matrix. Throughout this thesis, for any vector $\mathbf{v}$, $\hat{\mathbf{v}}$ denotes the unit vector pointing in the direction of $\mathbf{v}$,

so $\hat{\mathbf{x}} = \mathbf{x}/|\mathbf{x}|$. The Stokeslet is matrix valued because, for each $\mathbf{x}$, it is the linear transformation from the force at the origin to the velocity at $\mathbf{x}$. If $\mathbf{v}$ is any fixed vector in $\mathbb{R}^3$, the Stokeslet formally satisfies the following system of equations

$$\nabla p = \mu \Delta \mathcal{S}_0(\mathbf{x})\mathbf{v} + \mathbf{v}\delta(\mathbf{x}) \tag{2.11}$$

$$\nabla \cdot \mathcal{S}_0(\mathbf{x})\mathbf{v} = 0 \tag{2.12}$$

where the pressure is given by

$$p(\mathbf{x}) = \frac{1}{4\pi} \frac{\mathbf{x} \cdot \mathbf{v}}{|\mathbf{x}|^3}. \tag{2.13}$$

Given $\mathbf{f}$, we can solve for $\mathbf{u}$.

$$\mathbf{u}(\mathbf{x}) = \int_{\mathbb{R}^3} \mathcal{S}_0(\mathbf{x} - \mathbf{x}')\mathbf{f}(\mathbf{x}')\mathbf{dx}' \tag{2.14}$$

Combining equation (2.14) with equations (2.3) and (2.5) gives a Green's function, $\mathcal{G}_0$, relating the Lagrangian variables $\mathbf{F}$ and $\mathbf{U}$.

$$\mathcal{G}_0(\mathbf{q}, \mathbf{q}') = \iint_{\mathbb{R}^6} \delta(\mathbf{X}(\mathbf{q}) - \mathbf{x})\mathcal{S}_0(\mathbf{x} - \mathbf{x}')\delta(\mathbf{X}(\mathbf{q}') - \mathbf{x}')\mathbf{dx}\,\mathbf{dx}' \tag{2.15}$$

$$\mathbf{U}(\mathbf{q}) = \int_{\Omega} \mathcal{G}_0(\mathbf{q}, \mathbf{q}')\mathbf{F}(\mathbf{q}')\mathbf{dq}' \tag{2.16}$$

In fact this Green's function is simply the Stokeslet evaluated at $\mathbf{X}(\mathbf{q})-\mathbf{X}(\mathbf{q}')$.

$$\mathcal{G}_0(\mathbf{q},\mathbf{q}') = \mathcal{S}_0(\mathbf{X}(\mathbf{q}) - \mathbf{X}(\mathbf{q}')) \tag{2.17}$$

Equation (2.15) is written out for the purpose of comparing with the discretized version derived in the next section. For the discretized version, it will not be the case that the Green's function relating the Lagrangian variables is a function of $\mathbf{X}(\mathbf{q}) - \mathbf{X}(\mathbf{q}')$.

A convenient property of the Stokeslet is its scaling behavior, which comes from the scale invariance of the Stokes equations.

$$\mathcal{S}_0(\mathbf{x}) = \lambda\mathcal{S}_0(\lambda\mathbf{x}) \tag{2.18}$$

If $\mathbf{X}' = \lambda\mathbf{X}$, this scaling is inherited by the the Lagrangian Green's function.

$$\mathcal{G}_0(\mathbf{q},\mathbf{q}') = \lambda\mathcal{G}_0'(\mathbf{q},\mathbf{q}') \tag{2.19}$$

Another convenient property of the Stokeslet is its Fourier space representation, obtained by solving the Stokes equations, in particular equations (2.11) and (2.12), using the Fourier transform.

$$\mathcal{S}_0(\mathbf{x}) = \int_{\mathbb{R}^3} \frac{1}{4\pi^2\mu|\mathbf{k}|^2}(\mathcal{I} - \hat{\mathbf{k}}\hat{\mathbf{k}}^{\mathrm{T}})e^{2\pi i\mathbf{k}\cdot\mathbf{x}}\mathbf{dk} \tag{2.20}$$

2.2 The discrete immersed boundary method

We now discretize the Stokes equations on an *infinite* Eulerian grid with uniform grid-spacing h.

$$\mathbf{D}_h p = \mu \mathrm{L}_h \mathbf{u} + \mathbf{f} \tag{2.21}$$

$$\mathbf{D}_h \cdot \mathbf{u} = 0 \tag{2.22}$$

The variables $\mathbf{u}$, p, and $\mathbf{f}$ are now defined on the grid. The discrete divergence operator for functions on the grid is denoted by $\mathbf{D}_h$, and the discrete Laplacian operator by L_h. The exact choices of $\mathbf{D}_h$ and L_h do not affect how we solve the system, provided they satisfy reasonable assumptions. In our computations, we use two different choices so that we can check if our results depend on the discretization method used. One choice uses the second order centered finite difference operator for the gradient, $\mathbf{D}_h^{\mathrm{f}}$, and the second order seven-point finite difference discretization of the Laplacian, $\mathrm{L}_h^{\mathrm{f}}$. The other choice uses spectral differentiation for the gradient, $\mathbf{D}_h^{\mathrm{s}}$, and the spectral Laplacian, $\mathrm{L}_h^{\mathrm{s}}$. The boundary conditions continue to be that $\mathbf{u}$ and p approach zero as $|\mathbf{x}|$ approaches infinity.

The solid body is discretized into a Lagrangian mesh of what we call immersed boundary points. The variable $\mathbf{q}$ is now an element of a finite index set, Ω. The position of an immersed boundary point, $\mathbf{X}(\mathbf{q})$, need not be a point on the Eulerian grid. We do not, at this time, specify a discretization in time of the kinematic equation (2.1).

Each immersed boundary point is assigned a quadrature weight so that the integral in equation (2.5) may be approximated. We do not here specify how this would be done for a particular problem. To simplify the notation, we absorb the quadrature weights into $\mathbf{F}$ so that $\mathbf{F}(\mathbf{q})$ is the total force applied by the immersed boundary point $\mathbf{q}$ instead of the force density. In general, the immersed boundary points will not lie on the Eulerian grid, so there is no trivial notion of the Eulerian velocities, $\mathbf{u}$, and Lagrangian velocities, $\mathbf{U}$, being equal at corresponding points. Instead, the Lagrangian velocities are interpolated from the Eulerian grid by an approximate Dirac delta function, δ_h. Similarly, the Lagrangian force $\mathbf{F}$ is spread to the Eulerian grid by δ_h, producing the Eulerian force density $\mathbf{f}$.

$$\mathbf{U}(\mathbf{q}) = \sum_{\mathbf{x}\in(h\mathbb{Z})^3} \mathbf{u}(\mathbf{x})\delta_h(\mathbf{X}(\mathbf{q}) - \mathbf{x})h^3 \tag{2.23}$$

$$\mathbf{f}(\mathbf{x}) = \sum_{\mathbf{q}\in\Omega} \mathbf{F}(\mathbf{q})\delta_h(\mathbf{X}(\mathbf{q}) - \mathbf{x}) \tag{2.24}$$

It is customary to use the same approximate delta function for both interpolation of velocity and force spreading. Doing so makes spreading the dual operation to interpolation and guarantees that the rate of work done on the structure is the same in Eulerian and Lagrangian coordinates [26].

$$\sum_{\mathbf{x}\in(h\mathbb{Z})^3} \mathbf{f}(\mathbf{x}) \cdot \mathbf{u}(\mathbf{x})h^3 = \sum_{\mathbf{q}\in\Omega} \mathbf{F}(\mathbf{q}) \cdot \mathbf{U}(\mathbf{q}) \tag{2.25}$$

One goal of this work is to test the performance of a variety of approx-

imate delta functions that are in current use and also to construct and test the performance of new approximate delta functions. These functions are discussed in detail in chapter 4.

The discrete Stokes equations, (2.21) and (2.22), the kinematic equation, (2.1), and the discrete equations connecting the Eulerian and Lagrangian variables, (2.23) and (2.24), along with a specification of how $\mathbf{F}$ is determined, constitute the complete discretized system. We now describe the solution of this system.

The discrete Stokes equations are linear difference equations with constant coefficients, so a Green's function must exist. This function, which we refer to as the discrete Stokeslet, $\mathcal{S}$, allows us to solve for $\mathbf{u}$ in terms of $\mathbf{f}$.

$$\mathbf{u}(\mathbf{x}) = \sum_{\mathbf{x}' \in (h\mathbb{Z})^3} \mathcal{S}(\mathbf{x} - \mathbf{x}')\mathbf{f}(\mathbf{x}')h^3 \tag{2.26}$$

Finding $\mathcal{S}$ requires solving the discretized Stokes equations with $\mathbf{f}$ equal to zero except at the origin where it is equal to one of the standard basis vectors of $\mathbb{R}^3$. This is an elliptic system of difference equations with infinitely many variables. Solving such a system is a seemingly difficult task. However, as in the case of equation (2.20) for the Stokeslet, we can find a Fourier space representation of the discrete Stokeslet by taking the Fourier transform of the difference equations.

$$\mathcal{S}(\mathbf{x}) = \frac{1}{h\mu} \int_{\left[-\frac{1}{2},\frac{1}{2}\right]^3} \frac{1}{\alpha(\mathbf{k})} (\mathcal{I} - \hat{\mathbf{g}}(\mathbf{k})\hat{\mathbf{g}}(\mathbf{k})^{\mathrm{T}}) e^{2\pi i \mathbf{k}\cdot\mathbf{x}/h} \mathbf{dk} \tag{2.27}$$

The functions α and $\mathbf{g}$ depend on which discretization method is used for the Stokes equations. For the finite difference discretization

$$\alpha^{\mathrm{f}}(\mathbf{k}) = 4|\sin(\pi\mathbf{k})|^2, \qquad \mathbf{g}^{\mathrm{f}}(\mathbf{k}) = \sin(2\pi\mathbf{k}). \tag{2.28}$$

For the spectral discretization

$$\alpha^{\mathrm{s}}(\mathbf{k}) = 4\pi^2|\mathbf{k}|^2, \qquad \mathbf{g}^{\mathrm{s}}(\mathbf{k}) = \mathbf{k}. \tag{2.29}$$

These agree to second order when $|\mathbf{k}|$ is small.

The discrete Stokeslet is a real symmetric 3×3 matrix valued function of $\mathbf{x}$, which takes values on the infinite Eulerian grid. The integral in equation (2.27) converges absolutely for any consistent discretization of the Stokes equations, even though there is a singularity of degree two at the origin.

One way to calculate $\mathcal{S}$ is to compute these integrals, one instance of equation (2.27) for each grid point $\mathbf{x}$, by numerical quadrature. In chapter 3 we describe another method that is more efficient for large $|\mathbf{x}|$. Several observations simplify the task of computing these integrals. First, we make use of the scaling behavior of the discrete Stokeslet with respect to h and μ. If we let $\mathcal{S}_1$ be the Stokeslet for $h = \mu = 1$, then

$$\mathcal{S}(\mathbf{x}) = \frac{1}{h\mu}\mathcal{S}_1(\mathbf{x}/h) \tag{2.30}$$

We need only calculate $\mathcal{S}_1$ and we can scale to find the Stokeslet for arbitrary

h and μ.

Second, we make use of the symmetries of $\mathcal{S}$, which we briefly state. If s_1, s_2, and s_3 are ± 1, then the $(i,j)^{\text{th}}$ component of $\mathcal{S}(s_1 x, s_2 y, s_3 z)$ equals the $(i,j)^{\text{th}}$ component of $s_i s_j \mathcal{S}(x,y,z)$. Now, if s_1, s_2, and s_3 are a permutation of the numbers 1, 2, and 3, and if $\mathbf{x}_s$ is the vector whose i^{th} component is $\mathbf{x}_{s_i}$, then the $(i,j)^{\text{th}}$ component of $\mathcal{S}(\mathbf{x}_s)$ is the $(s_i,s_j)^{\text{th}}$ component of $\mathcal{S}(\mathbf{x})$. From these we deduce that we need only compute $\mathcal{S}(\mathbf{x})$ for $\mathbf{x}$ having non-negative components whose values are non-increasing. Finally, we can reduce the integration domain to $[0,1/2]^3$ and can eliminate the need for complex numbers by using the oddness and evenness properties of the integrand in equation (2.27).

To do the computations, we have devised a specialized quadrature method. We use a smooth partition of unity to isolate the singularity at the origin and also, for the finite difference discretization, the discontinuity singularities that occur at the other corners of the integration domain. The singular integrals are computed in spherical coordinates, which removes their singularities, using four point Gauss-Legendre quadrature. The remaining integral to be computed is highly oscillatory when $|\mathbf{x}|$ is large, so we use a specialized method for computing oscillatory integrals due to Ixaru and Paternoster [15]. Their method provides quadrature weights and abscissae so that functions of the form $k^n \exp(\pm 2\pi i \omega k)$ are integrated exactly for $n = 0 \ldots p$ and for fixed ω. We use $p = 3$. Further details of this method along with error estimates are described in appendix 7.2.

These quadrature computations are much too expensive to be done on the fly in a computation, meaning we can not compute $\mathcal{S}(\mathbf{x})$ by quadrature as needed for different values of $\mathbf{x}$. Fortunately, since $\mathcal{S}$ can be found from $\mathcal{S}_1$, which is universal, we may compute and tabulate values of $\mathcal{S}_1$ to high accuracy and simply reference the pre-computed values as needed. We need to compute these integrals only once for each discretization method. Still, if we need values of $\mathcal{S}_1(\mathbf{x})$ for $\mathbf{x}$ taking integral values between $-M$ and M, we must compute approximately $M^3/6$ integrals, each having six components. These integrals become more expensive as $|\mathbf{x}|$ gets larger. This quickly becomes a formidable task as M gets larger. Thus, while we have used quadrature to calculate $\mathcal{S}_1$ for small $|\mathbf{x}|$, it is more efficient to use the asymptotic methods described in chapter 3 when $|\mathbf{x}|$ is large.

Combining the discrete interaction equations, (2.23) and (2.24), with the equation relating the Eulerian force density and velocity, (2.26), we find an equation describing the relationship between the Lagrangian force applied by the immersed boundary points and velocity of the points.

$$\mathcal{G}(\mathbf{q},\mathbf{q}') = \sum_{\mathbf{x},\mathbf{x}'\in\mathbb{Z}^3} \delta_h(\mathbf{X}(\mathbf{q})-\mathbf{x})\mathcal{S}(\mathbf{x}-\mathbf{x}')\delta_h(\mathbf{X}(\mathbf{q}')-\mathbf{x}')h^6 \tag{2.31}$$

$$\mathbf{U}(\mathbf{q}) = \sum_{\mathbf{q}'\in\Omega} \mathcal{G}(\mathbf{q},\mathbf{q}')\mathbf{F}(\mathbf{q}') \tag{2.32}$$

The linear relationship between $\mathbf{F}$ and $\mathbf{U}$ is given by $\mathcal{G}$, the discrete Green's function for the Lagrangian variables. If there are N immersed boundary points, $\mathcal{G}$ is an $N\times N$ array of 3×3 matrices. Each 3×3 matrix is symmetric,

and $\mathcal{G}$ is symmetric in $\mathbf{q}$ and $\mathbf{q}'$. It is not the case, however, that $\mathcal{G}(\mathbf{q}, \mathbf{q}')$ is a function of $\mathbf{X}(\mathbf{q}) - \mathbf{X}(\mathbf{q}')$. Instead, $\mathbf{G}$ depends on the joint location of each pair of immersed boundary points with respect to the grid.

If the approximate delta functions have finite support, the sum in equation (2.31) has finitely many nonzero terms. Thus, $\mathcal{G}$ may be computed provided we can compute the necessary values of $\mathcal{S}$. For a large number of points, calculating $\mathcal{G}$ is computationally intensive. The complexity is of order N^2 in the number of points and d^6 in the width of the support of the delta function. Because of this sixth degree scaling, it is impractical to use a delta function whose support has width greater than six if $\mathcal{G}$ is computed as in equation (2.31). In chapter 3, we discuss a more efficient, approximate method of computing $\mathcal{G}$ when $|\mathbf{X}(\mathbf{q}) - \mathbf{X}(\mathbf{q}')|$ is large.

If the approximate delta function scales as $\delta_h(\mathbf{x}) = \delta_1(\mathbf{x}/h)/h^3$, which is the scaling required to hold its integral constant as h changes, and if we scale the location of the Lagrangian points by defining $\mathbf{X}_1$ so that $\mathbf{X}(\mathbf{q}) = \mathbf{X}_1(\mathbf{q})/h$, then the Green's function for the Lagrangian variables will inherit the scaling of the Stokeslet, i.e., if $\mathcal{G}_1$ is the Lagrangian Green's function with the scaled positions of the immersed boundary points, $\mathbf{X}_1$, and with h and μ set to one, then

$$\mathcal{G}(\mathbf{q}, \mathbf{q}') = \frac{1}{h\mu}\mathcal{G}_1(\mathbf{q}, \mathbf{q}'). \tag{2.33}$$

Given a configuration of immersed boundary points, $\mathbf{X}$, and given that we can compute the necessary values of $\mathcal{S}$ and that δ_h has finite support,

we can compute $\mathcal{G}$ by equation (2.31). Given the force distribution that the immersed boundary points apply to the fluid, $\mathbf{F}$, we can then find the velocities of the points by equation (2.32). Finally, the configuration of the points may be updated according to an explicit discretization of the kinematic equation, equation (2.1). Thus, one may perform a dynamic simulation.

If the linear transformation from forces to velocities represented by $\mathcal{G}$ is invertible, then we can also find the force distribution required to generate an arbitrary velocity distribution. $\mathcal{G}$ will be invertible if and only in there are no non-trivial force distributions that produce an identically zero velocity distribution or, from the dual perspective, every possible velocity distribution is achievable by some force distribution. In the continuous case, it is not the case that $\mathcal{G}_0$, defined in equation (2.15), is an invertible operator. If $\mathbf{f}(\mathbf{x})$ is the gradient of a potential which decays at infinity, then $p(\mathbf{x})$ will be simply equal to that potential and $\mathbf{u}$ will be identically zero. For instance, a symmetric uniform inward-pointing force on a spherical shell will result in zero velocity because the incompressibility of the fluid and structure creates an outward pressure to balance the force. From the dual perspective, no velocity distribution is achievable that is not incompressible.

It seems possible that certain symmetric configurations of immersed boundary points might create a situation similar to that of a spherical shell, where a force distribution can be balanced by the pressure so as to create a velocity field of zero. For $\mathbf{u}$ to be identically zero requires that p is a discrete gradient which is imposes infinitely many linear conditions on p. However, we need

only that $\mathbf{U}$ be zero for a non-trivial force distribution, which could happen even when $\mathbf{u}$ is non-zero in the close vicinity of the points. In practice, we find that simple symmetric configurations of reasonable numbers of points give transformations, $\mathcal{G}$, that are non-singular and that have reasonable condition numbers.

By reasonable numbers of points we mean that the density of points with respect to the grid size is not too high. It is easy to see that extreme densities will guarantee that $\mathcal{G}$ is singular. The rank of $\mathcal{G}$ is bounded above by the rank of the operator that spreads forces from the immersed boundary points to the grid. The rank of this operator is bounded above by three times the number of grid points that are no farther than the width of the support of the approximate delta function from the nearest immersed boundary point. If the width of the support of the delta function is d in each direction, then the rank of $\mathcal{G}$ is at most $3d^3$ times the number of grid boxes occupied by the immersed boundary points. If the density of points is greater than d^3 per grid box, $\mathcal{G}$ cannot possibly be invertible. In fact, if there is any one grid box with more than d^3 immersed boundary points, $\mathcal{G}$ will not be invertible because the sub-matrix of $\mathcal{G}$ corresponding to those points will be singular. Typically d is at least four, and our results suggest that immersed boundary points be spaced approximately one grid width from one another, corresponding to a density of one, so practical densities are far from the upper limit.

2.3 Constraints on motion

In this section, we describe how to add constraints on the motion of the immersed boundary points so that, for example, rigid bodies or bodies that are fixed in space may be simulated. In these cases a constraint force arrises that acts as a Lagrange multiplier to ensure that the motion obeys the imposed constraints. Throughout this section, we assume that $\mathcal{G}$ is invertible. We shall see that this implies that the constraint force is unique.

Suppose our constraints on the motion of the immersed boundary points take the form

$$\Phi(\mathbf{X}(\{\mathbf{q}\}, t)) = 0. \tag{2.34}$$

The function Φ, in general, will be vector valued unless we wish to impose only a single constraint. So, suppose $\Phi \in \mathbb{R}^m$ where m is the number of constraints and Φ_i are the component functions of Φ. The brackets around $\mathbf{q}$ are meant to indicate that Φ may be a function of the positions of all the immersed boundary points collectively. Such constraints could be used to tie an immersed boundary point to a particular position, to fix the distance between chosen pairs of points, or to constrain a collection of points to move as a rigid body. If we differentiate equation (2.34) with respect to time, we find that for all components i

$$\sum_{\mathbf{q}\in\Omega} \frac{\partial \Phi_i(\mathbf{X})}{\partial \mathbf{X}(\mathbf{q})} \cdot \mathbf{U}(\mathbf{q}, t) = 0. \tag{2.35}$$

The velocities of the immersed boundary points must lie in the tangent space to the manifold of admissible configurations. This is a linear space, which we call V, and which is $3N-m$ dimensional where N is the number of immersed boundary points. Often it is easiest to specify V directly instead of describing it as those velocity distributions which are normal to the gradient of some function Φ. Such is the case when we wish the points to move as a rigid body, in which case V is the six dimensional space spanned by the rigid body motions. Such is also the case if we wish to impose non-holonomic constraints that cannot be expressed in the form of equation (2.34), but can be expressed in the form of m linear equations that must be satisfied by $\mathbf{U}$ [21].

In the previous section, we found that $\mathbf{U}$ can be found from the force distribution $\mathbf{F}$ according to equation (2.32). We impose the desired constraints by introducing a constraint force $\mathbf{F}^{\mathrm{c}}(\mathbf{q},t)$ which is generated by the immersed boundary points. Equation (2.32) becomes

$$\mathbf{U}(\mathbf{q},t)=\sum_{\mathbf{q}\in\Omega}\mathcal{G}(\mathbf{q},\mathbf{q}')\left(\mathbf{F}(\mathbf{q}')+\mathbf{F}^{\mathrm{c}}(\mathbf{q}')\right). \tag{2.36}$$

For $\mathbf{F}^{\mathrm{c}}$ to be a constraint force it must act orthogonally to all possible allowed motions, so $\mathbf{F}^{\mathrm{c}}$ should be in the linear space orthogonal to V, which we call $V^{\perp}$. We could equivalently write

$$\mathbf{F}^{\mathrm{c}}(\mathbf{q},t)=\sum_{i=1}^{m}\lambda_i\frac{\partial\Phi_i(\mathbf{X})}{\partial\mathbf{X}(\mathbf{q})} \tag{2.37}$$

where the λ_i are Lagrange multipliers to be determined.

Under the assumption that $\mathcal{G}$ is invertible, the conditions that $\mathbf{U}$ be in V and $\mathbf{F}^{\mathrm{c}}$ be in $V^{\perp}$ are sufficient to uniquely determine $\mathbf{F}^{\mathrm{c}}$ and therefore $\mathbf{U}$. To do this, we think of $\mathbf{U}$ and $\mathbf{F}$ as vectors in $\mathbb{R}^{3N}$, and we think of $\mathcal{G}$ as a $3N$ by $3N$ matrix. Choose arbitrary orthonormal bases for V and $V^{\perp}$, so that, together, they form a complete orthonormal basis for $\mathbb{R}^{3N}$. Order the basis elements such that the first $3N-m$ of them span V. We express the vectors $\mathbf{U}$, $\mathbf{F}$ and $\mathbf{F}^{\mathrm{c}}$ in terms of this basis as

$$\mathbf{U} = \begin{pmatrix} \mathbf{U}_1 \\ 0 \end{pmatrix} \qquad \mathbf{F} = \begin{pmatrix} \mathbf{F}_1 \\ \mathbf{F}_2 \end{pmatrix} \qquad \mathbf{F}^{\mathrm{c}} = \begin{pmatrix} 0 \\ \mathbf{F}_2^{\mathrm{c}} \end{pmatrix} \tag{2.38}$$

where vectors with subscript 1 have the same dimension as V and vectors with subscript 2 have dimension m. We also express $\mathcal{G}$ in this basis, and we write equation (2.36) in block form.

$$\begin{pmatrix} \mathbf{U}_1 \\ 0 \end{pmatrix} = \begin{pmatrix} \mathcal{G}^{11} & \left(\mathcal{G}^{21}\right)^{\mathrm{T}} \\ \mathcal{G}^{21} & \mathcal{G}^{22} \end{pmatrix} \left[\begin{pmatrix} \mathbf{F}_1 \\ \mathbf{F}_2 \end{pmatrix} + \begin{pmatrix} 0 \\ \mathbf{F}_2^{\mathrm{c}} \end{pmatrix} \right] \tag{2.39}$$

Solving the block system, the constraint force and the velocity can be found.

$$\mathbf{F}_2^{\mathrm{c}} = -\mathbf{F}_2 - \left(\mathcal{G}^{22}\right)^{-1} \mathcal{G}^{21} \mathbf{F}_1 \tag{2.40}$$

$$\mathbf{U}_1 = \left(\mathcal{G}^{11} - \left(\mathcal{G}^{21}\right)^{\mathrm{T}} \left(\mathcal{G}^{22}\right)^{-1} \mathcal{G}^{21} \right) \mathbf{F}_1 \tag{2.41}$$

We have assumed that $\mathcal{G}$ is invertible (see the above discussion of this point). Since $\mathcal{G}$ is also symmetric, this implies that the diagonal sub-matrix $\mathcal{G}^{22}$ is also invertible. The resulting velocity does not depend on $\mathbf{F}_2$, so force distributions applied in the directions normal to V, the space of allowable velocities, have no effect on the motion. In the case of immersed boundary points constrained to move as rigid bodies, only the total forces and torques applied to each body will affect the velocities, not the higher moments of the force distribution. In the case of points tied to a fixed position in space, forces on those points with have no effect.

For a single rigid body, we would like to choose a conventional basis for V that allows us to express the linear relationship between the total forces and torques applied to the body and the velocities and angular velocities of the body in a standard way. We choose the elementary translations, $\mathbf{U} = \mathbf{e}_i$ for $i = 1, 2, 3$ where $\mathbf{e}_i$ is a standard basis element in $\mathbb{R}^3$, and the elementary rotations, $\mathbf{U} = \mathbf{e}_i \times (\mathbf{X}(\mathbf{q}) - \mathbf{X}_0)$ for $i = 1, 2, 3$ where $\mathbf{X}_0$ is the mean of $\mathbf{X}$, as our basis for V. Let $\mathcal{P}$ be the $3N \times 6$ matrix whose columns are these basis elements. The coordinates of $\mathbf{U}$ in this basis are the translational and rotational velocities of the body. We denote these by the vector $\mathscr{U}$ in $\mathbb{R}^6$, so that $\mathbf{U} = \mathcal{P}\mathscr{U}$. Let $\mathscr{F}$ be the vector in $\mathbb{R}^6$ whose components are the total forces and torques applied to the body. These components are dot products of the force with the basis elements of V so that $\mathscr{F} = \mathcal{P}^{\mathrm{T}}\mathbf{F}$. The range of $\mathcal{P}$

is V, so $\mathcal{P}$ can be written in block form as

$$\mathcal{P} = \begin{pmatrix} \mathcal{P}_1 \\ 0 \end{pmatrix}. \tag{2.42}$$

Thus $\mathbf{U}_1 = \mathcal{P}_1 \mathscr{U}$ and $\mathscr{F} = \mathcal{P}_1^{\mathrm{T}} \mathbf{F}_1$. The linear relationship between $\mathscr{U}$ and $\mathscr{F}$ is then given by a 6×6 symmetric matrix called the resistance matrix, $\mathcal{R}$.

$$\mathcal{R} = \mathcal{P}_1^{\mathrm{T}} \left(\mathcal{G}^{11} - \left(\mathcal{G}^{21}\right)^{\mathrm{T}} \left(\mathcal{G}^{22}\right)^{-1} \mathcal{G}^{21} \right)^{-1} \mathcal{P}_1 \tag{2.43}$$

$$\mathscr{F} = \mathcal{R} \mathscr{U} \tag{2.44}$$

For multiple rigid bodies one can similarly devise a so-called "grand" resistance matrix that the relates the total forces and torques on the bodies to their translational and rotational velocities.

In chapter 5 we will present calculations of the resistance matrices of configurations of immersed boundary points constrained to move as a single rigid body. In practice, for these calculations we do not need to invert $\mathcal{G}^{22}$, nor do we need to write the equation for $\mathbf{F}^{\mathrm{c}}$ in block form. Instead, we compute $\mathcal{G}^{-1}\mathcal{P}$ by Gaussian elimination to find the force vectors that produce each standard rigid motion. The total forces and torques are then calculated to be $\mathcal{P}^{\mathrm{T}}\mathcal{G}_1^{-1}\mathcal{P} = \mathcal{R}$. The two equations for $\mathcal{R}$ can be seen to be equivalent by noting that the inverse of the expression in parentheses in equation (2.43) is equal to the upper-left block of $\mathcal{G}^{-1}$. This equivalence can be derived by

block Gaussian elimination. In general, when the dimension of allowable velocity distributions V is much smaller than the number of constraints, it may be most efficient to choose a basis for V and to compute the complete resistance matrix as just described, and then to find the velocity distribution from $\mathbf{F}$ by projecting onto V and inverting the resistance matrix, as opposed to finding $\mathbf{F}^{\mathrm{c}}$ directly as in equation (2.40).

We have described how to calculate $\mathbf{U}(\mathbf{q})$ when constraints are imposed on the motion of the immersed boundary points. When performing a dynamic simulation, a discretization of equation (2.1) will be needed so that $\mathbf{X}(\mathbf{q})$ can be updated. One would like to update $\mathbf{X}$ in such a way so that the imposed constraints are maintained, meaning the new $\mathbf{X}$ exactly satisfies $\Phi(\mathbf{X}) = 0$. One way to do this is to choose coordinates for the positions of the immersed boundary points that make the constraints trivial. For instance, for a rigid body, the position of its points can be described in terms of the mean position of those points along with orientation angles. One then updates $\mathbf{X}$ by discretizing equation (2.1) in these coordinates.

Chapter 3

Asymptotics

In the previous chapter, we described how we solve the discretized equations for the immersed boundary method for Stokes flow. We showed how we can eliminate the fluid variables by using the discrete Stokeslet, which is the Green's function of the discretized system, and we described how to compute values of the discrete Stokeslet by quadrature. We also showed how to calculate $\mathcal{G}$, the linear relationship between the force and velocity distributions of the immersed boundary points. Unfortunately, these calculations can be quite expensive. It is computationally costly to compute $\mathcal{S}(\mathbf{x})$ by quadrature when $|\mathbf{x}|$ is large. It is also costly to compute $\mathcal{G}$ when the approximate delta function has large support. In this chapter, we describe asymptotic methods that vastly improve the efficiency of the these calculations. These methods also tell us about the types of discretization errors in the immersed boundary method. We first derive these methods. Then, we perform numerical experi-

ments that show that the asymptotic series for $\mathcal{S}$ and $\mathcal{G}$ converge quickly by comparing these series with calculations done in the straightforward manner presented in the previous chapter.

Our asymptotic expansions for $\mathcal{S}$ and $\mathcal{G}$ assume that we are using the spectral discretization method to discretize the Stokes equations. It will become clear why this assumption is important when we derive the expansions. Our method cannot be extended in a straightforward manner to a finite discretization method.

To simplify the formulas, throughout this chapter we set $h = \mu = 1$. Values of $\mathcal{S}$ and $\mathcal{G}$ for general h and μ can be found by the straightforward scaling described in the previous chapter.

3.1 Expansion for the discrete Stokeslet

We first derive an identity that will be used to find the asymptotic expansion for the discrete Stokeslet. Suppose f is a smooth function on the interval $[a, b]$. Let

$$I[f](x) = \int_a^b f(k)e^{2\pi ikx}dk. \tag{3.1}$$

The integral operator I simply computes the Fourier transform of f. Using integration by parts,

$$I[f](x) = \frac{f(b)e^{2\pi ibx} - f(a)e^{2\pi iax}}{2\pi ix} - \frac{1}{2\pi ix}I[f'](x). \tag{3.2}$$

The Riemann-Lebesgue lemma guarantees that the latter integral approaches zero as x approaches infinity. Therefore, the first term gives the leading behavior of $I[f]$ for large x. We iterate this procedure to find a complete asymptotic series for $I[f]$ for large x.

$$I[f](x) \sim \sum_{n=1}^{\infty} \left(\frac{-1}{2\pi i x}\right)^n \left[e^{2\pi i a x} f^{(n-1)}(a) - e^{2\pi i b x} f^{(n-1)}(b)\right] \tag{3.3}$$

If a or $b = \infty$, we can simply omit the terms corresponding to a or b, whichever is infinite, provided $f^{(n)}(k)$ approaches zero as $k \to \infty$ for all $n \geq 0$. This implies that for such a function the whole expansion is zero when $a = b = \infty$. Indeed, if f is a smooth function that decays at infinity and whose derivatives all decay at infinity then its Fourier transform on the whole line will decay faster than any power of x.

In the previous chapter, we derived an expression for the discrete Stokeslet in terms of a Fourier integral, equation (2.27). For the spectral discretization method, this expression becomes

$$\mathcal{S}(\mathbf{x}) = \int_{[-\frac{1}{2},\frac{1}{2}]^3} \frac{1}{4\pi^2|\mathbf{k}|^2} \left(\mathcal{I} - \hat{\mathbf{k}}\hat{\mathbf{k}}^{\mathrm{T}}\right) e^{2\pi i \mathbf{k}\cdot\mathbf{x}} \mathbf{dk}. \tag{3.4}$$

For convenience, we let $\mathcal{T}$ denote the integrand.

$$\mathcal{T}(\mathbf{k}) = \frac{1}{4\pi^2|\mathbf{k}|^2} \left(\mathcal{I} - \hat{\mathbf{k}}\hat{\mathbf{k}}^{\mathrm{T}}\right), \tag{3.5}$$

We use an asymptotic series of the form (3.3) to expand this integral in

an asymptotic series. We cannot directly apply the above identity because the integrand is singular at the origin. Instead, we make use of the fact that we know the integral of this integrand over all of $\mathbb{R}^3$. Recall the Stokeslet, $\mathcal{S}_0$, defined in the previous chapter in equation (2.10). Recall also from equation (2.20) that the Stokeslet has a Fourier space representation which is exactly the integral in equation (3.4) except over all space. So, we can write the discrete Stokeslet as follows:

$$\mathcal{S}(\mathbf{x}) = \mathcal{S}_0(\mathbf{x}) - \int_{\mathbb{R}^3 \setminus [-\frac{1}{2},\frac{1}{2}]^3} \mathcal{T}(\mathbf{k}) e^{2\pi i \mathbf{k}\cdot\mathbf{x}} \mathbf{dk}. \tag{3.6}$$

A few words about notation before we proceed: We will need to deal with the components of $\mathbf{x}$ and $\mathbf{k}$, so let $\mathbf{x} = (x, y, z)$ and $\mathbf{k} = (k, l, m)$. For orders of derivatives we will use the variable $\mathbf{p} = (p, q, r)$. We sometimes use multi-index notation for derivatives, factorials, and exponentiation, meaning that $\partial_{\mathbf{p}} = \partial_k^p \partial_l^q \partial_m^r$, $\mathbf{p}! = p!q!r!$, and $\mathbf{x}^{\mathbf{p}} = x^p y^q z^r$. Finally, we use $|\mathbf{p}| = p + q + r$ to denote the total order of differentiation.

We suppose that $|x| \geq |y| \geq |z|$. If not, we may use the symmetries of $\mathcal{S}$ to write $\mathcal{S}(\mathbf{x})$ in terms of a $\mathcal{S}(\tilde{\mathbf{x}})$ for some $\tilde{\mathbf{x}}$ whose components are non-increasing in magnitude. Our simplest expansion will be in inverse powers of x, so we also assume that $x \neq 0$.

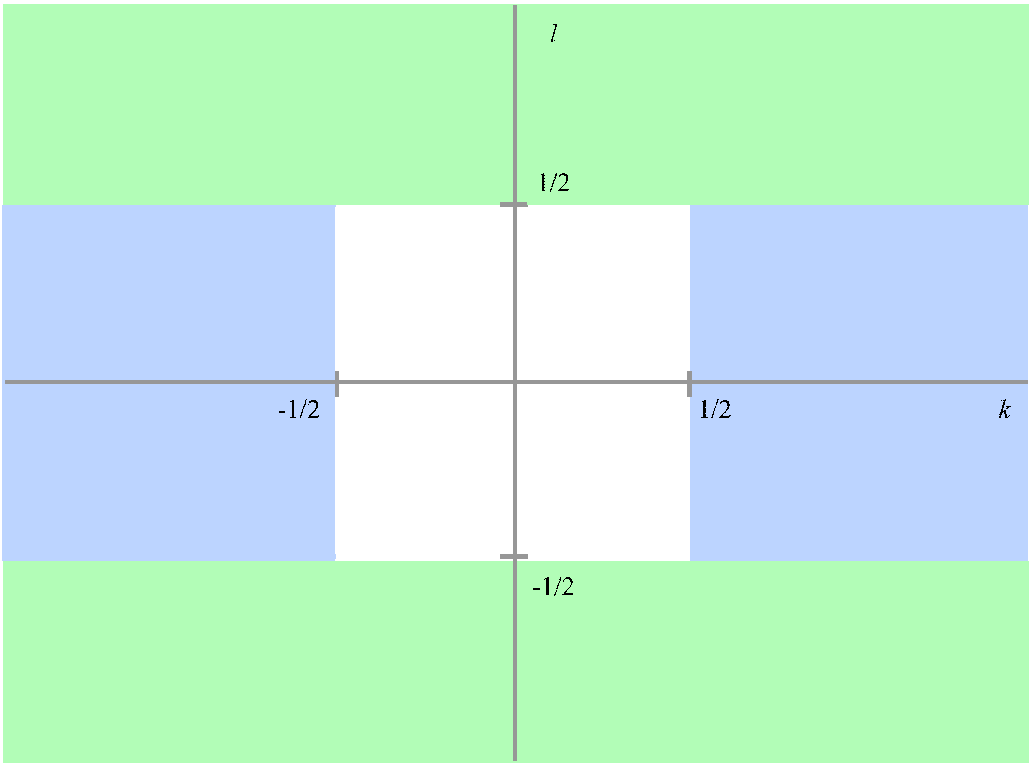


Figure 3.1: A two-dimensional representation of the two pieces into which we break the integration domain in equation (3.7). The first piece in this equation is shown in blue; the second is shown in green. Both pieces extend to infinity in the k direction. The green piece extends also in the l direction. The blue piece extends also from $-1/2$ to $1/2$ in the m direction, which is out of the page. The green piece extends from $-\infty$ to ∞ in the m direction when $|l| \geq 1/2$. It extends from $-\infty$ to $-1/2$ and also from $1/2$ to ∞ in the m direction when $|l| < 1/2$.

We break up the integration domain in equation (3.6) into two pieces.

$$\mathcal{S}(\mathbf{x}) = \mathcal{S}_0(\mathbf{x}) - \left[\int\limits_{\mathbb{R}\setminus[-\frac{1}{2},\frac{1}{2}]\times[-\frac{1}{2},\frac{1}{2}]^2} + \int\limits_{\mathbb{R}\times\mathbb{R}^2\setminus[-\frac{1}{2},\frac{1}{2}]^2} \mathcal{T}(k,l,m)e^{2\pi i\mathbf{k}\cdot\mathbf{x}}dl\,dm\,dk \right] \tag{3.7}$$

We claim that the second piece is asymptotically dominated by the first and so can be neglected. The next five pages constitute a somewhat technical proof of this claim and can be skipped if the reader wishes to simply continue with the development of the expansion. The general idea of the proof is that, away from the origin, $\mathcal{T}$ is a smooth function of $\mathbf{k}$ so that

$$\int\limits_{\mathbb{R}^2\setminus[-\frac{1}{2},\frac{1}{2}]^2} \mathcal{T}(k,l,m)e^{2\pi i(ly+mz)}dl\,dm \tag{3.8}$$

is a smooth function of k for all $\mathbf{x}$. The second piece then amounts to a Fourier transform in the k direction of a smooth function over all of $\mathbb{R}$, which we have shown decays faster than any inverse power of x. However, there are technical problems with this argument. We need the function defined in equation (3.8) to decay as $k \to \infty$, but for $y = z = 0$ the integral in equation (3.8) does not even exist for any value of k.

To make a rigorous argument for neglecting the second piece in equation (3.7), we first claim

$$\int\limits_{\mathbb{R}\times\mathbb{R}^2\setminus[-\frac{1}{2},\frac{1}{2}]^2} \partial_k \left(\frac{1}{2\pi i x}\mathcal{T}(k,l,m)e^{2\pi i\mathbf{k}\cdot\mathbf{x}} \right) \mathbf{dk} = 0. \tag{3.9}$$

This is true by Stokes' theorem since the boundary of the domain of integration is everywhere tangential to the k direction. The technical condition required to apply Stokes' theorem is that if one considers the intersection of the domain of integration with sequentially larger spheres, and if one considers the integral of the quantity in parentheses in equation (3.9) multiplied by $k/|\mathbf{k}|$ over these sets, then these integrals must converge to zero as the radii of the spheres become infinity. Namely, it is necessary that

$$\lim_{R\to\infty} \frac{1}{2\pi i x} \int\limits_{\{|\mathbf{k}|=R\}\setminus\{|l|,|m|\leq 1/2\}} \mathcal{T}(\mathbf{k}) e^{2\pi i \mathbf{k}\cdot\mathbf{x}} \frac{k}{|\mathbf{k}|} dS = 0. \tag{3.10}$$

Now, it is clear that

$$\lim_{R\to\infty} \frac{1}{2\pi i x} \int\limits_{\{|\mathbf{k}|=R\}\cap\{|l|,|m|\leq 1/2\}} \mathcal{T}(\mathbf{k}) e^{2\pi i \mathbf{k}\cdot\mathbf{x}} \frac{k}{|\mathbf{k}|} dS = 0 \tag{3.11}$$

(note the change in the domain of integration) since the absolute value of the integrand is bounded componentwise by $1/4\pi^2 R^2$ and the domain of integration has bounded total area. Therefore, we need only show that

$$\lim_{R\to\infty} \frac{1}{2\pi i x} \int\limits_{\{|\mathbf{k}|=R\}} \mathcal{T}(\mathbf{k}) e^{2\pi i \mathbf{k}\cdot\mathbf{x}} \frac{k}{|\mathbf{k}|} dS = 0. \tag{3.12}$$

Convert this integral into spherical coordinates where θ measures the angle

between $\mathbf{k}$ and $\mathbf{x}$. This results in

$$\frac{1}{8\pi^3 ix}\int_0^{\pi}\int_0^{2\pi}\left(\mathcal{I}-\hat{\mathbf{k}}\hat{\mathbf{k}}^{\mathrm{T}}\right)\frac{k}{|\mathbf{k}|}e^{2\pi iR|\mathbf{x}|\cos(\theta)}\sin(\theta)d\phi\,d\theta. \tag{3.13}$$

The function $(\mathcal{I}-\hat{\mathbf{k}}\hat{\mathbf{k}}^{\mathrm{T}})k/|\mathbf{k}|$ is bounded componentwise by 1 and -1. Considered as a function of the spherical coordinates (R,θ,ϕ), it depends only on θ and ϕ, not on R. Let

$$f(\theta)=\int_0^{2\pi}\left(\mathcal{I}-\hat{\mathbf{k}}\hat{\mathbf{k}}^{\mathrm{T}}\right)\frac{k}{|\mathbf{k}|}d\phi. \tag{3.14}$$

Then f is a continuous, bounded function of θ. Making the change of variables $u=\cos(\theta)$, the remaining integral is

$$\frac{1}{8\pi^3 ix}\int_{-1}^{1}f(\cos^{-1}(u))e^{2\pi iR|\mathbf{x}|u}du. \tag{3.15}$$

Since $|\mathbf{x}|\neq 0$ by assumption, this integral converges to zero as $R\to\infty$ by the Riemann-Lebesgue lemma. This completes our proof of the above claim, equation (3.9). It follows that

$$\int\limits_{\mathbb{R}\times\mathbb{R}^2\setminus[-\frac{1}{2},\frac{1}{2}]^2}\mathcal{T}(k,l,m)e^{2\pi i\mathbf{k}\cdot\mathbf{x}}\mathbf{dk}=-\frac{1}{2\pi ix}\int\limits_{\mathbb{R}}\int\limits_{\mathbb{R}^2\setminus[-\frac{1}{2},\frac{1}{2}]^2}\partial_k\mathcal{T}(k,l,m)e^{2\pi i\mathbf{k}\cdot\mathbf{x}}\mathbf{dk}. \tag{3.16}$$

Later, we show precisely how to compute derivatives of $\mathcal{T}$. For now, we only need estimates on the decay of these derivatives. In spherical coordinates, $\mathcal{T}$ is r^{-2} multiplied by a function of θ and ϕ alone. The gradient in

spherical coordinates is

$$\nabla = \hat{\mathbf{r}}\frac{\partial}{\partial r} + \frac{1}{r}\hat{\boldsymbol{\theta}}\frac{\partial}{\partial \theta} + \frac{1}{r\sin(\theta)}\hat{\boldsymbol{\phi}}\frac{\partial}{\partial \phi}. \tag{3.17}$$

Therefore, the gradient of $\mathcal{T}$ will be r^{-3} multiplied by a function of θ and ϕ alone. Using induction, we have shown that the $\mathbf{p}^{\text{th}}$ derivative of $\mathcal{T}$ will equal $r^{-(2+|\mathbf{p}|)}$ multiplied by a function of θ and ϕ, where $|\mathbf{p}|$ is the total order of differentiation. Since the function of θ and ϕ is continuous on a compact domain, it is bounded by some constant, which we call $C_{\mathbf{p}}$. Therefore, componentwise

$$|\partial_{\mathbf{p}}\mathcal{T}| \leq \frac{C_{\mathbf{p}}}{|\mathbf{k}|^{2+|\mathbf{p}|}}. \tag{3.18}$$

We now claim that

$$\int\limits_{\mathbb{R}^2\setminus[-\frac{1}{2},\frac{1}{2}]^2} \partial_k\mathcal{T}(k,l,m)e^{2\pi i(ly+mz)}dl\,dm \tag{3.19}$$

is a smooth function of k for all y and z which decays as $|k| \to \infty$ and whose derivatives with respect to k also decay as $|k| \to \infty$. We can easily estimate this function and its derivatives for large $|k|$. For the n^{th} derivative,

componentwise

$$\left|\partial_k^n \int\limits_{\mathbb{R}^2\setminus[-\frac{1}{2},\frac{1}{2}]^2} \partial_k \mathcal{T}(k,l,m) e^{2\pi i(ly+mz)} dl\, dm\right| \leq \int\limits_{\mathbb{R}^2} \left|\partial_k^{n+1}\mathcal{T}(k,l,m)\right| dl\, dm \tag{3.20}$$

$$\leq \int\limits_{\mathbb{R}^2} \frac{C_{n+1}}{(k^2+l^2+m^2)^{(n+3)/2}} dl\, dm \tag{3.21}$$

$$\leq \frac{C_{n+1}}{|k|^{n+3}} \int\limits_{\mathbb{R}^2} \frac{1}{(1+\frac{l^2+m^2}{k^2})^{(n+3)/2}} dl\, dm. \tag{3.22}$$

We now make the change of variables $l' = l/k$, $m' = m/k$, and the quantity to be estimated is bounded by

$$\frac{C_{n+1}}{|k|^{n+1}} \int\limits_{\mathbb{R}^2} \frac{1}{(1+l'^2+m'^2)^{(n+3)/2}} dl'\, dm' = \frac{2\pi C_{n+1}}{(n+1)|k|^{n+1}}. \tag{3.23}$$

These indeed decay to zero for large $|k|$ since $n \geq 0$.

We have shown that the smooth function defined in equation (3.19) and its derivatives decay at infinity. Therefore, its Fourier transform in the k direction, which is what is computed on the right hand side of equation (3.16), decays faster than any inverse power of x. Then, because of equation (3.16), the contribution of the second integral in equation (3.7) may be neglected in our asymptotic expansion of the discrete Stokeslet, which is in powers of

$1/x$.

After that technical diversion, we proceed to derive this expansion from the first integral in equation (3.7). Let

$$\mathcal{L}(k,y,z) = \int\limits_{[-\frac{1}{2},\frac{1}{2}]^2} \mathcal{T}(k,l,m) e^{2\pi i(ly+mz)} dl\, dm. \tag{3.24}$$

We have shown that

$$\mathcal{S}(\mathbf{x}) \sim \mathcal{S}_0(\mathbf{x}) - \left[\int_{-\infty}^{-1/2} + \int_{1/2}^{\infty} \mathcal{L}(k,y,z) e^{2\pi i k x} dk \right]. \tag{3.25}$$

The symbol $\sim$ indicates asymptotic equivalence, meaning the difference between the left and right hand sides of equation (3.25) decays faster than any power of $1/x$. Away from $k = 0$, $\mathcal{L}$ is a smooth function for all y and z. We would like to apply the asymptotic expansion from equation (3.3) to both integrals in equation (3.25). We need that $\mathcal{L}$ and its derivatives decay sufficiently rapidly for large $|k|$. This result is trivial, since componentwise

$$|\partial_k^n \mathcal{L}| \leq |\partial_k^n \mathcal{T}| \leq \frac{C_n}{|\mathbf{k}|^{2+n}} \leq \frac{C_n}{|k|^{2+n}}. \tag{3.26}$$

Applying equation (3.3) to equation (3.25) to find an asymptotic series, we find

$$\mathcal{S}(\mathbf{x}) \sim \mathcal{S}_0(\mathbf{x}) - \sum_{p=1}^{\infty} \left(\frac{-1}{2\pi i x} \right)^p \left[e^{\pi i x} \partial_k^{p-1} \mathcal{L}\left(\frac{1}{2}, y, z \right) - e^{-\pi i x} \partial_k^{p-1} \mathcal{L}\left(-\frac{1}{2}, y, z \right) \right]. \tag{3.27}$$

In our case, x is always an integer, so $\exp(\pi i x) = \exp(-\pi i x) = (-1)^x$. The diagonal components of $\mathcal{L}$ as well as the $(2,3)$ and $(3,2)$ components are even in k, which results in the cancellation of the terms in this sum with p odd. The $(1,2)$, $(2,1)$, $(1,3)$, and $(3,1)$ components are odd in k, which results in the cancellation of the terms with p even.

Let $\mathcal{L}_p = \partial_k^p \mathcal{L}$. We write the series for $\mathcal{S}$ as

$$\mathcal{S}(\mathbf{x}) \sim \mathcal{S}_0(\mathbf{x}) - \sum_{p=1}^{\infty} \frac{(-1)^x}{x^p} \mathcal{S}_p(y,z) \tag{3.28}$$

where

$$\mathcal{S}_p(y,z) = \left(\frac{-1}{2\pi i}\right)^p \left[\mathcal{L}_{p-1}\left(\frac{1}{2},y,z\right) - \mathcal{L}_{p-1}\left(-\frac{1}{2},y,z\right)\right]. \tag{3.29}$$

The diagonal, $(2,3)$, and $(3,2)$ components of $\mathcal{S}_p$ are zero for p odd. The other components are zero for p even (except for $\mathcal{S}_0$). Notice that for $p \geq 1$, $\mathcal{S}_p$ gives the $1/x^p$ behavior of $\mathcal{S}$, but that $\mathcal{S}_0$ also decays like $1/x$. What this means is that the $\mathcal{S}_1$ term is an order one error in the discrete Stokeslet as compared with the continuous Stokeslet, $\mathcal{S}_0$. What saves the method is the presence of the $(-1)^x$ factor, which will cause significant cancellation when $\mathcal{S}$ is convolved with a smooth function representing the force field. Since the force field is defined only on the grid, by a smooth field we mean one which varies slowly from one grid cell to the next. We, however, will not be convolving $\mathcal{S}$ with a smooth force field, but with the discrete delta

function. The properties of the delta function will determine the magnitude of the errors after they are convolved with the discrete Stokeslet. We shall see exactly how when we derive the asymptotic expansion for $\mathcal{G}$.

To compute the expansion for $\mathcal{S}(\mathbf{x})$ we need to be able to compute $\mathcal{S}_p(y,z)$ for some desired range of p, y, and z. This requires computing $\mathcal{L}_p(\pm 1/2, y, z)$, which, if we let $\partial_k^p \mathcal{T} = \mathcal{T}_p$, requires computing

$$\mathcal{L}_p\left(k,y,z\right) = \int\limits_{[-\frac{1}{2},\frac{1}{2}]^2} \mathcal{T}_p\left(k,l,m\right) e^{2\pi i(ly+mz)} dl\, dm. \tag{3.30}$$

These two-dimensional Fourier integrals can be easily computed to machine accuracy using high-order Gaussian quadrature provided y and z are not too large and provided that we can compute $\mathcal{T}_p$ for arbitrary p. We return to the problem of computing $\mathcal{T}_p$ later in this chapter, when we will show how to compute arbitrary mixed partial derivatives of $\mathcal{T}$.

When y is large, we may expand this Fourier integral in an asymptotic series in powers of $1/y$. Let

$$\mathcal{M}(k,l,z) = \int_{-1/2}^{1/2} \mathcal{T}(k,l,m) e^{2\pi i m z} dm \tag{3.31}$$

and

$$\mathcal{M}_p(k,l,z) = \partial_k^p \mathcal{M}(k,l,z) = \int_{-1/2}^{1/2} \mathcal{T}_p(k,l,m) e^{2\pi i m z} dm. \tag{3.32}$$

Further, let $\mathcal{T}_{pq} = \partial_k^p \partial_l^q \mathcal{T}$ and $\mathcal{M}_{pq}(k,l,m) = \partial_k^p \partial_l^q \mathcal{M}$ so that

$$\mathcal{M}_{pq}(k,l,z) = \int_{-1/2}^{1/2} \mathcal{T}_{pq}(k,l,m) e^{2\pi i m z} dm. \tag{3.33}$$

When $k = \pm 1/2$, $\mathcal{M}_p$ is a smooth function of l for all p and z. Now, $\mathcal{L}_p$ is the Fourier integral of $\mathcal{M}_p$ with respect to l.

$$\mathcal{L}_p(k,l,m) = \int_{-1/2}^{1/2} \mathcal{M}_p\left(k,l,z\right) e^{2\pi i l y} dl \tag{3.34}$$

We apply equation (3.3) to find an asymptotic series for this expression in powers of $1/y$.

$$\mathcal{L}_p(k,y,z) \sim (-1)^y \sum_{q=1}^{\infty} \left(\frac{-1}{2\pi i y}\right)^q \left[\mathcal{M}_{p,q-1}\left(k,-\frac{1}{2},z\right) - \mathcal{M}_{p,q-1}\left(k,\frac{1}{2},z\right)\right]. \tag{3.35}$$

Substituting the series for $\mathcal{L}$ into the series for $\mathcal{S}$, we generate an asymptotic series for $\mathcal{S}$ for large x and y.

$$\mathcal{S}(\mathbf{x}) \sim \mathcal{S}_0(\mathbf{x}) - \sum_{p=1}^{\infty}\sum_{q=1}^{\infty} \frac{(-1)^x}{x^p}\frac{(-1)^y}{y^q}\mathcal{S}_{pq}(z) \tag{3.36}$$

where

$$\mathcal{S}_{pq}(z) = \left(\frac{-1}{2\pi i}\right)^{p+q} \Big[\mathcal{M}_{p-1,q-1}\left(\frac{1}{2}, -\frac{1}{2}, z\right) - \mathcal{M}_{p-1,q-1}\left(\frac{1}{2}, \frac{1}{2}, z\right) + \mathcal{M}_{p-1,q-1}\left(-\frac{1}{2}, \frac{1}{2}, z\right) - \mathcal{M}_{p-1,q-1}\left(-\frac{1}{2}, -\frac{1}{2}, z\right)\Big]. \tag{3.37}$$

It is clear that this series, equation (3.36), is symmetric in x and y. The symmetries of $\mathcal{T}$ imply that $\mathcal{S}_{pq}$ is diagonal when p and q are even. When p and q are odd, only the (1,2) and (2,1) components of $\mathcal{S}_{pq}$ are non-zero. When p is even and q is odd, only the (2,3) and (3,2) components are non-zero, and when p is odd and q is even, only the (1.3) and (3.1) components are non-zero. To compute the coefficients of the expansion, $\mathcal{S}_{pq}$, we need to be able to compute $\mathcal{M}_{pq}$ for necessary values of p, q, and z. Each of these is a one-dimensional Fourier integral that can easily be computed to machine accuracy using high-order Gaussian quadrature provided z is not too large and provided we can compute $\mathcal{T}_{pq}$. Again, we return to the problem of computing mixed partial derivatives of $\mathcal{T}$ shortly.

If z is large, we may expand $\mathcal{M}_{pq}$ in an asymptotic series in powers of $1/z$ in the same way as we have done for x and y. Away from the origin, $\mathcal{M}_{pq}$ is a smooth function, so $\mathcal{M}_{pq}(\pm 1/2, \pm 1/2, m)$ is a smooth function of m for all p and q. We may therefore use equation (3.3) to expand $\mathcal{M}_{pq}$ in an

asymptotic series.

$$\mathcal{M}_{pq}(k,l,z) \sim (-1)^z \sum_{r=1}^{\infty} \left(\frac{-1}{2\pi i z}\right)^r \left[\mathcal{T}_{p,q,r-1}\left(k,l,-\frac{1}{2}\right) - [\mathcal{T}_{p,q,r-1}\left(k,l,\frac{1}{2}\right)\right] \tag{3.38}$$

where we have defined $\mathcal{T}_{pqr} = \partial_k^p \partial_l^q \partial_m^r \mathcal{T}$.

Finally, substituting this series into the expression for $\mathcal{S}_{pq}$, we find an asymptotic series for $\mathcal{S}$ for large x, y, and z.

$$\mathcal{S}(\mathbf{x}) \sim \mathcal{S}_0(\mathbf{x}) - \sum_{p,q,r=1}^{\infty} \frac{(-1)^{x+y+z}}{x^p y^q z^r} \mathcal{S}_{pqr} \tag{3.39}$$

where

$$\mathcal{S}_{pqr} = \left(\frac{-1}{2\pi i}\right)^{p+q+r} \sum_{a,b,c\in\{0,1\}} (-1)^{a+b+c} \mathcal{T}_{pqr}\left(\frac{(-1)^a}{2}, \frac{(-1)^b}{2}, \frac{(-1)^c}{2}\right). \tag{3.40}$$

To calculate the coefficients $\mathcal{S}_{pqr}$, we need only calculate the eight necessary values of $\mathcal{T}_{pqr}$. We show how to do this shortly. The symmetries of $\mathcal{T}$ are such that $\mathcal{S}_{pqr}$ will be zero when $p+q+r$ is odd. If two of p, q, and r are odd and the remaining index is even then $\mathcal{S}_{pqr}$ is zero except for the off-diagonal elements corresponding to the two odd indices. For instance, if p and r are odd and q is even, then the (1,3) and (3,1) components of $\mathcal{S}_{pqr}$ will be non-zero. If p, q, and r are all even, then $\mathcal{S}_{pqr}$ will be diagonal. The leading order error in $\mathcal{S}$ compared with $\mathcal{S}_0$ is of order $x^{-2}y^{-1}z^{-1} + x^{-1}y^{-2}z^{-1} + x^{-1}y^{-1}z^{-2}$. The leading order error in the diagonal elements is of order $x^{-2}y^{-2}z^{-2}$.

Let us summarize our results. We have found three asymptotic representations of $\mathcal{S}(\mathbf{x})$. The first is for large x only and is a series in powers of $1/x$. The series contains functions of y and z which are two-dimensional Fourier integrals of k derivatives of $\mathcal{T}$. The second is for large x and y and is a series in powers of $1/x$ times powers of $1/y$. The series contains functions of z which are one-dimensional Fourier integrals of k and l derivatives of $\mathcal{T}$. The third is for large x, y, z and is a series in $x^{-p}y^{-q}z^{-r}$. The terms in the series can be computed from the values of the k, l, and m derivatives of $\mathcal{T}$ at the eight corners of the cube $[-1/2,\, 1/2]^3$.

In the previous chapter, we described how to calculate $\mathcal{S}$ by quadrature. This method has the problems that the integrals are difficult to calculate for large $|\mathbf{x}|$ and also that many values of $\mathcal{S}$ much be tabulated if we need to know $\mathcal{S}(\mathbf{x})$ for large $|\mathbf{x}|$. By using the three asymptotic representations, we can now easily calculate $\mathcal{S}$ on the fly for large $|\mathbf{x}|$ using the following procedure. When all the components of $\mathbf{x}$ are large, we use the expansion in equation (3.39), where we have tabulated the values of $\mathcal{S}_{pqr}$ for $1 \le p, q, r \le M$ for some sufficiently large M. In section 3.4 of this chapter, we present numerical experiments which show approximately how many terms are needed in this expansion to achieve the desired accuracy and which also show how large the components of $\mathbf{x}$ must be to be large enough to use this expansion. When only two components of $\mathbf{x}$ are large, we use the expansion in equation (3.36), where we have tabulated values of $\mathcal{S}_{pq}(z)$ for $1 \le p, q \le M$ for some sufficiently large M and for $0 \le z \le R$, where R is such that for x, y, and

$z > R$, we could use the three term expansion, equation (3.39). When only one component of $\mathbf{x}$ is large, we use the expansion in equation (3.28), where we have tabulated $\mathcal{S}_p(y,z)$ for $1 \le p \le M$ for some sufficiently large M and for $0 \le y, z \le R$. When no components of $\mathbf{x}$ are large, we use tabulated values of $\mathcal{S}$ that have been computed by quadrature as described in chapter 2.

Nothing we have done so far has depended on the particular formula for $\mathcal{T}$. This procedure could be used for any spectral method on an infinite grid in any number of dimensions provided the necessary estimates involving the decay of $\mathcal{T}$ and its derivates at infinity are valid.

3.2 Computing the derivatives of $\mathcal{T}$

We now describe how to compute mixed partial derivatives of $\mathcal{T}$. In matrix form

$$\mathcal{T}(\mathbf{k}) = \frac{1}{4\pi^2|\mathbf{k}|^4} \begin{pmatrix} l^2+m^2 & -kl & -km \\ -kl & k^2+m^2 & -lm \\ -km & -lm & k^2+l^2 \end{pmatrix}. \tag{3.41}$$

If we let

$$\mathcal{T}^{abc}_{pqr}(\mathbf{k}) = \partial_k^p \partial_l^q \partial_m^r \frac{k^a l^b m^c}{|\mathbf{k}|^4}, \tag{3.42}$$

then

$$\mathcal{T}_{pqr} = \frac{1}{4\pi^2} \begin{pmatrix} \mathcal{T}^{020}_{pqr} + \mathcal{T}^{002}_{pqr} & -\mathcal{T}^{110}_{pqr} & -\mathcal{T}^{101}_{pqr} \\ -\mathcal{T}^{110}_{pqr} & \mathcal{T}^{200}_{pqr} + \mathcal{T}^{002}_{pqr} & -\mathcal{T}^{011}_{pqr} \\ -\mathcal{T}^{101}_{pqr} & -\mathcal{T}^{011}_{pqr} & \mathcal{T}^{200}_{pqr} + \mathcal{T}^{020}_{pqr} \end{pmatrix}. \tag{3.43}$$

Now, we can easily calculate $\mathcal{T}^{abc}_{pqr}$ in terms of the $\mathcal{T}^{000}_{pqr}$. For instance, if p and $q > 0$,

$$\mathcal{T}^{110}_{pqr} = kl\mathcal{T}^{000}_{pqr} + pl\mathcal{T}^{000}_{(p-1)qr} + kq\mathcal{T}^{000}_{p(q-1)r} + pq\mathcal{T}^{000}_{(p-1)(q-1)r}. \tag{3.44}$$

Assuming $p > 1$,

$$\mathcal{T}^{200}_{pqr} = k^2\mathcal{T}^{000}_{pqr} + 2kp\mathcal{T}^{000}_{(p-1)qr} + p(p-1)\mathcal{T}^{000}_{(p-2)qr}. \tag{3.45}$$

Formulas for the remaining $\mathcal{T}^{abc}_{pqr}$ are similar to these two formulas. So, we can compute $\mathcal{T}_{pqr}$ provided we can compute

$$\partial^p_k \partial^q_l \partial^r_m \frac{1}{|\mathbf{k}|^4}. \tag{3.46}$$

To compute these derivatives, we use a recurrence relation from Duan and Krasny [10] and Lindsay and Krasny [23], which we re-derive here. Let

$$\psi^\nu(\mathbf{k}) = \frac{1}{|\mathbf{k}|^\nu} \tag{3.47}$$

and let

$$\psi^{\nu}_{\mathbf{p}} = \frac{1}{\mathbf{p}!}\partial_{\mathbf{p}}\psi^{\nu} \tag{3.48}$$

where we are using multi-index notation, described above. Note that this notation differs from our usual convention of having subscripts indicate partial derivatives. Here, we also multiply by $1/\mathbf{p}!$. We do so to simplify the formulas that we will derive.

First, note that ψ^{ν} satisfies

$$|\mathbf{k}|^2\partial_k\psi^{\nu} + \nu k\psi^{\nu} = 0. \tag{3.49}$$

Differentiating this expression $p-1$ times with respect to k, we find

$$|\mathbf{k}|^2\partial_k^p\psi^{\nu} + (2p+\nu-2)k\partial_k^{p-1}\psi^{\nu} + (p-1)(p+\nu-2)\partial_k^{p-2}\psi^{\nu} = 0. \tag{3.50}$$

The key reason that this is such a simple expression is that derivatives of $|\mathbf{k}|^2$ with respect to k of order three or more are zero. We now differentiate this expression q times with respect to l and r times with respect to m and we divide the whole expression by $\mathbf{p}!$ to find

$$|\mathbf{k}|^2\psi^{\nu}_{\mathbf{p}} + 2\sum_{i=1}^{3} k_i\psi^{\nu}_{\mathbf{p}-\mathbf{e}_i} + \sum_{i=1}^{3}\psi^{\nu}_{\mathbf{p}-2\mathbf{e}_i} + \frac{\nu-2}{p}(k\psi^{\nu}_{p-1,q,r} + \psi^{\nu}_{p-2,q,r}) = 0. \tag{3.51}$$

By k_i we mean the i^{th} component of $\mathbf{k}$, and by $\mathbf{e}_i$ we mean the vector with i^{th} component equal to one and with other components equal to zero. It is

to be understood that $\psi^\nu_{\mathbf{p}}$ is zero if any component of $\mathbf{p}$ is less than zero. If we multiply this expression by p, it is valid for any $\mathbf{p}$ with non-negative components. By symmetry, the same expression is true if we permute coordinates so that l or m takes the place of k, and q or r takes the place of p. Taking the three expressions, in the form of equation (3.51), multiplying respectively by p, q, and r, and summing, we find a recurrence relation for $\psi^\nu_{\mathbf{p}}$ that is symmetric in the components of $\mathbf{p}$.

$$|\mathbf{p}||\mathbf{k}|^2\psi^\nu_{\mathbf{p}} + (2|\mathbf{p}| + \nu - 2)\sum_{i=1}^{3} k_i\psi^\nu_{\mathbf{p}-\mathbf{e}_i} + (|\mathbf{p}| + \nu - 2)\sum_{i=1}^{3}\psi^\nu_{\mathbf{p}-2\mathbf{e}_i} = 0 \quad (3.52)$$

Recall that $|\mathbf{p}| = p + q + r$. This expression is valid for any $\mathbf{p}$, though it is trivial when $\mathbf{p} = 0$. Given $\psi^\nu_{000}(\mathbf{k}) = \psi^\nu(\mathbf{k}) = |\mathbf{k}|^{-\nu}$, we can use this recurrence relation to calculate $\psi^\nu_{\mathbf{p}}$ for all $\mathbf{p}$ such that $|\mathbf{p}| = 1$. We can proceed to calculate $\psi^\nu_{\mathbf{p}}$ for all $\mathbf{p}$ such that $|\mathbf{p}| = 2$, and repeating this procedure we can calculate $\psi^\nu_{\mathbf{p}}$ for any $\mathbf{p}$. There are $(|\mathbf{p}| + 1)(|\mathbf{p}| + 2)/2$ values of $\mathbf{p}$ with a given $|\mathbf{p}|$, therefore in general it takes order $|\mathbf{p}|^3$ operations to calculate a given value of $\psi^\nu_{\mathbf{p}}$. However, it is not necessary to calculate intermediate $\psi^\nu_{\mathbf{q}}$ for any $\mathbf{q}$ with any component greater than the corresponding component of $\mathbf{p}$. Therefore, if two components of $\mathbf{p}$ are zero, we can calculate $\psi^\nu_{\mathbf{p}}$ in order $|\mathbf{p}|$ operations, and if one component of $\mathbf{p}$ is zero, we can calculate $\psi^\nu_{\mathbf{p}}$ in order $|\mathbf{p}|^2$ operations.

Once we can calculate $\psi^\nu_{\mathbf{p}}(\mathbf{k})$ for any needed $\mathbf{p}$, we may calculate $\mathcal{T}_{\mathbf{p}}(\mathbf{k})$ for any needed $\mathbf{p}$ using equation (3.43) and equations similar to (3.44) and

(3.45). It is $\mathcal{T}_{\mathbf{p}}$ that we need in order to calculate the coefficients in the asymptotic expansions for the discrete Stokeslet, $\mathcal{S}_p(y,z)$, $\mathcal{S}_{pq}(z)$, and $\mathcal{S}_{pqr}$. It is not critical that these calculations be done extremely efficiently, since we tabulate the needed values of these coefficients and so they need only be computed once. The algorithm we have described computes $\mathcal{T}_p$ and therefore $\mathcal{S}_p(y,z)$ in order p operations, computes $\mathcal{T}_{pq}$ and therefore $\mathcal{S}_{pq}(z)$ in order pq operations, and computes $\mathcal{T}_{pqr}$ and therefore $\mathcal{S}_{pqr}$ in order pqr operations.

In future work, we would like to develop rigorous, sharp error estimates for the partial expansions for the discrete Stokeslet. Such estimates could be used to select the number of terms needed to compute $\mathcal{S}$ to a desired accuracy. For now, we refer to section 3.4 which shows numerical experiments that examine the errors in these expansions.

3.3 Expansion for the Lagrangian Green's function

In the previous chapter, we derived an expression for the Green's function, $\mathcal{G}(\mathbf{q},\mathbf{q}')$, relating the Lagrangian variables $\mathbf{U}(\mathbf{q})$ and $\mathbf{F}(\mathbf{q})$, equation (2.31). We restate this equation here, for convenience.

$$\mathcal{G}(\mathbf{q},\mathbf{q}') = \sum_{\mathbf{x},\mathbf{x}'\in(h\mathbb{Z})^3} \delta_h(\mathbf{X}(\mathbf{q})-\mathbf{x})\mathcal{S}(\mathbf{x}-\mathbf{x}')\delta_h(\mathbf{X}(\mathbf{q}')-\mathbf{x}')h^6 \tag{3.53}$$

In this expression, $\mathcal{G}$ is represented as a double sum over all grid points. This sum will have only finitely many non-zero terms if the discrete delta function has compact support. However, if the support width of the delta function is d, the sum will have d^6 non-zero terms, and so order d^6 values of $\mathcal{S}$ will be required and computing the sum will take order d^6 operations. Even for a simple delta function of support width 4, this will be order 4048 operations. In this section, we derive a more efficient method of computing $\mathcal{G}$ when one or more of the components of $\mathbf{X}(\mathbf{q}) - \mathbf{X}(\mathbf{q}')$ are large.

To simplify notation, we let h be one, drop the h subscript from δ_h, and let $\mathbf{X} = \mathbf{X}(\mathbf{q}) = (X, Y, Z)$ and $\mathbf{X}' = \mathbf{X}(\mathbf{q}') = (X', Y', Z')$. Also, let $\mathbf{x} = (x, y, z)$ and $\mathbf{x}' = (x', y', z')$. We suppose $|X - X'| \geq |Y - Y'| \geq |Z - Z'|$. If not, we may make use of the symmetries of $\mathcal{G}$ to permute the coordinates of $\mathcal{X}$ and $\mathcal{X}'$ so that these inequalities hold. $\mathcal{G}$ will have same symmetries as $\mathcal{S}$ with respect to permutations of the coordinates provided $\delta(\mathbf{x})$ is invariant to permutations of the components of $\mathbf{x}$, which will be the case for all the approximate delta functions used in this thesis.

Our strategy is to use the asymptotic expansions for the discrete Stokeslet to reduce the operations required to compute $\mathcal{G}$. Assuming that $|X - X'|$ is sufficiently large, in particular assuming it is large in comparison to d, then $x - x'$ will be large for all non-zero terms in the sum in equation (3.53). We therefore can substitute the one-term asymptotic expansion for the discrete

Stokeslet into equation (3.53) to find

$$\mathcal{G}(\mathbf{X},\mathbf{X}') \sim \mathcal{G}_0(\mathbf{X},\mathbf{X}') - \sum_{p=1}^{\infty} \sum_{\mathbf{x},\mathbf{x}'\in\mathbb{Z}^3} \delta(\mathbf{X}-\mathbf{x}) \frac{(-1)^{x-x'}}{(x-x')^p} \mathcal{S}_p(y-y', z-z') \delta(\mathbf{X}'-\mathbf{x}') \tag{3.54}$$

where $\mathcal{G}_0$ is defined by

$$\mathcal{G}_0(\mathbf{X},\mathbf{X}') = \sum_{\mathbf{x},\mathbf{x}'\in\mathbb{Z}^3} \delta(\mathbf{X}-\mathbf{x}) \mathcal{S}_0(\mathbf{x}-\mathbf{x}') \delta(\mathbf{X}'-\mathbf{x}'). \tag{3.55}$$

While $\mathcal{G}$ is the double convolution of $\mathcal{S}$ with a discrete delta function centered at $\mathbf{X}$ and a discrete delta function centered at $\mathbf{X}'$, $\mathcal{G}_0$ is the double convolution of the continuous Stokeslet, $\mathcal{S}_0$, with the same two discrete delta functions.

Naively, it will take as many operations to compute $\mathcal{G}_0$ as to compute $\mathcal{G}$ by equation (3.53). We later show that we can devise a more efficient method to compute $\mathcal{G}_0$ using the formula for $\mathcal{S}_0$. First, we show how to compute efficiently the remaining terms in equation (3.54). All of the delta functions that we use are tensor products of functions of the individual coordinates. Thus, there is some function ϕ such that

$$\delta_h(\mathbf{x}) = \frac{1}{h^3} \phi\left(\frac{x}{h}\right) \phi\left(\frac{y}{h}\right) \phi\left(\frac{z}{h}\right). \tag{3.56}$$

To our knowledge, no approximate delta function with compact support has been devised that is not a tensor product of the coordinates but still has the property that its sum over the grid points multiplied by h^3 is exactly one for

any shift relative to the grid, i.e. that

$$\sum_{\mathbf{x}\in(h\mathbb{Z})^3} \delta_h(\mathbf{X}-\mathbf{x})h^3 = 1 \quad \forall\, \mathbf{X}\in\mathbb{R}^3. \tag{3.57}$$

This condition is required for the approximate delta function to correctly interpolate constant fields, and is a minimum requirement for any delta function. Without it, order one errors will result from interpolation of the velocity field and spreading of force to the grid. This condition and other conditions on approximate delta functions are discussed in detail in chapter 4. We can now clarify that when we say the width of support of the approximate delta function is d grid cells, we mean that ϕ is supported on $[a,b]$ with $b-a=d$. All of the functions ϕ that we use are even, so they are supported on $[-d/2, d/2]$.

Because $\mathcal{S}_0$ is infinite at the origin, $\mathcal{G}_0(\mathbf{X},\mathbf{X}')$ is undefined if there is an $\mathbf{x}$ such that $\delta(\mathbf{X}-\mathbf{x})$ and $\delta(\mathbf{X}'-\mathbf{x})$ are non-zero. If the delta function has support width d, this may be the case if all components of $\mathbf{X}-\mathbf{X}'$ have magnitude less than d. $\mathbf{G}_0$ will certainly be undefined if all components of $\mathbf{X}-\mathbf{X}'$ have magnitude less than or equal to $d-1$.

Assuming the delta function is a tensor product of one dimensional functions, we may simplify equation (3.54). Let

$$\mathcal{H}_p(X,X') = \sum_{x,x'\in\mathbb{Z}} \phi(X-x)\frac{(-1)^{x-x'}}{(x-x')^p}\phi(X'-x') \tag{3.58}$$

and let

$$\mathcal{G}_p(Y,Y',Z,Z') = \sum_{y,y',z,z'\in\mathbb{Z}} \phi(Y-y)\phi(Y'-y')\phi(Z-z)\phi(Z'-z')\mathcal{S}_p(y-y',z-z'). \tag{3.59}$$

Like $\mathcal{S}_p$, the diagonal, (2,3), and (3,2) components of $\mathcal{G}_p$ are zero when p is odd, and the other components are zero when p is even. We now have

$$\mathcal{G}(\mathbf{X},\mathbf{X}') \sim \mathcal{G}_0(\mathbf{X},\mathbf{X}') - \sum_{p=1}^{\infty} \mathcal{H}_p(X,X')\mathcal{G}_p(Y,Y',Z,Z'). \tag{3.60}$$

This expansion is valid when $|X-X'|$ is large in comparison to d. If $|X-X'| < d$ it may be that $\mathcal{H}_p$ is undefined since a non-zero term in the sum will have $x = x'$. If $|X - X'| \leq d-1$ then $\mathcal{H}_p$ must be undefined. It takes of order d^2 operations to compute $\mathcal{H}_p$ and order d^4 operations to compute $\mathcal{G}_p$. The computational complexity can be considered constant in p because we have tabulated the necessary values of $\mathcal{S}_p$. Therefore, if M terms are retained in the sum in equation (3.60), and ignoring for now the need to compute $\mathcal{G}_0$, the operations needed to compute $\mathcal{G}$ have been reduced from order d^6 to order d^4M. We shall see in section 3.4 that in practice we can achieve high accuracy with M much less than d^2.

When $|Y - Y'|$ is large in addition to $|X - X'|$ being large, we may substitute the asymptotic expansion for the discrete Stokeslet in x and y, equation (3.36), into equation (3.53) to produce an expansion for $\mathcal{G}$. Again, we assume the approximate delta function has the form of a tensor product.

We find

$$\mathcal{G}(\mathbf{X},\mathbf{X}') \sim \mathcal{G}_0(\mathbf{X},\mathbf{X}') - \sum_{p,q=1}^{\infty} \mathcal{H}_p(X,X')\mathcal{H}_q(Y,Y')\mathcal{G}_{pq}(Z,Z') \tag{3.61}$$

where

$$\mathcal{G}_{pq}(Z,Z') = \sum_{z,z'\in\mathbb{Z}} \phi(Z-z)\phi(Z'-z')\mathcal{S}_{pq}(z-z'). \tag{3.62}$$

Depending on the oddness or evenness of p and q, $\mathcal{G}_{pq}$ will have the same non-zero components as $\mathcal{S}_{pq}$. This expansion is valid when $|X-X'|$ and $|Y-Y'|$ are large in comparison to d. Computing $\mathcal{H}_p$ and $\mathcal{G}_{pq}$ take order d^2 operations and so if we retain terms in the expansion with $p+q \leq M$, and if we again ignore the need to compute $\mathcal{G}_0$, order d^2M^2 total operations are needed to compute $\mathcal{G}$.

When all components of $\mathbf{X}-\mathbf{X}'$ are large in magnitude, we may substitute the asymptotic expansion for the discrete Stokeslet in terms of x, y, and z, equation (3.39), into equation (3.53) to produce an expansion for $\mathcal{G}$. We find, assuming a tensor-product delta function,

$$\mathcal{G}(\mathbf{X},\mathbf{X}') \sim \mathcal{G}_0(\mathbf{X},\mathbf{X}') - \sum_{p,q,r=1}^{\infty} \mathcal{S}_{pqr}\mathcal{H}_p(X,X')\mathcal{H}_q(Y,Y')\mathcal{H}_r(Z,Z'). \tag{3.63}$$

This expansion is valid when $|X-X'|$, $|Y-Y'|$, and $|Z-Z'|$ are all large in comparison to d. If we retain terms in the expansion with $p+q+r \leq M$, then order M^3 terms are needed in the sum and we need to compute order M values of $\mathcal{H}_p$. The total computational complexity is therefore or order

$M^3 + d^2 M$. Moreover, many of the terms in this expansion are zero because $\mathcal{S}_{pqr}$ is zero when $p+q+r$ is odd, only two components of $\mathcal{S}_{pqr}$ are non-zero when two of p, q, and r are odd, and $\mathcal{S}_{pqr}$ is diagonal when p, q, and r are all even.

We can improve the efficiency of computing $\mathcal{H}_p(X, X')$ when d is moderately large but $|X - X'|$ is still large in comparison to d by expanding the formula for $\mathcal{H}_p$ for large $|X - X'|$. Doing so will also reveal the leading behavior of $\mathcal{H}_p$ for large $|X - X'|$. Recall that we assume ϕ is supported on $[-d/2, d/2]$. Then, for those x and x' such that $\phi(X - x)$ and $\phi(X' - x')$ are nonzero, $|X - X'| - d \leq |x - x'| \leq |X - X'| + d$. We suppose that $|X - X'| > d$. Let $r = X - x$ and $r' = X' - x'$ so $|r - r'| \leq d$. Then, using the binomial theorem twice,

$$\frac{1}{(x - x')^p} = \frac{1}{[(X - X') - r + r']^p} \tag{3.64}$$

$$= \frac{1}{(X - X')^p} \sum_{j=0}^{\infty} \begin{pmatrix} p + j - 1 \\ j \end{pmatrix} \left(\frac{r - r'}{X - X'} \right)^j \tag{3.65}$$

$$= \frac{1}{(X - X')^p} \sum_{j=0}^{\infty} \sum_{a=0}^{j} \begin{pmatrix} p + j - 1 \\ j \end{pmatrix} \begin{pmatrix} j \\ a \end{pmatrix} \frac{r^a (-r')^{j-a}}{(X - X')^j}. \tag{3.66}$$

This is a convergent series because $|r - r'| \leq |X - X'|$.

Let

$$M_n(X) = \sum_{x \in \mathbb{Z}} \phi(X - x)(X - x)^n \tag{3.67}$$

and

$$N_n(X) = \sum_{x \in \mathbb{Z}} (-1)^x \phi(X - x)(X - x)^n. \tag{3.68}$$

The $M_n(X)$ are known as the discrete moments of ϕ. We call the $N_n(X)$ the discrete alternating moments of ϕ. These moments will play a major role in the conditions that we impose on approximate delta functions in chapter 4 and will be discussed in detail there. We see in this chapter how some of the errors in the immersed boundary method depend on the discrete moments and the discrete alternating moments. These results will motivate conditions that we place on the delta functions in chapter 4. For now, we note that the summation condition on delta functions mentioned above in equation (3.57) is equivalent to $M_0(X) \equiv 1$ and that some of the conditions imposed in chapter 4 are equivalent to $M_n(X) \equiv 0$ or $N_n(X) \equiv 0$ for some n. We also note that the $M_n(X)$ are periodic functions of X with period one, and the $N_n(X)$ are periodic with period two. Moreover, $N_n(X + 1) = -N_n(X)$.

We now calculate an expansion for $\mathcal{H}_p(X, X')$.

$$\mathcal{H}_p(X, X') = \frac{1}{(X - X')^p} \sum_{j=0}^{\infty} \sum_{a=0}^{j} \begin{pmatrix} p + j - 1 \\ j \end{pmatrix} \begin{pmatrix} j \\ a \end{pmatrix} \frac{(-1)^{j-a} N_a(X) N_{j-a}(X')}{(X - X')^j} \tag{3.69}$$

If we cut off the outer sum and use only finitely many j, then the cost of computing $\mathcal{H}_p$ by this formula is linear in d, instead of proportional to d^2 because computing each $N_a(X)$ is linear in d. If d is large, computing $\mathcal{H}_p$ this way may be cheaper than computing it directly. Typically, one is

dealing with a large number of immersed boundary points and one needs to compute $\mathcal{G}$ for each pair of points. The alternating moments, $N_a(X)$ need only be computed for each point individually, not for each pair of points. The total cost of computing all these moments will be linear in the number of immersed boundary points and therefore negligible compared with the cost of computing $\mathcal{G}$ for each pair of points, which is quadratic in the total number of points. We may then consider the cost of computing $\mathcal{H}_p$ by equation (3.69), if terms with $j \leq M$ to be of order M^2 and to be independent of d. We have devised an asymptotic method of computing $\mathcal{G}$ that, ignoring the need to compute $\mathcal{G}_0$, has a computational cost that is completely independent of d when all components of $\mathbf{X} - \mathbf{X}'$ are large in comparison to d.

Equation (3.69) shows that the leading behavior of $\mathcal{H}_p$ is to decay like $|X - X'|^{-p}$. Many of the approximate delta functions that we derive in chapter 4 will have $N_0 \equiv 0$. In this case, the terms in the sum in equation (3.69) with $j = 0$ and $j = 1$ are zero and the leading behavior of $\mathcal{H}_p$ is to decay like $|X - X'|^{-(p+2)}$. If it were the case that $N_1 \equiv 0$ for a particular delta function, $\mathcal{H}_p$ would decay like $|X - X'|^{-(p+4)}$, and each additional N_n that is identically zero adds two orders to the decay of $\mathcal{H}_p$. If we look now at the expansions for $\mathcal{G}$, equations (3.60), (3.61), and (3.63), we have discovered the leading behavior of the terms in the expansion for large values of the components of $\mathbf{X} - \mathbf{X}'$. For the expansion in large $|X - X'|$, equation (3.60), the first term in the expansion decays like $|X - X'|^{-1}$ unless $N_0 \equiv 0$ in which case it decays like $|X - X'|^{-3}$. For the expansion in large $|X - X'|$

and $|Y - Y'|$, equation (3.61), the leading terms in the expansion decay like $|X-X'|^{-1}|Y-Y'|^{-1}$ unless $N_0 \equiv 0$ in which case the leading behavior is like $|X-X|^{-3}|Y-Y'|^{-3}$. For the expansion when all components of $\mathbf{X}-\mathbf{X}'$ are large in magnitude, recall that $\mathcal{S}_{111} = 0$ and that various components of $\mathcal{S}_{pqr}$ are zero depending on the oddness or evenness of p, q, and r. The leading terms in this expansion decay like $|X-X'|^{-1}|Y-Y'|^{-1}|Z-Z'|^{-2}$ for the (1,2) and (2,1) component of $\mathcal{G}$. They decay like $|X-X'|^{-1}|Y-Y'|^{-2}|Z-Z'|^{-1}$ for the (1,3) and (3,1) component, like $|X-X'|^{-2}|Y-Y'|^{-1}|Z-Z'|^{-1}$ for the (2,3) and (3,2) component and like $|X-X'|^{-2}|Y-Y'|^{-2}|Z-Z'|^{-2}$ for the diagonal components. If $N_0 \equiv 0$, one should add two to all exponents to find the leading behavior. The decay is very fast when $|X-X'|$, $|Y-Y'|$ and $|Z-Z'|$ are all large, particularly if $N_0 \equiv 0$. In this case, to a good approximation, $\mathcal{G} = \mathcal{G}_0$.

We can derive an error estimate that suggests how many terms are needed in the sum in equation (3.69) to achieve a desired accuracy for $\mathcal{H}_p$. Let $\mathcal{H}_p^M$ denote the sum using terms with $j \leq M$ in equation (3.69).

$$\mathcal{H}_p^M(X,X') = \frac{1}{(X-X')^p}\sum_{j=0}^{M}\sum_{a=0}^{j}\begin{pmatrix} p+j-1 \\ j \end{pmatrix}\begin{pmatrix} j \\ a \end{pmatrix}\frac{(-1)^{j-a}N_a(X)N_{j-a}(X')}{(X-X')^j}. \tag{3.70}$$

Suppose there is a constant C such that

$$\sum_{x\in\mathbb{Z}} |\phi(X-x)| \leq C \quad \forall\, X \in \mathbb{R} \tag{3.71}$$

If $\phi(x) \geq 0$ for all x then the equality holds for all X with $C = 1$ when the summation condition, equation (3.57), holds or equivalently when $M_1(X) \equiv 1$. For a reasonable ϕ, we would expect C to be no greater than 2. Then,

$$\begin{aligned}
&|\mathcal{H}_p - \mathcal{H}_p^M| \\
&\quad \leq \frac{1}{|X-X'|^p} \left| \sum_{x,x'\in\mathbb{Z}} \sum_{j=M+1}^{\infty} \begin{pmatrix} p+j-1 \\ j \end{pmatrix} \frac{(r-r')^j}{(X-X')^j} \phi(X-x)\phi(X'-x') \right| \\
&\quad \leq \frac{C^2}{|X-X'|^p} \sum_{j=M+1}^{\infty} \begin{pmatrix} p+j-1 \\ j \end{pmatrix} \left(\frac{d}{|X-X'|} \right)^j .
\end{aligned} \tag{3.72}$$

We can compute this sum. Let $r = d/|X - X'|$, so that $0 < r < 1$.

$$\begin{aligned}
\sum_{j=M+1}^{\infty} \binom{p+j-1}{j} r^j &= \frac{1}{(p-1)!} \partial_r^{p-1} \sum_{j=M+1}^{\infty} r^{j+p-1} \\
&= \frac{1}{(p-1)!} \partial_r^{p-1} \frac{r^{M+p}}{1-r} \\
&= \frac{1}{(p-1)!} \sum_{j=0}^{p-1} \binom{p-1}{j} \partial_r^j \left(r^{M+p}\right) \partial_r^{p-1-j} \left(\frac{1}{1-r}\right) \\
&= \frac{1}{(1-r)^{p-1}} \sum_{j=0}^{p-1} \binom{M+p}{j} r^{M+p-j} (1-r)^j.
\end{aligned} \tag{3.73}$$

For small r, the final quantity is dominated by the term with $j = p-1$, which is bounded by

$$\binom{M+p}{p-1} r^{M+1}. \tag{3.74}$$

We make the crude estimate that the sum is less than or equal to

$$\frac{r^{M+1}}{(1-r)^{p-1}} \sum_{j=0}^{p-1} \binom{M+p}{j} =: A_p^M \frac{r^{M+1}}{(1-r)^{p-1}}. \tag{3.75}$$

We conclude

$$|\mathcal{H}_p - \mathcal{H}_p^M| \leq \frac{A_p^M C^2 d^{M+1}}{|X - X'|^{p+M+1}} \left(1 - \frac{d}{|X - X'|}\right)^{1-p}. \tag{3.76}$$

For a given value of $|X - X'| > d$, we can find an M that makes this error less than any desired ϵ. The error decays like $|X - X'|^{-(p+M+1)}$.

We have so far not discussed the efficient computation of $\mathcal{G}_0$, defined in equation (3.55). If computed naively, it will take as many operations to compute $\mathcal{G}_0$ as it took to compute $\mathcal{G}$ naively, and our asymptotic expansions will not have resulted in any savings. Fortunately, we may use the fact that we have an analytic formula for the Stokeslet, $\mathcal{S}_0$, to generate an expansion for $\mathcal{G}_0$, valid when the coordinates of $\mathbf{X} - \mathbf{X}'$ are large in magnitude, that allows for its efficient computation.

To generate this expansion, we first Taylor expand $\mathcal{S}_0$ about $\mathbf{X}$ in the x direction.

$$\mathcal{S}_0(\mathbf{X} + (x, 0, 0)) = \sum_{p=0}^{\infty} \mathcal{S}_0^p(\mathbf{X}) x^p \tag{3.77}$$

where we let

$$\mathcal{S}_0^p(\mathbf{x}) = \frac{1}{p!} \partial_x^p \mathcal{S}_0(\mathbf{x}). \tag{3.78}$$

We can calculate these derivatives of $\mathcal{S}_0$ much as we did above with $\mathcal{T}$. We later discuss exactly how these derivatives are computed. As above, we assume for the remainder of this section that the approximate delta function has the form of a tensor product of one-dimensional functions. We can now write an expansion for $\mathcal{G}_0$ valid when $|X - X'|$ is large. Let $\delta x = X - x$,

$\delta x' = X' - x'$, and similarly define δy, $\delta y'$, δz, and $\delta z'$. Let

$$\mathcal{G}_0^p(X-X', Y, Z, Y', Z') = \sum_{y,z,y',z' \in \mathbb{Z}} \mathcal{S}_0^p(X-X', y-y', z-z')\phi(\delta y)\phi(\delta z)\phi(\delta y')\phi(\delta z') \tag{3.79}$$

and let

$$\mathcal{H}_0^p(X, X') = \sum_{x,x' \in \mathbb{Z}} \phi(\delta x)\phi(\delta x')(\delta x' - \delta x)^p. \tag{3.80}$$

Then,

$$\begin{aligned}\mathcal{G}_0(\mathbf{X}, \mathbf{X}') &= \sum_{\mathbf{x},\mathbf{x}' \in \mathbb{Z}^3} \delta(\mathbf{X} - \mathbf{x})\delta(\mathbf{X}' - \mathbf{x}') \sum_{p=0}^{\infty} \mathcal{S}_0^p(X - X', y - y', z - z')(\delta x' - \delta x)^p \\ &= \sum_{p=0}^{\infty} \mathcal{G}_0^p(X - X', Y, Z, Y', Z')\mathcal{H}_0^p(X, X'). \end{aligned} \tag{3.81}$$

The terms $\mathcal{H}_0^p$ can be computed in order d^2 operations, and $\mathcal{G}_0^p$ can be computed in order d^4 operations, so this expansion would appear to be more efficient than computing $\mathcal{G}_0$ in the naive fashion, which takes order d^6 operations. However, this argument relies on our being able to compute $\mathcal{S}_0^p$ efficiently. We shall discuss its computation below. Note that $\mathcal{H}_0^p(X, X')$ depends only the fractional parts of X and X', so it will depend only on the positions of $\mathbf{X}$ and $\mathbf{X}'$ relative to the grid. In other words, $\mathcal{H}_0^p(X, X')$ is doubly periodic with period 1. This is not the case for $\mathcal{H}^p(X, X')$, which decays as $|X - X'|$ becomes large.

We can construct a more efficient expansion for $\mathcal{G}_0$ when $|X - X'|$ and

$|Y-Y'|$ are large. For this, we first Taylor expand $\mathcal{S}_0$ in the x and y directions.

$$\mathcal{S}_0(\mathbf{X}+(x,y,0)) = \sum_{p,q=0}^{\infty} \mathcal{S}_0^{pq}(\mathbf{X}) x^p y^q \tag{3.82}$$

where we let

$$\mathcal{S}_0^{pq}(\mathbf{x}) = \frac{1}{p!q!}\partial_x^p \partial_y^q \mathcal{S}_0(\mathbf{x}). \tag{3.83}$$

The expansion takes the form

$$\mathcal{G}_0(\mathbf{X},\mathbf{X}') = \sum_{p,q=0}^{\infty} \mathcal{G}_0^{pq}(X-X', Y-Y', Z, Z')\mathcal{H}_0^p(X,X')\mathcal{H}_0^q(Y,Y') \tag{3.84}$$

where we let

$$\mathcal{G}_0^{pq}(X-X', Y-Y', Z, Z') = \sum_{z,z'\in\mathbb{Z}} \mathcal{S}_0^{pq}(X-X', Y-Y', z-z')\phi(\delta z)\phi(\delta z'). \tag{3.85}$$

The terms $\mathcal{G}_0^{pq}$ can be computed in order d^2 operations, as can $\mathcal{H}_0^p$, so the total expansion has complexity d^2. This will be significantly more efficient than the naive calculation, provided we can compute $\mathcal{S}_0^{pq}$ efficiently, as discussed below.

When all components of $\mathbf{X}-\mathbf{X}'$ are large in magnitude, we may expand the expression for $\mathcal{G}_0$ in all directions. A full Taylor expansion of $\mathcal{S}_0$ is

$$\mathcal{S}_0(\mathbf{X}+\mathbf{x}) = \sum_{p,q,r=0}^{\infty} \mathcal{S}_0^{pqr}(\mathbf{X}) x^p y^q z^r \tag{3.86}$$

where we let

$$\mathcal{S}_0^{pqr}(\mathbf{x}) = \frac{1}{p!q!r!}\partial_x^p\partial_y^q\partial_z^r\mathcal{S}_0(\mathbf{x}). \tag{3.87}$$

The Taylor expansions for $\mathcal{S}_0$ are all convergent provided $|\mathbf{x}| < |\mathbf{X}|$ in equation (3.86). The expansion for $\mathcal{G}_0$ is then

$$\mathcal{G}_0(\mathbf{X}, \mathbf{X}') = \sum_{p,q,r=0}^{\infty} \mathcal{S}_0^{pqr}(\mathbf{X} - \mathbf{X}')\mathcal{H}_0^p(X, X')\mathcal{H}_0^q(Y, Y')\mathcal{H}_0^r(Z, Z'). \tag{3.88}$$

This expansion has computational complexity of order d^2, and its efficiency relies on our ability to efficiently compute $\mathcal{S}_0^{pqr}$, the mixed partial derivatives of the Stokeslet. Before we discuss doing this, we note several ways to improve the efficiency of the above expansions.

First, we can simplify the expression for $\mathcal{H}_0^p$, equation (3.80).

$$\mathcal{H}_0^p(X, X') = \sum_{n=0}^{p}(-1)^n \begin{pmatrix} p \\ n \end{pmatrix} M_n(X)M_{p-n}(X') \tag{3.89}$$

where $M_n(X)$ are the discrete moments of ϕ defined above in equation (3.67). The M_n can be computed in d operations. In the typical situation where $\mathcal{G}(\mathbf{X}, \mathbf{X}')$ is to be computed for each pair of a large collection of immersed boundary points, the M_n need only be computed once for each point, so the operations needed to compute all the M_n is linear in the number of immersed boundary points and therefore negligible compared with the number of operations needed to compute the values of $\mathcal{G}$, which is quadratic in the number

of immersed boundary points. We may then consider that $\mathcal{H}_0^p$ is computable in order p operations, independent of d.

As discussed in chapter 4, some of the conditions that we impose on ϕ take the form $M_n(x) \equiv 0$ for some $n > 0$. We also typically impose the condition $M_0 \equiv 1$, which is equivalent to equation (3.57). If $M_0 \equiv 1$, then $\mathcal{H}_0^0(X, X') = 1$ for all X and X'. In this case, the first term in the expansion for $\mathcal{G}_0(\mathbf{X}, \mathbf{X}')$ is simply $\mathcal{S}_0(\mathbf{X} - \mathbf{X}')$, the Stokeslet. If $M_n \equiv 0$ for $1 \leq n \leq k$ for some k, then $\mathcal{H}_0^p \equiv 0$ for $1 \leq p \leq k$.

We expect the linear relationship between forces on one immersed boundary point and the velocities generated at another immersed boundary point to be approximately given by the Stokeslet. Other terms can be interpreted as corrections or errors resulting from the fact that we are using an approximate delta function to represent the points and from the fact that we are using a grid with finite resolution. The terms in the expansion for $\mathcal{G}_0$ do not depend on the discretization method for the Stokes equations. They only depend on the choice of approximate delta function. Therefore, we may consider the corrections coming from the expansion for $\mathcal{G}_0$ as attributable only to the approximate delta function. The corrections that come from the remaining terms in the expansion for $\mathcal{G}$ depend both of the discretization method and on the choice of delta function. We have already analyzed the magnitudes of the latter. These were seen to depend on $N_n(x)$, and we have seen how they decay as the coordinates of $\mathbf{X} - \mathbf{X}'$ become large.

As for the corrections in the expansion for $\mathcal{G}_0$, we first argue that, using

multi-index notation, $\mathcal{S}_0^{\mathbf{p}}(\mathbf{x})$ decays like $|\mathbf{x}|^{-(1+|\mathbf{p}|)}$. First, note that $\mathcal{S}_0(\mathbf{x})$, in spherical coordinates (r, θ, ϕ), is r^{-1} multiplied by a function of θ and ϕ alone. Our conclusion then follows from the same argument used above to estimate the decay of $\mathcal{T}_{\mathbf{p}}$. In particular, $\mathcal{S}_0^{\mathbf{p}}(\mathbf{x})$ will be $|\mathbf{x}|^{-(1+|\mathbf{p}|)}$ multiplied by a function of θ and ϕ alone. Since the values of ϕ (now the function from which the delta function is constructed, not the spherical coordinate) are order one, we conclude from this that $\mathcal{G}_0^p$ decays like $|X - X'|^{-(1+p)}$ and that $\mathcal{G}_0^{pq}$ decays like $(|X - X'| + |Y - Y'|)^{-(1+p+q)}$.

If ϕ does not satisfy $M_0(x) \equiv 1$, then $\mathcal{G}_0(\mathbf{X}, \mathbf{X}')$ and $\mathcal{S}_0(\mathbf{X} - \mathbf{X}')$ will differ by a factor that decays only like $|\mathbf{X} - \mathbf{X}'|^{-1}$, which is the same order of decay as the Stokeslet. If $M_0 \equiv 1$ and $M_n \equiv 0$ for $1 \leq n \leq k$, then $\mathcal{H}_0^p$ will be zero for $1 \leq p \leq k$ and so $\mathcal{G}_0(\mathbf{X}, \mathbf{X}')$ and $\mathcal{S}_0(\mathbf{X} - \mathbf{X}')$ will differ by a factor that decays like $|\mathbf{X} - \mathbf{X}'|^{-(1+k)}$. The error in $\mathcal{G}_0$ relative to the Stokeslet can thus be considered k^{th} order accurate as $|\mathbf{X} - \mathbf{X}'|$ becomes large. Recall, however, that there are additional corrections apart from $\mathcal{G}_0$ that contribute to a difference between $\mathcal{G}(\mathbf{X}, \mathbf{X}')$ and $\mathcal{S}_0(\mathbf{X} - \mathbf{X}')$ and that these corrections depend on the alternating moments of ϕ, $N_n(x)$, defined in equation (3.68).

To complete our discussion of the method of efficiently computing $\mathcal{G}_0$ using expansions we must describe how we calculate the mixed partial derivatives of $\mathcal{S}_0$. This will also complete our description of the asymptotic method of computing $\mathcal{G}$. We again use the recursion relation of Duan and Krasny and

Lindsay and Krasny. We need to compute

$$\mathcal{S}_0^{\mathbf{p}}(\mathbf{X}) = \frac{1}{\mathbf{p}!}\partial_{\mathbf{x}}^{\mathbf{p}}\mathcal{S}_0(\mathbf{X}). \tag{3.90}$$

From the formula for the Stokeslet, equation (2.10), we can deduce a simplified representation.

$$\mathcal{S}_0(\mathbf{x}) = \frac{1}{8\pi}\left(\frac{2\mathcal{I}}{|\mathbf{x}|} - \nabla\nabla|\mathbf{x}|\right). \tag{3.91}$$

The two gradient symbols indicate the operator that generates the Hessian matrix of second-order partial derivatives of the function to which it is applied.

Recall our definitions above of the functions ψ^{ν}, equation (3.47) and $\psi_{\mathbf{p}}^{\nu}$, equation (3.48) for which we generated the recurrence relation, equation (3.52). To compute the mixed partial derivatives of the Stokeslet, we need to be able to calculate $\psi_{\mathbf{p}}^{1}$ and $\psi_{\mathbf{p}}^{-1}$. In particular, from equation (3.91), we deduce for the $(i,j)^{\text{th}}$ component of $\mathcal{S}_0^{\mathbf{p}}$

$$\mathcal{S}_0^{\mathbf{p}}(\mathbf{x})_{ij} = \frac{1}{8\pi}\left(2\delta_{ij}\psi_{\mathbf{p}}^{1}(\mathbf{x}) - \left[(\mathbf{p}_i+1)(\mathbf{p}_j+1) + \delta_{ij}(\mathbf{p}_i+1)\right]\psi_{\mathbf{p}+\mathbf{e}_i+\mathbf{e}_j}^{-1}(\mathbf{x})\right). \tag{3.92}$$

We can calculate the necessary values of $\psi_{\mathbf{p}}^{\nu}$ using the recursion relation, equation (3.52). With these, we may calculate the needed values of $\mathcal{S}_0^{\mathbf{p}}$. Computing $\psi_{\mathbf{p}}^{\nu}$, in general, takes order $|\mathbf{p}|^3$ operations. However, the expansions for $\mathcal{G}_0$, equations (3.81), (3.84), and (3.88), require many values of $\mathcal{S}_0^{\mathbf{p}}$.

In the case of the expansion when $|X - X'|$ is large, equation (3.81), $\mathcal{S}_0^p$ is required for $0 \leq p \leq M$ for some M. Each value of $\mathcal{S}_0^p$ can be computed in order p operations. However, we can compute all the needed values of $\mathcal{S}_0^p$ in order M operations because the recursion computes, in succession, each needed value of $\psi_{\mathbf{p}}^{\nu}$. In the case of the expansion when $|X - X'|$ and $|Y - Y'|$ are large, equation (3.84), all the required $\mathcal{S}_0^{pq}$ with $0 \leq p + q \leq M$ can be computed in order M^2 operations. In the case of the expansion when all coordinates of $\mathbf{X} - \mathbf{X}'$ are large in magnitude, all the required $\mathcal{S}_0^{\mathbf{p}}$ with $0 \leq |\mathbf{p}| \leq M$ can be computed in order M^3 operations.

We have now specified completely the asymptotic method for efficient computation of the Green's function relating the Lagrangian variables, $\mathcal{G}$. The method consists of an expansion that efficiently computes $\mathcal{G}_0$ which involves computing derivatives of the Stokeslet, $\mathcal{S}_0$, by a recursive method and which involves computing coefficients, $\mathcal{H}_0^p$, which depend on the discrete moments of the approximate delta function, $M_n(x)$. To $\mathcal{G}_0$ are added corrections which involve pre-computed coefficients, $\mathcal{S}_p$, $\mathcal{S}_{pq}$, and $\mathcal{S}_{pqr}$, involving derivatives of the Fourier kernel of the Stokeslet, $\mathcal{T}$, which are computed by a recursive method, and the Fourier integrals thereof. The corrections also involve coefficients $\mathcal{H}_p$ which depend on the discrete alternating moments of the approximate delta function, $N_n(x)$. The most computationally intensive task involved in computing $\mathcal{G}$ is computing the derivatives of $\mathcal{S}_0$, $\mathcal{S}_0^{\mathbf{p}}$, for the expansion for $\mathcal{G}_0$.

Missing from our description of this method of computing $\mathcal{G}$ are rigorous,

sharp error estimates that would suggest how many terms to use in each expansion for $\mathcal{G}$ and $\mathcal{G}_0$ to achieve a desired accuracy. We hope to develop such estimates in future work. For now, we refer the reader to the next section in which the rates of convergence of the expansions are demonstrated numerically.

3.4 Numerical experiments

In this section, we demonstrate the rates of convergence of the asymptotic expansions for the discrete Stokeslet, $\mathcal{S}$ and for the Lagrangian Green's function, $\mathcal{G}$ derived above. We do so by showing numerical results. As above, throughout this section we assume $h = \mu = 1$. Our results scale easily with these parameters, as we have shown in the previous chapter.

3.4.1 Expansion for $\mathcal{S}$

We begin with the expansions for the discrete Stokeslet, equations (3.28), (3.36), and (3.39). We refer to these expansions respectively as the one, two, and three-coordinate expansions for the discrete Stokeslet. We have tabulated the necessary values of $\mathcal{S}_p(y,z)$, $\mathcal{S}_{pq}(z)$, and $\mathcal{S}_{pqr}$ to machine accuracy. Our experiments consist of choosing values of $\mathbf{x}$ on the grid and calculating a partial expansion for $\mathcal{S}$. Let $\mathcal{S}^M(\mathbf{x})$ be, in the case of the one-coordinate expansion, (3.28), the partial sum of this equation with $1 \leq p \leq M$. In the case of the two-coordinate expansion, let $\mathcal{S}^M(\mathbf{x})$ be the partial sum of equation

(3.36) with $2 \leq p+q \leq M$. In the case of the three-coordinate expansion, let $\mathcal{S}^M(\mathbf{x})$ be the partial sum of equation (3.39) with $3 \leq p+q+r \leq M$. We show results with $M = 0$, which means that no terms in partial sums in the expansions are included and so $\mathcal{S}^M = \mathcal{S}_0$, the Stokeslet. We will compare $\mathcal{S}^M(\mathbf{x})$ with values of $\mathcal{S}(\mathbf{x})$ which we have computed by quadrature, as described in the previous chapter. Let $\mathcal{S}^Q(\mathbf{x})$ be these values. Our results show the relative difference between $\mathcal{S}^M(\mathbf{x})$ and $\mathcal{S}^Q(\mathbf{x})$ for various values of $\mathbf{x}$ and M, a quantity we call $E^M(\mathbf{x})$. In particular, let

$$E^M(\mathbf{x}) = \frac{\|\mathcal{S}^M(\mathbf{x}) - \mathcal{S}^Q(\mathbf{x})\|}{\|\mathcal{S}^Q(\mathbf{x})\|}. \tag{3.93}$$

Because of quadrature error, we cannot assume $\mathcal{S}^Q(\mathbf{x}) = \mathcal{S}(\mathbf{x})$. In appendix 7.2, we estimate the quadrature error in these values. There it is shown that the relative accuracy of $\mathcal{S}^Q(\mathbf{x})$, using our quadrature method, depends on $|\mathbf{x}|$. For small $|\mathbf{x}|$, $\mathcal{S}^Q$ is accurate to approximately twelve digits, and the accuracy of $\mathcal{S}^Q$ degrades to approximately six digits when $|\mathbf{x}| = 50$. E^M measures the relative difference between $\mathcal{S}^M$ and $\mathcal{S}$ computed by partial asymptotic expansion. If the quadrature error is much larger than the difference between $\mathcal{S}$ and $\mathcal{S}^M$, then E^M will be approximately equal to the quadrature error. We show that this happens for certain values of $\mathbf{x}$ and M.

Figures 3.2 through 3.8 show results for the one-coordinate expansion. In each plot, we vary x with fixed values of y and z. Values of $E^M(\mathbf{x})$ are shown for various values of M. The figures demonstrate that the one-coordinate

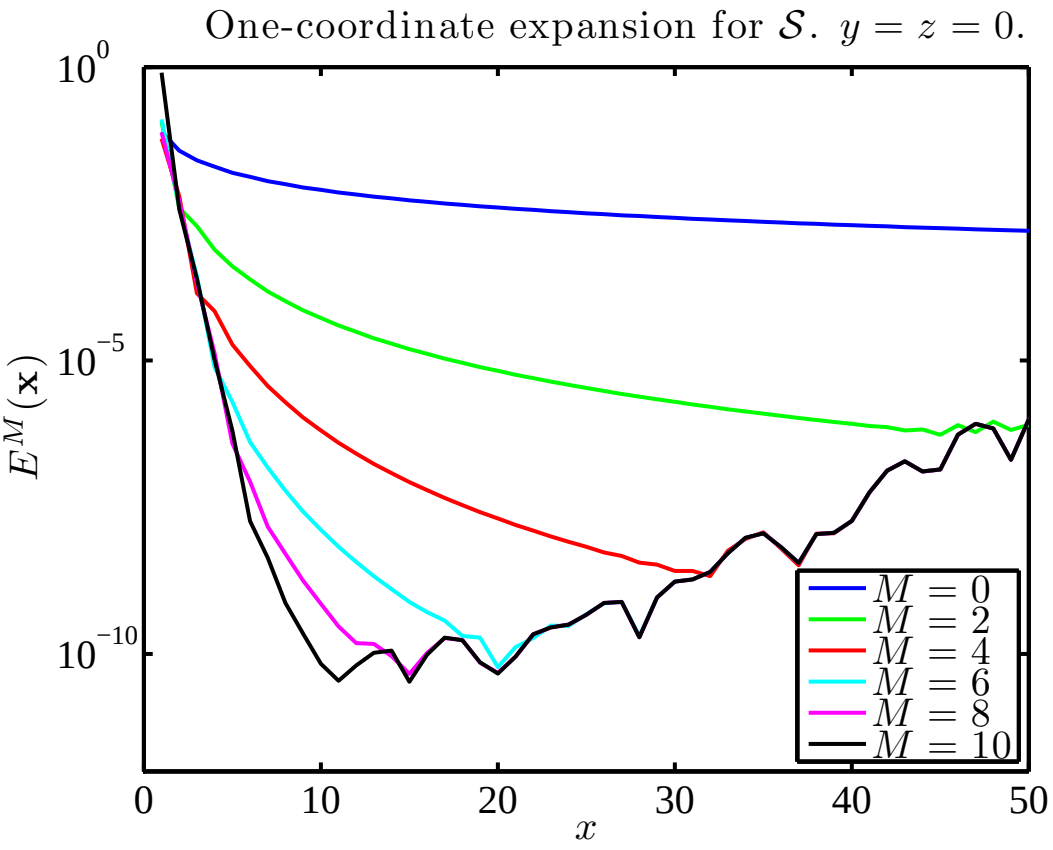


Figure 3.2: Plot showing convergence of the one-coordinate expansion for the discrete Stokeslet, $\mathcal{S}$. Shown are values of $E^M(\mathbf{x})$, the relative difference of the Stokeslet computed by quadrature and the Stokeslet computed by the one-coordinate expansion with M terms, for various values of M and for $\mathbf{x} = (x, 0, 0)$. Because $y = z = 0$, the odd terms in the expansion are identically zero, so we show only even values of M. Beyond $x = 10$, quadrature error begins to dominate for the expansions with larger M.

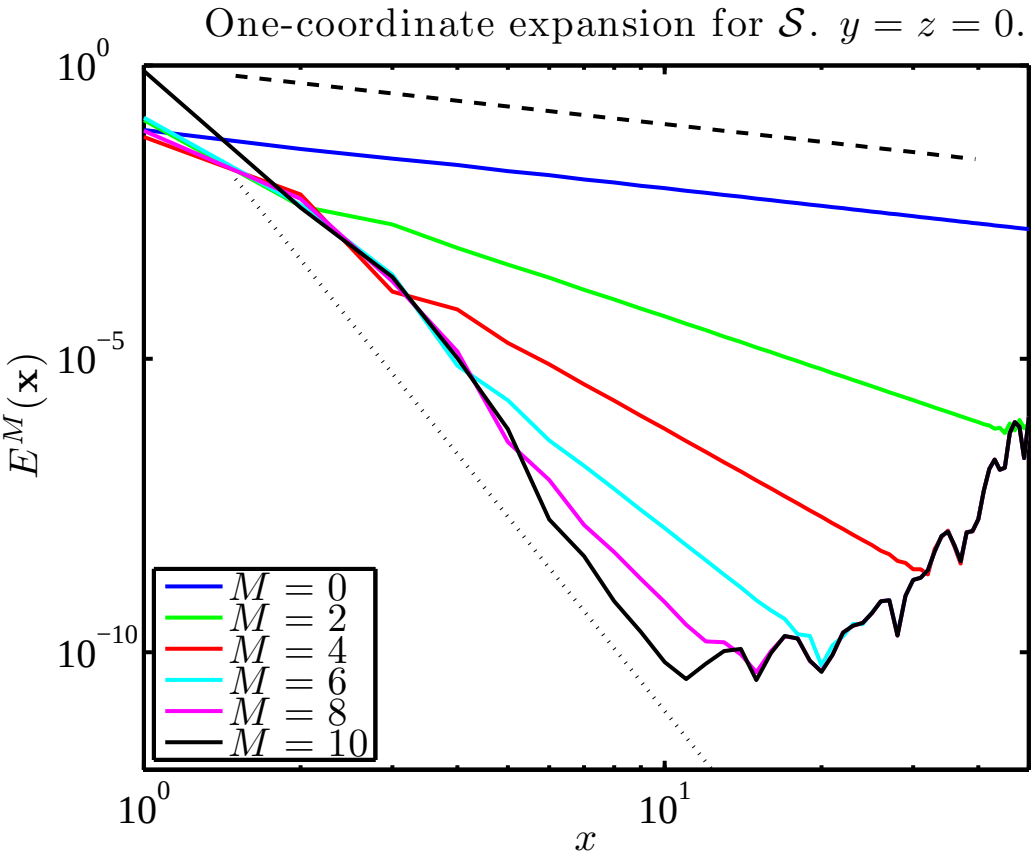


Figure 3.3: Same as previous plot, except on a log-log scale. The dashed line has slope -1. The dotted line has slope -11.

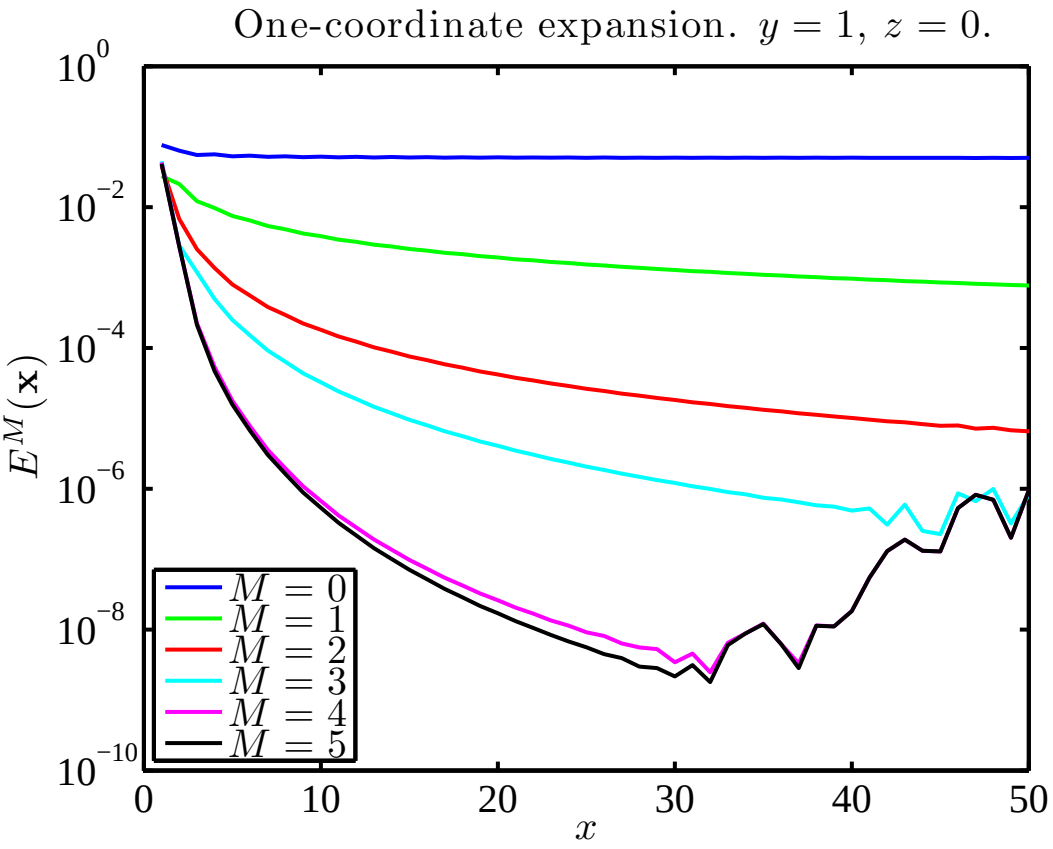


Figure 3.4: Plot showing $E^M(\mathbf{x})$ for the one-coordinate expansion for various M with $\mathbf{x} = (x, 1, 0)$. Now, the odd terms in the expansion are not zero, so we show both even and odd values of M.

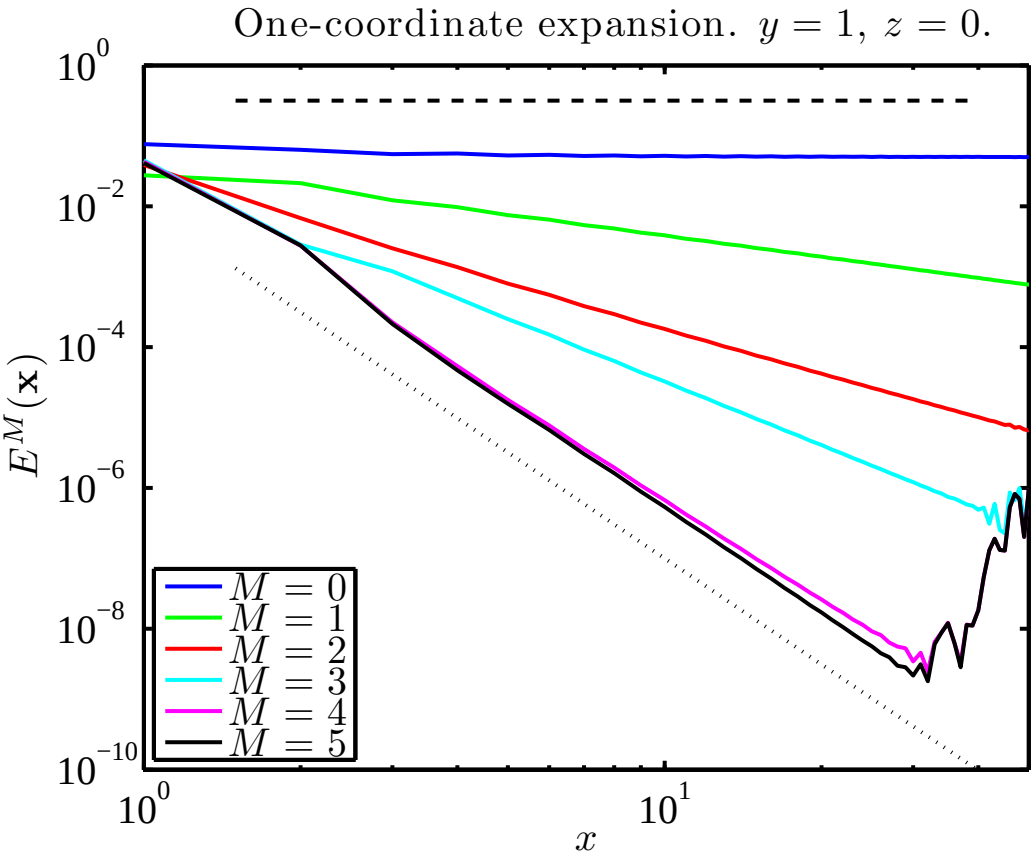


Figure 3.5: Same as previous plot, except on a log-log scale. The dashed line has slope 0. The dotted line has slope -5.

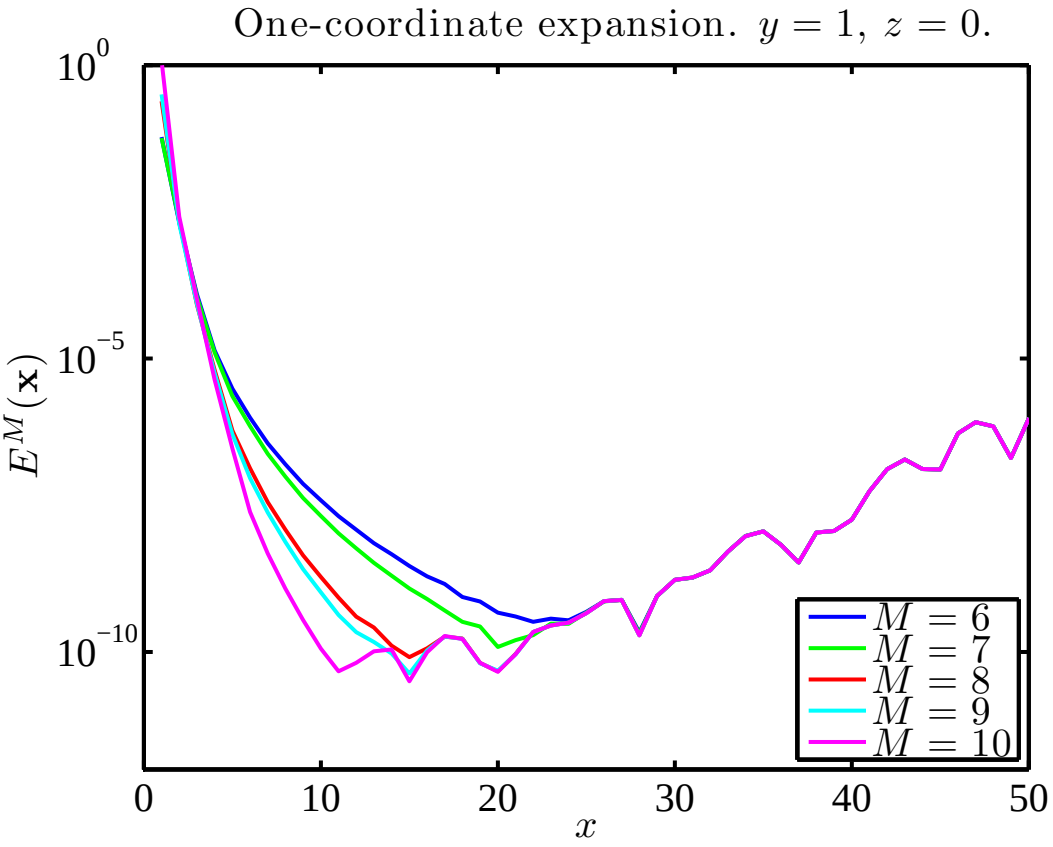


Figure 3.6: Plot showing $E^M(\mathbf{x})$ for the one-coordinate expansion for various M with $\mathbf{x} = (x, 1, 0)$. This plot shows larger values of M than the previous plot.

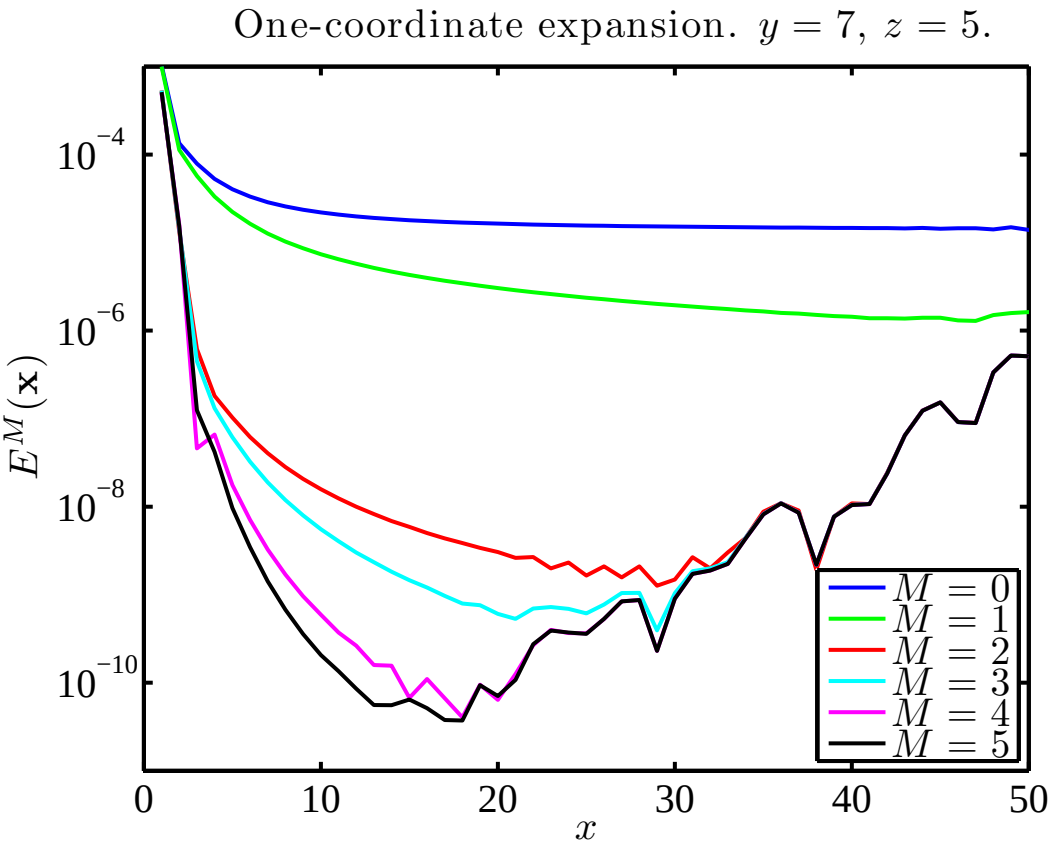


Figure 3.7: Plot showing $E^M(\mathbf{x})$ for the one-coordinate expansion for various M with $\mathbf{x} = (x, 7, 5)$.

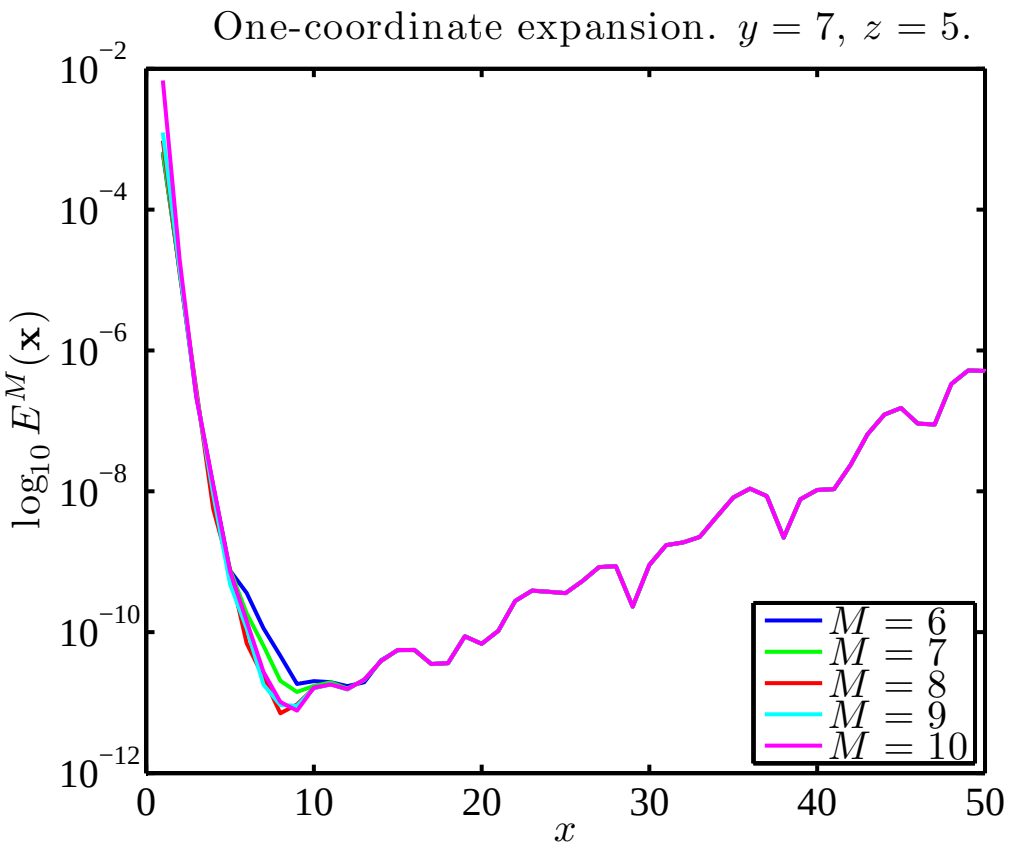


Figure 3.8: Plot showing $E^M(\mathbf{x})$ for the one-coordinate expansion for various M with $\mathbf{x} = (x, 7, 5)$. This plot shows larger values of M than the previous plot, and quadrature error dominates almost immediately.

asymptotic series for $\mathcal{S}(\mathbf{x})$ converges quickly to the values of $\mathcal{S}(\mathbf{x})$ that have been computed by quadrature, even for small values of x.

The case of small y and z should result in the largest errors in the asymptotic expansion. We know this because the two and three-coordinate expansions show that the coefficients, $\mathcal{S}_p(y,z)$, decay as y and z become large. We therefore show results when $y = z = 0$ in figures 3.2 and 3.3. Because of symmetries, when $y = z = 0$ the terms in the expansions with p odd are identically zero, i.e. $\mathcal{S}_p(0,0) = 0$. We therefore also show results when $y = 1$ and $z = 0$ in figures 3.4, 3.5, and 3.6.

When x is only 10, meaning we are calculating the discrete Stokeslet at a distance of 10 grid cells, and when $y = z = 0$, using only two terms in the expansion, meaning $M = 2$, gives four digits of accuracy. When $M = 4$ we obtain six digits of accuracy, when $M = 6$ we obtain eight digits of accuracy, and when $M = 10$ we obtain better than ten digits of accuracy. When $x > 10$, quadrature error begins to dominate the expansion with $M = 10$, resulting in the jagged black line that increases from $x = 10$ to $x = 50$. At $x = 15$ quadrature error begins to dominate when $M = 8$, and the expansions with smaller M eventually can be seen to be overtaken by quadrature error as they become coincident with the jagged black line. The magnitude of the quadrature error is consistent with our estimate in appendix 7.2. When just the Stokeslet, $\mathcal{S}_0$, is used to approximate the discrete Stokeslet, meaning $M = 0$, fewer than three digits of accuracy are obtained even when $x = 50$.

When $y = 1$ and $z = 0$, lack of symmetry reduces somewhat the con-

vergence of the expansions. Still, even when $x = 10$, only four terms are needed in the expansion to obtain six digits of accuracy. As when $y = z = 0$, accuracy only improves for larger x until quadrature error dominates.

The rate of convergence of the expansions as x becomes large can be seen in figures 3.3 and 3.5. When $y = z = 0$, it can be seen that the expansion with $M = 0$ converges at first order and the expansion with $M = 10$ converges at eleventh order. Because $\mathcal{S}_p(0, 0)$ is zero with p odd, this is consistent with the form of the expansion given in equation (3.28). To see why, first note that $\mathcal{S}^Q(x, 0, 0)$ is proportional to $1/x$ so if the first non-zero omitted term in the expansion is proportional to x^{-n}, we should expect the expansion to converge at order $n - 1$. When $M = 0$ the first non-zero omitted term in the expansion is proportional to x^{-2}, and when $M = 10$ the first non-zero omitted term is proportional to x^{-12}. Expansions with intermediate values of M can be seen to converge at intermediate rates.

When $y = 1$ and $z = 0$, symmetry no longer adds one to the rate of convergence. Now when $M = 0$ there is no convergence, meaning there is an order one relative difference between $\mathcal{S}$ and $\mathcal{S}_0$ even as x becomes very large. This was predicted above when we derived the expansion for $\mathcal{S}$. The convergence when $M = 5$ is fifth order, consistent with the fact that the first omitted term in the expansion is proportional to x^{-6}.

Figures 3.7 and 3.8 show results for larger values of y and z, namely $y = 7$ and $z = 5$. As predicted, convergence is even faster than when y and z take small values. When $x = 10$ and $M = 4$ nine digits of accuracy are obtained

as opposed to six when $y = 1$ and $z = 0$ with the same values of x and M. This result indicates that even if many digits of accuracy are required of $\mathcal{S}$, only a few terms in the expansion need be used unless y and z are only a few grid cells. As above, convergence is rapid for values of x on the order of ten grid cells.

While, theoretically, our expansion, (3.28), is valid in the limit as $x \to \infty$, we conclude that, in practice, we can achieve high accuracy even when x is not particularly large, with a practical value of M. When x becomes larger, even smaller values of M will suffice.

Figures 3.9 through 3.13 show results for the two-coordinate expansion. This expansion converges for large x and y, so in each plot we set $x = y$ and vary x with a fixed value of z. Values of $E^M(\mathbf{x})$ are shown for various values of M. The figures demonstrate that the two-coordinate asymptotic series for $\mathcal{S}(\mathbf{x})$ converges quickly to the values of $\mathcal{S}(\mathbf{x})$ that have been computed by quadrature, even for small values of $x = y$.

The case of small z should result in the largest errors in the asymptotic expansion because the three-coordinate expansion implies that $\mathcal{S}_{pq}(z)$ decays for large z. We therefore show results when $z = 0$ in figures 3.9 and 3.10. Because of symmetries when $z = 0$, when $p + q$ is odd $\mathcal{S}_{pq}(0) = 0$. We therefore also show results when $z = 1$ in figures 3.11, 3.12, and 3.13.

When x is only 10, when $z = 0$, and when $M = 4$ we obtain six digits of accuracy. When $M = 0$, meaning just the Stokeslet is used to approximate $\mathcal{S}$, we obtain only two digits of accuracy and only three digits of accuracy

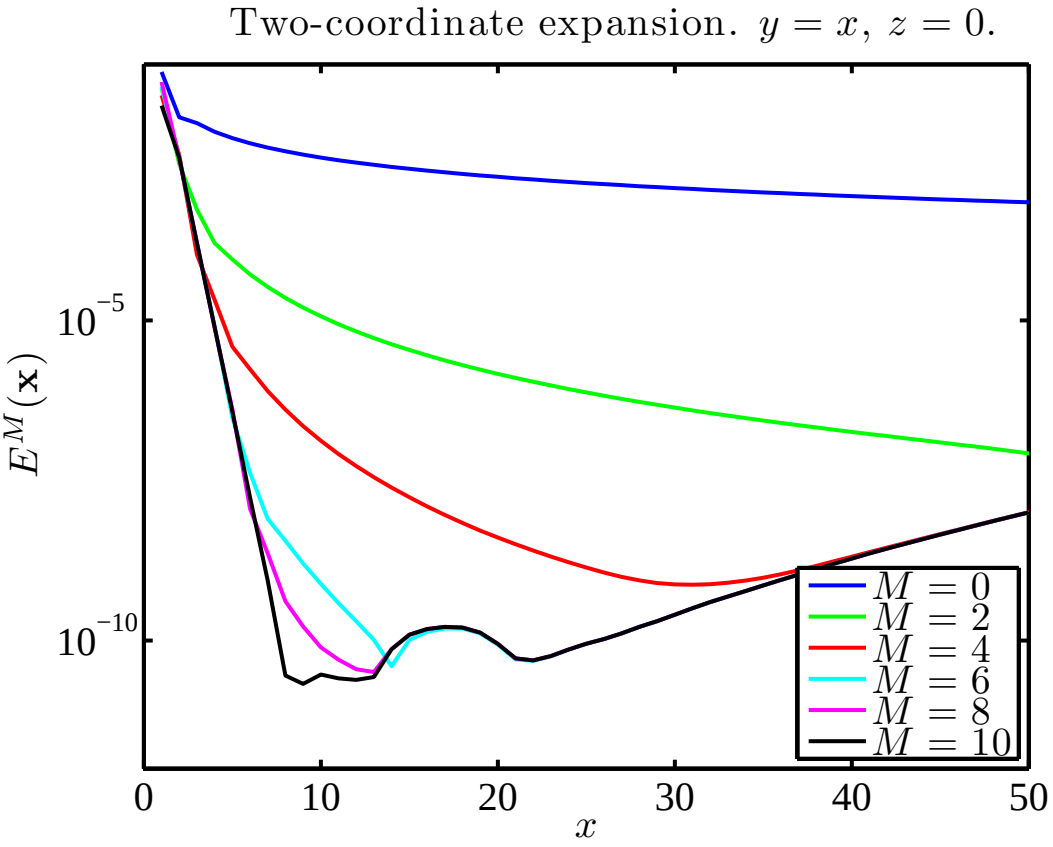


Figure 3.9: Plot showing convergence of the two-coordinate expansion for the discrete Stokeslet. Shown are values of $E^M(\mathbf{x})$, the relative difference of the Stokeslet computed by quadrature and the Stokeslet computed by the two-coordinate expansion with $2 \leq p + q \leq M$, for various values of M and for $\mathbf{x} = (x, x, 0)$. Because $z = 0$, the odd terms in the expansion are identically zero, so we show only even values of M.

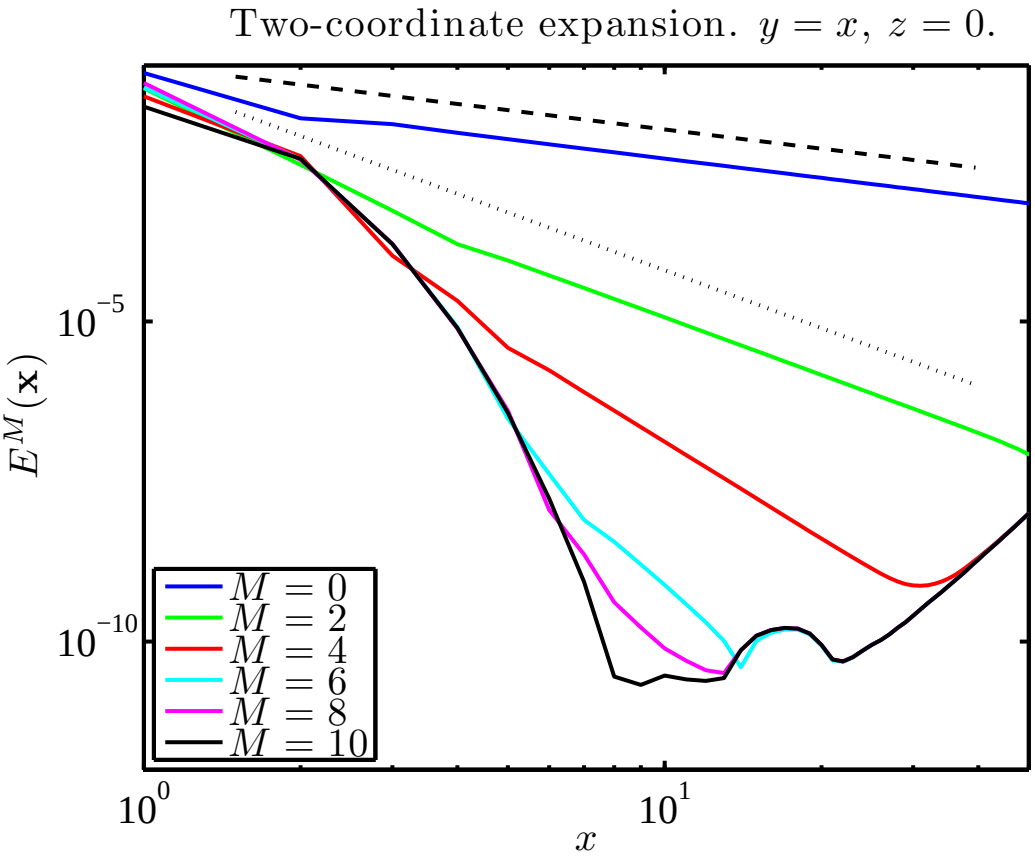


Figure 3.10: Same as previous plot, except on a log-log scale. The dashed line has slope -1. The dotted line has slope -3.

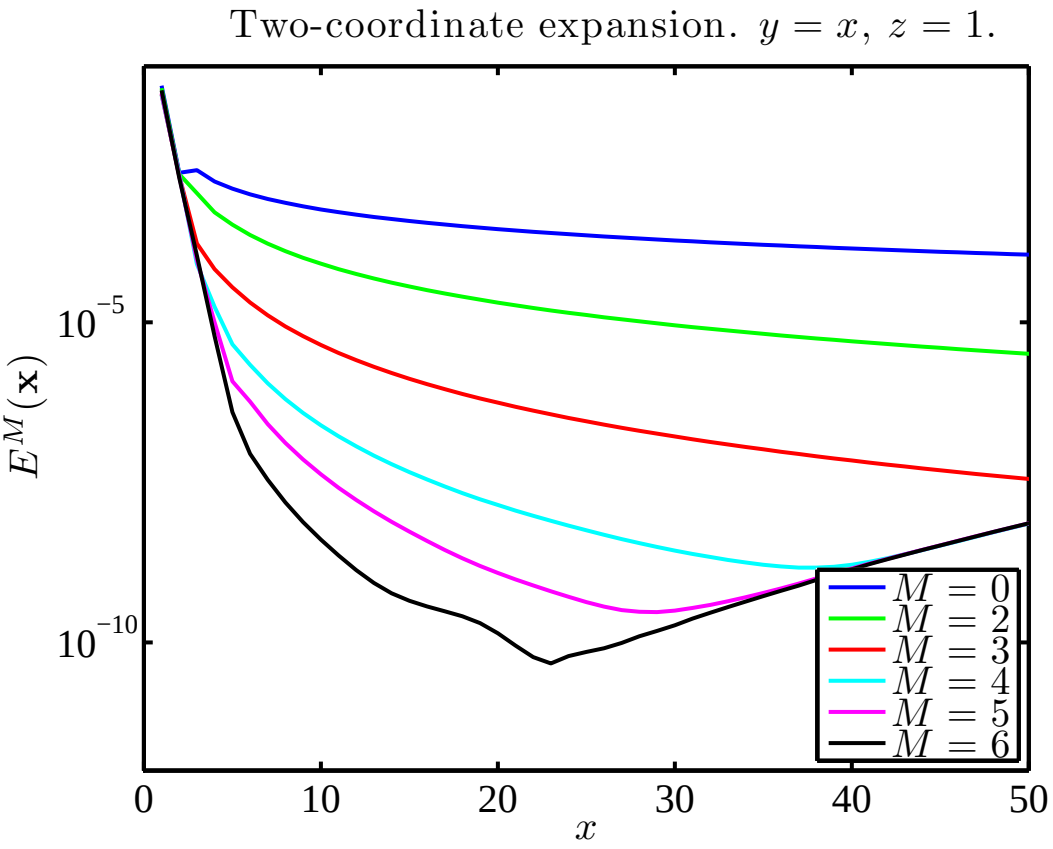


Figure 3.11: Plot showing $E^M(\mathbf{x})$ for the two-coordinate expansion for various M with $\mathbf{x} = (x, x, 1)$. Now, the odd terms in the expansion are not zero, so we show even and odd values of M

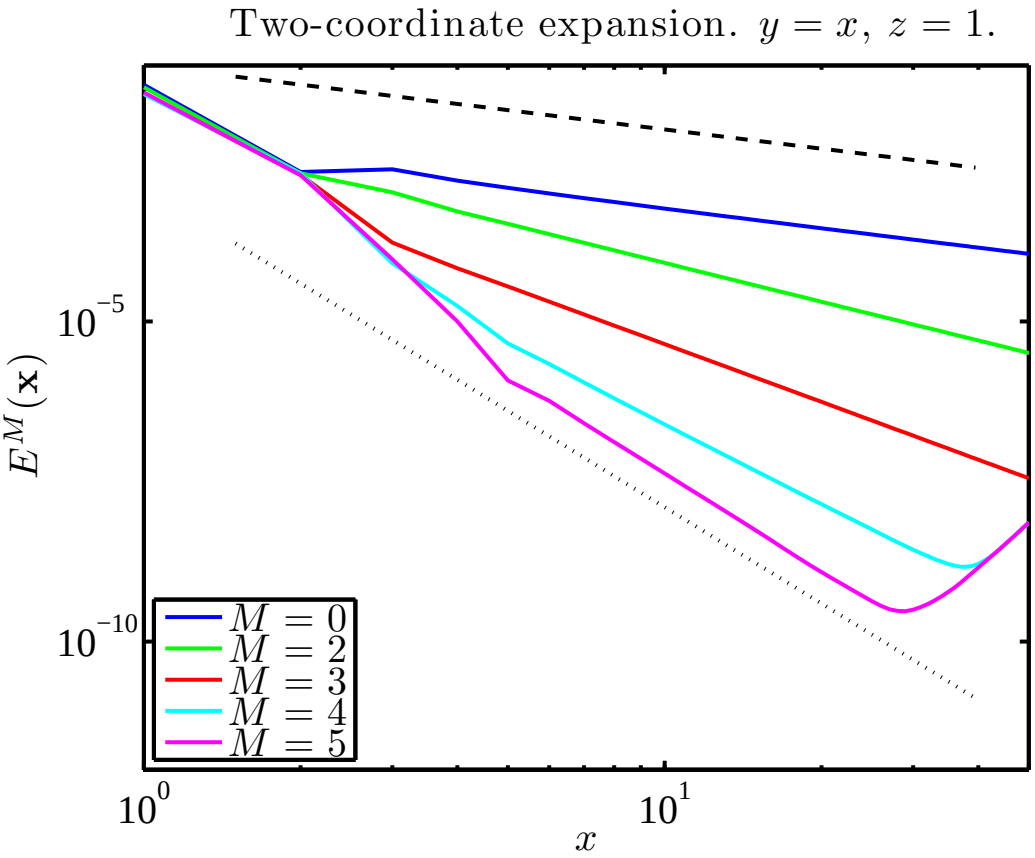


Figure 3.12: Same as previous plot, except on a log-log scale. The dashed line has slope -1. The dotted line has slope -5.

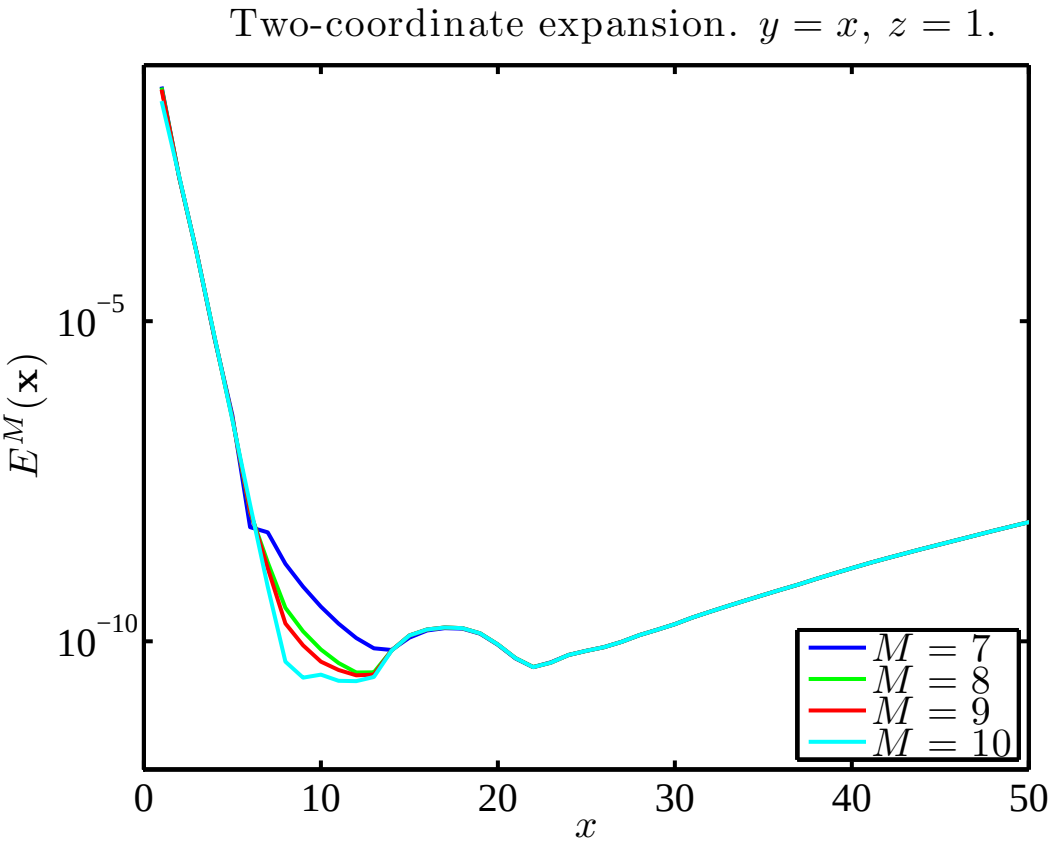


Figure 3.13: Plot showing $E^M(\mathbf{x})$ for the two-coordinate expansion for various M with $\mathbf{x} = (x, x, 1)$. This plot shows larger values of M than the previous plot. Quadrature error begins to dominate almost immediately.

when $x = 50$. When $x = 10$ and $M = 8$ we obtain ten digits of accuracy. As in the one-coordinate expansion, quadrature error dominates for larger x and M.

When $z = 1$, the fact that the odd terms in the expansions are no longer zero reduces the rate of convergence of the expansions when $M > 0$. When $M = 0$ the convergence rate is the same as when $z = 0$ because there are no terms which have $p+q = 1$. Still, when $x = 10$, $M = 4$ is sufficient to obtain six digits of accuracy.

The precise rates of convergence of the expansions can be seen in figures 3.10 and 3.12. These show that the expansion with $M = 0$ converges like x^{-1}. When $z = 0$, the expansions with M even converge like $x^{-(M+1)}$. When $z = 1$ and $M > 0$ the expansions converge like x^{-M}. These results are consistent with the asymptotic formula given in equation (3.36).

As with the one-coordinate expansion, we conclude that, in practice, we can achieve high accuracy with the two-coordinate expansion for the discrete Stokeslet even when x and y are not particularly large and with practical values of M. This conclusion holds even though, theoretically, the expansion is only valid in the limit as x and $y \to \infty$.

Figures 3.14 and 3.15 show results for the three-coordinate expansion. This expansion converges when x, y, and z are large, so in each plot we set $x = y = z$ and vary x. Values of $E^M(\mathbf{x})$ are shown for various values of M. The figures demonstrate that the three-coordinate asymptotic series for $\mathcal{S}(\mathbf{x})$ converges quickly to the values of $\mathcal{S}(\mathbf{x})$ that have been computed by

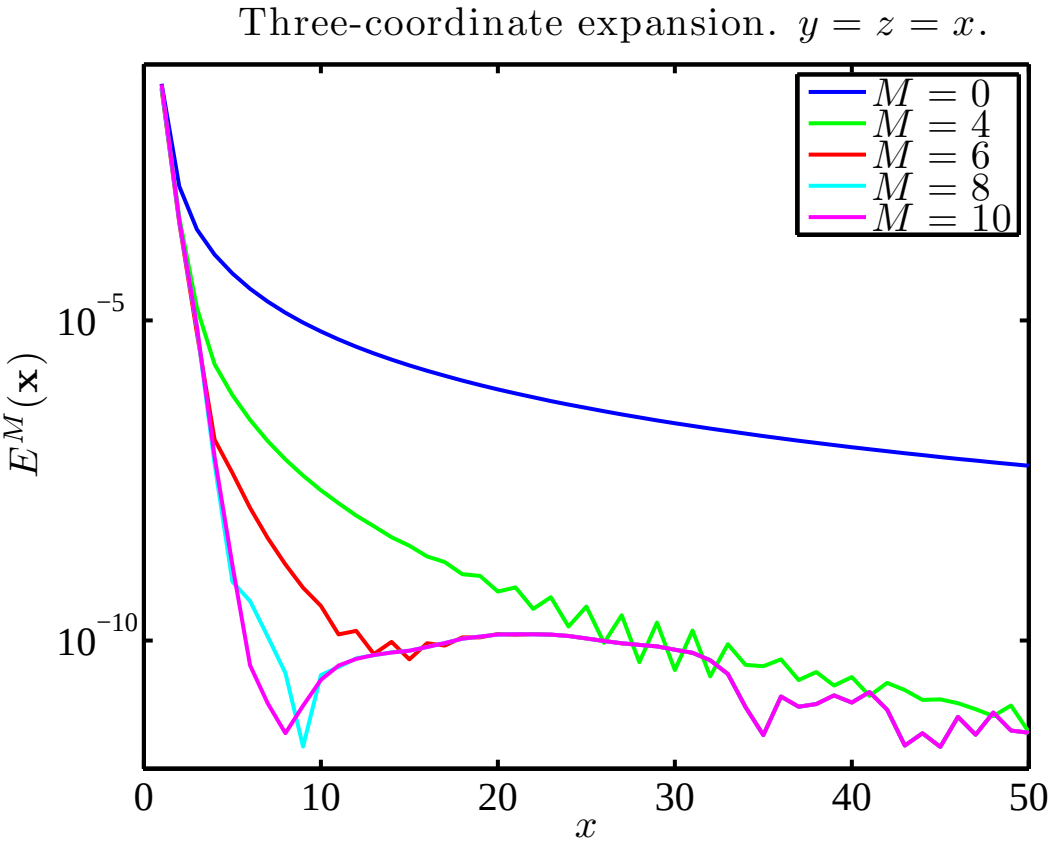


Figure 3.14: Plot showing convergence of the three-coordinate expansion for the discrete Stokeslet. Shown are values of $E^M(\mathbf{x})$, the relative difference of the Stokeslet computed by quadrature and the Stokeslet computed by the three-coordinate expansion with $3 \leq p+q+r \leq M$, for various values of M and for $\mathbf{x} = (x, x, x)$. The odd terms in the expansion are identically zero for any value of $\mathbf{x}$, so we show only even values of M.

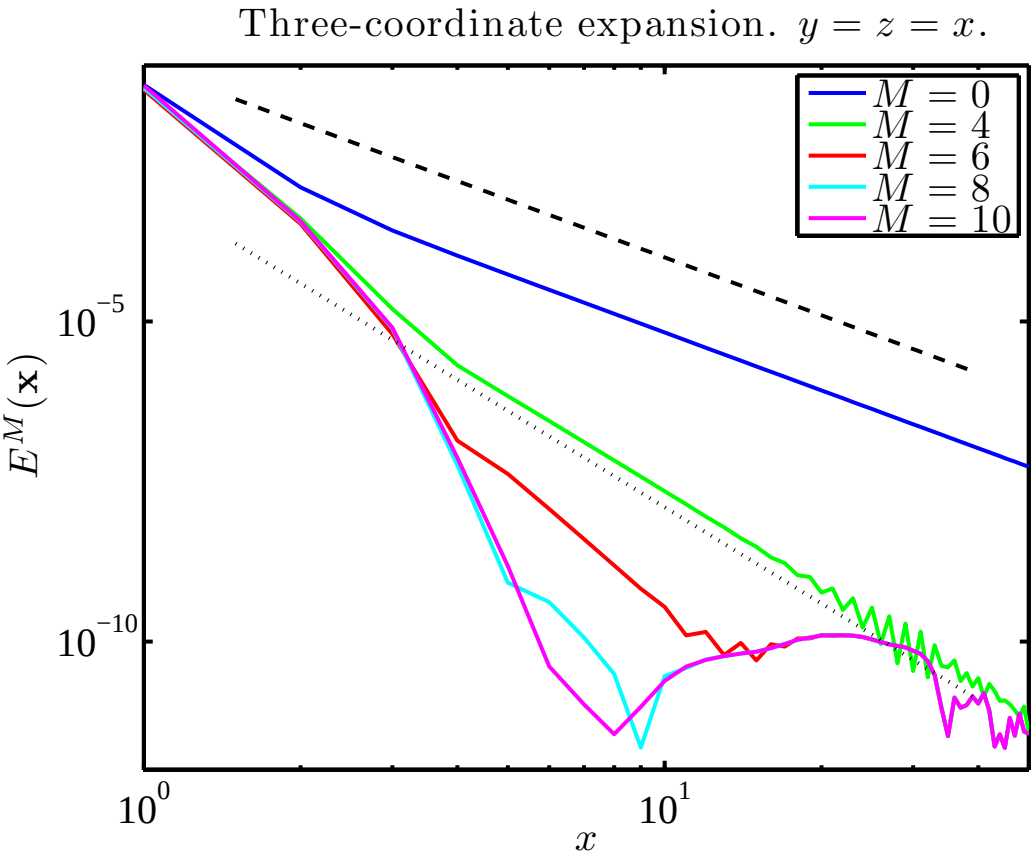


Figure 3.15: Same as previous plot, except on a log-log scale. The dashed line has slope -3. The dotted line has slope -5.

quadrature, even for small values of $x = y = z$ and even for very small M.

Even when x, y, and z are all only of moderate size, the three-coordinate expansion, equation (3.39), converges very quickly. When $M = 0$, meaning we are approximating $\mathcal{S}$ by the Stokeslet, $\mathcal{S}_0$, we obtain five digits of accuracy when $x = y = z = 10$, and seven digits when $x = y = z = 50$. There are no terms with $1 \leq p + q + r < 3$, and the terms in the expansion with $p + q + r$ odd are zero since $\mathcal{S}_{pqr} = 0$ for $p+q+r$ odd. Therefore, we show results only for M even, and the next expansion we show after $M = 0$ is $M = 4$. When $M = 4$ we obtain nearly eight digits of accuracy when $x = 10$ and we do better for larger M or larger x. As with the previous expansions, quadrature error dominates for larger M and $x = y = z$.

The rates of convergence of the expansions can be seen in figure 3.15. When $M = 0$, now E^M is proportional to x^{-3}, when $M = 4$, E^M is proportional to x^{-5}, and for general M which is positive and even, E^M is proportional to $x^{-(M+1)}$. These results are consistent with the asymptotic formula given in equation (3.39).

As with the one and two-coordinate expansions, we conclude that, in practice, we can achieve high accuracy with the three-coordinate expansion for the discrete Stokeslet even when x, y, and z are not particularly large and with practical values of M. This conclusion holds even though, theoretically, the expansion is valid only in the limit as x, y, and $z \to \infty$.

3.4.2 Expansion for $\mathcal{G}$

We now examine the rates of convergence of the expansions for $\mathcal{G}$, the Green's function relating the Lagrangian forces $\mathbf{F}$ and velocities $\mathbf{U}$ of the immersed boundary points. We examine the convergence of what we refer to as the one-, two-, and three-coordinate expansions for $\mathcal{G}$, respectively equations (3.60), (3.61), and (3.63). These expansions include the term $\mathcal{G}_0$, defined in equation (3.55). We also examine the convergence of what we refer to as the one-, two-, and three-coordinate expansions for $\mathcal{G}_0$, respectively equations (3.81), (3.84), and (3.88). We shall also examine the convergence of the expansion for $\mathcal{H}_p$, defined in equation (3.58). This expansion, equation (3.69), involves the alternating moments of the discrete delta function, N_n, which are defined in equation (3.68).

Unlike our expansions for the discrete Stokeslet, all of these expansions depend on our choice of the discrete delta function. In chapter 4, we discuss in detail the various delta functions that we use and how they are constructed. Here, we make use of two representative delta functions. The first, denoted by δ_4^{IB}, has support width 4 and is one of the delta functions traditionally used in immersed boundary method computations. It satisfies moment conditions which imply that $M_0(X) \equiv 1$ and $M_1(X) \equiv 0$. It also satisfies the so-called balanced condition which implies that $N_0(X) \equiv 0$. In the next chapter, we discuss these conditions in detail, we discuss the derivation of this function, and we give the formula for the corresponding one-dimensional function ϕ_4^{IB}. The second delta function we use is denoted by δ_4^{M}. It also has support width

4, and it provides the maximum possible interpolation order for that width of support. It satisfies $M_0(X) \equiv 1$, and $M_n(X) \equiv 0$ for $n = 1$, 2, and 3. It does not satisfy $N_0 \equiv 0$. As with δ_4^{IB}, the conditions satisfied by δ_4^{M} and the derivation of the function are discussed in detail in chapter 4, and a formula for the corresponding function ϕ_4^{M} is given there as well.

We first show, in figure 3.16, the discrete moments, $M_n(X)$, defined in equation (3.67), and the the discrete alternating moments, $N_n(X)$, defined in equation (3.68), for these two delta functions. As we have seen in section 3.3, the expansions for $\mathcal{G}$ and $\mathcal{G}_0$ depend on these moments. Only those values of n are shown for which M_n and N_n are not identically 0 or identically 1. It can be seen that $M_n(X)$ is even about $X = 1/2$ when n is even and is odd about $X = 1/2$ when n is odd. Generally, the magnitude of M_n increases as n increases. $N_n(X)$ is even about $X = 1$ when n is even and is odd about $X = 1$ when n is odd. It is always the case that $N_n(X + 1) = -N_n(X)$. Although the plots of N_n might suggest that these functions are bounded by -1 and 1, this is not the case for larger values of n. Like M_n, the magnitude of N_n generally increases as n increases.

Figures 3.17 and 3.18 show the functions $\mathcal{H}_p(X, X')$ for the two delta functions and for various values of p. For our calculations of these functions and throughout this section we fix the primed variables and change the unprimed variables. In particular, we choose a random value of X' in $[0, 1)$. For this range of values of X', and for these delta functions, both of which have support width 4, $\mathcal{H}_p(X, X')$ is undefined when $|X| < 4$. We therefore

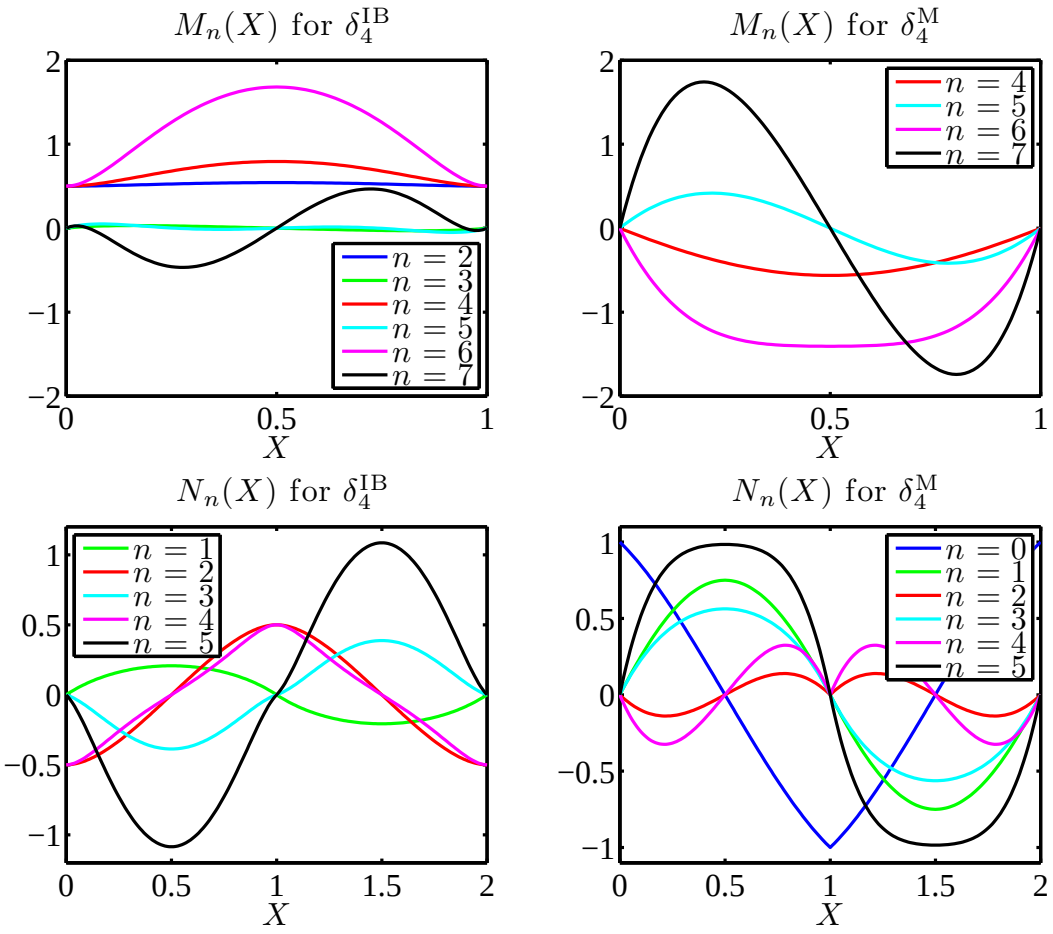


Figure 3.16: Discrete moments, $M_n(X)$, and discrete alternating moments, $N_n(x)$, for the two representative delta functions. For both delta functions, $M_0 \equiv 1$ and $M_1 \equiv 0$. For δ_4^{IB}, we have additionally that $N_0 \equiv 0$. For δ_4^{M}, we have additionally that $M_2 \equiv M_3 \equiv 0$.

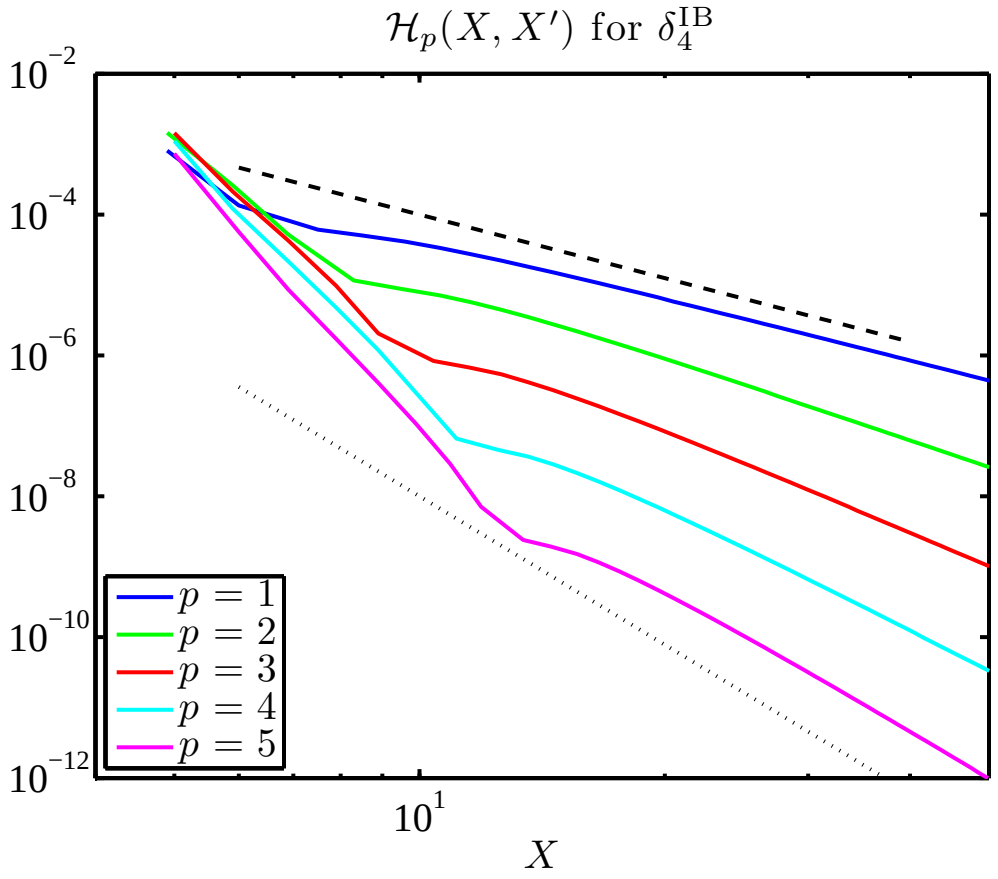


Figure 3.17: Plot showing $\mathcal{H}_p(X, X')$ for various values of p and for the delta function δ_4^{IB}. The quantity X varies while X' is fixed and $X' \in [0, 1)$. In actuality, $\mathcal{H}_p$ oscillates about zero as X increases with a period of approximately 2. Thus, we have plotted $|\mathcal{H}_p(X, X')|$ for those X such that $|\mathcal{H}(X, X')|$ has a local maximum. The dashed line has slope -3. The dotted line has slope -7.

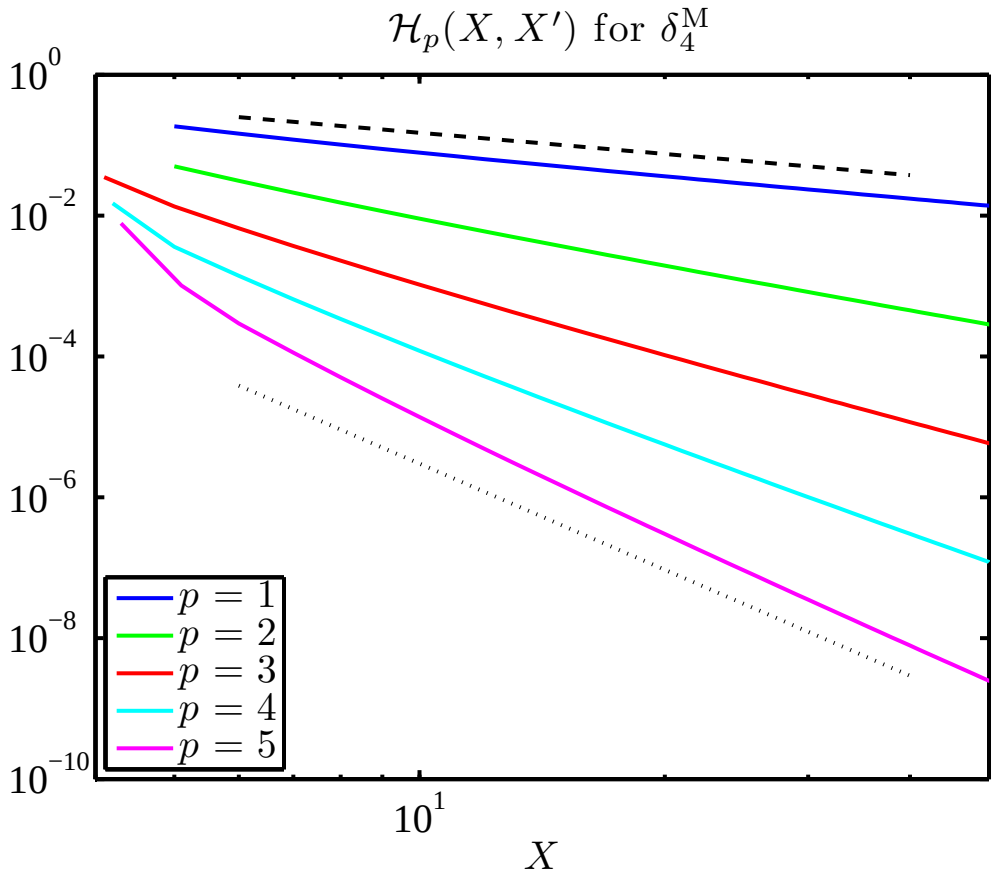


Figure 3.18: Same plot as above except for the delta function δ_4^{M}. Again, X' is fixed in $[0, 1)$, and we plot the local maxima of $|\mathcal{H}(X, X')|$. The dashed line has slope -1. The dotted line has slope -5.

use only values of X that are at least 4.

As X increases, each function $\mathcal{H}_p(X, X')$ both oscillates about zero and decays. The period of oscillation is approximately but not exactly equal to 2. The decay of $\mathcal{H}_p$ is rapid enough that for its values to be seen properly, we must display them on a logarithmic scale. Since $\mathcal{H}_p$ oscillates about zero, we cannot simply plot its logarithm, both because $\mathcal{H}_p$ takes negative values for which the logarithm is undefined (or complex) and because $\mathcal{H}_p$, every period, takes positive values arbitrarily close to zero that would be represented on a logarithmic scale by using arbitrarily negative exponents. Instead we plot only the local maxima of the absolute value of $\mathcal{H}_p(X, X')$ as X varies. Doing this results in relatively smooth curves and gives a sense of the magnitudes of $\mathcal{H}_p(X, X')$ in the neighborhood of a particular X even though for some values of X in this neighborhood $\mathcal{H}_p(X, X')$ may be closer to zero. This procedure of plotting only the local maxima of the absolute value of the functions $\mathcal{H}_p(X, X')$ is something we shall repeat later for other functions that either oscillate about zero or oscillate with minima equal to (or nearly equal to) zero.

It can be seen in figures 3.17 and 3.18 that, for the delta function δ_4^{IB}, $\mathcal{H}_p(X, X')$ decays like $|X-X'|^{-(p+2)}$, while for the delta function δ_4^{M}, $\mathcal{H}_p(X, X')$ decays like $|X - X'|^{-p}$. These results are consistent with our predictions in section 3.3 above (see equation (3.69)). The fact that $\mathcal{H}_p$ decays more rapidly for δ_4^{IB} is a consequence of the fact that $N_0(X) \equiv 0$ for this delta function.

Curiously all the curves in figure 3.17, which is for the delta function δ_4^{IB},

are kinked. The value of X at which the kink occurs increases as p increases. For smaller values of X the rate of decay of $\mathcal{H}_p$ is more rapid than predicted. For larger values of X the rate of decay is, at first, slower than predicted. The rate then approaches the predicted rate asymptotically.

In figures 3.19 and 3.20, we examine the convergence of the expansion for $\mathcal{H}_p(X, X')$ given in equation (3.69). We define $E^M(X, X')$ to be the error caused by computing $\mathcal{H}_p$ with the expansion truncated at $j = M$ compared with computing $\mathcal{H}_p$ exactly. We choose the special case $p = 1$ to investigate the convergence. Recall that we defined $H_p^M(X, X')$ in equation (3.70) to be the truncated computation. We then let

$$E^M(X, X') = |\mathcal{H}_1^M(X, X') - \mathcal{H}_1(X, X')|. \tag{3.94}$$

Because $N_n(X) \equiv 0$ for δ_4^{IB}, $\mathcal{H}_1^0$ and $\mathcal{H}_1^1$ are identically zero for this delta function, and so E^M is not shown for these values of M. As a function of X, $\mathcal{H}_1^M(X, X') - \mathcal{H}_1(X, X')$ oscillates around zero, so $E^M(X, X')$ takes the value zero for certain values of X. Because of this, and for reasons explained above, we plot only the local maxima of $E^M(X, X')$.

We do not make $E^M(X, X')$ into a relative error by dividing by the absolute value of $\mathcal{H}_1(X, X')$ because $\mathcal{H}_1$ oscillates around zero and so we would be dividing by zero for certain values of X. Instead, recall figures 3.17 and 3.18, which show that the local maxima of the absolute values of $\mathcal{H}_1$ decay like $|X - X'|^{-3}$ when δ_4^{IB} is used and like $|X - X'|^{-1}$ when δ_4^{M} is used. Fig-

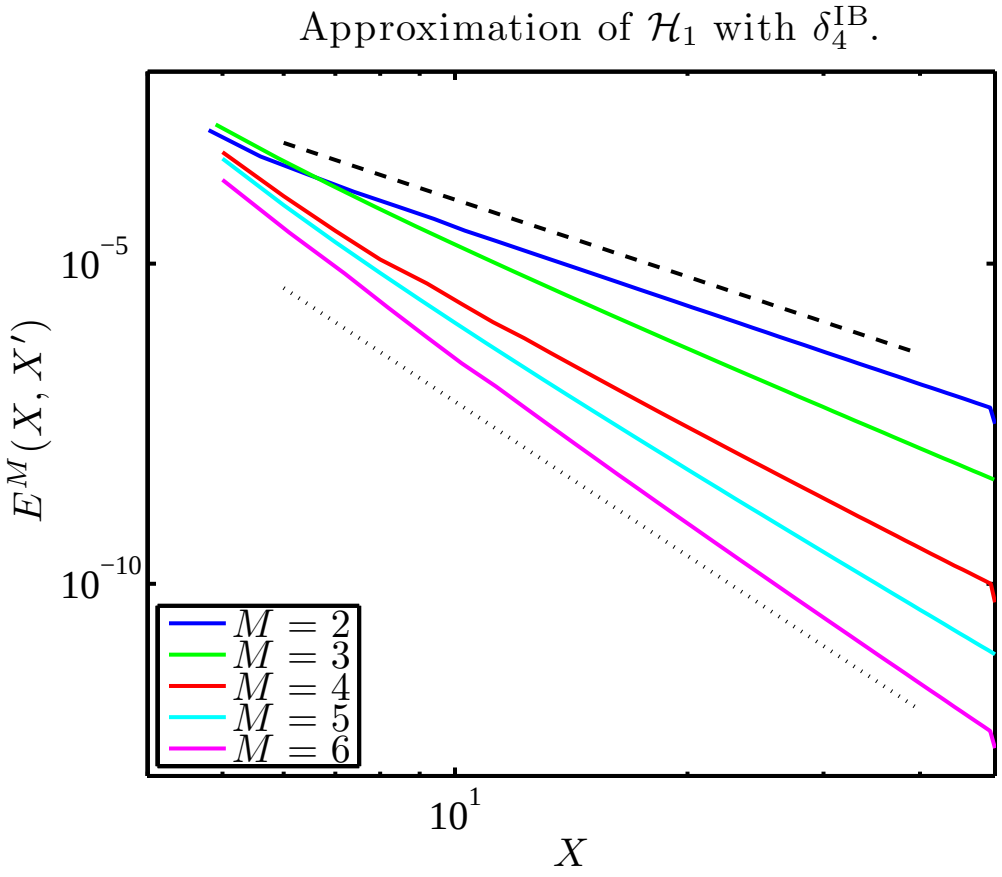


Figure 3.19: Plot comparing exact calculation of $\mathcal{H}_1(X, X')$ with the approximate calculation $\mathcal{H}_1^M(X, X')$. X' is fixed in $[0, 1)$. We plot the local maxima of the error, E^M. The dashed line has slope -4. The dotted line has slope -8.

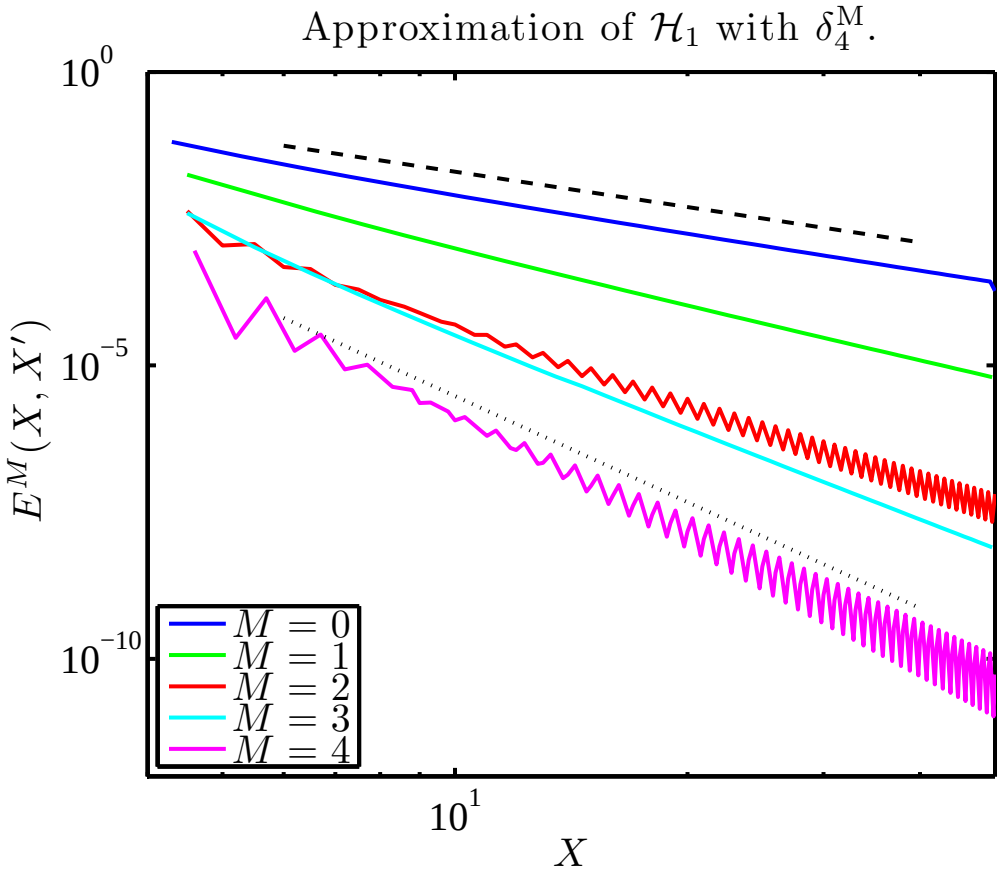


Figure 3.20: Same plot as above except for the delta function δ_4^{M}. The dashed line has slope -2. The dotted line has slope -6. Note that because we plot only the local maxima of E^M, the line segments connecting these maxima have no significance. The reason that some of the curves in this plot are jagged is that E^M sometimes has two local maxima with different magnitudes in a given period.

ure 3.19 and 3.20 show that for both delta functions, $E^M(X, X')$ decays like $|X - X'|^{-(M+2)}$. These orders of decay are consistent with our error estimate in equation (3.76) because $p = 1$.

We now examine the errors associated with truncating expansions for $\mathcal{G}$. We examine the one-, two-, and three-coordinate expansions, respectively equations (3.60), (3.61), and (3.63). For the one-coordinate expansion we truncate the sum so that only terms with $1 \leq p \leq M$ are included. For the two-coordinate expansion we include terms with $2 \leq p + q \leq M$, and for the three-coordinate expansion we include terms with $3 \leq p + q + r \leq M$. In all of these computations, we compute $\mathcal{G}_0$ and $\mathcal{H}_p$ exactly. We compare computations with the truncated expansion, which we denote $\mathcal{G}^M$, with $\mathcal{G}$ computed exactly by the naive method described in chapter 2. For all expansions, we let $\mathcal{G}^0$ be simply $\mathcal{G}_0$ computed exactly. To compute $\mathcal{G}$ exactly, we need values of the discrete Stokeslet, $\mathcal{S}$. We compute these values to machine precision, either by the quadrate method described in chapter 2 or by using one the expansions described in section 3.1 of this chapter. To measure the relative error associated with truncating the expansions, we define a quantity, $E^M(\mathbf{X}, \mathbf{X}')$. Its definition is the same for the one-, two-, and three-coordinate expansions.

$$E^M(\mathbf{X}, \mathbf{X}') = \frac{\|\mathcal{G}^M(\mathbf{X}, \mathbf{X}') - \mathcal{G}(\mathbf{X}, \mathbf{X}')\|}{\|\mathcal{G}(\mathbf{X}, \mathbf{X}')\|} \tag{3.95}$$

Figures 3.21 and 3.22 show results for the one-coordinate expansion.

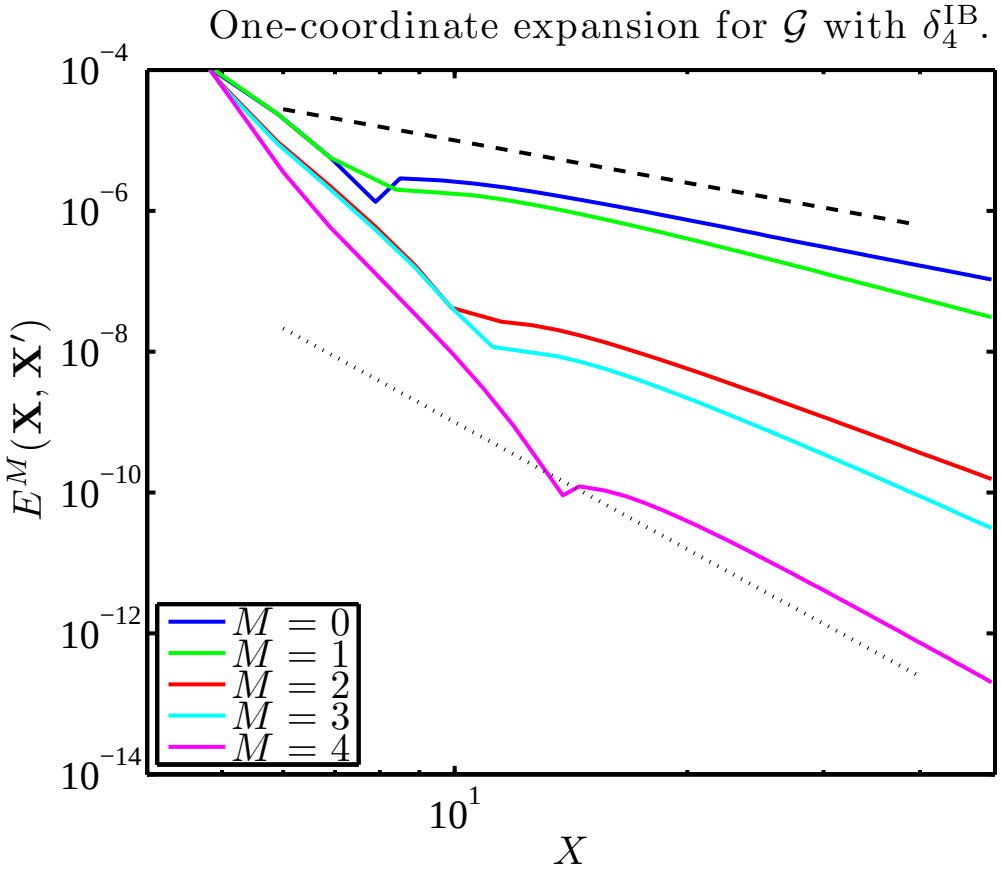


Figure 3.21: Plot showing, E^M, the error of $\mathcal{G}$ computed by the one-coordinate expansion for various values of M relative to $\mathcal{G}$ computed exactly. The delta function used is δ_4^{IB}. The coordinate X varies while Y, Z, X', Y', and Z' are all fixed in $[0, 1)$. In actuality, E^M is oscillatory as X varies with period approximately equal to 1. We plot the local maxima of E^M. The dashed line has slope -2. The dotted line has slope -6.

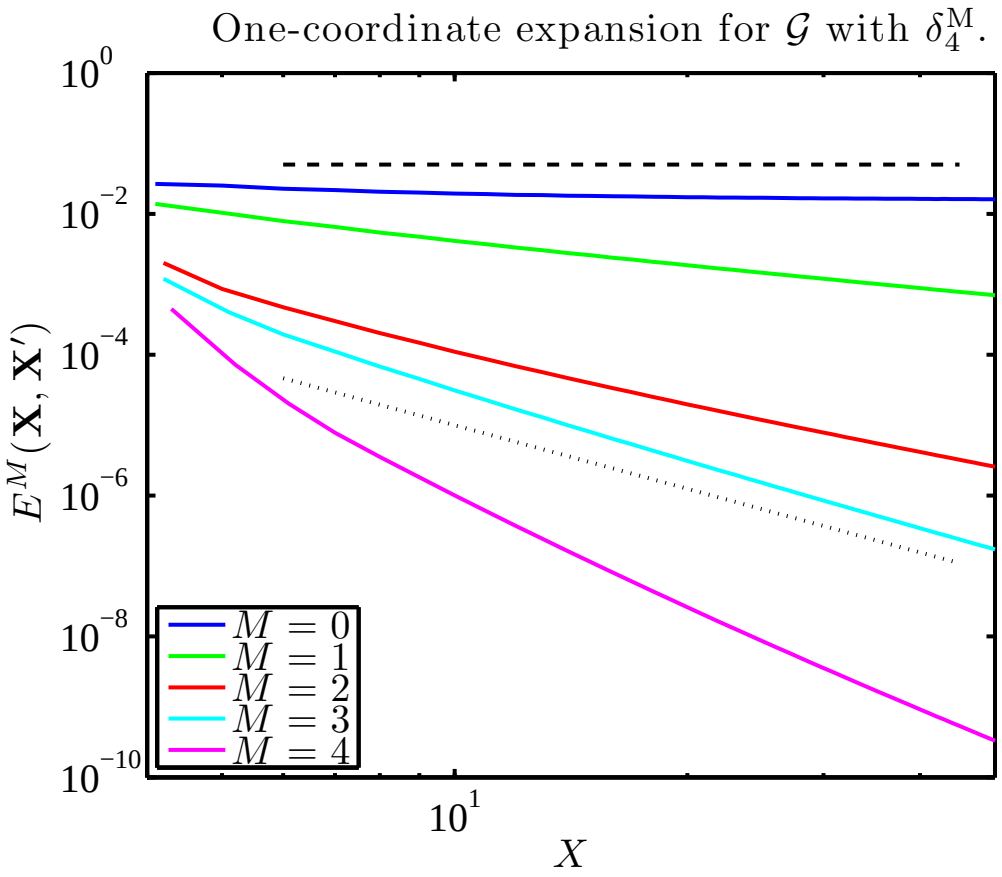


Figure 3.22: Same plot as above except for the delta function δ_4^{M}. The dashed line has slope 0. The dotted line has slope -3.

Shown are values of $E^M(\mathbf{X}, \mathbf{X}')$ for various values of M and for both representative delta functions. We choose the coordinates of $\mathbf{X}'$ and also Y and Z randomly from $[0, 1)$. With Y, Z, and $\mathbf{X}'$ fixed, we let X vary and calculate $E^M(\mathbf{X}, \mathbf{X}')$. For the expansion to be defined we must have $X \geq 4$. We find that for certain values of X, separated approximately by integers, $E^M(\mathbf{X}, \mathbf{X}')$ takes values at least several orders of magnitude smaller than its values for nearby values of X. We do not suspect that E^M actually takes the value zero for certain values of X. If E^M were exactly zero it would mean that all components of $\mathcal{G}$ and $\mathcal{G}^M$ were in exact agreement simultaneously, an unlikely scenario. Still, the clarity of plots of E^M is much improved by showing only its local maxima, and this is what we have done in figures 3.21 and 3.22.

The figures show that $E^M(\mathbf{X}, \mathbf{X}')$ decays like $|X - X'|^{-(M+2)}$ when $|X - X'|$ is large and the delta function δ_4^{IB} is used. $E^M(\mathbf{X}, \mathbf{X}')$ decays like $|X - X'|^{-M}$ when the delta function δ_4^{M} is used. This is as we expect. The lowest order correction not included in the sum that computes $\mathcal{G}^M$ is $\mathcal{H}_{M+1}\mathcal{G}_p$, where $\mathcal{G}_p$ does not depend on $X - X'$. This term therefore has the same rate of decay as $\mathcal{H}_{M+1}$. The normalizing factor in E^M, $\mathcal{G}$, decays like $|X - X'|^{-1}$. Therefore E^M should decay like $|X - X'|\mathcal{H}_{M+1}(X, X')$ does, which is what we observe. The curves in figure 3.21, which is for the delta function δ_4^{IB}, are kinked in a similar fashion as the curves in figure 3.17, which show $\mathcal{H}_p$ for this delta function.

Note the magnitudes of the errors in figures 3.21 and 3.22. For the delta

function δ_4^{IB}, nearly six digits of accuracy are obtained with $M = 0$ when X is as small as 10. This means that $\mathcal{G}$ and $\mathcal{G}_0$ agree to six digits for this delta function. If $M = 4$, eight digits of accuracy are obtained when $X = 10$. The errors are not as small for the delta function δ_4^{M}, nor is the rate of decay as rapid as $|X - X'|$ becomes large. Less than two digits of accuracy are obtained when $M = 0$, and this error does not decay for large X. Six digits are obtained when $M = 10$ and $X = 10$. The reason that the delta function δ_4^{IB} performs better is that it satisfies $N_0(X) \equiv 0$ unlike δ_4^{M}. In chapter 4, we refer to the requirement that a delta function satisfy $N_0 \equiv 0$ as the balanced condition, and this condition is used explicitly to construct δ_4^{IB} as well as similar delta functions.

Figures 3.23 and 3.24 show results for the two-coordinate expansion. Shown are values of $E^M(\mathbf{X}, \mathbf{X}')$ for various values of M and for both representative delta functions. This expansion is valid when $X - X'$ and $Y - Y'$ are large in magnitude. We choose the coordinates of $\mathbf{X}'$ and also Z randomly from $[0, 1)$. For these calculations we fix Z and $\mathbf{X}'$. We let X vary and set $Y = X$, and we calculate the relative error, $E^M(\mathbf{X}, \mathbf{X}')$. We must have $X = Y \geq 4$. As with the one-coordinate expansion, we plot only the local maxima of E^M for the reasons listed above.

We depict only even values of M in these figures. The indices p and q must be at least one in the expansion, so E^1 always equals E^0 identically. We find that for larger, even values of M, E^M is very nearly equal to E^{M+1} such that they would be nearly indistinguishable in these plots. We believe

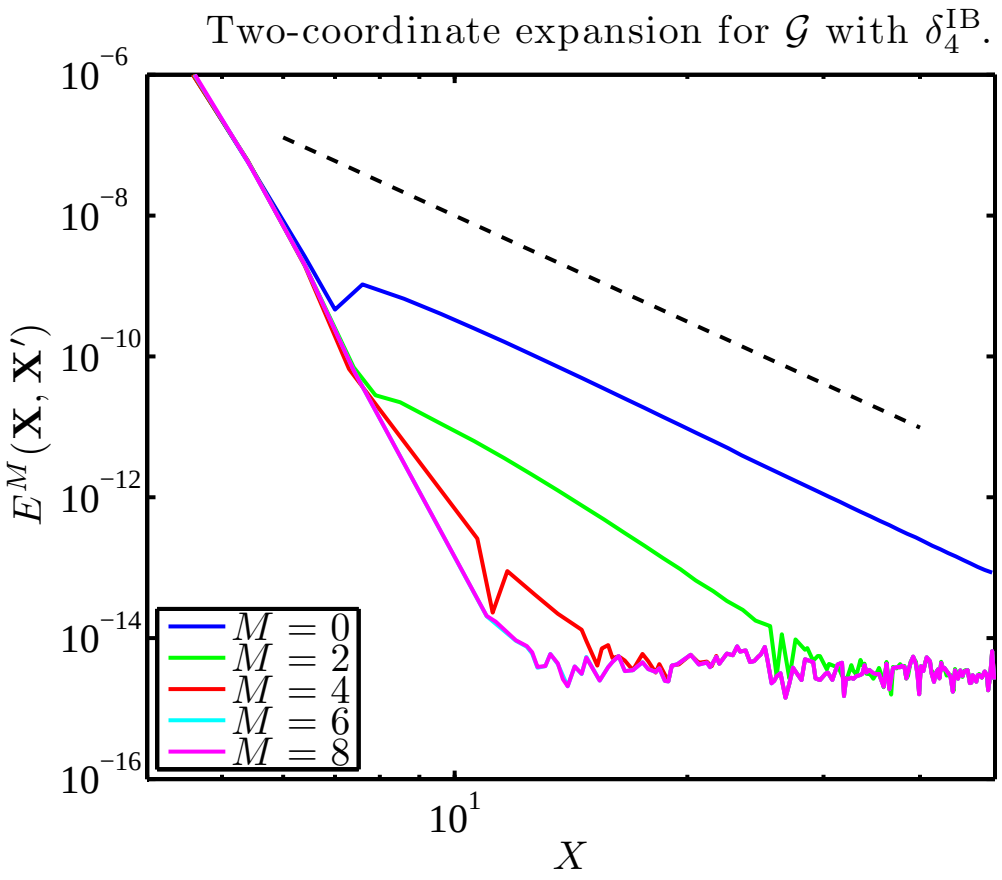


Figure 3.23: Plot showing, E^M, the error of $\mathcal{G}$ computed by the two-coordinate expansion for various values of M relative to $\mathcal{G}$ computed exactly. We show only even values of M because for M even $E^M \approx E^{M+1}$. The delta function used is δ_4^{IB}. The coordinate X varies, and we set $Y = X$. Z, X', Y', and Z' are all fixed in $[0, 1)$. We plot the local maxima of E^M. The dashed line has slope -5. For large values of M and $X = Y$, the relative error is smaller than machine precision.

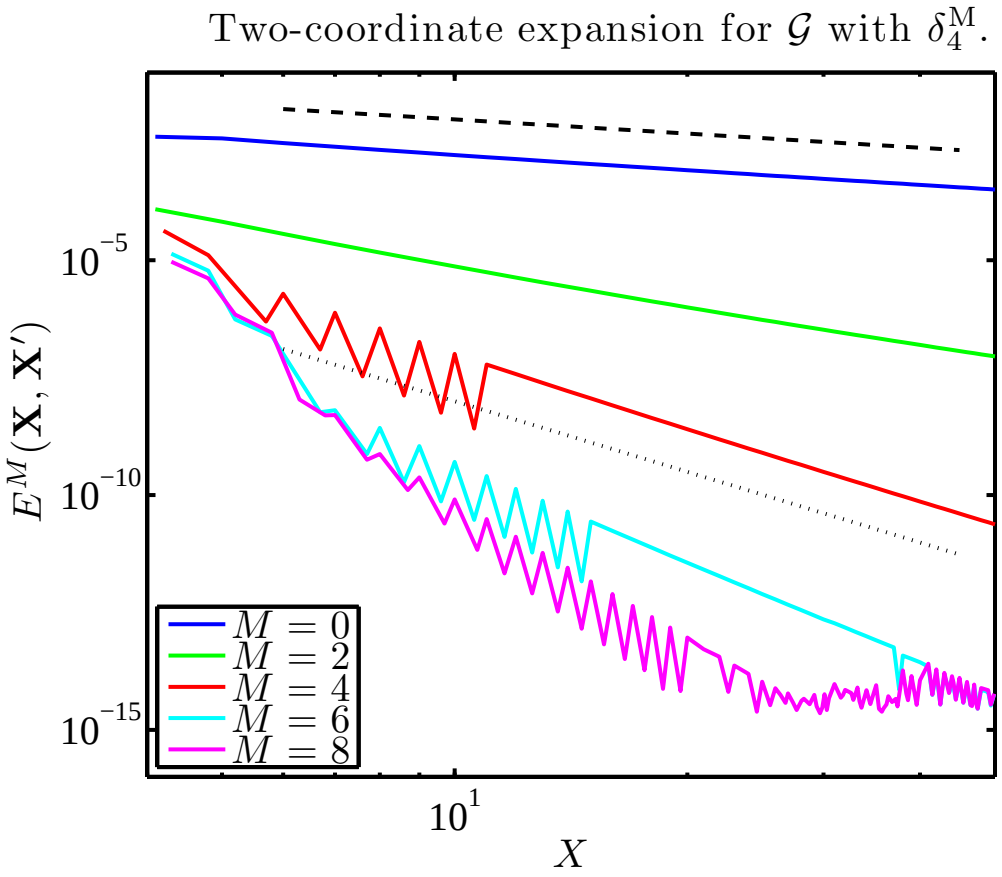


Figure 3.24: Same plot as above except for the delta function δ_4^{M}. The dashed line has slope -1. The dotted line has slope -5. The reason that some of the curves in this plot are jagged is that E^M sometimes has two local maxima with different magnitudes in a given period.

the underlying reason for this near equality is that $\mathcal{G}_{pq}$ is zero on the diagonal when $p + q$ is odd.

The figures show that when the delta function δ_4^{IB} is used, E^M decays like $|X - X'|^{-(M+5)}$. When the delta function δ_4^{M} is used, E^M decays like $|X - X'|^{-(M+1)}$. These rates of decay are one order faster than we would expect given the rates of decay of $\mathcal{H}_p$. They are the rates of decay we would expect for E^{M+1}. The fact that, for M even, E^M very nearly equals E^{M+1} gives E^M one "extra" order of decay. Note that the difference in the orders of decay for the two delta functions is now 4, while it was only 2 for the one-coordinate expansion. The magnitudes of the errors are now smaller than for the one-coordinate expansion. When $X = Y$ is only 10, $\mathcal{G}$ and $\mathcal{G}_0$ agree to better than nine digits when the delta function is δ_4^{IB}. When X is somewhat larger than 10 the error is below machine precision even for $M = 4$. When the delta function is δ_4^{M} and $X = 10$, $M = 4$ is sufficient to obtain seven digits of precision.

Figures 3.25 shows results for the three-coordinate expansion and for the delta function δ_4^{M}. We do not show results for the delta function δ_4^{IB} because the values of E^M are below machine precision for any M, even for X of order 10. The three-coordinate expansion is valid when $X - X'$, $Y - Y'$, and $Z - Z'$ are large in magnitude. We choose the coordinates of $\mathbf{X}'$ randomly from $[0, 1)$. For these calculations we fix $\mathbf{X}'$. We let X vary and set $Y = Z = X$, and we calculate the relative error, $E^M(\mathbf{X}, \mathbf{X}')$. We must have $X = Y = Z \geq 4$. We plot only the local maxima of E^M.

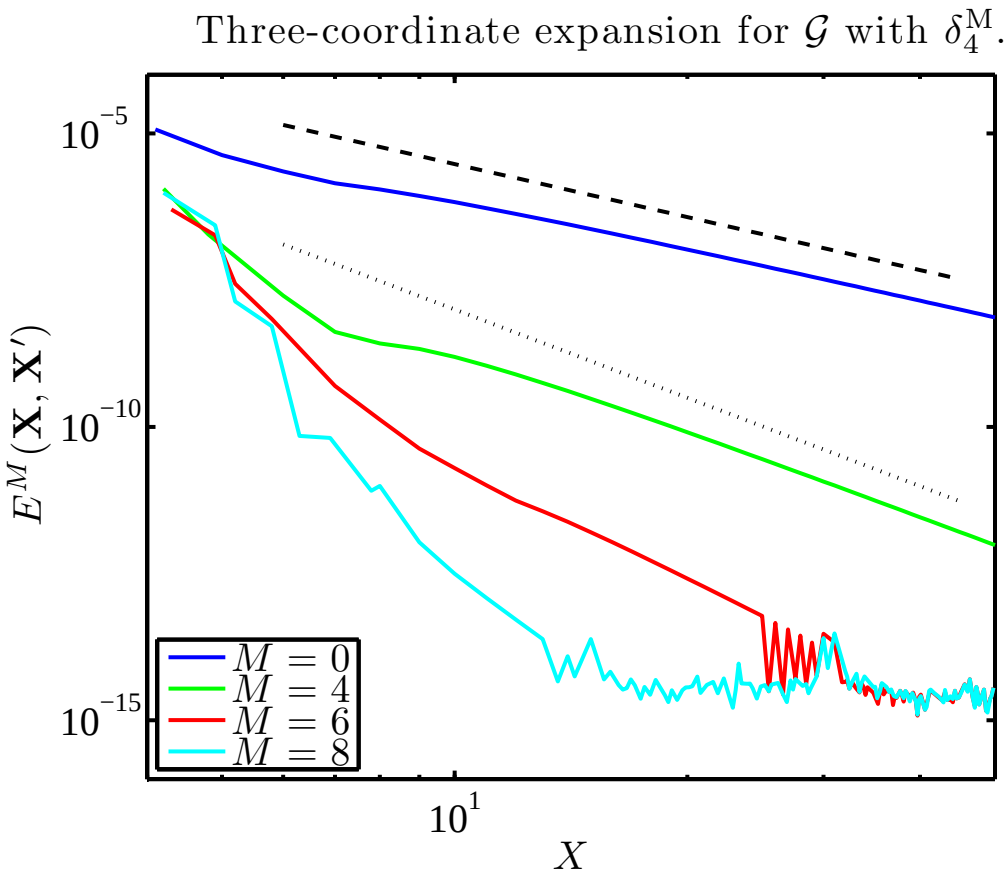


Figure 3.25: Plot showing, E^M, the error of $\mathcal{G}$ computed by the three-coordinate expansion for various values of M relative to $\mathcal{G}$ computed exactly. We show only even values of M because for M even $E^M = E^{M+1}$. Also E^2 is not pictured because it equals E^0. The delta function used is δ_4^{M}. The coordinate X varies, and we set $Y = X$ and $Z = X$. X', Y', and Z' are all fixed in $[0, 1)$. We plot the local maxima of E^M. The dashed line has slope -3. The dotted line has slope -5.

The indices p, q, and r must be at least one in the expansion, so E^M always equals E^0 identically when $M = 1$ or 2. The coefficient $\mathcal{S}_{pqr}$ is zero when $p + q + r$ is odd, so for M even E^M always equals E^{M+1} identically. Thus, we only show even values of M in figure 3.25.

The figure shows that E^M decays like $|X - X'|^{-(M+1)}$ except when $M = 0$ in which case E^M decays like $|X - X'|^{-3}$. These rates are consistent with what we would expect if we recognize that the leading correction to $\mathcal{G}^M$ with M even comes when $p + q + r = M + 2$ (unless $M = 0$, in which case the leading correction comes when $p + q + r = 4$). The magnitudes of the errors are somewhat smaller than for the two-coordinate expansion. When $X = 10$, $M = 4$ is now sufficient to obtain nine digits of precision.

If the delta function δ_4^{IB} is used, we would expect E^M with M even to decay like $|X - X'|^{-(M+7)}$ and like $|X - X'|^{-9}$ when $M = 0$. These rates of decay are six orders faster than when the delta function δ_4^{M} is used. Even for small values of X, very few terms will be needed to achieve any desired accuracy above machine precision. The expansion is, in fact, so accurate that we are unable to show a meaningful plot of the errors.

We now turn to the expansions for $\mathcal{G}_0$, equations (3.81), (3.84), and (3.88), which we refer to respectively as the one-, two-, and three-coordinate expansions for $\mathcal{G}_0$. We define $\mathcal{G}_0^M$ to be $\mathcal{G}_0$ computed by a truncated expansion. For the one-coordinate expansion, the truncated expansion uses terms with $0 \leq p \leq$M, for the two-coordinate expansion $0 \leq p + q \leq M$, and for the three-coordinate expansion $0 \leq p+q+r \leq M$. To measure the relative error

associated with truncating the expansions, we define $E_0^M(\mathbf{X}, \mathbf{X}')$ by

$$E_0^M(\mathbf{X}, \mathbf{X}') = \frac{\|\mathcal{G}_0^M(\mathbf{X}, \mathbf{X}') - \mathcal{G}_0(\mathbf{X}, \mathbf{X}')\|}{\|\mathcal{G}_0(\mathbf{X}, \mathbf{X}')\|} \tag{3.96}$$

where $\mathcal{G}_0$ is computed exactly by the naive method described in chapter 2. Both delta functions we test here satisfy $M_0 \equiv 1$, therefore for both delta functions and for all expansions $\mathcal{G}_0^0(\mathbf{X}, \mathbf{X}') = \mathcal{S}_0(\mathbf{X} - \mathbf{X}')$ where $\mathcal{S}_0$, recall, is the (continuous) Stokeslet. Thus, E_0^0 is the relative difference between $\mathcal{G}_0$ and the Stokeslet.

We first show, in figures 3.26 and 3.27, plots of the functions $\mathcal{H}_0^p(X, X')$ for the two delta functions. $\mathcal{H}_0^p(X, X')$ is doubly periodic with period one, so we fix X', chosen randomly from $[0, 1)$, and let X vary between 0 and 1. We do not show $\mathcal{H}_0^p$ for values of p such that it is either identically 1 or identically 0. Thus, $p = 0$ and $p = 1$ are not shown for either delta function. In addition, $p = 2$ and $p = 3$ are not show for the delta function δ_4^{M}. Generally, $\mathcal{H}_0^p$ increases in magnitude as p increases.

Figures 3.28 - 3.33 show values of the error, E_0^M, for the one-, two-, and three-coordinates expansions. For all expansions, X', Y', and Z' are fixed and chosen randomly from $[0, 1)$. For the one-coordinate expansion, Y and Z are also fixed and chosen from $[0, 1)$, while X varies. For the two-coordinate expansion, Z is fixed and chosen from $[0, 1)$, while X varies, and we set $Y = X$. For the three-coordinate expansion, we set $Y = X$ and $Z = X$. For all expansions, we must have $X \geq 4$.

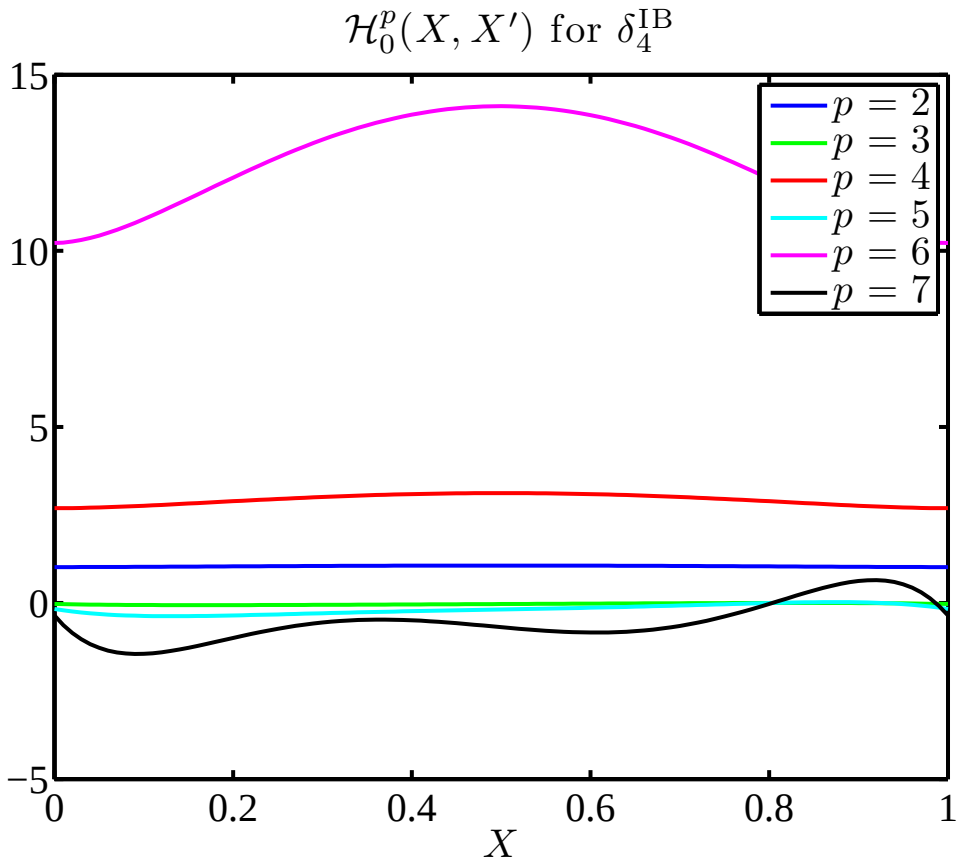


Figure 3.26: Plot showing $\mathcal{H}_p^0(X, X')$ for various values of p and for the delta function δ_4^{IB}. The quantity X varies while X' is fixed and $X' \in [0, 1)$. $\mathcal{H}_0^p$ is identically 1 when $p = 0$ and is identically 0 when $p = 1$.

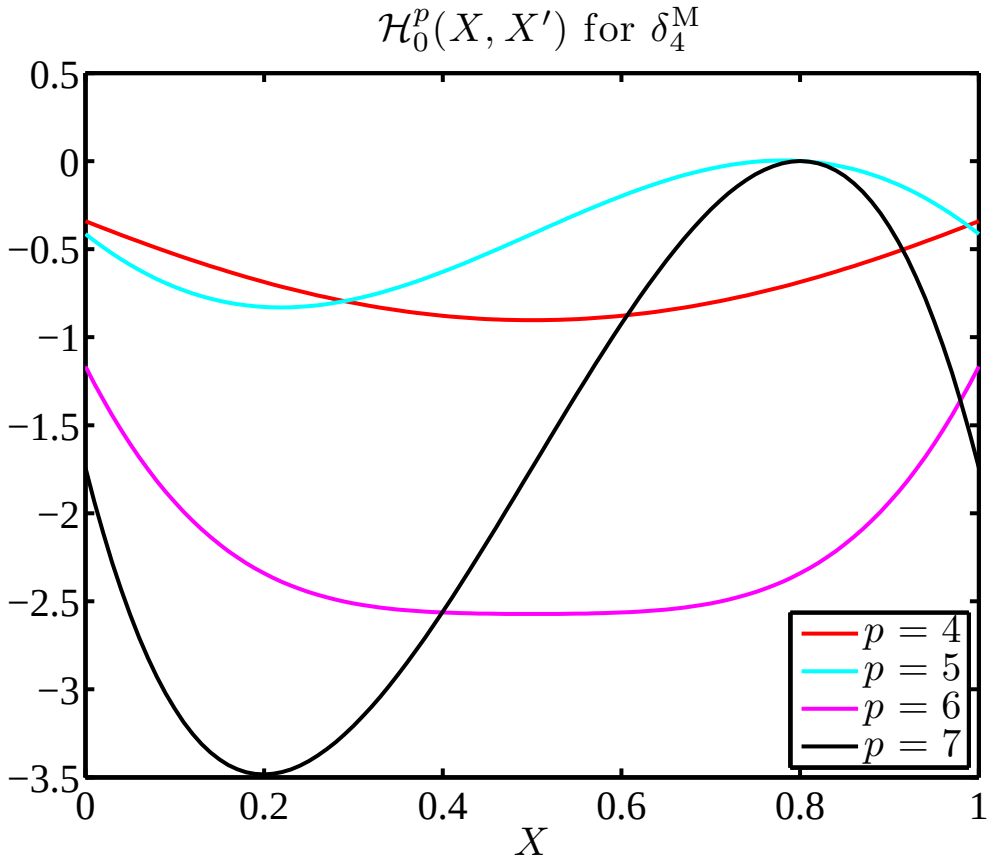


Figure 3.27: Same plot as above except for the delta function δ_4^{M}. $\mathcal{H}_0^p$ is identically 1 when $p = 0$ and is identically 0 when $p = 1$, 2, or 3.

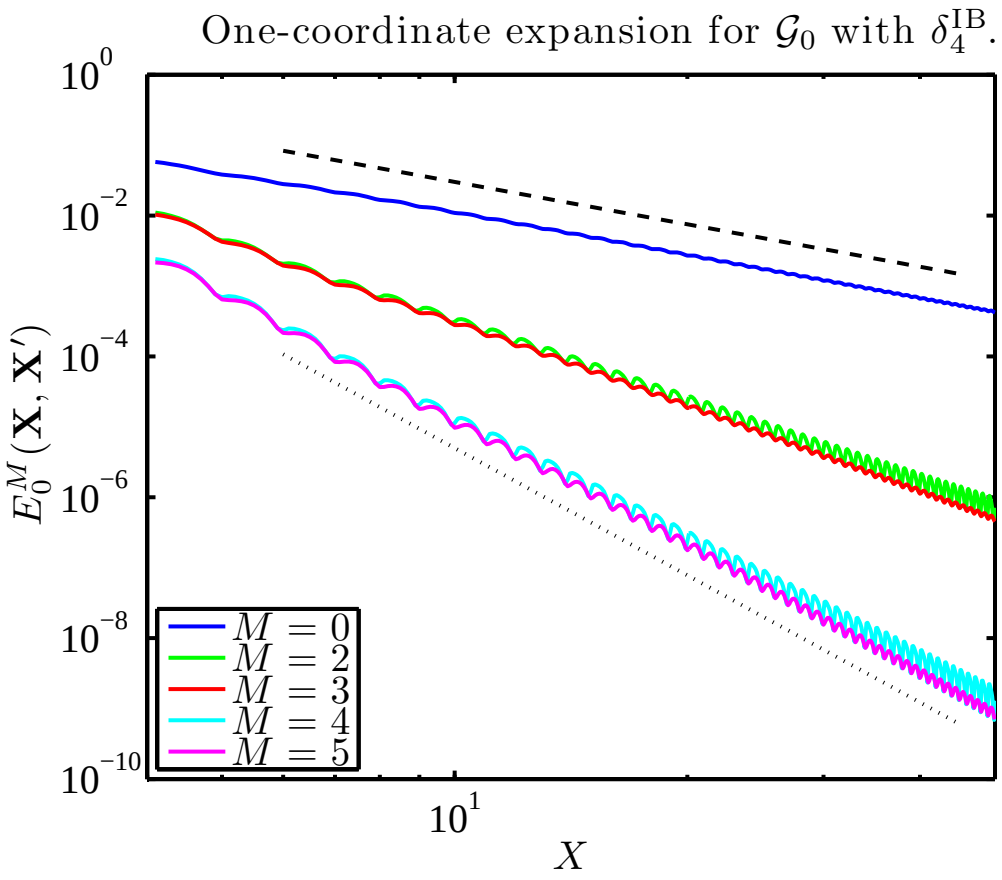


Figure 3.28: Plot showing, E_0^M, the error of $\mathcal{G}_0$ computed by the one-coordinate expansion for various values of M relative to $\mathcal{G}_0$ computed exactly. The delta function used is δ_4^{IB}. The coordinate X varies while Y, Z, X', Y', and Z' are all fixed in $[0, 1)$. Unlike the plots for E^M, this plot shows E_0^M for all values of X, not just those for which E_0^M is at a local maximum. We do not show the case $M = 1$ because E_0^1 is identically equal to E_0^0. The dashed line has slope -2. The dotted line has slope -6.

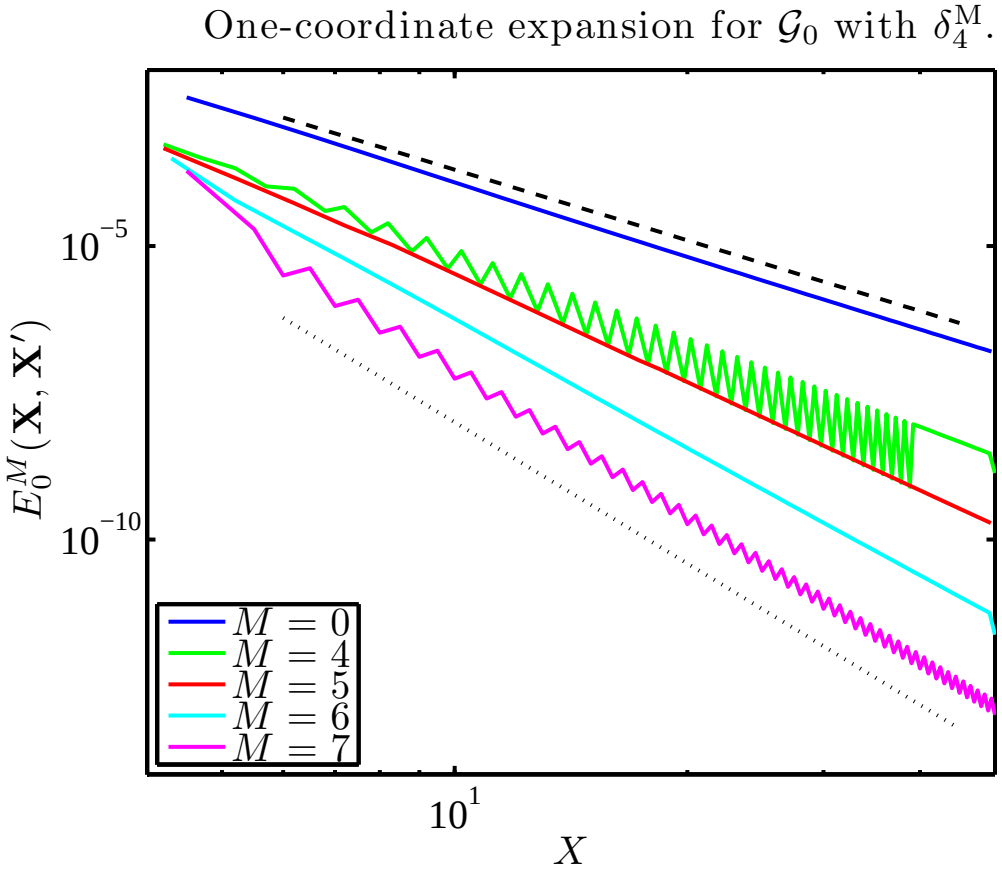


Figure 3.29: Same plot as above except for the delta function δ_4^{M}. Also, we now plot only the local maxima of E_0^M. We do not show the cases $M = 1$, 2, or 3 because E_0^M is identically equal to E_0^0 for these values of M. The dashed line has slope -4. The dotted line has slope -8. The reason that some of the curves in this plot are jagged is that E_0^M sometimes has two local maxima with different magnitudes in a given period.

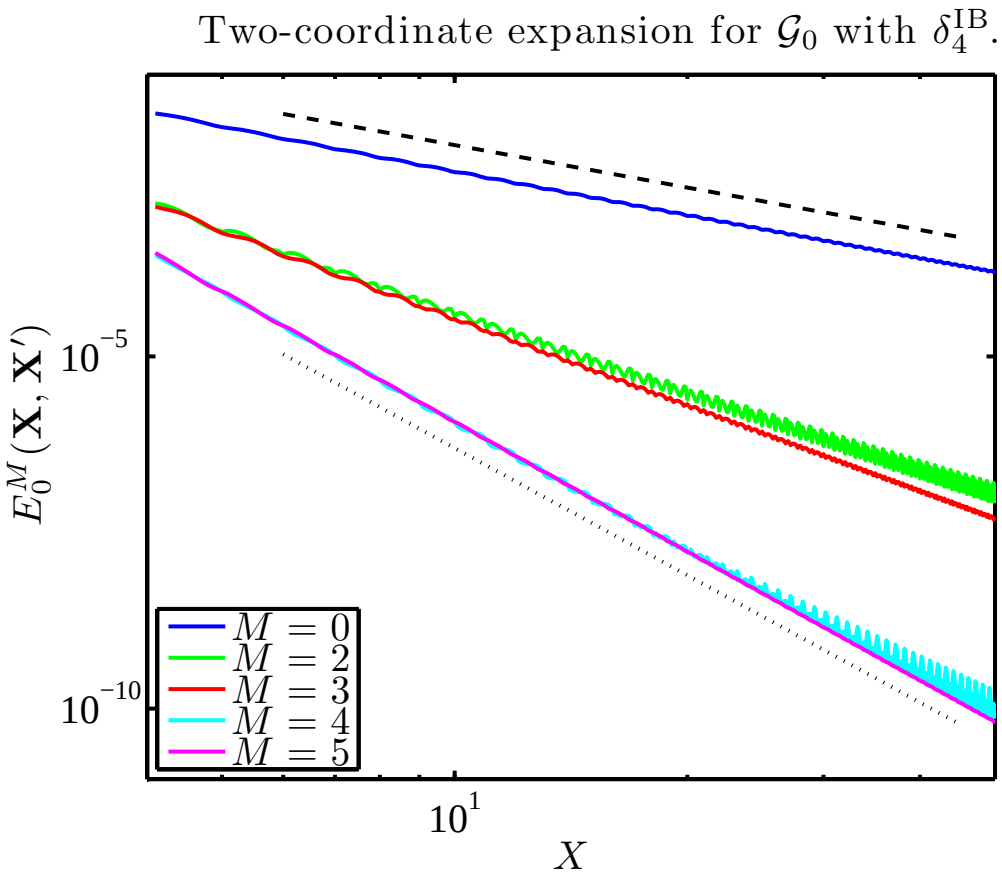


Figure 3.30: Plot showing, E_0^M, the error of $\mathcal{G}_0$ computed by the two-coordinate expansion for various values of M relative to $\mathcal{G}_0$ computed exactly. The delta function used is δ_4^{IB}. The coordinate X varies, and we set $Y = X$. Z, X', Y', and Z' are all fixed in $[0, 1)$. This plot shows E_0^M for all values of X, not just those for which E_0^M is at a local maximum. We do not show the case $M = 1$ because E_0^1 is identically equal to E_0^0. The dashed line has slope -2. The dotted line has slope -6.

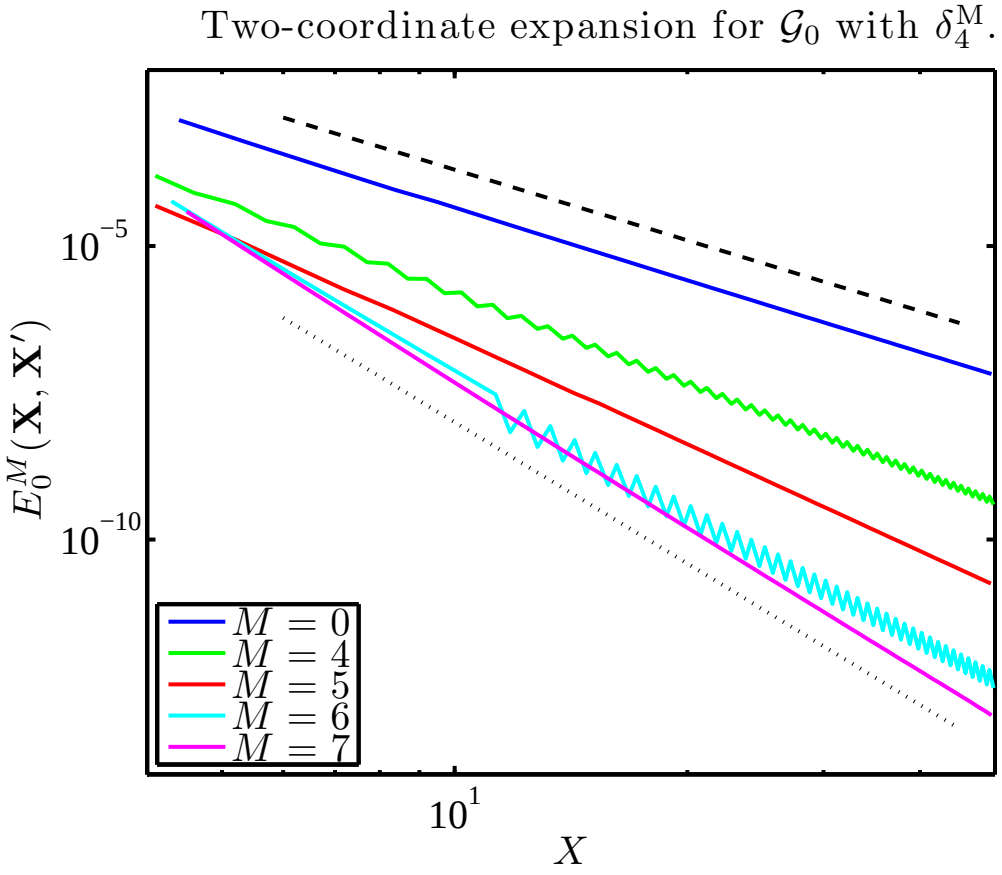


Figure 3.31: Same plot as above except for the delta function δ_4^{M}. Also, we now plot only the local maxima of E_0^M. We do not show the cases $M = 1$, 2, or 3 because E_0^M is identically equal to E_0^0 for these values of M. The dashed line has slope -4. The dotted line has slope -8. The reason that some of the curves in this plot are jagged is that E_0^M sometimes has two local maxima with different magnitudes in a given period.

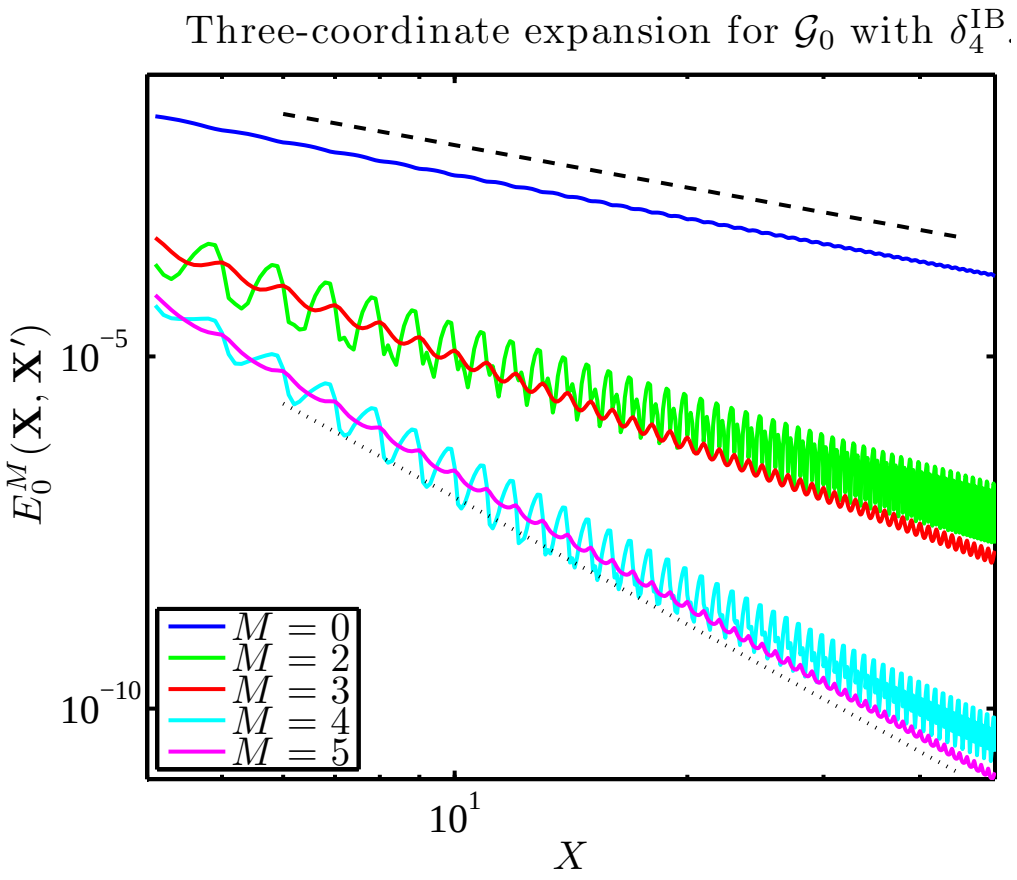


Figure 3.32: Plot showing, E_0^M, the error of $\mathcal{G}_0$ computed by the three-coordinate expansion for various values of M relative to $\mathcal{G}_0$ computed exactly. The delta function used is δ_4^{IB}. The coordinate X varies, and we set $Y = X$ and $Z = X$. X', Y', and Z' are all fixed in $[0, 1)$. This plot shows E_0^M for all values of X, not just those for which E_0^M is at a local maximum. We do not show the case $M = 1$ because E_0^1 is identically equal to E_0^0. The dashed line has slope -2. The dotted line has slope -6.

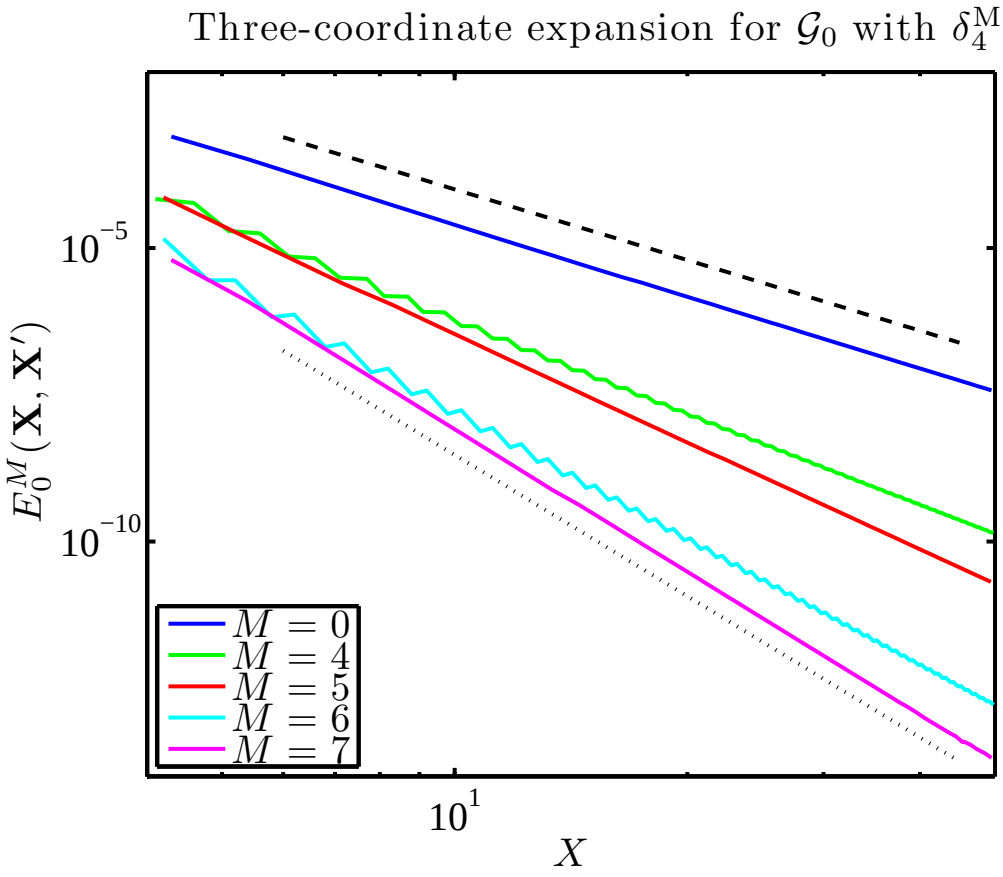


Figure 3.33: Same plot as above except for the delta function δ_4^{M}. Also, we now plot only the local maxima of E_0^M. We do not show the cases $M = 1$, 2, or 3 because E_0^M is identically equal to E_0^0 for these values of M. The dashed line has slope -4. The dotted line has slope -8. The reason that some of the curves in this plot are jagged is that E^M sometimes has two local maxima with different magnitudes in a given period.

When the delta function δ_4^{IB} is used, we are able to plot all values of E_0^M, not just the local maxima, because E_0^M does not have periodic rapid changes in its magnitude. For this delta function, $\mathcal{H}_0^1$ is identically zero because $M_1(X) \equiv 0$. Therefore, E_0^1 is equal to E_0^0. The figures show that for larger even values of M when X not too large, E_0^M is of the same order of magnitude and has approximately the same rate of decay as E_0^{M+1}. This rate of decay is $|X - X'|^{-(M+2)}$ when M is even and $|X - X'|^{-(M+1)}$ when M is odd. It seems that for larger values of X the rate of decay with M even decreases to $|X - X'|^{-(M+1)}$. This phenomenon is easiest to see in figure 3.32 for the three-coordinate expansion. A rate of decay of $|X - X'|^{-(M+1)}$ is what we expect given that the leading corrections to $\mathcal{G}_0^M$ decay like $|\mathbf{X} - \mathbf{X}'|^{-(M+2)}$ and $\mathcal{G}_0$ decays like $|\mathbf{X} - \mathbf{X}'|^{-1}$. An exception is when $M = 0$ in which case we expect E^M to decay like $|X - X'|^{-2}$, which is what we observe. The magnitudes of the errors are larger than we observed for the expansions for $\mathcal{G}$. When $X = 10$, $M = 4$ results in five digits of accuracy for the one-coordinte expansion, six digits of accuracy for the two-coordinate expansion, and seven digits of accuracy for the three-coordinate expansion.

When the delta function δ_4^{M} is used, we again must plot only the local maxima of E_0^M. This delta function satisfies $M_n(X) \equiv 0$ for $n = 1$, 2, and 3. As a result, $\mathcal{H}_0^p \equiv 0$ for $p = 1$, 2, and 3. Therefore E_0^M is equal to E_0^0 when $M = 1$, 2, or 3. The figures show that E_0^M decays like $|X - X'|^{-(M+1)}$ except when $M = 0$ and E_0^M decays like $|X - X'|^{-4}$. These are the decay rates that we would expect. The magnitudes of the errors for a given M are similar for

the two delta functions with the exception of when $M = 0$ in which case E_0^M is much smaller for the delta function δ_4^{M}.

We conclude that, for both delta functions and for the one-, two-, and three-coordinate expansions for $\mathcal{G}_0$, convergence is rapid. Only a few terms are needed to achieve high accuracy even when the coordinates of $\mathbf{X}-\mathbf{X}'$ have magnitudes as small as 10. When these coordinates have larger magnitudes, the errors decay quickly. Those delta functions that satisfy $M_n(X) = 0$ for many $n \geq 1$ will have faster decay when $M = 0$ but will not generally have faster decay for larger values of M.

We found above that the expansions for $\mathcal{G}$ also converge rapidly with few terms needed to achieve high accuracy. For these expansions, decay as the coordinates of $\mathbf{X}-\mathbf{X}'$ grow larger in magnitude is more rapid for any value of M if the delta function used satisfies $N_n = 0$ for some collection of $n \geq 0$. In fact, we found that if only $N_0 = 0$, the two-coordinate and three-coordinate expansions quickly converge to machine precision.

Combining these results, our numerical experiments show that we can compute $\mathcal{G}(\mathbf{X}, \mathbf{X}')$ to high accuracy using our asymptotic expansions, and using only a few terms in these expansions, even when the coordinates of $\mathbf{X} - \mathbf{X}'$ are not particularly large. Computing $\mathcal{G}$ by these expansions is much less expensive computationally than computing it by the naive method which requires order d^6 operations where d is the support width of the delta function, even when $d = 4$. For larger values of d the asymptotic methods generate even more savings.

Before we conclude the chapter, we say a few words about computing these expansions. The most expensive part of these computations is computing the values of $\mathcal{S}_0^{pqr}$, the mixed partial derivatives of the Stokeslet. We do this by the recursive method described above. Since, for example, the three-coordinate expansion requires all the values of $\mathcal{S}_0^{pqr}(\mathbf{X}-\mathbf{X}')$ for $0 \leq p+q+r \leq M$, we can run the recursive method once to generate all of these values. We do not have precise error estimates for these expansions, though we would like to develop them in the future. Thus, in computations, we can not calculate beforehand how many terms in the expansions will be needed to achieve a desired level of accuracy for given $\mathbf{X}$ and $\mathbf{X}'$ and a given choice of the discrete delta function. Instead, we specify an error tolerance and calculate $\mathcal{G}^M$ or $\mathcal{G}_0^M$ for successively larger values of M. If $\|\mathcal{G}^M - \mathcal{G}^{M+1}\|/\|\mathcal{G}^{M+1}\|$ is less than the tolerance, we stop calculating (likewise for $\mathcal{G}_0$). We take care that $\mathcal{G}^M$ and $\mathcal{G}^{M+1}$ are not exactly equal or nearly equal (as with the two-coordinate expansion for $\mathcal{G}$ when M is even), which could cause us to prematurely truncate the expansion. We prefer the three-coordinate expansions for $\mathcal{G}$ and $\mathcal{G}_0$ and use them whenever possible. The three-coordinate expansions have the optimum computational complexity in d, the width of the delta function, and also require fewer computations of $\mathcal{S}_0^{pqr}$ and fewer values of $\mathcal{S}_{pqr}$.

We have built all of this asymptotic machinery into a computer code that computes $\mathcal{G}(\mathbf{X},\mathbf{X}')$ to a given tolerance for arbitrary values of $\mathbf{X}$ and $\mathbf{X}'$. In particular, $\mathbf{X}-\mathbf{X}'$ may have arbitrarily large or small components. The code

also computes $\mathcal{G}(\mathbf{X}(\mathbf{q}), \mathbf{X}(\mathbf{q}'))$ for all pairs of a collection of immersed boundary points indexed by $\mathbf{q}$. We can use this code to compute the resistance matrix of an arbitrary configuration of immersed boundary points, which is what we shall do in chapter 5.

The computational complexity of this procedure is, unfortunately, proportional to the square of the number of immersed boundary points. However, the same analytic methods used in this chapter to generate the expansions for $\mathcal{G}$ and $\mathcal{G}_0$, it seems, can be adapted to generate a fast summation algorithm that would allow us to calculate the complete Lagrangian velocity field $\mathbf{U}(\mathbf{q})$ generated by the Lagrangian force distribution $\mathbf{F}(\mathbf{q})$ using a number of operations proportional to $N \log N$ where N is the number of immersed boundary points. We have not fully developed, implemented, or tested this algorithm, though we plan to do so in future work.

Chapter 4

The approximate delta function

In this chapter we discuss the construction of the approximate Dirac delta function $\delta_h(\mathbf{x})$ used to interpolate the velocity of immersed boundary points from the velocity defined on the grid and also used to spread force from the immersed boundary points to the grid. This function should have approximately the properties of the actual Dirac delta function, meaning it should have its weight concentrated near the origin and its integral, in some appropriate sense, should be one. In general, immersed boundary points will not lie on the grid, so the approximate delta function needs to have broad enough support to allow effective communication between the grid and the immersed boundary point no matter its location. We have seen in chapter 3 several other properties of the approximate delta function that affect the rates of convergence of the asymptotic expansions for $\mathcal{G}$.

In this chapter, we discuss how to derive approximate delta functions by

specifying their properties. We derive several classes of functions which have been used in the immersed boundary method and elsewhere, and which are used in subsequent chapters that present results. We also suggest new ways to derive delta functions and identify the important properties of the delta functions. The results in this section may be of interest to those outside the immersed boundary method community. Many numerical methods used mixed Lagrangian and Eulerian equations and use an approximate Dirac delta function in some way to communicate between these two descriptions. For instance, a front-tracking method may be used to represent an interface that moves in a fluid whose dynamics are governed by the Navier–Stokes equations. As in the immersed boundary method, the properties of the delta functions affect the rates of convergence of these methods.

4.1 Form of the delta function

We generally assume that the three-dimensional approximate delta functions are tensor products of one-dimensional functions, so that

$$\delta_h(\mathbf{x}) = \frac{1}{h^3}\phi(x/h)\phi(y/h)\phi(z/h), \tag{4.1}$$

where $\mathbf{x} = (x, y, z)$.

We do this for several reasons. One is that we are unaware of any approximate delta functions which do not satisfy this property, have compact

support, and still satisfy the zeroth moment condition, discussed fully below. This condition implies that that the values of the approximate delta function on the grid, multiplied by h^3, sum to 1 no matter where in space the delta function is centered. If this condition is not satisfied, the delta function will create order one errors when used for interpolation. Also, when used to spread force to the grid, the total force on the grid will not equal the total force produced by the immersed boundary points. One might like to use a radially symmetric delta function, but to our knowledge, none have been found which satisfies the zeroth moment condition and has compact support. A radially symmetric gaussian delta function is also a tensor product, but we later show that no such gaussian delta function can satisfy the zeroth moment condition.

Another reason we use the tensor product formulation for the delta function is that we would like to be able to use the asymptotic expansions for $\mathcal{G}$ and $\mathcal{G}_0$ derived in chapter 3. As seen in that chapter, that the delta function is a tensor product of one-dimensional functions is essential to our derivation of the expansions. Without this property, we could not compute $\mathcal{G}$ efficiently.

Finally, we assume the delta function is a tensor product because we then need only specify a one-dimensional function ϕ as opposed to a three dimensional function. We would like to use conditions on the delta function that will determine it uniquely. These conditions imply conditions on ϕ which have a simpler form than the conditions on the full delta function. It is thus much easier to uniquely determine the one-dimensional ϕ by imposing

conditions than to determine a fully three-dimensional delta function.

An interesting fact is that because we use approximate delta functions of the form shown in equation (4.1), the matrix $\mathcal{G}(\mathbf{q}, \mathbf{q})$, which describes the self-induced velocity of an immersed boundary point, is always exactly diagonal. To see why, recall equation (2.31), which defines $\mathcal{G}(\mathbf{q}, \mathbf{q}')$ to be the double convolution of $\mathcal{S}$ with an approximate delta function centered at $\mathbf{X}(\mathbf{q})$ and another centered at $\mathbf{X}(\mathbf{q}')$. First, note that when $\mathbf{q}' = \mathbf{q}$ the factor $\delta_h(\mathbf{x} - \mathbf{X}(\mathbf{q}))\delta_h(\mathbf{x}' - \mathbf{X}(\mathbf{q}))$ does not change if $\mathbf{x}$ and $\mathbf{x}'$ exchange one of their components. Second, note that the $(i, j)^{\text{th}}$ off-diagonal element of $\mathcal{S}(\mathbf{x} - \mathbf{x}')$ does change sign if $\mathbf{x}$ and $\mathbf{x}'$ exchange their i^{th} or j^{th} component. Finally, note that the $(i, j)^{\text{th}}$ off-diagonal element of $\mathcal{S}(\mathbf{x})$ is zero if the i^{th} or j^{th} component of $\mathbf{x}$ is zero. These facts imply that the off-diagonal components of the summands in equation (2.31) are either zero or cancel pairwise when $\mathbf{q}' = \mathbf{q}$. The implication of this conclusion is that if an immersed boundary point applies force to the fluid in one of the three coordinate directions, the velocity of that point which results from that force will be in the same coordinate direction and not skew to the grid. However, it is not the case that $\mathcal{G}(\mathbf{q}, \mathbf{q})$ will be a multiple of the identity, so it is not the case that the the self-induced velocity of an immersed boundary point will always be in the same direction as the force. In general this will be true only when the force is in one of the coordinate directions.

The reason we scale the approximate delta function with h as we do in equation (4.1) is that doing so ensures that the discrete equations of the

immersed boundary method are scale invariant, provided the Lagrangian variables are scaled appropriately. The approximate delta function, which is a numerical parameter, scaled thusly will have the same support in grid cells if we change the size of the grid. Its other properties relative to the grid will also not change. One could image a situation in which one wanted to refine the grid, reducing h, but not to change the approximate delta function. Our perspective is that doing so creates a "new" approximate delta function with larger support relative to the grid. We later see which refinements of h will result in new delta functions which have similar properties to the unrefined delta functions.

4.2 Conditions on the delta functions

A delta function is constructed by imposing enough conditions on ϕ so that it is uniquely determined. We speak interchangeably of ϕ and δ_h satisfying a particular condition, with the understanding that if δ_h is said to satisfy a condition, we mean that the ϕ from which it is constructed satisfies the corresponding condition.

We require that all approximate delta functions we use be continuous. We do so to ensure that the velocities of immersed boundary points that are interpolated from the grid and the forces that are spread to the grid are continuous functions of the location of the immersed boundary point. For δ_h to be continuous it is necessary and sufficient that ϕ be continuous. One

might wish to impose further smoothness conditions on ϕ. Care must be taken when doing so, as such conditions can lead to a non-unique choice of ϕ or can overdetermine ϕ.

Perhaps the most important condition that we impose upon ϕ is that it has compact support with support width equal to some integer d. We have seen in chapter 2 that to be able to compute $\mathcal{G}$ in finitely many operations it is necessary that ϕ have compact support. Moreover, the complexity of this computation depends strongly on the width of support d. In chapter 3, we saw how to reduce the complexity with respect to d, but we needed that the immersed boundary points be separated by a distance greater than d in one coordinate direction to apply any of the expansions in that chapter. Finally, restricting the support of ϕ and imposing an appropriate number of other conditions described below leads to a unique choice of ϕ.

Another condition that is imposed is that the delta function provides a specified order of interpolation. It can be shown that a delta function will provide order of interpolation K if and only if the following discrete moment conditions are satisfied by ϕ [33]:

$$\sum_{j\in\mathbb{Z}} \phi(x-j) = 1 \quad \forall x \in \mathbb{R} \tag{4.2}$$

$$\sum_{j\in\mathbb{Z}} (x-j)^k \phi(x-j) = 0 \quad \forall x \in \mathbb{R}, \quad 1 \leq k \leq K-1. \tag{4.3}$$

These conditions imply that for the full, three-dimensional delta function

$$\sum_{\mathbf{x}\in(h\mathbb{Z})^3} \delta_h(\mathbf{X}-x)h^3 = 1 \quad \forall \mathbf{X}\in\mathbb{R}^3 \tag{4.4}$$

$$\sum_{\mathbf{x}\in(h\mathbb{Z})^3} (X-x)^k(Y-y)^l(Z-z)^m\delta_h(\mathbf{X}-\mathbf{x})h^3 = 0 \quad \forall \mathbf{X}\in\mathbb{R}^3 \tag{4.5}$$

for $0 \leq k,l,m \leq K-1$ and $(k,l,m) \neq (0,0,0)$.

Recall the discrete moments $M_n(X)$ defined in chapter 3, equation (3.67). These conditions are equivalent to $M_0(X) \equiv 1$ and $M_k(X) \equiv 0$ for $1 \leq k \leq K-1$. We have seen in the previous chapter that discrete moments affect the convergence rates of our asymptotic expansions for the Lagrangian Green's function, $\mathcal{G}$, which we derived for the spectral discretization method. In particular, $M_0 \equiv 1$ implies that $\mathcal{G}_0(\mathbf{X},\mathbf{X}') \approx \mathcal{S}_0(\mathbf{X}-\mathbf{X}')$ and otherwise there is an order one difference between $\mathcal{G}_0$ and $\mathcal{S}_0$. We have also seen that if $M_k(X) \equiv 0$ for $1 \leq k \leq K-1$ the next $K-1$ corrections in the expansions for $\mathcal{G}_0(\mathbf{X},\mathbf{X}')$ in any of the three coordinate directions will be zero. Therefore, the relative difference between $\mathcal{G}_0(\mathbf{X},\mathbf{X}')$ and $\mathcal{S}_0(\mathbf{X}-\mathbf{X}')$ decays like $|\mathbf{X}-\mathbf{X}'|^{-K}$. In other words, $\mathcal{G}_0(\mathbf{X},\mathbf{X}')$ converges at K^{th} order to $\mathcal{S}_0(\mathbf{X}-\mathbf{X}')$ as $\mathbf{X}-\mathbf{X}'$ becomes large.

That the delta function satisfies K moment conditions guarantees that certain moments of the Lagrangian forces, $\mathbf{F}(\mathbf{q})$, will be preserved when the force is spread to the Eulerian grid to create the Eulerian force density, $\mathbf{f}(\mathbf{x})$. It can be seen easily that the total force will be preserved provided $K \geq 0$,

meaning

$$\sum_{q\in\Omega}\mathbf{F}(\mathbf{q}) = \sum_{\mathbf{x}\in(h\mathbb{Z})^3}\mathbf{f}(\mathbf{x})h^3. \tag{4.6}$$

If $K > 0$, moments with orders up to K will be preserved, meaning

$$\sum_{q\in\Omega}\mathbf{F}(\mathbf{q})X(\mathbf{q})^k Y(\mathbf{q})^l Z(\mathbf{q})^m = \sum_{\mathbf{x}\in(h\mathbb{Z})^3}\mathbf{f}(\mathbf{x})x^k y^l z^m h^3 \tag{4.7}$$

where $0 \leq k, l, m \leq K-1$ and $\mathbf{X}(\mathbf{q}) = (X(\mathbf{q}), Y(\mathbf{q}), Z(\mathbf{q}))$. In particular, if the delta function satisfies two discrete moment conditions, meaning $K = 1$, the torque in the Lagrangian and Eulerian coordinates will be the same. That the torques are the same is shown in [26]. We prove the general case here.

For the sake of simplicity, we prove this in the case when $l = m = 0$. The method of proof for general l and m can be easily seen from this special case. The proof is straightforward.

$$\sum_{\mathbf{x}\in(h\mathbb{Z})^3}\mathbf{f}(\mathbf{x})x^k h^3 = \sum_{q\in\Omega}\mathbf{F}(\mathbf{q})\sum_{\mathbf{x}\in(h\mathbb{Z})^3} x^k\delta_h(\mathbf{X}(\mathbf{q})-\mathbf{x})h^3 \tag{4.8}$$

$$= \sum_{q\in\Omega}\mathbf{F}(\mathbf{q})\sum_{\mathbf{x}\in(h\mathbb{Z})^3}(x - X(\mathbf{q}) + X(\mathbf{q}))^k\delta_h(\mathbf{X}(\mathbf{q})-\mathbf{x})h^3 \tag{4.9}$$

The part of this last equation beginning with the second summation sign can

be expanded to equal

$$\sum_{j=0}^{k} \begin{pmatrix} k \\ j \end{pmatrix} X(\mathbf{q})^{k-j} \sum_{\mathbf{x}\in(h\mathbb{Z})^3} (x - X(\mathbf{q}))^j \delta_h(\mathbf{X}(\mathbf{q}) - \mathbf{x}) h^3. \tag{4.10}$$

Because $j \leq K - 1$ by assumption, the moment conditions satisfied by δ_h imply that the sum over $\mathbf{x}$ is 0 if $j > 0$ and 1 if $j = 0$. We conclude that

$$\sum_{\mathbf{x}\in(h\mathbb{Z})^3} \mathbf{f}(\mathbf{x}) x^k h^3 = \sum_{q\in\Omega} \mathbf{F}(\mathbf{q}) X(\mathbf{q})^k \tag{4.11}$$

which completes the proof.

Another condition that can be imposed on ϕ we call the balanced condition:

$$\sum_{j\in\mathbb{Z} \text{ even}} \phi(x - j) = \sum_{j\in\mathbb{Z} \text{ odd}} \phi(x - j) \quad \forall x \in \mathbb{R}. \tag{4.12}$$

This condition implies that half of the weight of ϕ lies on the odd and half on the even grid cells. If the zeroth moment condition is also satisfied, each of these sums will be exactly 1/2. For the full, three dimensional delta function, the balanced condition implies that the delta function gives equal weight to each of the eight sub-grids $\Omega' \subset (h\mathbb{Z}^3)$ which consist of those grid points whose coordinates are equal to h times either odd or even integers in each coordinate direction. If the zeroth moment condition is satisfied and δ_h

satisfies the balanced condition, then

$$\sum_{\mathbf{x}\in\Omega'} \delta_h(\mathbf{X}-x)h^3 = \frac{1}{8} \quad \forall \mathbf{X} \in \mathbb{R}^3 \tag{4.13}$$

for all such subg-grids Ω'. This condition, discussed further in [26], has often been motivated by the need to reduce spurious oscillations in fluid velocity and pressure fields that sometimes arise when the immersed boundary method is used for non-zero Reynolds number problems which are hyperbolic in nature. A standard method for solving for the pressure has the effect of decoupling the eight sub-grids in the fluid equations, absent viscosity, which tends to re-couple the sub-grids. If the Reynolds number is not very small, unphysical oscillations can be seen. Using an approximate delta function which satisfies the balanced condition has been seen to reduce these oscillations [26].

At zero Reynolds number, we do not expect to see these oscillations, since viscosity strongly couples the eight sub-grids. However, we find later in our results that those approximate delta function that satisfy the balanced condition perform better than those that do not. An explanation of why this is so is revealed in the previous chapter. Recall our asymptotic expansions for the Lagrangian Green's function, $\mathcal{G}$, derived under the assumption that we use the spectral discretization. With a spectral discretization, one would be particularly surprised to find decoupling of the eight sub-grids. These expansions showed that the difference between $\mathcal{G}$ and $\mathcal{G}_0$ depends on the so-

called alternating moments of ϕ, $N_n(X)$, defined in equation (3.68). The zeroth alternating moment is

$$N_0(x) = \sum_{j \in \mathbb{Z}} (-1)^j \phi(x - j). \tag{4.14}$$

This quantity will be zero if and only if ϕ has half its weight on the odd grid points and half on the even. Therefore $N_0 \equiv 0$ if and only if the balanced condition is satisfied. We found in the previous chapter that the first correction in the one-coordinate expansion for $\mathcal{G}$ after $\mathcal{G}_0$ decays faster by a factor of approximately $|\mathbf{X} - \mathbf{X}'|^{-2}$ when $N_0 \equiv 0$. The factor is $|\mathbf{X} - \mathbf{X}'|^{-4}$ for the two-coordinate expansion and $|\mathbf{X} - \mathbf{X}'|^{-6}$ for the three-coordinate expansion. If the balanced condition is not satisfied and if only one coordinate of $\mathbf{X} - \mathbf{X}'$ is large (so that we use the one-coordinate expansion), the first correction is of the same magnitude as the Stokeslet, $\mathcal{S}_0$, meaning there is an order one error.

The underlying reason that the alternating moments appear in the expansion for $\mathcal{G}$ is that the discrete Stokeslet, $\mathcal{S}$, equals the continuous Stokeslet plus corrections that oscillate from grid point to grid point. These oscillations are smoothed by a delta function that satisfies the balanced condition. Higher alternating moments also appear in the expansion for $\mathcal{G}$. This suggests that we impose conditions similar to the balanced condition but involving the higher moments of ϕ. We say that ϕ satisfies K alternating moment

conditions if

$$\sum_{j\in\mathbb{Z}}(-1)^j(x-j)^k\phi(x-j)=0 \quad \forall x\in\mathbb{R}, \quad 0\le k\le K-1. \tag{4.15}$$

This is equivalent to requiring that $N_k \equiv 0$ for $0 \le k \le K-1$. Imposing further alternating moment conditions implies that the higher moments of the Lagrangian force are distributed equally among the eight sub-grids Ω'. Specifically, if $0 \le k, l, m \le K-1$

$$\sum_{\mathbf{x}\in\Omega'} \mathbf{f}(\mathbf{x})x^k y^l z^m h^3 \tag{4.16}$$

will be independent of the choice of Ω'. If both K moment and K alternating moment conditions are satisfied, these higher moments will be one-eighth of the moments of the Lagrangian force $\mathbf{F}$. In particular, if two moment and alternating moment conditions are satisfied, the torque applied on each sub-grid Ω' will be one-eighth of the total torque applied by the Lagrangian points.

Another condition that can be imposed on ϕ is called the sum of squares condition. This condition and the motivation for imposing it are discussed in detail in reference [26]. The condition is that

$$\sum_{j\in\mathbb{Z}}\phi(x-j)^2 = C \quad \forall x\in\mathbb{R} \tag{4.17}$$

where C is a constant. If the quantities $\phi(x-j)$ with fixed x and j taking

all values in $\mathbb{Z}$ are thought of as a vector in the space of sequences, the sum of squares condition specifies that the Euclidean norm, or L^2 norm, of this vector is independent of x. For ϕ to be continuous, one typically cannot specify the constant C. Instead, one simply requires that the above sum is equal to *some* constant, independent of x. For the delta functions that we derive, there is a unique value of the sum of squares, C, that makes ϕ a continuous function.

For the full three-dimensional delta function, the sum of squares condition implies

$$\sum_{\mathbf{x}\in(h\mathbb{Z})^3} \delta_h(\mathbf{X}-\mathbf{x})^2 h^6 = C^3 \quad \forall \mathbf{X} \in \mathbb{R}^3. \tag{4.18}$$

The following argument provides justification for imposing the sum of squares condition. Suppose that the discrete Stokeslet $\mathcal{S}(\mathbf{x})$ were equal to $\lambda\delta_{\mathbf{x}}\mathcal{I}$. This Stokeslet is a multiple of the identity when $\mathbf{x}$ is zero and is zero otherwise. This means the the fluid velocity field is simply a constant multiple of the applied force field. This is the simplest conceivable relationship between the force and velocity fields. The actual discrete Stokeslet is sharply peaked at $\mathbf{x} = 0$ and is a multiple of the identity there, so our simplified discrete Stokeslet is not too far from being realistic. With the simplified Stokeslet, the Lagrangian Green's function is equal to

$$\mathcal{G}(\mathbf{X},\mathbf{X}') = \lambda\mathcal{I} \sum_{\mathbf{x}\in(h\mathbb{Z})^3} \delta_h(\mathbf{X}-\mathbf{x})\delta_h(\mathbf{X}'-\mathbf{x})h^6. \tag{4.19}$$

When $\mathbf{X} = \mathbf{X}'$ the sum over $\mathbf{x}$ is simply the sum of squared values of the delta function, which, if δ_h satisfies the sum of squares condition, will be equal to C^3, independent of $\mathbf{X}$. Therefore, $\mathcal{G}(\mathbf{X}, \mathbf{X})$ is independent of $\mathbf{X}$. Furthermore, the Schwarz inequality implies that, for the diagonal components of $\mathcal{G}$ (the off-diagonal components are all zero),

$$\begin{aligned} |\mathcal{G}(\mathbf{X}, \mathbf{X}')| &\leq \lambda \left(\sum_{\mathbf{x} \in (h\mathbb{Z})^3} \delta_h(\mathbf{X} - \mathbf{x})^2 h^6 \right)^{\frac{1}{2}} \left(\sum_{\mathbf{x} \in (h\mathbb{Z})^3} \delta_h(\mathbf{X}' - \mathbf{x})^2 h^6 \right)^{\frac{1}{2}} \\ &= \lambda C^3 = |\mathcal{G}(\mathbf{X}, \mathbf{X})|. \end{aligned} \tag{4.20}$$

For the hypothetical simplified discrete Stokeslet, we have shown that if the delta function satisfies the sum of squares condition, the velocity self-induced by a force acting on an immersed boundary point will be independent of its position relative to the grid. Also, the velocity induced at any other immersed boundary point will be less than or equal to the self-induced velocity. These qualities are desirable and will be discussed further in chapter 5. We show there that those delta functions which satisfy the sum of squares condition result in better grid-independence than those which do not.

The moment conditions, alternating moment conditions (including the balanced condition), and the sum of squares condition are all of the form of conditions on the vector $\phi(x - j)$ with x fixed and $j \in \mathbb{Z}$. If we also impose that ϕ is supported on $[-d/2, d/2]$, then we know this vector will have at most d non-zero values. Therefore, it is generally the case that d

such conditions are needed to uniquely specify ϕ. Empirically, we find that if we impose d conditions on ϕ with support width d, then we must impose an even number of moment conditions for the resulting ϕ to be continuous. There exist functions ϕ which satisfy an odd number of moment conditions, but not which have support width d and satisfy d total conditions. For instance, the function

$$\phi(x) = \begin{cases} \frac{1}{4}\left(1 + \cos\frac{\pi x}{2}\right) & 0 \leq |x| \leq 2 \\ 0 & 2 < |x|, \end{cases} \tag{4.21}$$

which was used in early immersed boundary method computations [26], has support width 4, satisfies 1 moment condition, the balanced condition, and the sum of squares condition, so the total number of conditions satisfied is 3. All the delta functions we derive will satisfy an even number of moment conditions.

4.3 Derivation of the delta functions

In this thesis, we test the performance of a variety of approximate delta functions. We classify the delta functions that we use into families based on the conditions that the delta functions satisfy. In this section we derive various families of delta functions and give formulas for functions that we use in subsequent chapters.

In the immersed boundary method, it is essential that the approximate

delta function have a small support. In a typical implementation of the immersed boundary method the computational complexity is proportional to the width of the delta function cubed. In the naive implementation of our method, described in chapter 2, it is even more essential that the delta function have small support because the computational complexity is proportional to the width of the delta function to the sixth power. The improvements to our method described in chapter 3 improve this situation significantly. There we construct an asymptotic method whose complexity is independent of the width of the delta function. This method computes $\mathcal{G}$ for pairs of immersed boundary particles with $\mathbf{X}(\mathbf{q}) - \mathbf{X}(\mathbf{q}')$ having all components large compared with the width of the delta function. For particles that are closer together in one or more dimensions a less efficient method whose complexity depends on some power of the width of the delta function must be used. In this way, the width of the delta function will still affect the efficiency of the computation of $\mathcal{G}$ for a large number of pairs of particles because a delta function with a larger width of support will require that $\mathcal{G}$ is computed inefficiently for a larger proportion of the pairs of particles.

We therefore would like to derive delta functions with small support. We do so by requiring that ϕ have a small support. We derive three families of ϕ, each containing a hierarchy of functions of increasing support and which satisfy and increasing number of moment conditions. For each function, we find that the conditions we impose along with the requirements that ϕ be continuous and have a given support are sufficient to uniquely specify ϕ.

The first family of delta functions we consider satisfy neither the sum or squares nor the balanced condition. Instead, they provide the maximum possible order of interpolation [33]. We denote these functions by $\delta^{\mathrm{M}}_{d,h}$. The index d is an even integer which indicates the support width of the delta function in units of h. The order of interpolation is d. The superscript M is meant to stand for "maximum moment conditions". In subsequent chapters, we use the functions $\delta^{\mathrm{M}}_{2,h}$, $\delta^{\mathrm{M}}_{4,h}$, and $\delta^{\mathrm{M}}_{6,h}$. To each delta function corresponds a ϕ, and our convention throughout this thesis is that we use the same subscripts and superscripts (except for h) for the ϕ that corresponds to a particular delta function. For instance, ϕ^{M}_4 corresponds to $\delta^{\mathrm{M}}_{4,h}$.

To construct the functions ϕ for this family of delta functions, choose $x \in \mathbb{R}$. We specify that the support of ϕ^{M}_d is contained in $[-d/2, d/2]$ so there are at most d non-zero values of $\phi(x-j)$ for $j \in \mathbb{Z}$. Moreover, we know which values of j may result in non-zero $\phi(x-j)$. We require that ϕ^{M}_d satisfy d moment conditions. These moment conditions are d linear equations in the d unknown values of $\phi(x-j)$. The matrix of this system is a Vandermonde matrix and so it is non-singular. Consequently there exists a unique set of values of $\phi(x-j)$ that satisfy the d discrete moment conditions for every value of x. This uniquely defines ϕ^{M}_d. Empirically, we find that d must be an even integer for ϕ^{M}_d to be continuous. Formulas for the first three ϕ in this

family are given by

$$\phi_2^{\mathrm{M}}(x) = \begin{cases} 1 - |x| & 0 \le |x| \le 1 \\ 0 & 1 < |x| \end{cases} \tag{4.22}$$

$$\phi_4^{\mathrm{M}}(x) = \begin{cases} 1 - \frac{1}{2}|x| - |x|^2 + \frac{1}{2}|x|^3 & 0 \le |x| \le 1 \\ 1 - \frac{11}{6}|x| + |x|^2 - \frac{1}{6}|x|^3 & 1 < |x| \le 2 \\ 0 & 2 < |x| \end{cases} \tag{4.23}$$

$$\phi_6^{\mathrm{M}}(x) = \begin{cases} 1 - \frac{1}{3}|x| - \frac{5}{4}|x|^2 + \frac{5}{12}|x|^3 + \frac{1}{4}|x|^4 - \frac{1}{12}|x|^5 & 0 \le |x| \le 1 \\ 1 - \frac{13}{12}|x| - \frac{5}{8}|x|^2 + \frac{25}{24}|x|^3 - \frac{3}{8}|x|^4 + \frac{1}{24}|x|^5 & 1 < |x| \le 2 \\ 1 - \frac{137}{60}|x| + \frac{15}{8}|x|^2 - \frac{17}{24}|x|^3 + \frac{1}{8}|x|^4 - \frac{1}{120}|x|^5 & 2 < |x| \le 3 \\ 0 & 3 < |x| \end{cases} \tag{4.24}$$

Plots of these functions are shown in figure 4.1. They are even about the origin, as are all ϕ we construct, though this is not a condition that we impose *a priori*. They are piecewise smooth but have derivative discontinuities at integer values. In particular, ϕ_d^{M} is a piecewise polynomial of degree $d-1$ in $|x|$. In every case, ϕ_d^{M} is one at the origin and is zero at all other integers.

The second family of delta functions we consider satisfy the sum of squares condition but not the balanced condition. We denote these functions by $\delta_{d,h}^{\mathrm{IB}}$, where d is an odd integer which indicates the function's support width. These

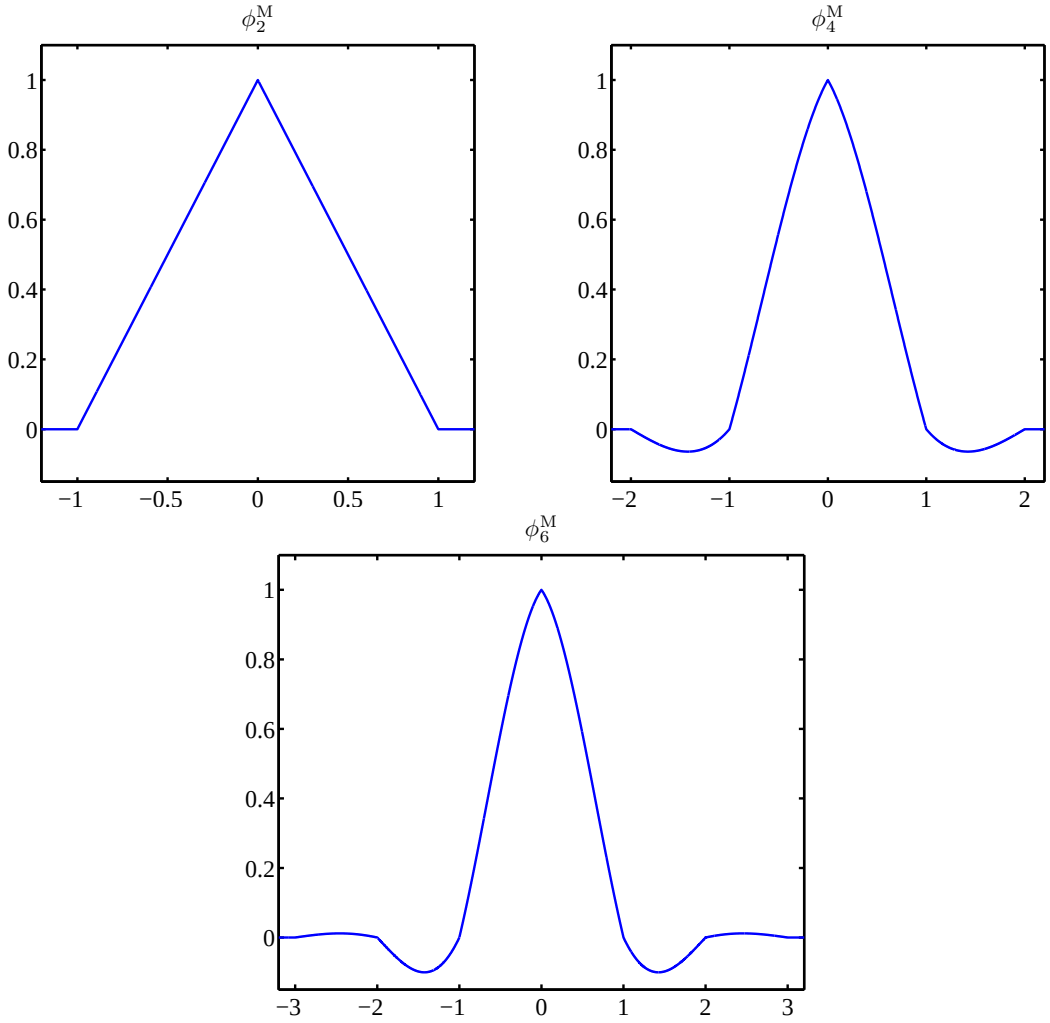


Figure 4.1: Plot of ϕ_d^{M}, which have maximum moment order.

functions have interpolation order $d-1$. In subsequent chapters, we use the functions $\delta_{3,h}^{\mathrm{IB}}$ and $\delta_{5,h}^{\mathrm{IB}}$. The third family of delta functions satisfy both the sum of squares and the balanced condition. We also denote these functions by $\delta_{d,h}^{\mathrm{IB}}$, where d is an even integer (so there is no ambiguity) which indicates the support width. These functions have interpolation order $d-2$. In subsequent chapters, we use the functions $\delta_{4,h}^{\mathrm{IB}}$ and $\delta_{6,h}^{\mathrm{IB}}$.

We use the superscript IB because the immersed boundary method has traditionally used delta functions which satisfy the sum of squares condition. The standard delta function for immersed boundary method computations is $\delta_{4,h}^{\mathrm{IB}}$, and it is described in detail in reference [26]. The function $\delta_{3,h}^{\mathrm{IB}}$ was first used in reference [28], and higher order versions of these functions were introduced in reference [32].

The derivations of the corresponding functions ϕ for these two families of delta functions are closely related. Details of the derivations are given in reference [26]. A function ϕ_d^{IB} with d odd is required to satisfy $d-1$ moment conditions. For each value of $x \in \mathbb{R}$, these are $d-1$ linear equations in the d non-zero unknowns $\phi(x-j)$ with $j \in \mathbb{Z}$. A function ϕ_d^{IB} with d even is required to satisfy $d-2$ moment conditions as well as the balanced condition. For each value of $x \in \mathbb{R}$, these conditions together are $d-1$ linear equations in the d non-zero unknowns $\phi(x-j)$ with $j \in \mathbb{Z}$. Therefore, in both the cases with d odd and d even, all of the unknowns may be expressed in terms of a single particular unknown by inverting the system of $d-1$ linear equations. Substituting these expressions into the sum of squares condition

gives a quadratic equation for the single remaining unknown. Solving this quadratic equation gives a formula for ϕ. Only one of the two roots of the quadratic equation results in a ϕ that is continuous, and this is the root that is chosen. Formulas for the first two functions ϕ in each family are given by

$$\phi_3^{\mathrm{IB}}(x) = \begin{cases} \frac{1}{3}\left(1+\sqrt{1-3|x|^2}\right) & 0 \le |x| \le \frac{1}{2} \\ \frac{1}{6}\left(5-3|x|-\sqrt{-2+6|x|-3|x|^2}\right) & \frac{1}{2} < |x| \le \frac{3}{2} \\ 0 & \frac{3}{2} < |x| \end{cases} \tag{4.25}$$

$$\phi_5^{\mathrm{IB}}(x) = \begin{cases} \frac{17}{35} - \frac{1}{7}|x|^2 + \sqrt{\frac{3123}{39200} - \frac{311}{980}|x|^2 + \frac{101}{490}|x|^4 - \frac{1}{28}|x|^6} & 0 \le |x| \le \frac{1}{2} \\ 1 + \frac{1}{6}|x| - \frac{2}{3}|x|^2 + \frac{1}{6}|x|^3 - \frac{2}{3}\phi_5^{\mathrm{IB}}(|x|-1) & \frac{1}{2} < |x| \le \frac{3}{2} \\ 1 - \frac{19}{12}|x| + \frac{2}{3}|x|^2 - \frac{1}{12}|x|^3 + \frac{1}{6}\phi_5^{\mathrm{IB}}(|x|-2) & \frac{3}{2} < |x| \le \frac{5}{2} \\ 0 & \frac{5}{2} < |x| \end{cases} \tag{4.26}$$

$$\phi_4^{\mathrm{IB}}(x) = \begin{cases} \frac{1}{8}\left(3-2|x|+\sqrt{1+4|x|-4|x|^2}\right) & 0 \le |x| \le 1 \\ \frac{1}{8}\left(5-2|x|-\sqrt{-7+12|x|-4|x|^2}\right) & 1 < |x| \le 2 \\ 0 & 2 < |x| \end{cases} \tag{4.27}$$

$$\phi_6^{\mathrm{IB}}(x) = \begin{cases} \frac{61}{112} - \frac{11}{42}|x| - \frac{11}{56}|x|^2 + \frac{1}{12}|x|^3 + \frac{\sqrt{3}}{336}\left(243 + 1584|x|\right. & \\ \left. - 748|x|^2 - 1560|x|^3 + 500|x|^4 + 336|x|^5 - 112|x|^6\right)^{\frac{1}{2}} & 0 \le |x| \le 1 \\ \frac{21}{16} + \frac{7}{12}|x| - \frac{7}{8}|x|^2 + \frac{1}{6}|x|^3 - \frac{3}{2}\phi_6^{\mathrm{IB}}(|x| - 1) & 1 < |x| \le 2 \\ \frac{9}{8} - \frac{23}{12}|x| + \frac{3}{4}|x|^2 - \frac{1}{12}|x|^3 + \frac{1}{2}\phi_6^{\mathrm{IB}}(|x| - 2) & 2 < |x| \le 3 \\ 0 & 3 < |x| \end{cases} \tag{4.28}$$

Plots of these functions are shown in figure 4.2. Again, these functions are even about the origin and are piecewise smooth. In fact, they are C^1 and only have discontinuities in their second derivatives at integer values of x (when d is even) or half-integer values of x (when d is odd). They are piecewise sums of polynomials and the square roots of polynomials.

Any function ϕ can be dilated and scaled by a positive integer λ to make a new function ψ where $\psi(x) = \phi(x/\lambda)/\lambda$. If ϕ has support width d, then ψ will have support width λd. The new function ψ satisfies the same number of moment conditions as ϕ. If ϕ satisfies the balanced or the sum of squares condition then ψ will as well. If ϕ satisfies K moment conditions and λ is even, then ψ will satisfy K alternating moment conditions as well. In particular, if ϕ satisfies the zeroth moment condition and λ is even, then ψ will satisfy the balanced condition. If λ is not an integer then, in general, ψ will not satisfy even the zeroth moment condition no matter what conditions are satisfied by ϕ. This means that delta functions may be dilated only by integers. Therefore, if one wishes to refine the grid-size in a simulation but

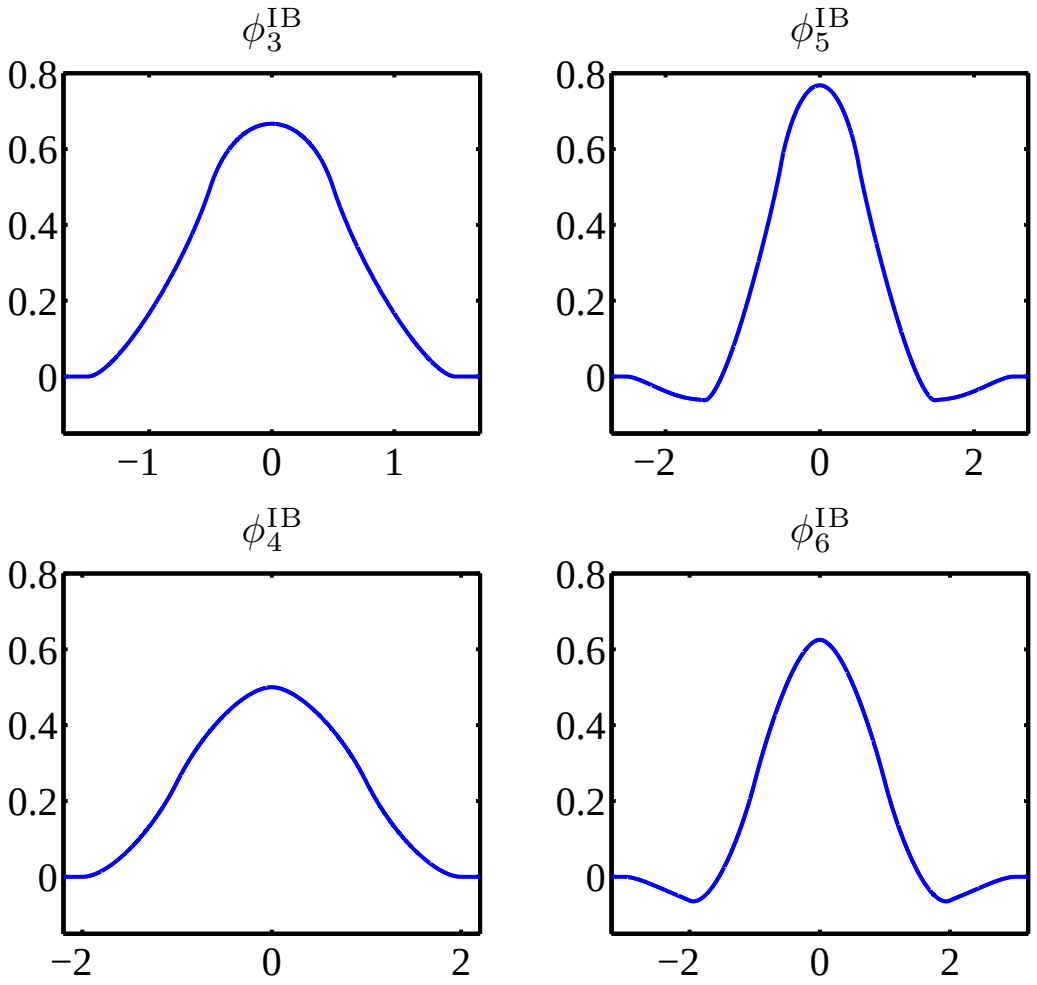


Figure 4.2: Plot of ϕ_d^{IB}, which are traditionally used in the immersed boundary method. Though these functions may appear to have derivative discontinuities, they are in fact C^1.

to leave the approximate delta function unchanged then one must refine in such a way that the coarse grid spacing is an integral multiple of the fine grid spacing.

In subsequent chapters we test one such dilated function, ϕ_2^{M} dilated by a factor of 2. We call the resulting function ϕ_4^{D} which corresponds to the three dimensional delta function $\delta_{h,d}^{\mathrm{D}}$. The superscript D is meant to stand for "dilated".

We may define additional families of delta functions by requiring that ϕ satisfy higher-order alternating moment conditions as well as regular moment conditions and possibly the sum of squares condition. The total number of conditions must equal the support-width of ϕ, d. Also, the number of regular moment conditions must be even and must be greater than or equal to the number of alternating moment conditions. We adopt the following notation for these families of delta functions: $\phi_d^{m,a,s}$ satisfies m moment conditions, a alternating moment conditions, and has support width d. If $s = 1$ the sum of squares condition is imposed, and if $s = 0$ it is not. We therefore must have $d = m + a + s$, $m \geq a$, and m even.

If the sum of squares condition is not imposed, a linear system of d equations and unknowns results for each value of x. If the sum of squares condition is imposed, $d - 1$ linear equations allow the expression of the d unknowns in terms of a single unknown for each value of x. A quadratic equation in this remaining unknown may then be solved by the quadratic formula.

We briefly list some examples of the functions ϕ that result. If 2 moment

and 2 alternating moment conditions are imposed, but not the sum of squares condition, the resulting $\phi_4^{2,2,0}$ is exactly ϕ_2^{M} dilated by 2, which we have called ϕ_4^{D}. Generally, if d moment conditions and d alternating moment conditions are imposed, but not the sum of squares condition, the resulting $\phi_{2d}^{d,d,0}$ will be ϕ_d^{M} dilated by 2. If 2 moment conditions and 1 alternating moment condition (the balanced condition) are imposed, but not the sum of squares condition, the resulting $\phi_3^{2,1,0}$ is given by

$$\phi_3^{2,1,0}(x) = \begin{cases} \frac{1}{2} & 0 \le |x| \le \frac{1}{2} \\ \frac{3}{4} - \frac{1}{2}|x| & \frac{1}{2} < |x| \le \frac{3}{2} \\ 0 & \frac{3}{2} < |x|. \end{cases} \tag{4.29}$$

If 4 moment conditions and the balanced condition are imposed, but not the sum of squares condition, the resulting $\phi_5^{4,1,0}$ is given by

$$\phi_5^{4,1,0}(x) = \begin{cases} \frac{5}{8} - \frac{1}{4}|x|^2 & 0 \le |x| \le \frac{1}{2} \\ \frac{3}{4} - \frac{1}{6}|x| - \frac{1}{2}|x|^2 + \frac{1}{6}|x|^3 & \frac{1}{2} < |x| \le \frac{3}{2} \\ \frac{15}{16} - \frac{17}{12}|x| + \frac{5}{8}|x|^2 - \frac{1}{12}|x|^3 & \frac{3}{2} < |x| \le \frac{5}{2} \\ 0 & \frac{5}{2} < |x|. \end{cases} \tag{4.30}$$

If 4 moment and 2 alternating moment conditions are imposed, the resulting

$\phi_6^{4,2,0}$ is given by

$$\phi_6^{4,2,0}(x) = \begin{cases} \frac{5}{8} - \frac{5}{24}|x| - \frac{1}{4}|x|^2 + \frac{1}{12}|x|^3 & 0 \le |x| \le 1 \\ \frac{9}{16} - \frac{11}{48}|x| - \frac{1}{8}|x|^2 + \frac{1}{24}|x|^3 & 1 < |x| \le 2 \\ \frac{13}{16} - \frac{49}{48}|x| + \frac{3}{8}|x|^2 - \frac{1}{24}|x|^3 & 2 < |x| \le 3 \\ 0 & 3 < |x|. \end{cases} \tag{4.31}$$

If 2 moment and 2 alternating moment conditions are imposed, and the sum of squares condition is also imposed, the resulting $\phi_5^{2,2,1}$ is given by

$$\phi_5^{2,2,1}(x) = \begin{cases} \frac{1}{6} + \frac{\sqrt{5}}{12}\sqrt{2 - 3|x|^2} & 0 \le |x| \le \frac{1}{2} \\ \frac{1}{2} - \frac{1}{4}|x| & \frac{1}{2} < |x| \le \frac{3}{2} \\ \frac{15}{12} - \frac{1}{8}|x| - \frac{\sqrt{5}}{24}\sqrt{-10 + 12|x| - 3|x|^2} & \frac{3}{2} < |x| \le \frac{5}{2} \\ 0 & \frac{5}{2} < |x|. \end{cases} \tag{4.32}$$

Plots of these functions are shown in figure 4.3. Again, these functions are even about the origin and are piecewise smooth. The function which satisfies the sum of squares condition is C^1, while the other functions have derivative discontinuities.

We consider those delta functions, $\delta_d^{m,a,s}$, with the same values of a and s and with various values of m to comprise a family. The family of delta functions δ_d^{M} is the same as the family $\delta_d^{m,0,0}$, the family δ_d^{IB} with d odd is the same as the family $\delta_d^{m,0,1}$, and the family δ_d^{IB} with d even is the same as the

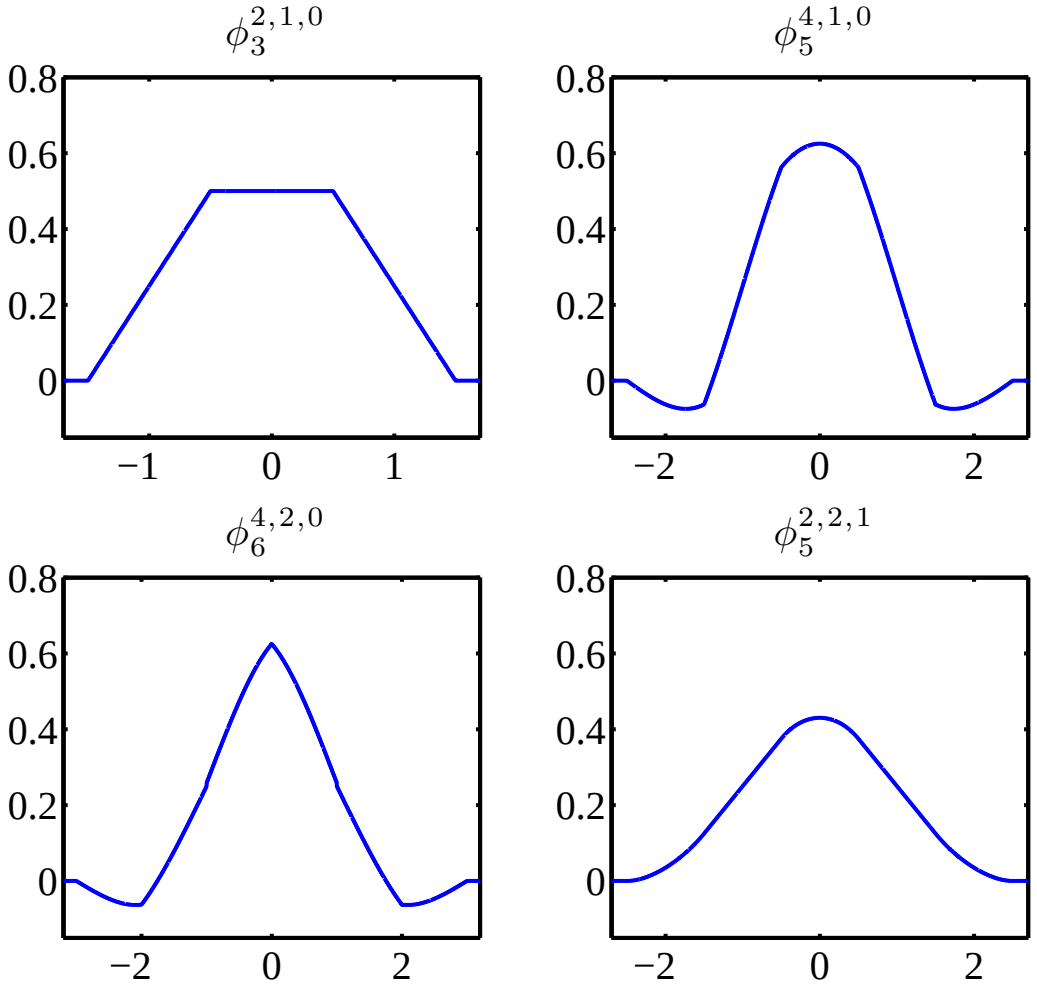


Figure 4.3: Plot of $\phi_d^{m,a,s}$, for various numbers of moment conditions, m, and alternating moment conditions, a, satisfied by ϕ, and for ϕ satisfying or not satisfying the sum of squares condition (respectively $s = 1$ and $s = 0$).

family $\delta_d^{m,1,1}$. The dilated delta function that we have called δ_4^{D} is a member of the family $\delta_d^{m,2,0}$.

4.4 Conditions in Fourier space

Another method of deriving approximate delta functions is by specifying the Fourier transform of the corresponding function ϕ and computing the inverse transform. All of the conditions that can be imposed on ϕ that we have discussed can be easily written as equivalent conditions on the Fourier transform of ϕ. In this section, we derive those equivalent conditions. To complete our derivations, we require some technical arguments which rely on assumptions about the smoothness and decay at infinity of ϕ. We try to make the minimal assumptions on ϕ necessary for the derivations. Doing so is more than an academic exercise, as some of ϕ that we have derived have derivative discontinuities. We are able to devise assumptions satisfied by the functions ϕ that we have derived, so that for all of these ϕ the results of this section hold.

We define the Fourier transform of ϕ. Let

$$\hat{\phi}(k) = \int_{\mathbb{R}} \phi(x) e^{-2\pi i k x} dx. \tag{4.33}$$

We assume ϕ is in $L^1(\mathbb{R})$ so this integral is well-defined and $\hat{\phi}$ is bounded. We also define the Fourier transform of ϕ with ϕ viewed as a function on the

grid of integers. Let

$$\tilde{\phi}(k,x) = \sum_{j\in\mathbb{Z}} \phi(x-j)e^{-2\pi ik(x-j)}. \tag{4.34}$$

Smoothness conditions on ϕ imply conditions on the decay of $\hat{\phi}$, and conditions on the decay of ϕ imply smoothness conditions on $\hat{\phi}$. These are well known results of real analysis and we do not discuss them further here except to state that if ϕ has compact support then $\hat{\phi}$ must be C^∞. Likewise if $\hat{\phi}$ has compact support then ϕ will be C^∞ and will necessarily be supported on the whole real line.

Consider a function $g(x)$ with Fourier transform $\hat{g}(k)$. The aliasing formula says

$$\sum_{j\in\mathbb{Z}} g(j)e^{-2\pi ikj} = \sum_{n\in\mathbb{Z}} \hat{g}(k+n). \tag{4.35}$$

By the definition of $\tilde{\phi}(k,x)$, the zeroth moment condition can be written

$$\tilde{\phi}(0,x) = 1 \quad \forall x \in \mathbb{R}. \tag{4.36}$$

We apply the aliasing formula to $g(j) = \phi(x+j)$. By the translation property of the Fourier transform $\hat{g}(k) = \hat{\phi}(k)\exp(2\pi ikx)$. We find that

$$\tilde{\phi}(k,x) = \sum_{n\in\mathbb{Z}} \hat{\phi}(k+n)e^{2\pi inx}. \tag{4.37}$$

The zeroth moment condition is therefore equivalent to

$$\sum_{n\in\mathbb{Z}} \hat{\phi}(n) e^{2\pi i n x} = 1 \quad \forall x \in \mathbb{R}. \tag{4.38}$$

We claim that this condition uniquely determines $\hat{\phi}(n)$ for all $n \in \mathbb{Z}$. In particular, we claim the zeroth moment condition is equivalent to

$$\hat{\phi}(0) = 1, \qquad \hat{\phi}(n) = 0 \quad \forall n \in \mathbb{Z} \setminus \{0\}. \tag{4.39}$$

This follows from a standard result in the theory of Fourier series, provided we make some additional technical assumptions about ϕ. Generally, suppose we specify a function $\psi(x)$ such that

$$\psi(x) = \sum_{n\in\mathbb{Z}} \hat{\psi}(n) e^{2\pi i n x} \tag{4.40}$$

for some sequence $\hat{\psi}(n)$. This function $\psi(x)$ will be periodic with period 1. Moreover, suppose that this infinite sum converges in the sense of $L^2([0,1])$ if the functions are restricted to $[0,1]$ and that ψ restricted to $[0,1]$ is in $L^2([0,1])$. Then, $\hat{\psi}(n)$ is uniquely determined for all $n \in \mathbb{Z}$ because $\exp(2\pi i n x)$ form a basis for the Hilbert space $L^2([0,1])$. Moreover,

$$\hat{\psi}(n) = \int_0^1 \psi(x) e^{-2\pi i n x} dx. \tag{4.41}$$

For the zeroth moment condition, the function ψ in question is identically

equal to 1, which is in $L^2([0,1])$, so that $\hat{\psi}(n)$ is uniquely determined with the values shown in equation (4.39), provided we can show that the sum in equation (4.38) converges in the sense of $L^2([0,1])$. We do this by showing that, with some extra assumptions on ϕ, the sequence $\hat{\phi}(n)$ for $n \in \mathbb{Z}$ is in $l^2(\mathbb{Z})$. For, suppose the sequence $\hat{\psi}(n)$ in equation (4.40) is in $l^2(\mathbb{Z})$, then

$$\left\| \psi - \sum_{n=-M}^{M} \hat{\psi}(n) e^{2\pi i n x} \right\|_{L^2([0,1])} = \sum_{n=-\infty}^{-M-1} |\hat{\psi}(n)|^2 + \sum_{n=M+1}^{\infty} |\hat{\psi}(n)|^2 \qquad (4.42)$$

which converges to 0 as $M \to \infty$.

To show that $\hat{\phi}(n)$ is in $l^2(\mathbb{Z})$, we make the additional assumptions that ϕ is piecewise C^1, that ϕ' is in $L^1(\mathbb{R})$, and also that $\phi(x)$ has the limit zero as x approaches plus or minus infinity. All the ϕ that we have derived satisfy these assumptions. Under these assumptions, we first show that the Fourier transform of ϕ satisfies $\hat{\phi}(k) = o(1/|k|)$ as k approaches plus or minus infinity. Let a_n be the points of discontinuity of $\phi'(x)$, arranged sequentially, where $1 \leq n \leq N$. Formally, let $a_0 = -\infty$ and $a_{N+1} = \infty$. Then, integrating by parts in each interval over which ϕ is C^1,

$$\begin{aligned} \hat{\phi}(k) &= \int_{\mathbb{R}} \phi(x) e^{-2\pi i k x} dx \\ &= \sum_{n=0}^{N} \left[\frac{-1}{2\pi i k} \phi(x) e^{-2\pi i k x} \right] \Bigg|_{a_n}^{a_{n+1}} + \frac{1}{2\pi i k} \int_{\mathbb{R}} \phi'(x) e^{-2\pi i k x} dx. \end{aligned} \qquad (4.43)$$

Because ϕ is continuous and decays at plus and minus infinity, the sum in this equation telescopes and is zero. The second term in this equation is $o(1/k)$

by the Riemann-Lebesgue lemma, which completes the proof that $\hat{\phi}(k) = o(1/|k|)$. We can generalize this proof to the case when ϕ' has countably many discontinuities if we also assume that ϕ decays sufficiently rapidly so that we may rearrange the terms in the telescoping sum.

Now, because $\hat{\phi}(k) = o(1/|k|)$, we have shown that the sequence $\hat{\phi}(n)$ with $n \in \mathbb{Z}$ is in $l^2(\mathbb{Z})$. We conclude that ϕ satisfies the zeroth moment condition if and only if $\hat{\phi}(n)$ takes the values given in equation (4.39) for integer values of n. For this proof, we needed only that $\hat{\phi}(n) \in l^2(\mathbb{Z})$, which is stronger than $\hat{\phi}(k) = o(1/|k|)$. It is possible that we could relax somewhat our assumptions on ϕ.

We look now at the balanced condition. Note that the balanced condition implies that for all $x \in \mathbb{R}$

$$\sum_{j \in \mathbb{Z} \text{ even}} \phi(x-j) - \sum_{j \in \mathbb{Z} \text{ odd}} \phi(x-j) = \sum_{j \in \mathbb{Z}} \phi(x-j) e^{\pi i j} = 0. \tag{4.44}$$

Therefore, the balanced condition can be written

$$\tilde{\phi}\left(\frac{1}{2}, x\right) = 0 \quad \forall x \in \mathbb{R}. \tag{4.45}$$

We again apply the aliasing formula to $g(j) = \phi(x+j)$ but with $k = 1/2$. We find that the balanced condition is equivalent to

$$\sum_{n \in \mathbb{Z}} \hat{\phi}(n + 1/2) e^{2\pi i n x} = 0 \quad \forall x \in \mathbb{R}. \tag{4.46}$$

Under the above assumptions, the sequence $\hat{\phi}(n+1/2)$ is in $l^2(\mathbb{Z})$. Applying the Fourier series argument from above with $\psi \equiv 0$, which is in $L^2([0,1])$, we conclude that the balanced condition is equivalent to

$$\hat{\phi}(n+1/2) = 0 \quad \forall n \in \mathbb{Z}. \tag{4.47}$$

We turn now to the higher moment conditions and the higher alternating moment conditions. Let

$$f_n(x) = \phi(x)x^n. \tag{4.48}$$

We assume that ϕ decays sufficiently rapidly that f_n has a well-defined Fourier transform. The Fourier transform of f_n is related to the n^{th} derivative of $\hat{\phi}$.

$$\hat{f}_n(k) = \frac{1}{(2\pi i)^n}\partial_k^n \hat{\phi}(k). \tag{4.49}$$

Let

$$\tilde{f}_n(k,x) = \sum_{j\in\mathbb{Z}} f_n(x-j)e^{-2\pi ik(x-j)}. \tag{4.50}$$

The n^{th} moment condition is equivalent to

$$\tilde{f}_n(0,x) = 0 \quad \forall x \in \mathbb{R}. \tag{4.51}$$

We now apply the aliasing formula to find

$$\tilde{f}_n(k,x) = \sum_{m\in\mathbb{Z}} \hat{f}_n(k+m)e^{2\pi imx} = \frac{1}{(2\pi i)^n}\sum_{m\in\mathbb{Z}} \partial_k^n \hat{\phi}(k+m)e^{2\pi imx}. \tag{4.52}$$

The n^{th} moment condition is then equivalent to

$$\sum_{m\in\mathbb{Z}} \partial_k^n \hat{\phi}(m) e^{2\pi i m x} = 0 \quad \forall x \in \mathbb{R}. \tag{4.53}$$

Assuming ϕ is piecewise C^1, then f_n is as well. We need the extra assumption that f_n' is in $L^1(\mathbb{R})$. Then, by our argument above, we have that the sequence $\partial_k^n \hat{\phi}(m)$ for $m \in \mathbb{Z}$ is in $l^2(\mathbb{Z})$. We again use the Fourier series argument from above to conclude that the n^{th} moment condition is equivalent to

$$\partial_k^n \hat{\phi}(m) = 0 \quad \forall m \in \mathbb{Z}. \tag{4.54}$$

The n^{th} alternating moment condition can be stated as

$$\tilde{f}_n\left(\frac{1}{2}, x\right) = 0 \quad \forall x \in \mathbb{R}. \tag{4.55}$$

Using the formula given in equation (4.52), we see that this is equivalent to

$$\sum_{m\in\mathbb{Z}} \partial_k^n \hat{\phi}(m+1/2) e^{2\pi i m x} = 0 \quad \forall x \in \mathbb{R}. \tag{4.56}$$

Under the same assumptions as for the ordinary moment conditions, the sequence $\partial_k^n \hat{\phi}(m+1/2)$ for $m \in \mathbb{Z}$ will be in $l^2(\mathbb{Z})$. We conclude that the n^{th} alternating moment condition is equivalent to

$$\partial_k^n \hat{\phi}(m+1/2) = 0 \quad \forall m \in \mathbb{Z}. \tag{4.57}$$

We finally consider the sum of squares condition. We continue to assume that ϕ is piecewise C^1, has limit zero at infinity, and that ϕ' is in $L^1(\mathbb{R})$. We use Plancherel's theorem, which says that if $g(j)$ is defined for $j \in \mathbb{Z}$, if this sequence is in $l^2(\mathbb{Z})$, and if we define

$$\tilde{g}(k) = \sum_{j \in \mathbb{Z}} g(j) e^{-2\pi i j k} \tag{4.58}$$

then

$$\sum_{j \in \mathbb{Z}} g(j)^2 = \int_0^1 |\tilde{g}(k)|^2 dk. \tag{4.59}$$

Let $g(j) = \phi(x + j)$, then the discrete Fourier transform,

$$\tilde{g}(k) = \tilde{\phi}(k, x) e^{2\pi i k x}. \tag{4.60}$$

If the sum of the squares of $\phi(x - j)$ for $j \in \mathbb{Z}$ is finite for all x, then $g(j)$ is in $l^2(\mathbb{Z})$ for all x. Plancherel's theorem and the aliasing formula imply

$$\sum_{j \in \mathbb{Z}} \phi(x - j)^2 = \int_0^1 |\tilde{\phi}(k, x)|^2 dk = \int_0^1 \left| \sum_{n \in \mathbb{Z}} \hat{\phi}(k + n) e^{2\pi i n x} \right|^2 dk. \tag{4.61}$$

The sum of squares condition requires that the quantity on the left be equal to C independent of x. We expand the sum on the right, to find that the sum of squares condition requires

$$\sum_{n,m \in \mathbb{Z}} e^{2\pi i (m-n) x} \int_0^1 \overline{\hat{\phi}(k + n)} \hat{\phi}(k + m) dk = C \quad \forall x \in \mathbb{R} \tag{4.62}$$

Let $p = m - n$ and change variables so that p replaces m. The sum of squares condition is then equivalent to the following being equal to C for all $x \in \mathbb{R}$:

$$\sum_{p\in\mathbb{Z}} e^{2\pi ipx} \sum_{n\in\mathbb{Z}} \int_0^1 \overline{\hat{\phi}(k+n)}\hat{\phi}(k+n+p)dk = \sum_{p\in\mathbb{Z}} e^{2\pi ipx} \int_{\mathbb{R}} \overline{\hat{\phi}(k)}\hat{\phi}(k+p)dk. \tag{4.63}$$

Let the sequence $a(p)$ for $p \in \mathbb{Z}$ be defined by

$$a(p) = \int_{\mathbb{R}} \overline{\hat{\phi}(k)}\hat{\phi}(k+p)dk. \tag{4.64}$$

By the Schwarz inequality, these integrals will be finite for all p provided $\hat{\phi}$ is in $L^2(\mathbb{R})$, which is the case because ϕ is in $L^2(\mathbb{R})$ when it satisfies the sum of squares condition and is continuous (in which case $\|\phi\|_{L^2} = \sqrt{C}$).

We wish to show that the sequence $a(p)$ is in $l^2(\mathbb{Z})$. Equation (4.63) implies that the sum of squares condition is equivalent to

$$\sum_{p\in\mathbb{Z}} a(p)e^{2\pi ipx} = C \quad \forall x \in \mathbb{R}. \tag{4.65}$$

If $a(p)$ is in $l^2(\mathbb{Z})$, we can apply the Fourier series argument to conclude that $a(p) = C$ when $p = 0$ and $a(p) = 0$ otherwise. Thus, the sum of squares condition is equivalent to the conditions

$$\int_{\mathbb{R}} |\hat{\phi}(k)|^2 dk = C, \quad \int_{\mathbb{R}} \overline{\hat{\phi}(k)}\hat{\phi}(k+p)dk = 0 \quad \forall p \in \mathbb{Z} \setminus \{0\}. \tag{4.66}$$

This means that the Fourier transform of ϕ becomes orthogonal to itself when

shifted by a non-zero integer. This has an interesting consequence if we now apply the Fourier transform version of Parseval's theorem. We find that the following condition on $\phi(x)$ is equivalent to the sum of squares condition:

$$\int_{\mathbb{R}} \phi(x)^2 dx = C, \quad \int_{\mathbb{R}} \phi(x)^2 e^{2\pi i p x} dx = 0 \quad \forall p \in \mathbb{Z} \setminus \{0\}. \tag{4.67}$$

So, $\hat{\phi}^2(p)$ is C when $p = 0$ and is 0 for all other integers p. Actually, this result is not surprising since the sum of squares condition implies that ϕ^2 satisfies what is essentially the zeroth moment condition, except that it is required that the sum be C instead of 1.

To show that $a(p)$ is in $l^2(\mathbb{Z})$, we use that $\hat{\phi}(k) = o(1/k)$. This means there is some constant b so that $|\hat{\phi}(k)| \leq b/k$. We now estimate $a(p)$ assuming $p > 0$. The argument when $p < 0$ requires a small, obvious modification.

$$\begin{aligned} |a(p)| &\leq \int_{-\infty}^{-p/2} |\hat{\phi}(k)||\hat{\phi}(k+p)|dk + \int_{-p/2}^{\infty} |\hat{\phi}(k)||\hat{\phi}(k+p)|dk \\ &\leq \int_{-\infty}^{-p/2} |\hat{\phi}(k+p)|\frac{b}{|k|}dk + \int_{-p/2}^{\infty} |\hat{\phi}(k)|\frac{b}{k+p}dk. \end{aligned} \tag{4.68}$$

We now use Hölder's inequality on both integrals. The Hölder exponents are

3/2 and 3.

$$
\begin{aligned}
|a(p)| &\leq b\left(\int_{-\infty}^{-p/2} |\hat{\phi}(k+p)|^{\frac{3}{2}} dk\right)^{\frac{2}{3}} \left(\int_{-\infty}^{-p/2} \frac{1}{|k|^3} dk\right)^{\frac{1}{3}} \\
&\quad + b\left(\int_{-p/2}^{\infty} |\hat{\phi}(k)|^{\frac{3}{2}} dk\right)^{\frac{2}{3}} \left(\int_{-p/2}^{\infty} \frac{1}{(k+p)^3} dk\right)^{\frac{1}{3}} \\
&\leq 2^{\frac{4}{3}} b \|\hat{\phi}\|_{L^{3/2}} \frac{1}{p^{2/3}} \qquad (4.69)
\end{aligned}
$$

Because $\hat{\phi}$ is bounded and $o(1/k)$, it must be in $L^{3/2}(\mathbb{R})$. Therefore, we have shown that $a(p)$ decays at least as fast as $|p|^{-2/3}$. This is sufficiently fast to conclude that $a(p)$ is in $l^2(\mathbb{Z})$. This completes the proof that equation (4.66) is equivalent to the sum of squares condition.

We have now derived conditions on the Fourier transform of ϕ that are equivalent to each of the conditions on ϕ in real space that we proposed in the previous section. One way to construct ϕ that satisfy the desired conditions is to specify the Fourier transform of ϕ in such a way that the equivalent conditions are met and then to compute the inverse transform.

It is easy to construct functions that take specified values and whose derivatives takes specified values at the integers and the half-integers. However, in general the inverse Fourier transforms of these functions will not have compact support. For practical computations, one might truncate the resulting function ϕ so that it does have compact support, though it will then only approximately satisfy, for instance, the moment conditions. We are currently working on optimizing this process to minimize these errors.

We can also represent the Lagrangian Green's function $\mathcal{G}(\mathbf{X}, \mathbf{X}')$ in terms of the Fourier transform of the delta function. Let

$$\hat{\delta}_h(\mathbf{k}) = \int_{\mathbb{R}^3} \delta_h(\mathbf{x}) e^{-2\pi i \mathbf{k}\cdot\mathbf{x}/h} \mathbf{dx}. \tag{4.70}$$

Also, define the Fourier transform of the delta function on the Cartesian grid

$$\tilde{\delta}_h(\mathbf{k}, \mathbf{X}) = \sum_{\mathbf{x}\in(h\mathbb{Z})^3} \delta_h(\mathbf{X}-\mathbf{x}) e^{-2\pi i \mathbf{k}\cdot(\mathbf{X}-\mathbf{x})/h} h^3. \tag{4.71}$$

By the three-dimensional version of the aliasing formula

$$\tilde{\delta}_h(\mathbf{k}, \mathbf{X}) = \sum_{\mathbf{n}\in\mathbb{Z}^3} \hat{\delta}_h(\mathbf{k}+\mathbf{n}) e^{2\pi i \mathbf{n}\cdot\mathbf{X}/h}. \tag{4.72}$$

In particular, if $\hat{\delta}_h$ is supported on $[-1/2, 1/2]^3$, then for $|\mathbf{k}| \leq 1/2$, $\tilde{\delta}_h(\mathbf{k}, \mathbf{X}) = \hat{\delta}_h(\mathbf{k})$ independent of $\mathbf{X}$. If δ_h is a tensor product of one-dimensional functions ϕ, then $\hat{\delta}_h$ and $\tilde{\delta}_h$ will be tensor products of the corresponding functions $\hat{\phi}$ and $\tilde{\phi}$ respectively. If $\hat{\phi}$ is supported on $[-1/2, 1/2]$, then $\tilde{\phi}(k) = \hat{\phi}(k)$ for $|k| \leq 1/2$.

Recall that the Green's function relating the Lagrangian variables $\mathbf{U}$ and $\mathbf{F}$, $\mathcal{G}(\mathbf{X}, \mathbf{X}')$, is defined by equation (2.31) to be a double convolution sum of the discrete Stokeslet with an approximate delta function centered at $\mathbf{X}$ and an approximate delta function centered at $\mathbf{X}'$. We can write this convolution sum as an integral over the appropriately defined Fourier transforms of the summands. Fortunately, we know the Fourier representation of the dis-

crete Stokeslet, shown in equation (2.27). Applying the Fourier convolution theorem, we find that we can write $\mathcal{G}$ as

$$\mathcal{G}(\mathbf{X},\mathbf{X}') = \frac{1}{h\mu}\int\limits_{\left[-\frac{1}{2},\frac{1}{2}\right]^3} \frac{1}{\alpha(\mathbf{k})}(\mathcal{I}-\hat{\mathbf{g}}(\mathbf{k})\hat{\mathbf{g}}(\mathbf{k})^{\mathrm{T}})\tilde{\delta}_h(\mathbf{k},\mathbf{X})\overline{\tilde{\delta}_h(\mathbf{k},\mathbf{X}')}e^{2\pi i\mathbf{k}\cdot(\mathbf{X}-\mathbf{X}')/h}\mathbf{dk}. \tag{4.73}$$

Recall that $\alpha(\mathbf{k})$ and $\mathbf{g}(\mathbf{k})$ are defined in chapter 2 and depend on which discretization method is used for the Stokes equations. For the spectral discretization, $\alpha = 4\pi^2|\mathbf{k}|^2$ and $\mathbf{g} = \mathbf{k}$. The carat above the $\mathbf{g}$ in equation (4.73) means that $\mathbf{g}$ is normalized to be a unit vector, not that any Fourier transform of $\mathbf{g}$ is taken.

If the delta function is supported on $[-1/2, 1/2]^3$, this expression for $\mathcal{G}$ becomes

$$\mathcal{G}(\mathbf{X},\mathbf{X}') = \frac{1}{h\mu}\int\limits_{\left[-\frac{1}{2},\frac{1}{2}\right]^3} \frac{1}{\alpha(\mathbf{k})}(\mathcal{I}-\hat{\mathbf{g}}(\mathbf{k})\hat{\mathbf{g}}(\mathbf{k})^{\mathrm{T}})|\hat{\delta}_h(\mathbf{k})|^2 e^{2\pi i\mathbf{k}\cdot(\mathbf{X}-\mathbf{X}')/h}\mathbf{dk}. \tag{4.74}$$

It is evident that in this case $\mathcal{G}(\mathbf{X},\mathbf{X}')$ is a function of $\mathbf{X}-\mathbf{X}'$ alone, not of $\mathbf{X}$ and $\mathbf{X}'$ independently. This means that the resulting dynamics of the immersed boundary points will be invariant to translations relative to the grid. If $\hat{\delta}_h$ also happens to be radially symmetric, then the dynamics of the immersed boundary points will also be invariant to rotations relative to the grid provided the discretization method for the Stokes equations is such that $\alpha(\mathbf{k})$ is invariant to rotations of $\mathbf{k}$ and $\mathbf{g}(\mathbf{k})$ transforms like the vector $\mathbf{k}$

under rotations. One such discretization method is the spectral discretization method described in chapter 2. Any traditional finite-difference discretization will not satisfy these rotational invariance properties.

If we specify $\hat{\delta}_h$ (or $\hat{\phi}$), we can compute $\mathcal{G}$ directly by computing these integrals. Specifying $\hat{\phi}$ allows us easily to impose desired moment conditions, alternating moment conditions, or the sum of squares condition. Note that any function ϕ whose Fourier transform is supported on $[-1/2, 1/2]$ will satisfy the sum of squares condition. Unfortunately, computing these integrals is difficult for the same reason that directly computing the discrete Stokeslet by quadrature was difficult. They have a singularity of degree 2 at the origin and are highly oscillatory when $|\mathbf{X} - \mathbf{X}'|/h$ is large.

This discussion motivates the definition of a delta function whose Fourier transform is 1 on $[-1/2, 1/2]^3$ and 0 elsewhere. So, $\hat{\phi}(k) = 1$ for $k \in [-1/2, 1/2]$ and $\hat{\phi}(k) = 0$ otherwise. We call this the spectral delta function, δ_h^{S}. We can easily compute

$$\phi^{\mathrm{S}}(x) = \frac{\sin \pi x}{\pi x}. \tag{4.75}$$

This function satisfies infinitely many moment conditions and the sum of squares condition but not the balanced condition. It has infinite support and decays only like $1/x$ for large x. For this delta function, we have

$$\mathcal{G}(\mathbf{X} - \mathbf{X}') = \frac{1}{h\mu} \int\limits_{\left[-\frac{1}{2},\frac{1}{2}\right]^3} \frac{1}{\alpha(\mathbf{k})} (\mathcal{I} - \hat{\mathbf{g}}(\mathbf{k})\hat{\mathbf{g}}(\mathbf{k})^{\mathrm{T}}) e^{2\pi i \mathbf{k}\cdot(\mathbf{X}-\mathbf{X}')/h} \mathbf{dk}. \tag{4.76}$$

When $\mathbf{X}-\mathbf{X}'$ has integer coefficients, $\mathcal{G}$ agrees with the discrete Stokeslet, $\mathcal{S}$. If we use the spectral discretization method, we can use the same asymptotic expansion that we developed for $\mathcal{S}$ in chapter 3 to create an expansion for $\mathcal{G}$ with similar convergence properties. Thus, we may efficiently compute $\mathcal{G}$ for this choice of delta function when $\mathbf{X}-\mathbf{X}'$ has at least one component of reasonable size compared with h. If all components are small, we must use quadrature.

The above discussion also motivates the definition of a delta function whose Fourier transform is 1 on the ball of radius 1/2 centered at the origin and 0 elsewhere. This delta function will be radially symmetric, and will not be a tensor product of one-dimensional functions ϕ. We call this the spectral radial delta function, δ_h^{R}. We can compute the inverse transform of this delta function to find

$$\delta_h(\mathbf{x}) = \frac{1}{2\pi h|\mathbf{x}|^2}\left(\frac{h\sin\frac{\pi|\mathbf{x}|}{h}}{\pi|\mathbf{x}|} - \cos\frac{\pi|\mathbf{x}|}{h}\right). \tag{4.77}$$

Indeed, this delta function depends only on the magnitude of $\mathbf{x}$. It decays like $1/|\mathbf{x}|^2$ and is regular at the origin. For the spectral discretization, $\mathcal{G}$ will be such that the dynamics of the immersed boundary points are invariant to translations and rotations relative to the grid. For this discretization and

this delta function, we can directly compute $\mathcal{G}$

$$\mathcal{G}(\mathbf{X}) = \frac{1}{4\pi^2\mu|\mathbf{X}|}\left[\mathrm{Si}\left(\frac{\pi|\mathbf{X}|}{h}\right)\left(\mathcal{I}+\hat{\mathbf{X}}\hat{\mathbf{X}}^{\mathrm{T}}\right)+ \frac{h^2\sin\frac{\pi|\mathbf{X}|}{h}-\pi h|\mathbf{X}|\cos\frac{\pi|\mathbf{X}|}{h}}{\pi^2|\mathbf{X}|^2}\left(\mathcal{I}-3\hat{\mathbf{X}}\hat{\mathbf{X}}^{\mathrm{T}}\right)\right] \tag{4.78}$$

where $\mathrm{Si}(x)$ is the sine integral function defined by

$$\mathrm{Si}(x) = \int_0^x \frac{\sin t}{t}dt \tag{4.79}$$

and discussed extensively in reference [1], section 5.2. If we fix $\mathbf{X} \neq 0$ and let h decrease to 0, $\mathrm{Si}(\pi|\mathbf{X}|/h) \to \pi/2$, the other terms in equation (4.78) converge to 0, and $\mathcal{G}(\mathbf{X})$ converges to the continuous Stokeslet, $\mathcal{S}_0(\mathbf{X})$. The same conclusion holds if we fix h and let $|\mathbf{X}|$ increase to infinity.

These are all the delta functions that we shall define in this chapter. As mentioned above, we are currently working on methods to devise delta functions that decay rapidly in physical space and that obey many moment conditions by specifying their Fourier transforms.

To close this chapter, we show that no radially symmetric Gaussian delta function function can satisfy the zeroth moment condition. For suppose δ_h were a radially symmetric Gaussian, then δ_h would have the form of a tensor product as in equation (4.1) with ϕ a one-dimensional Gaussian function. The Fourier transform of a Gaussian is a Gaussian, a function that is everywhere non-zero, but the zeroth moment condition implies that $\hat{\phi}(k)$ is zero at

all non-zero integer values of k. This argument shows also that no Gaussian delta function can satisfy the balanced condition. In fact, no radial Gaussian delta function can satisfy any moment condition or any alternating moment condition. The reason is that the n^{th} derivative of a Gaussian is equal to an n^{th} degree polynomial (a scaled Hermite polynomial) multiplied by a Gaussian. The polynomial has at most n real roots, but the moment conditions require that infinitely many values of $\partial_k^n \hat{\phi}$ are zero. Finally, no radial Gaussian delta function can satisfy the sum of squares condition either. Since the Fourier transform of $\hat{\phi}$ is a real-valued Gaussian, the integrals in equation (4.66) with $p \neq 0$ will all be positive.

Chapter 5

Simple bodies

In this chapter, we conduct numerical experiments which examine the interactions with the fluid of some simple configurations of immersed boundary points. In particular, we look at a single, isolated point and at an array of equally spaced points that are constrained to move as a rigid body.

There are several reasons why we choose to test these particularly simple configurations of points. First, we conjecture that a single point is an accurate representation of a sphere and that an array of points is an accurate representation of a slender cylinder. Objects that can be modeled as spherical particles or as slender bodies are ubiquitous in biological and engineering problems at low Reynolds number. Moreover, many biological tissues are composed of fibers that can be modeled as individual slender bodies. Considerable computational savings can be gained if these bodies can be represented by simple configurations of immersed boundary points

as opposed to two- or three-dimensional meshes of points. Using such large meshes requires a reduction in the grid-spacing and the time-step that makes doing three-dimensional computations prohibitively expensive. If points and arrays of points can be used to model spheres and slender bodies, we would like to know the physical parameters (i.e. radius and length) that correspond to the numerical parameters of the method (i.e. grid spacing and choice of delta function). We find these correspondences in this chapter.

Second, using simple configurations of immersed boundary points allows us to compare our results with exact or asymptotically accurate solutions for a sphere or slender body in Stokes flow. The exact drag coefficient and velocity field of a translating sphere in Stokes flow is known, and slender-body theory may be used to find approximate drag coefficients and velocity fields for a translating or rotating cylinder. In both cases, fluid surrounding the bodies is unbounded, and so it is critical that our method is for an unbounded fluid for us to be able to make a comparison of our results with these. Also, in an unbounded fluid symmetry implies that the interactions of a body with the fluid should be independent of its position and orientation. We test this by varying the position and, in the case of the slender cylinder, orientation of the immersed boundary points relative to the grid.

Third, we feel that simple configurations of immersed boundary points present the most difficult test of the errors of immersed boundary method as the points change their position and orientation relative to the fixed Cartesian grid. One would like to quantify these errors, and it seems likely that

an upper bound will be obtained by examining them in context of simplest, barest configurations of immersed boundary points. More complicated configurations of points should result in smaller grid effects due to averaging. For the case of slender bodies, we examine how the grid effects depend on the spacing between immersed boundary points. We find that there is an optimal spacing so that, in particular, points should not be spaced to close together. This optimal spacing should guide users of the immersed boundary method in choosing of parameters.

While chapter 3 focused on the behavior of the Green's function relating the Lagrangian variables, $\mathcal{G}(\mathbf{X}, \mathbf{X}')$ as the components of $\mathbf{X} - \mathbf{X}'$ became large, this chapter focuses on $\mathcal{G}(\mathbf{X}, \mathbf{X}')$ when $\mathbf{X}$ and $\mathbf{X}'$ are close together or are the same point. We look at how $\mathcal{G}$ changes as $\mathbf{X}$ and $\mathbf{X}'$ change their position and orientation relative to the grid.

Again we examine a variety of discrete Dirac delta functions, and we find that the performance depends on the conditions satisfied by the delta functions. The families of delta functions are defined and derived in chapter 4. The delta function $\delta_d^{m,a,s}$ satisfies m ordinary moment conditions and a alternating moment conditions. If $s = 0$ it does not satisfy the sum of squares condition and if $s = 1$ it does satisfy this condition. The subscript d indicates the support width of the delta function and $d = m + a + s$. Necessarily, m is an even number and $m \geq a$. Those delta functions which have common values of a and s are considered to be in the same family. Commonly used families are $\delta_d^{m,0,0}$ which we denote by δ_d^{M}, $\delta_d^{m,0,1}$, and $\delta_d^{m,1,1}$. These last two

families are both denoted by δ_d^{IB}, where there is no ambiguity because the former family has d odd and the latter has d even. In some cases in this chapter we test only a subset of the delta functions derived in chapter 4. We also test both discretization methods for the Stokes equations, described in chapter 2, a finite difference method and a spectral method.

To examine the fluid interactions of the simple configurations of immersed boundary points, we calculate their resistance matrices as described in chapter 2. The resistance matrices contain the drag coefficients of the bodies, which we compare to the exact solution for the drag on a sphere or to results from slender-body theory for drag on a cylinder. We also compute the velocity field generated by these bodies as described in chapter 2 and compare with theory.

Results in this chapter all scale in a simple way with respect to the grid spacing, h, and the viscosity, μ (see chapter 2). Therefore, we set $h = \mu = 1$ in this chapter and drop the h subscript from all the approximate delta functions. Lengths in this chapter, then, can be thought of in units of the grid spacing, so a sphere of radius 1 has a radius of 1 mesh-width and a cylinder of length 10 has a length of 10 mesh-widths. Translational drag coefficients are proportional to $h\mu$, and rotational drag coefficients are proportional to $h^3\mu$. When we deduce the effective radii of a sphere or cylinder represented by immersed boundary points, we mean the radii in units of h.

The first section of this chapter shows that a single immersed boundary point interacts with the fluid very much like a sphere of some particular

radius. Significant grid effects are seen for some delta functions, but these effects are very small for those delta functions typically used in the immersed boundary method. The choice of discretization method makes little qualitative difference to the results.

The next section examines arrays of immersed boundary points that move as a rigid body. We first determine the optimum spacing of points in the array relative to the grid, which is the spacing that minimizes position and orientation dependence. Surprisingly, we find that the points must not be spaced too closely together. Again, the delta functions typically used in the immersed boundary method outperform other delta functions, and the choice of discretization method matters little. We use heuristic arguments to infer the dimensions of a rigid cylinder represented by an array of points from the radius of a sphere represented by a single point. These dimensions result in drags and velocity fields for the immersed boundary points that are very close to those of an actual cylinder, calculated from slender-body theory. At the end of this section, we extend our results to look at cylinders of very high aspect ratio using the asymptotic methods to perform calculations that we derived in chapter 3. These results allow us to examine the possibility of convergence in the limit of infinite aspect ratio. Since the convergence rate is only proportional to an inverse power of the logarithm of the aspect ratio, convergence is slow and our results are not conclusive. It seems possible that as aspect ratio becomes infinitely large, both the dependence on position and orientation relative to the grid and the error in the resistance matrix relative

to results from slender-body theory converge to zero.

In summary, this chapter shows that, for some delta functions, an immersed boundary point can be considered to be a sphere with a well-defined size, which depends on the delta function and discretization method. Grid effects are small. Moreover, these points, if spaced appropriately, can be combined to make more complicated geometric objects such as cylinders whose dimensions can be derived easily from the dimensions of a single point. Again, grid effects are small if we choose parameters appropriately, and we suggest choices of parameters. We believe that our results will be applicable to more complicated configurations of immersed boundary points. We also believe that the results of this chapter should be applicable to the immersed boundary method if the Reynolds number is finite or if finite boundaries are used.

5.1 Representing a sphere

We hypothesize that a single immersed boundary point in the discrete immersed boundary method is a good representation of a sphere of radius a, where a is to be determined. We would like that the resistance matrix of the immersed boundary point be close to the resistance matrix of a sphere of radius a, independent of the location of the immersed boundary point with respect to the grid. If the resistance matrices are close, then a force applied to an immersed boundary point will result in a velocity close to that of a sphere of radius a to which the same force is applied. We would also like the

external velocity field generated by the immersed boundary point to be close to that generated by a sphere. We apply both these tests in this section.

Some interactions between a sphere and the fluid cannot be replicated by a single immersed boundary point. Immersed boundary points have no orientation, so it is impossible for a single point to rotate. Also, it is impossible to apply torque to a single point. For a single point, then, the space of possible rigid motions is only three-dimensional and is the whole space of possible motions, so no constraint force is needed. In the notation introduced in section 2.3, the space V of rigid motions is simply $\mathbb{R}^3$. Thus, the resistance matrix is 3×3: $\mathcal{R} = \mathcal{G}^{-1}$. We have shown that if we use a delta function that is a tensor product of one-dimensional functions, then $\mathcal{G}(\mathbf{q}, \mathbf{q})$ is a diagonal matrix. In this case, which comprises the vast majority of delta functions that we consider, $\mathcal{R}$ will also be diagonal.

We compare the results for an immersed boundary point to those for a sphere to which a force but no torque is applied. The resistance matrix of a sphere of radius a, ignoring torque and rotation, is a 3×3 matrix that is a multiple of the identity.

$$\mathcal{R}_{\text{sphere}} = 6\pi a \mathcal{I} \tag{5.1}$$

The drag on a sphere is isotropic and is proportional to the radius. Recall that we have set $\mu = 1$.

To test whether the resistance matrices of an immersed boundary point and a sphere are close, we perform the following procedure for each choice

of approximate delta function and for each discretization method. We find the resistance matrices for a single immersed boundary point positioned at one of a large number (10,000) of randomly selected locations in a grid box. For each resistance matrix, we let the effective radius $a = \mathrm{tr}(\mathcal{R})/18\pi$, so that the resistance matrix has the same trace as that of a sphere of radius a. Averaging over all locations, we find the average effective radius, $\overline{a}$, for the particular choice of delta function and discretization method. The issue of how different the three diagonal elements of the resistance matrix are from one another will be discussed below.

Figure 5.1 shows the results of the effective radii for different delta functions and discretization methods. The delta functions that we test are derived in chapter 4, and their formulas are given there. The two discretization methods that we use (finite-difference and spectral) are discussed in chapter 2. The upper left plot shows a histogram of the effective radii obtained for δ_4^{IB} and the finite difference discretization. The mean of the distribution is $\overline{a} = 1.255$, so a single immersed boundary point interacts with the fluid like a sphere with radius 1.255 grid cells. The distribution does not have long tails and has a total width of only about 0.017 grid cells, so for all of the 10,000 locations, a fell within 1 percent of $\overline{a}$.

The upper right corner shows a histogram of the effective radii obtained for δ_4^{IB} and the spectral discretization. The results are very similar to those for the finite difference method. The distribution has a similar shape, again without long tails, and is again very narrow. Generally, we find that the

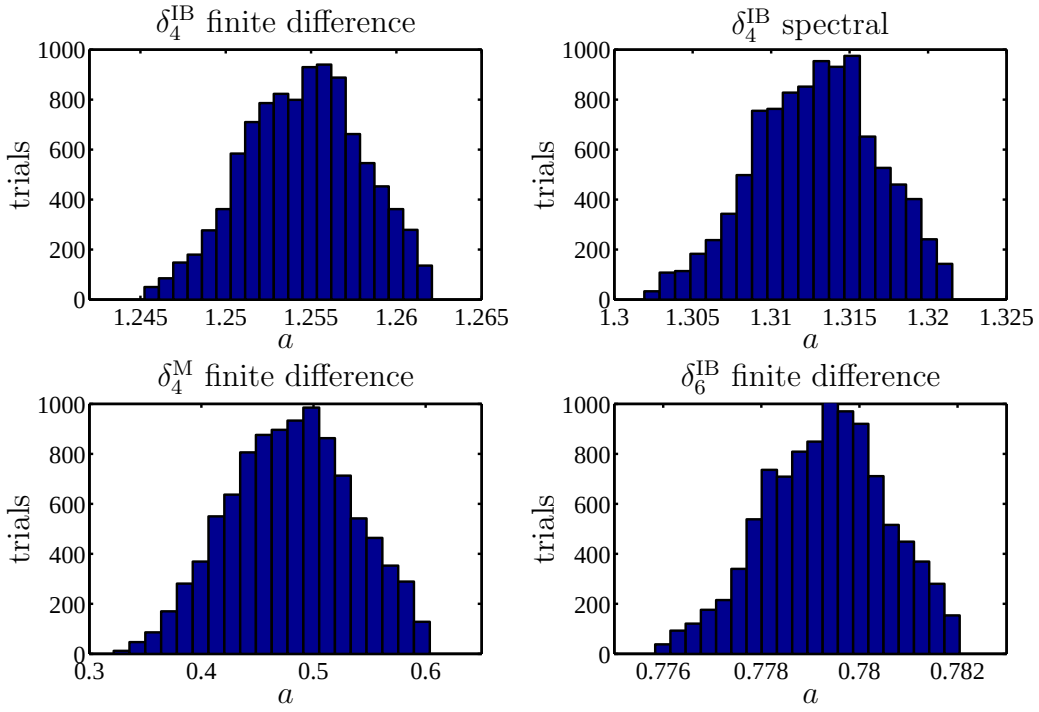


Figure 5.1: Histograms of the effective radii a obtained for various delta functions and discretization methods. Upper left: δ_4^{IB} and the finite difference discretization. Upper right: δ_4^{IB} and the spectral discretization. Lower left: δ_4^{M} and the finite difference discretization. Note the drastically different horizontal scale of this plot from those of the plots above (see also figure 5.2). Lower right: δ_6^{IB} and the finite difference discretization. For definitions of these functions, see chapter 4.

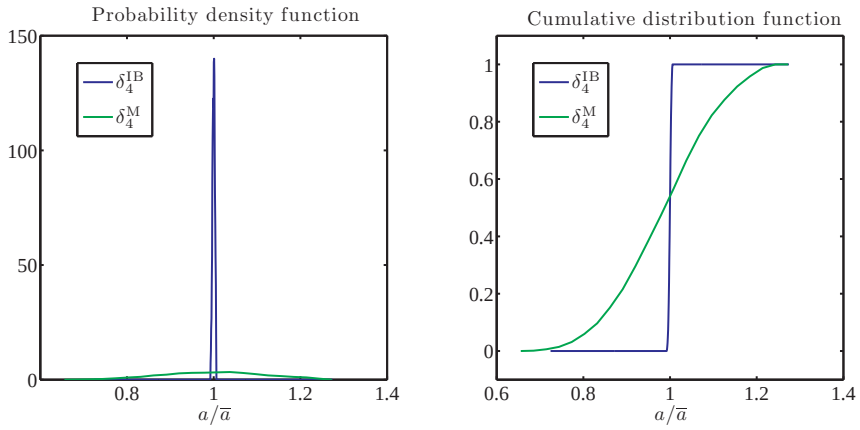


Figure 5.2: Comparison of the effective radii obtained for δ_4^{IB} (blue line) and δ_4^{M} (green line). The plot on the left shows the probability density function of the scaled effective radius $a/\overline{a}$ for the two delta functions, inferred from the a obtained from 10,000 randomly selected locations of the immersed boundary point. The plot on the right shows the cumulative distribution function.

choice of discretization method has only a small effect on the results. The lower left corner shows a histogram of the effective radii obtained for δ_4^{M} and the finite difference discretization. The distribution has a similar shape, but it is centered about a smaller value and is *much* wider than those for δ_4^{IB}. See figure 5.2 for a direct comparison. For some locations, a differed from $\overline{a}$ by almost 30 percent. The lower right corner shows a histogram of the effective radii obtained for δ_6^{IB} and the finite difference discretization. The shape of the distribution is similar to the others. Although this delta function has a larger support width than δ_4^{IB}, its effective radii are smaller. Generally, we find that delta functions in the same family with larger support actually have smaller effective radii. This is because the delta functions with larger support have negative tails that serve to concentrate their weight closer to the origin. The total width of the distribution of effective radii for δ_6^{IB} is less than 1 percent of the average.

As a measure of error, we calculate

$$\epsilon = \|\mathcal{R}/6\pi\overline{a} - \mathcal{I}\| \tag{5.2}$$

for each location, where the double bars indicate the matrix operator norm induced by the Euclidean vector norm. Precisely, ϵ is the maximum relative error in the drag force on an immersed boundary point in comparison to the drag on a sphere of radius $\overline{a}$ moving at the same velocity, where the maximum is over all possible orientations of this velocity with respect to the grid. We

let $\overline{\epsilon}$ be the maximum of ϵ over the 10,000 trials. Since ϵ is a continuous, periodic function of the position of the immersed boundary point, it has a finite maximum, and $\overline{\epsilon}$ will approach this maximum as the number of trials becomes very large. For a given delta function and discretization method, $\overline{\epsilon}$ represents the maximum possible error in the drag force on an immersed boundary point relative to that on a sphere with radius $\overline{a}$.

Figure 5.3 shows histograms of the values of ϵ obtained over the many trials for various delta functions and discretization methods. Again, results for the finite difference method and the spectral method for δ_4^{IB} are very similar. In both cases, ϵ is always less than 1 percent and is about 0.3 percent on average. Again, the shape of the histogram for δ_4^{M} is similar to that for δ_4^{IB}, but the magnitudes of the errors are much larger. The smallest errors of all are obtained with the delta function δ_6^{IB}.

Figure 5.4 shows a summary of our findings for a variety of delta functions and for both discretization methods. Each point on these plots represents one choice of delta function. The horizontal coordinate shows $\overline{a}$, and the vertical coordinate shows $\overline{\epsilon}$. Each shape and color represents a different family of delta function. In each family, the delta functions with greater support (and thus higher interpolation order) have *smaller* $\overline{a}$ and smaller $\overline{\epsilon}$, so as the width of the support of δ increases, the points on the plot go down and to the left. As stated above, the reason that $\overline{a}$ decreases for the delta functions with greater support is that these have negative tails which serve to concentrate their masses closer to the origin. For all the families, the first

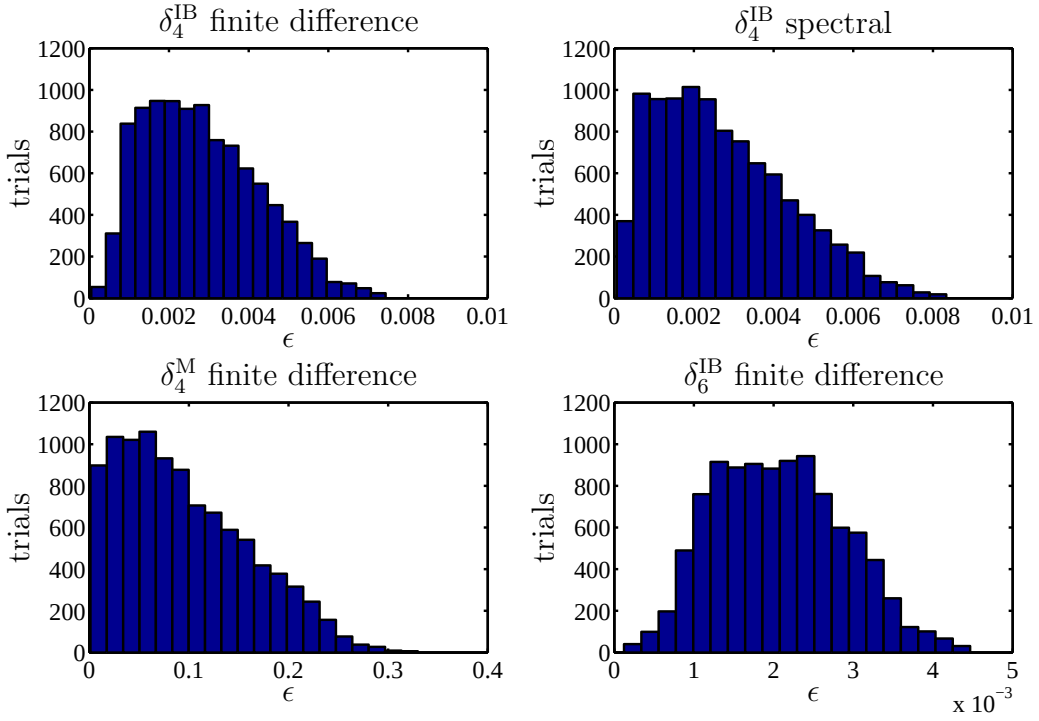


Figure 5.3: Histograms of ϵ, the error in the computed resistance matrices relative the that of a sphere of radius $\overline{a}$, obtained for various delta functions and discretization methods. Upper left: δ_4^{IB} and the finite difference discretization. Upper right: δ_4^{IB} and the spectral discretization. Lower left: δ_4^{M} and the finite difference discretization. Note again the drastically different horizontal scale of this plot from those of the plots above. Lower right: δ_6^{IB} and the finite difference discretization.

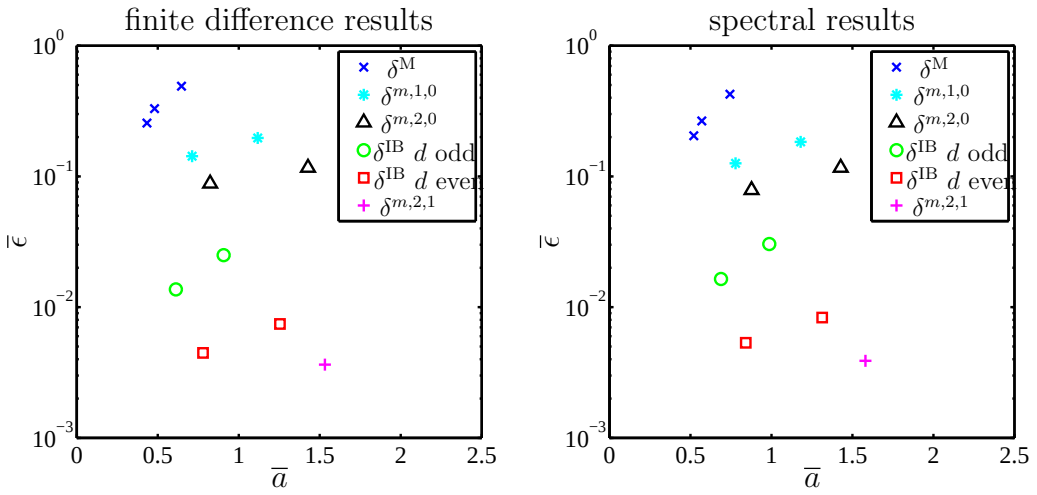


Figure 5.4: Summary of results obtained with various delta functions and discretization methods. For the purpose of visual clarity, the legends omit the subscript d on the delta functions. The maximum relative error in the resistance matrix $\bar{\epsilon}$ is plotted on a logarithmic scale against the mean effective radius $\bar{a}$. Each data point corresponds to one particular choice of delta function. Points with the same symbol and color correspond to delta functions in the same family. Within each family, delta functions with larger support have *smaller* $\bar{a}$ and smaller $\bar{\epsilon}$. Left: results obtained with the finite difference discretization method. Right: results obtained with the spectral discretization method. These two sets of results are nearly indistinguishable. For definitions of these functions, see chapter 4.

(i.e. upper-rightmost) point on the plot corresponds to the delta function with interpolation order 2 (satisfying 2 moment conditions), the second point corresponds the the delta function with interpolation order 4, etc. The results depend very little on the choice of discretization method. Generally, we find slightly larger values of $\overline{a}$ for the spectral method as opposed to the finite difference method. For those delta functions that do not satisfy the sum of squares condition, we find slightly smaller values of $\overline{\epsilon}$ for the spectral method. For those delta functions that do satisfy the sum of squares condition, we find slightly larger values of $\overline{\epsilon}$ for the spectral method.

Functions in the family δ_d^{M} show large errors, at least 25 percent. Functions in the family δ_d^{IB} with d odd have errors around 2 percent. Functions in the family δ_d^{IB} with d even are better still, with errors around 0.6 percent. Looking at the new families of delta functions, $\delta^{m,1,0}$, $\delta^{m,2,0}$ (of which δ_4^{D} is a member), and $\delta^{m,2,1}$, we see that adding alternating moment conditions reduces error and increases the effective radius of a delta function that satisfies a given number or ordinary moment conditions. In all cases, those delta functions satisfying the sum of squares condition have significantly smaller errors than those which do not.

The spectrally defined delta functions δ^{S} and δ^{R} are defined so that $\mathcal{G}$ is translation invariant. Therefore, their resistance matrices are independent of their location with respect to the grid and, in fact, are multiples of the identity, so that $\overline{\epsilon} = 0$ for these delta functions. For the spectral delta function, δ^{S}, $\mathcal{G}(\mathbf{X}, \mathbf{X})$ is simply $\mathcal{S}(0)$, the discrete Stokeslet evaluated at 0,

which we have calculated by quadrature. The effective radius, $\overline{a}$, of this delta function is then $1/(6\pi S)$ where S is any diagonal component of $\mathcal{S}(0)$. For the spectral radial delta function, δ^{R}, and the spectral discretization method, we have a formula for $\mathcal{G}$ given in equation (4.78), and we can directly compute that $\overline{a} = 1/2$. With the finite difference discretization method, we compute $\overline{a}$ by computing $\mathcal{G}(0)$ by quadrature.

As a reference, the values of $\overline{a}$ and $\overline{\epsilon}$ for all the delta functions and for both discretization methods are tabulated in table 5.1.

For many of the delta functions for which $\overline{\epsilon}$ is small, an immersed boundary point does have a resistance matrix close to that of a sphere of a particular radius regardless of the location of the immersed boundary point with respect to the grid. This effective radius depends on which delta function (and somewhat upon which discretization method) is used.

Having a delta function with a high interpolation order does not seem to be an advantage when it comes to representing a sphere by a single immersed boundary point. In fact, δ_4^{M}, with an interpolation order of 4 does not fare as well as δ_4^{D} with an interpolation order of 2. Much better, though, is δ_4^{IB} which has an interpolation order of 2 and also satisfies the sum of squares condition. For a given width of support, the best delta function (meaning the one with the smallest errors) is one that satisfies the sum of squares condition and the maximum number of alternating moment conditions. This delta function will actually have the minimum interpolation order of those we have considered with the same width of support. For support widths 2,

	Finite difference		Spectral	
Delta function	$\overline{a}$	$\overline{\epsilon}$	$\overline{a}$	$\overline{\epsilon}$
δ_2^{M}	0.647	0.490	0.744	0.425
δ_4^{M}	0.4800	0.330	0.5697	0.266
δ_6^{M}	0.4330	0.256	0.5204	0.205
$\delta_3^{2,1,0}$	1.1173	0.197	1.1803	0.184
$\delta_5^{4,1,0}$	0.7121	0.143	0.7779	0.126
δ_4^{D}	1.4276	0.117	1.4802	0.116
$\delta_6^{4,2,0}$	0.8235	0.0882	0.8773	0.0787
δ_3^{IB}	0.90678	0.0250	0.98666	0.0304
δ_5^{IB}	0.61170	0.0137	0.68864	0.0164
δ_4^{IB}	1.25455	0.00744	1.31286	0.00833
δ_6^{IB}	0.77931	0.00447	0.84112	0.00534
$\delta_5^{2,2,1}$	1.53188	0.00363	1.58043	0.00388
δ^{S}	0.31487	0	0.40937	0
δ^{R}	0.41662	0	1/2	0

Table 5.1: Reference table of results for the various delta functions and discretization methods used in this chapter. Shown are the computed effective radius of an immersed boundary point meant to represent a sphere, $\overline{a}$, and the maximum relative error in the resistance matrix of a point meant to represent a sphere, $\overline{\epsilon}$. These numbers are computed for the case $h = 1$. For general h, the radii should be multiplied by h. The delta functions are arranged by family with different families separated by horizontal lines.

3, 4, 5, and 6 respectively the best delta functions are δ_2^{M}, δ_3^{IB}, δ_4^{IB}, $\delta_5^{2,2,1}$, and δ_6^{IB}. We suspect that the best delta function of support width 7 will be $\delta_7^{4,2,1}$, etc.

The role of the balanced condition and the higher order alternating moment conditions is elucidated in chapter 3. The discrete Stokeslet oscillates from one grid point to the next, and these alternating moment conditions guarantee that the delta function will smooth these oscillations. The role of the ordinary moment conditions is also elucidated in chapter 3. Note that satisfying additional ordinary moment conditions does reduce error if the other conditions satisfied are fixed. Only when the support width is fixed is it advantageous to satisfy other conditions at the expense of a high moment order. Satisfying many moment conditions makes $\mathcal{G}_0$ close to the continuous Stokeslet, $\mathcal{S}_0$, which is translation invariant.

The role of the sum of squares condition is unclear, though it is likely significant that those delta functions satisfying the sum of squares condition are C^1 while the other delta functions have derivative discontinuities. The reduction in error that we see when the sum of squares condition is imposed, no matter the other conditions, is significant enough to suggest that it is a good condition to impose on any delta function when representing a sphere by a single immersed boundary point. If the interaction of a single point with the fluid depends significantly on the location of the point with respect to the grid, it seems likely that the interaction of many points with the fluid will also depend significantly on their location with respect to the grid. Our

results may imply that one should use a delta function that satisfies the sum of squares condition even when representing a more complicated solid boundary by many immersed boundary points. We test this hypothesis for the case of a rigid cylinder in the next section.

We now check whether the external velocity field created by an immersed boundary point is close to that created by a sphere of radius $\overline{a}$. The exact solution can be found for the external velocity field created when a force $\mathbf{F}$ is applied to a sphere of radius $\overline{a}$, centered at $\mathbf{x}_0$. The velocity is the sum of the continuous Stokeslet, $\mathcal{S}_0$, defined in equation (2.10) and a multiple of what is called the doublet, $\mathcal{D}_0$, applied to $\mathbf{F}$.

$$\mathcal{D}_0(\mathbf{x}) = \frac{1}{8\pi\mu}\frac{\mathcal{I} - 3\hat{\mathbf{x}}\hat{\mathbf{x}}^{\mathrm{T}}}{|\mathbf{x}|^3} \tag{5.3}$$

$$\mathbf{u}(\mathbf{x}) = \left(\mathcal{S}_0(\mathbf{x}-\mathbf{x}_0) + \frac{\overline{a}^2}{3}\mathcal{D}_0(\mathbf{x}-\mathbf{x}_0)\right)\mathbf{F} \tag{5.4}$$

For completeness, we show the scaling of the doublet with μ, even though μ is still set to one. A derivation of this solution can be found in [3], section 4.9. Since the sphere is rigid, the interior velocity is everywhere $\mathbf{u} = \mathbf{F}/6\pi\mu a$.

To see whether the velocity created by an immersed boundary point is close to that created by a sphere, we choose one random location for the immersed boundary point in a grid box, $\mathbf{X}_0$, and a random force, $\mathbf{F}$ to be applied to the point. We then use equations (2.24) and (2.26) to calculate $\mathbf{u}$ at grid points near $\mathbf{X}_0$. We compare these $\mathbf{u}$ with the exact solution for the velocity field of a sphere of radius $\overline{a}$ by calculating the relative error at

every grid point and finding the L_2 average of this quantity over cubic shells of grid points around the immersed boundary point.

Figure 5.5 shows a two-dimensional slice of a vector field plot of the velocity, $\mathbf{u}$, obtained using the delta function δ_4^{IB} and the finite difference discretization. For this plot, we chose $\mathbf{F} = \hat{x}$. The velocity has been translated by $-\mathbf{U}$ into the frame in which the immersed boundary point is stationary, so we can interpret the plot as showing the velocity field generated with the immersed boundary point held fixed and with the velocity equal to $-\mathbf{U}$ at infinity. The red circle represents the effective surface of the immersed boundary point. It is the intersection of a sphere centered at $\mathbf{X}_0$ with radius $\overline{a}$ with the two-dimensional plane that is shown. Notice that the fluid velocity seems to approach zero on the sphere boundary as dictated by the no-slip condition. The velocity inside the boundary should be zero, and we observe small, but non-zero, velocities there.

Figure 5.6 shows the relative error in the velocity field, again using δ_4^{IB} and the finite difference discretization, as a function of the distance of the cubic shell from the immersed boundary point measured in the infinity norm. The relative error is small, even at small distances, and it declines as the distance from the point increases. For other delta functions and for the spectral discretization method, the results are similar. In particular, the errors are only slightly greater for delta functions in the family δ_d^{M}. This is likely because the velocity field at a distance of a few grid points from a sphere is not very sensitive to the radius of the sphere when the radius is on the

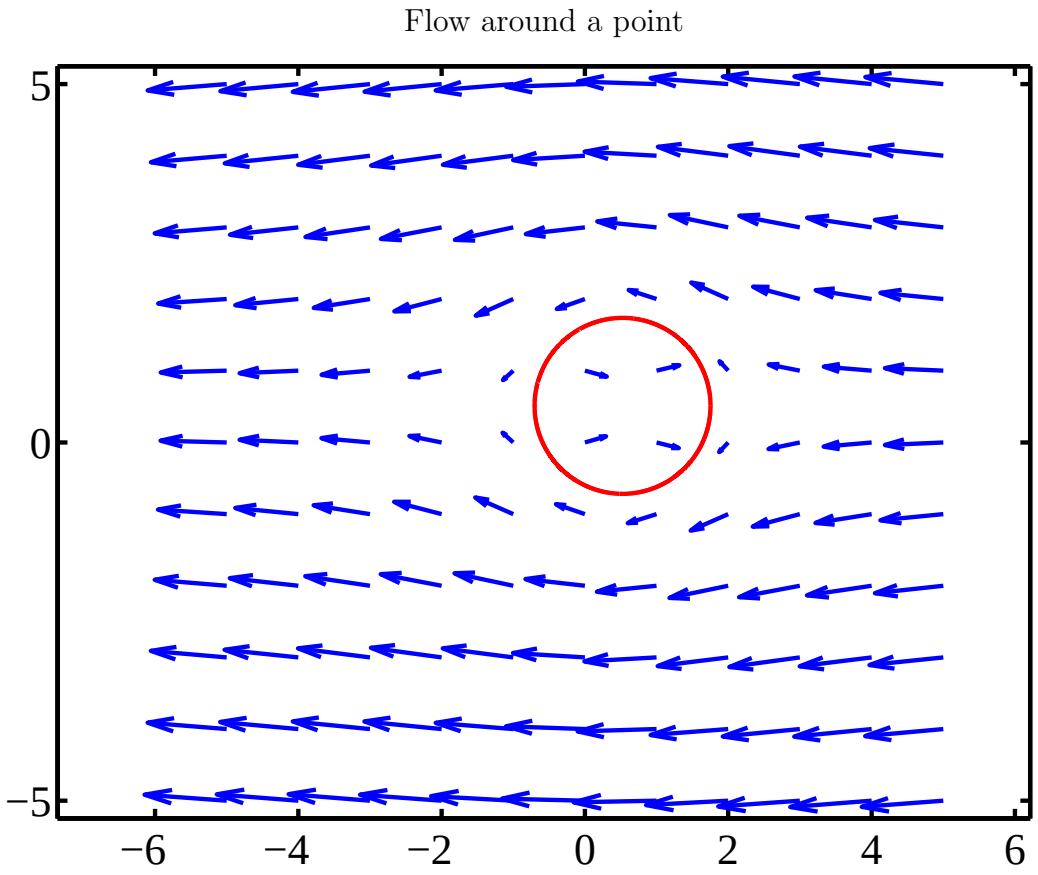


Figure 5.5: Results obtained using δ_4^{IB} and the finite difference discretization. Two-dimensional slice of the three-dimensional vector field $\mathbf{u}$, for $\mathbf{F} = \hat{x}$. For clarity, the velocity field has been translated by $-\mathbf{U}$, so the immersed boundary point is at rest and there is a flow of $-\mathbf{U}$ at infinity. The red circle shows the effective surface of the sphere represented by the immersed boundary point. This sphere has radius $\overline{a}$, which we found earlier by measuring the drag on immersed boundary points at many locations.

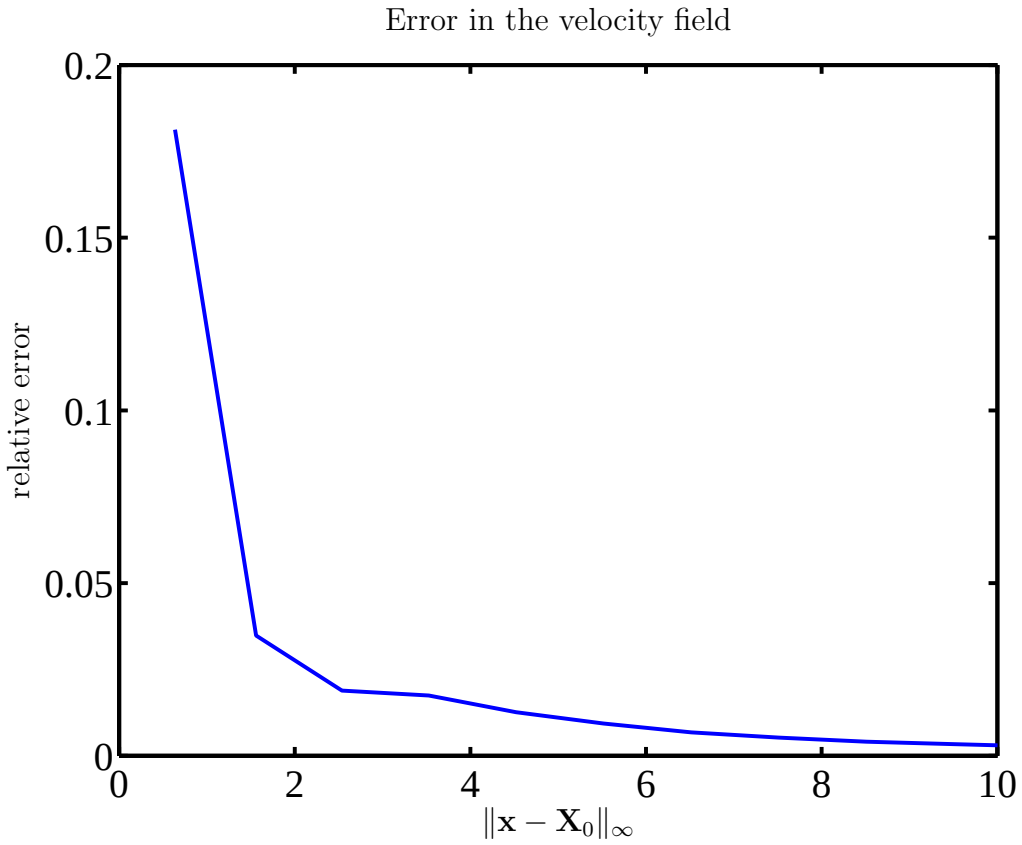


Figure 5.6: Results obtained using δ_4^{IB} and the finite difference discretization. Relative error in $\mathbf{u}$ is plotted as a function of distance from the center of the sphere, averaged over cubic shells. Distance is measured in the infinity norm. The error decays rapidly with distance and is under 5 percent even at a distance of 2 grid cells.

order of a grid point. However, as seen earlier, for some delta functions the self-interaction of an immersed boundary point can vary wildly depending on the location of the point with respect to the grid.

We conclude that, for an appropriate choice of delta function, a single immersed boundary point interacts with the fluid very much like a sphere of some particular radius, $\overline{a}$, independent of the position of the point relative the the grid. The point experiences similar drag forces to those of a sphere, and also the velocity field created by a moving point is similar to that created by a sphere. For general h an immersed boundary point will interact with the fluid like a sphere of radius $h\overline{a}$. If one wishes to represent a sphere of radius a_{S} by a single immersed boundary point, and one has chosen a delta function and a discretization method, then one should set $h = a_{\mathrm{S}}/\overline{a}$. We emphasize that our results recommend use of a delta function in the family δ_d^{IB} with d even or with d odd. It can be possible to represent spheres of several radii simultaneously by using a different delta function for each and by properly choosing h.

5.2 Representing a cylinder

5.2.1 Computing the resistance matrix

We now consider the problem of representing a cylinder by a linear array of immersed boundary points that is constrained to move as a rigid body. We refer to such an array is a pseudo-cylinder. Our approach is similar to that

for the sphere. We show that for certain choices of parameters the resistance matrix of a pseudo-cylinder is close to that of an actual rigid cylinder of a certain length and radius, independent of the position and orientation of the pseudo-cylinder with respect to the Eulerian grid. We then show that the external velocity field created by a pseudo-cylinder is also close to that created by an actual cylinder.

We have an additional parameter that we did not have to choose in the case of the sphere, namely the number of immersed boundary points in the array. We call this variable N, and in section 5.2.2 we show that N can be chosen to minimize the position and orientation dependence of the resistance matrix of the pseudo-cylinder. We shall see that N can be too big as well as too small for a pseudo-cylinder of a given length. Having chosen N, we compare the resistance matrix of a pseudo-cylinder with that of an actual cylinder in section 5.2.3. We must pick the dimensions of the cylinder to which we want to compare. We call these the effective radius r and effective length $\tilde{L}$ of the pseudo-cylinder, and we show that these can be chosen in a natural way. Finally, in section 5.2.4 we compare the generated velocity fields.

Although they need not necessarily be so, we consider only pseudo-cylinders made up of equally spaced immersed boundary points. We let L be the distance between the first and last points. Again, N is the number of immersed boundary points. The remaining parameters are the delta function, the discretization method, and the position and orientation of the pseudo-cylinder

with respect to the grid.

An array of immersed boundary points in a straight line can translate in three directions and rotate in two, but cannot spin about its axis; force can be applied in three directions and torque in two. So, the space of possible rigid motions, V, is five-dimensional and the resistance matrix, $\mathcal{R}$, is five by five. A slight modification is needed to the procedure described in section 2.3. We use a basis for V different from the translations and rotations in the coordinate directions. We identify the unit tangent vector to the centerline of the pseudo-cylinder, $\mathbf{t}$, choose an arbitrary unit normal vector $\mathbf{n}_1$, and let $\mathbf{n}_2 = \mathbf{t} \times \mathbf{n}_1$. We let $\mathbf{X}_0$ be the mean position of the immersed boundary points. As a basis for V we pick the elementary translations, $\mathbf{U} = \mathbf{t}$, $\mathbf{n}_1$, and $\mathbf{n}_2$, and the elementary rotations, $\mathbf{U}(\mathbf{q}) = \mathbf{n}_1 \times (\mathbf{X}(\mathbf{q}) - \mathbf{X}_0)$ and $\mathbf{n}_2 \times (\mathbf{X}(\mathbf{q}) - \mathbf{X}_0)$. We then calculate $\mathcal{R}$ as described in section 2.3.

By the symmetries of a cylinder, we expect $\mathcal{R}$ to be close to diagonal in this basis. Forces or torques in one of these directions should not cause motion in another. The diagonal elements are the translational and rotational drags of the array. We expect the drag in the $\mathbf{n}_1$ and $\mathbf{n}_2$ directions to be approximately equal. We also expect the rotational drag in the $\mathbf{n}_1$ and $\mathbf{n}_2$ directions to be approximately equal. For definiteness, when presenting results we refer to the drag in the $\mathbf{n}_1$ direction as the normal drag, and we refer to the rotational drag in the $\mathbf{n}_1$ direction as the rotational drag.

For a given choice of delta function, discretization method, L, and N, we calculate the resistance matrix of 100 pseudo-cylinders with randomly

selected positions and orientations with respect to the grid. We find the mean resistance matrix, $\mathcal{R}_{\text{mean}}$, and also the five by five matrices $\mathcal{R}_{\text{min}}$ and $\mathcal{R}_{\text{max}}$ whose entries are the minimum and maximum values of the entries of $\mathcal{R}$ over the 100 trials. The resistance matrix is a continuous, periodic function of the position and orientation of the pseudo-cylinder, so its entries have finite maximums and minimums. For a large number of trials, the entries $\mathcal{R}_{\text{min}}$ and $\mathcal{R}_{\text{max}}$ will approach these extremal values.

To quantify the difference between $\mathcal{R}$ for a trial and $\mathcal{R}_{\text{mean}}$, we should take into account that the eigenvalues of $\mathcal{R}_{\text{mean}}$ vary greatly in magnitude. To this end, we define a measure of position and orientation dependence, σ, as follows:

$$\sigma = \left\| \mathcal{R}_{\text{mean}}^{-1/2} \, \mathcal{R} \, \mathcal{R}_{\text{mean}}^{-1/2} - \mathcal{I} \right\| \tag{5.5}$$

The double bars again indicate the matrix operator norm induced by the Euclidean vector norm. This definition gives equal weight to each eigendirection of $\mathcal{R}_{\text{mean}}$. Precisely, σ is the maximum relative deviation in the drag forces and torques on a cylinder moving with some specified translational and rotational velocities, provided we use the norm induced by the symmetric matrix $\mathcal{R}_{\text{mean}}^{-1}$ to measure the sizes of vectors: $\|\mathscr{F}\|^2 = \mathscr{F}^{\text{T}} \mathcal{R}_{\text{mean}}^{-1} \mathscr{F}$. We let $\overline{\sigma}$ be the maximum of σ over the 100 trials.

5.2.2 Choosing the number of immersed boundary points

We determine the appropriate number of points, N, to use for each pseudo-cylinder length, L. For a good choice of N, we would like the resistance matrix to be close to diagonal and to be nearly independent of the position and orientation of the pseudo-cylinder with respect to the grid. We would also like our choice of N to be robust, meaning we do not want our resistance matrices to depend sensitively on the exact choice of N. Further, we would like N to be proportional to L so that there is an appropriate range of densities of immersed boundary points. We define the immersed boundary point density to be $\rho = (N-1)/L$. A robust choice of N that results in a consistent, accurate resistance matrix suggests that even a non-rigid slender body may be accurately represented by an array of immersed boundary points.

We first investigate the limit as N approaches infinity. Calculations using large N are computationally expensive, so we restrict our investigation to the special case $L = 20$, to the finite difference discretization method, and to the delta functions δ_4^{IB}, δ_4^{M}, and δ_6^{IB}. We let N vary from 5 to 400 in increments of 5. At very large densities, we occasionally find that $\mathcal{R}$ has extremely large values, probably because the matrix $\mathcal{G}$, which relates the force distribution $\mathbf{F}$ to the velocity distribution $\mathbf{U}$, is nearly singular in this case, and so the condition number for the computation of $\mathcal{R}$ can be large. To exclude these anomalies, we let $\mathcal{R}_{\mathrm{mean}}$ be the trimmed mean, excluding the largest and smallest 5 percent of values in each component. Similarly, $\mathcal{R}_{\mathrm{min}}$ and $\mathcal{R}_{\mathrm{max}}$ are the minimum and maximum values of each component excluding the

largest and smallest 5 percent, and $\overline{\sigma}$ excludes that largest 10 percent of trials. These changes only apply to the results in this investigation of high densities.

Results for high densities of immersed boundary points are seen in figure 5.7. The solid lines show the trimmed mean tangential drag (blue) and normal drag (green) as a function of the density ρ. The dashed lines on either side of the solid lines show the trimmed maximum and minimum drags. For all choices of delta function, the drags seem to converge to a limit as ρ becomes very large, but with significant position and orientation dependence. Our quantitative measure of orientation dependence, $\overline{\sigma}$, is very large for large ρ: around 25 percent for δ_4^{IB} and δ_4^{M} and 45 percent for δ_6^{IB}, even though the worst 10 percent of trials are excluded.

We can do better by focussing more closely on the regime of small ρ. We now use a greater variety of delta functions: δ_d^{M} for $d = 2$, 4, and 6; δ_d^{IB} for $d = 3$, 4, 5, and 6; and δ_4^{D}. We also use both discretization methods. We let L vary from 2 to 52 in increments of 2, and we let N vary over all integers between 2 and $3L + 1$ so that ρ is between 0 and 3.

Figure 5.8 shows results for the delta function δ_4^{IB} and the finite difference discretization. Results are shown for several values of L, ranging from 10 to 50 in increments of 10. The plots show drag in the tangential, normal, and rotational directions, as well as the off-diagonal component of $\mathcal{R}$ that couples together the two normal directions. This component ought to be close to zero. Results for the other off-diagonal components are similar.

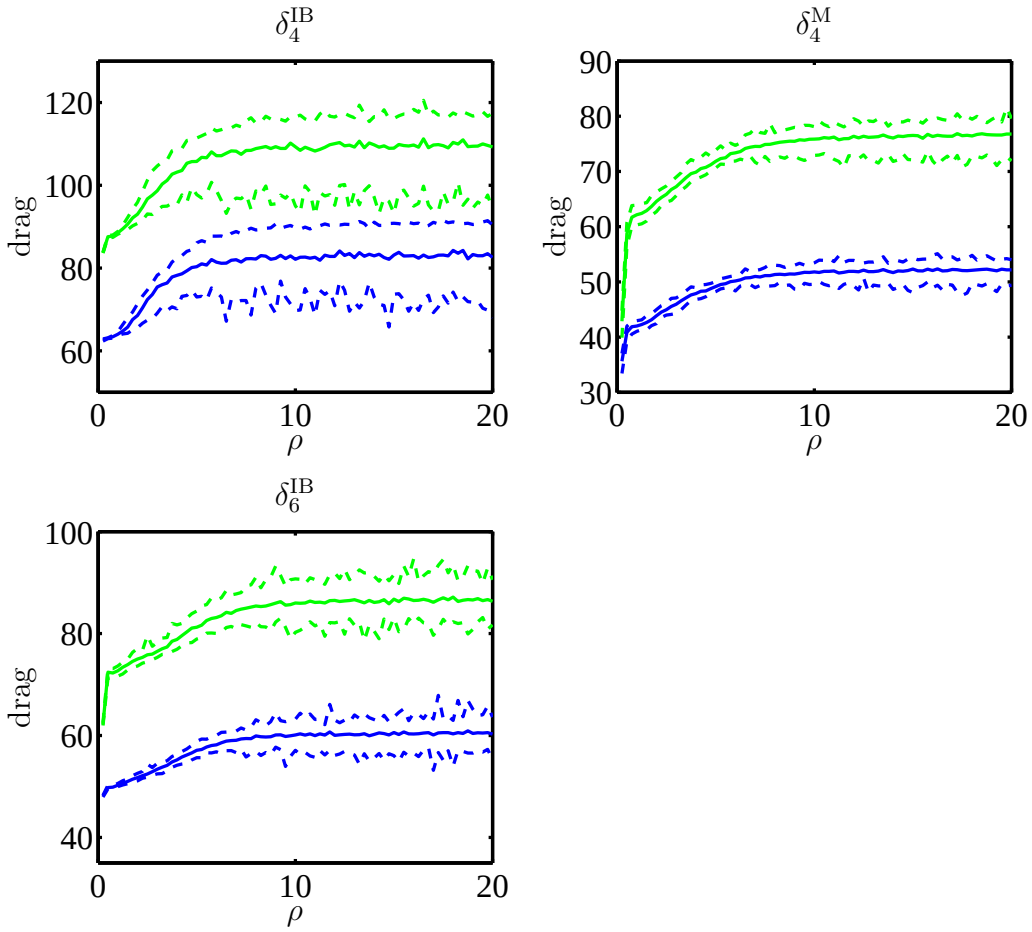


Figure 5.7: Results for high densities of immersed boundary points. The solid lines show mean drag in the normal (shown in green) and tangential (shown in blue) directions as a function of immersed boundary point density ρ. $L = 20$, and we use the finite difference discretization. Dashed lines show the maximum and minimum drags in these directions. Upper left: results for δ_4^{IB}. Upper right: results for δ_4^{M}. Lower left: results for δ_6^{IB}. In all cases, as ρ becomes very large, the mean, maximum, and minimum drags seem to converge to a finite limit. At this limit, the drags depend significantly on the position and orientation of the pseudo-cylinder.

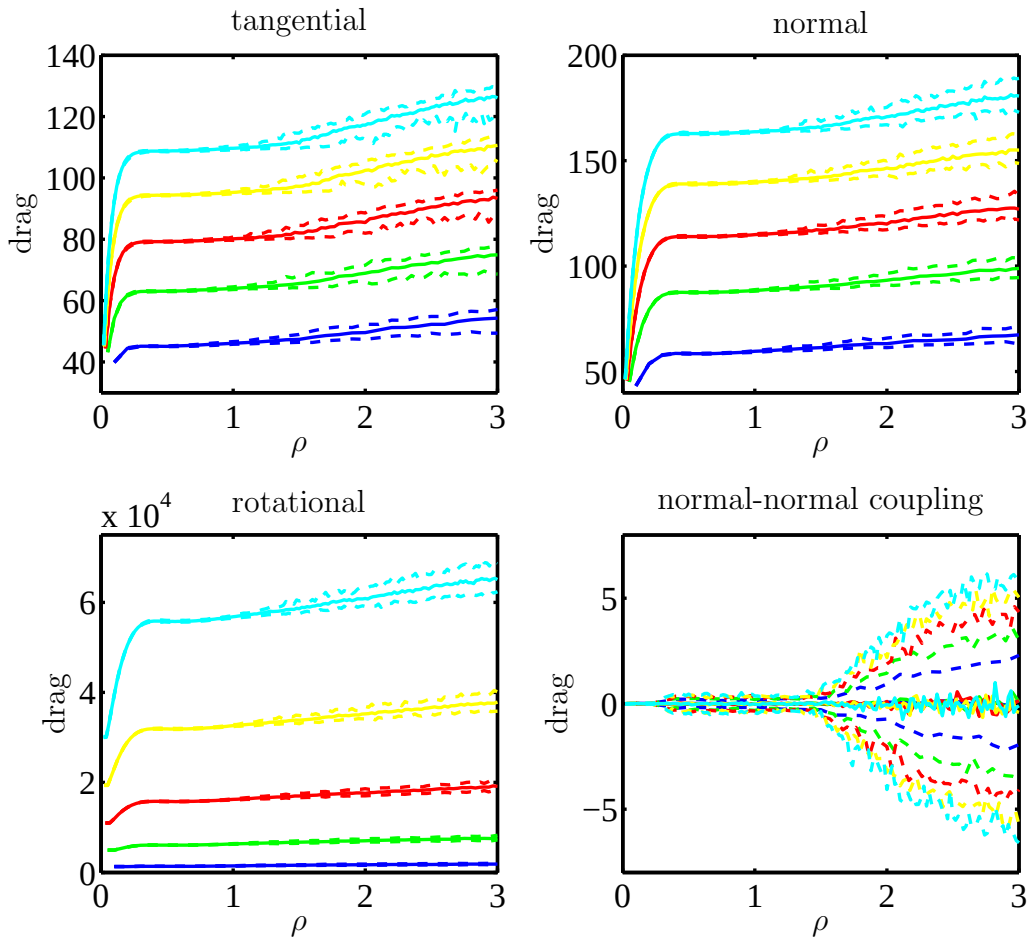


Figure 5.8: Results for low densities of immersed boundary points. Plots showing drags for δ_4^{IB} and the finite difference discretization as a function of immersed boundary point density. Solid lines show mean drags. Dashed lines show maximum and minimum drags. Results are shown for $L = 10$ (blue), 20 (green), 30 (red), 40 (yellow), and 50 (cyan). Upper left: tangential drag. Upper right: normal drag. Lower left: rotational drag. Lower right: off-diagonal element of $\mathcal{R}$ showing drag in one normal direction as a result of velocity in the orthogonal normal direction. We note that the qualitative behavior of the drags seems to depend only on ρ, and not on L and N independently. Moreover, there is a range of densities, $0.4 < \rho < 1.0$, where the drags are approximately constant, independent of position and orientation, and where there is little off-diagonal coupling.

This figure shows that, to a remarkable degree, the qualitative behavior of $\mathcal{R}$ as a function of the number of immersed boundary points depends only on the density of immersed boundary points, independent of the cylinder length. This is a very fortunate result, because if we are interested in using an array of immersed boundary points to represent a cylinder, we need only determine the best value of ρ, not the best value of N for every L. Moreover, we can be more confident in representing a non-rigid slender body by an array of immersed boundary points because there seems to be a preferred range of local densities, a fact that will not change if the body has small curvature, i.e. curvature with radius that is large in comparison to the grid spacing.

At small ρ, the drags increase sharply as density increases, indicating that the immersed boundary points are still allowing fluid to pass between them. At densities between 0.4 and 1.0, the drags are all very flat as functions of density, the maximum and minimum drags are very close to the mean drag, and coupling between the two normal directions is insignificant. At higher densities, the mean drag begins to increase as a function of ρ, the maximum and minimum drags diverge from the mean, and the maximum and minimum coupling between the two normal directions ceases to be negligible compared with the normal drag. We know from figure 5.7 that at very large ρ the mean, maximum, and minimum drags converge eventually, but to values where there is significant orientation and position dependence.

We see the same qualitative behavior with different delta functions and

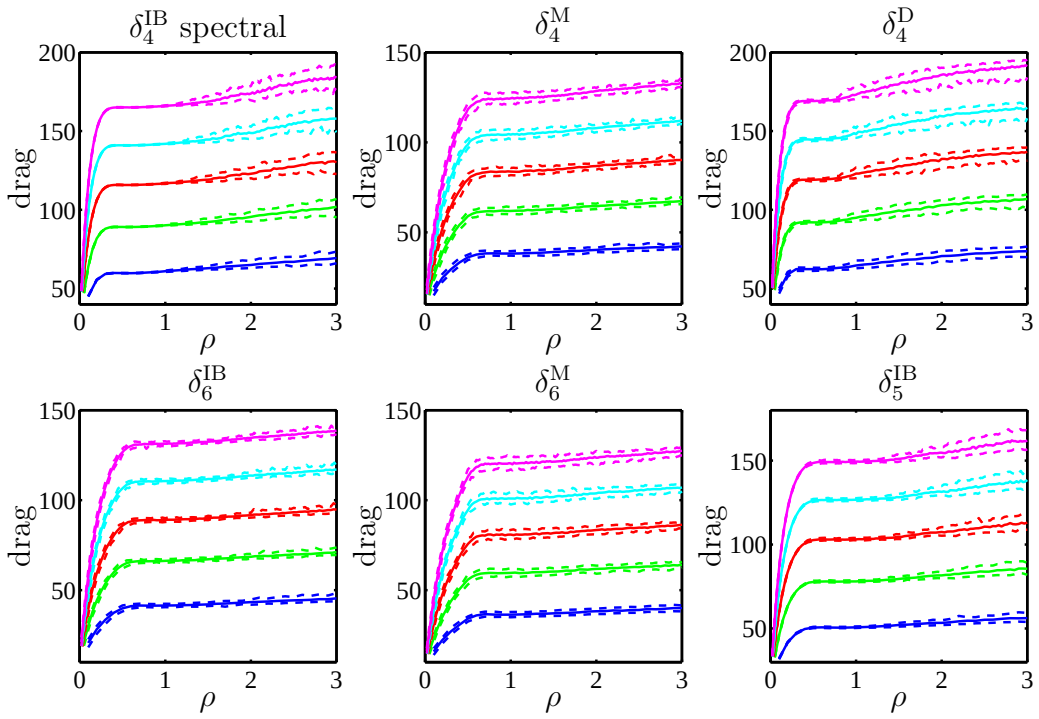


Figure 5.9: Plots showing normal drags for different delta functions and discretization methods as a function of immersed boundary point density. Solid lines show mean drags. Dashed lines show maximum and minimum drags. Results are shown for $L = 10$ (blue), 20 (green), 30 (rid), 40 (cyan), and 50 (magenta) with shorter lengths represented by darker lines. Upper left: δ_4^{IB} and the spectral discretization. The remaining plots use the finite difference discretization. Upper middle: δ_4^{M}. Upper right: δ_4^{D}. Lower left: δ_6^{IB}. Lower middle: δ_6^{M}. Lower right: δ_5^{IB}. The results are similar to those for δ_4^{IB} with the finite difference discretization shown in figure 5.8.

discretization methods, as seen in figure 5.9. The upper left plot in this figure, which is for δ_4^{IB} and the spectral discretization, is nearly identical to the upper right plot in figure 5.8. As when representing a sphere, the choice of discretization method made little difference in the results for any delta function.

The plots for δ_4^{D}, δ_6^{IB}, and δ_5^{IB} are qualitatively similar to that for δ_4^{IB}. There is a distinct range of ρ where the normal drag is approximately position and orientation independent and also independent of N. This range is much smaller for δ_4^{D} than for the immersed boundary method delta functions. Surprisingly, the orientation and position dependence in this range is largest for δ_6^{IB}. On the other hand, the divergence of the maximum and minimum drags from the mean for large ρ and the slope of the mean drag at large ρ are smaller. If we compare back to the lower left plot in figure 5.7, we see that the divergence eventually becomes large for very large ρ.

Less similar are the plots for δ_4^{M} and δ_6^{M}. While the drag increases as a function of ρ at large ρ, it does not seem as though the maximum and minimum drags diverge from the mean. We again refer back to figure 5.7 to see that this does occur at very large ρ. For these two delta functions there is significant position and orientation dependence for all choices of ρ, and the range where the mean drag is independent of ρ is small.

The quantitative position and orientation dependence of the resistance matrices as a function of density for the various delta functions can be seen more clearly in figure 5.10. Here, our measure of position and orientation

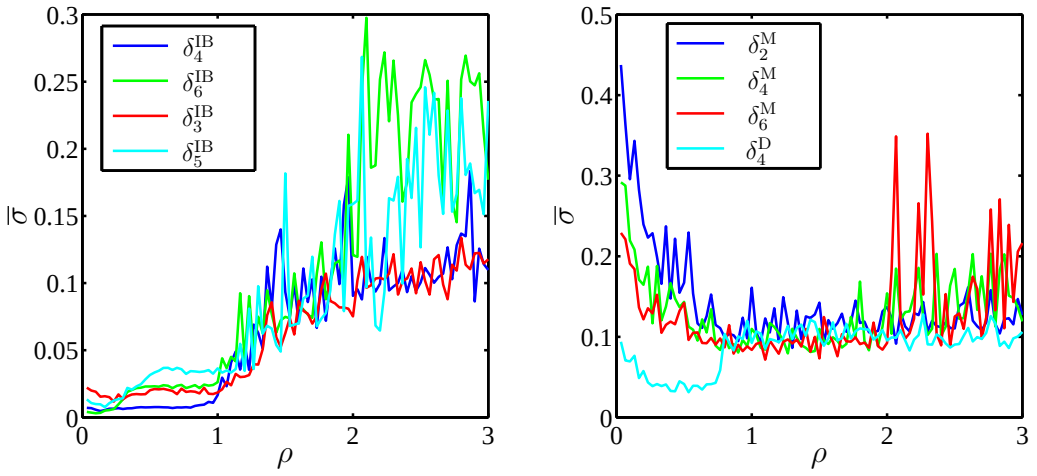


Figure 5.10: Position and orientation dependence of the pseudo-cylinder resistance matrices as a function of the density ρ. The quantity $\overline{\sigma}$ is a measure of maximum relative deviation (see equation (5.5)). For delta functions in the families δ_d^{IB} with d odd or even, $\overline{\sigma}$ is small when ρ is less than 1. Delta functions in the family δ_d^{M} never have $\overline{\sigma}$ below 10 percent, though $\overline{\sigma}$ still has a local minimum at a density of about 1.

dependence, $\overline{\sigma}$, is plotted against ρ for various delta functions, for the finite difference discretization, and for the case $L = 30$. Results for the spectral discretization and for different L are similar. Delta functions in the family δ_d^{IB} have $\overline{\sigma}$ less than 5 percent provided the density is less than about 1. Delta functions in the family δ_d^{M} have $\overline{\sigma}$ greater than 10 percent for all densities, but seem to have a minimum position and orientation dependence at a density of around 1. Finally, the function δ_4^{D} requires a density somewhat less than 1 to achieve a small $\overline{\sigma}$.

For every delta function there is a finite range of densities, which we call the preferred range, in which the position and orientation dependence of the resistance matrix is minimal, in which the resistance matrix does not depend sensitively on the exact choice of density, and in which the resistance matrix is nearly diagonal. This density interval tends to be near 1. Its exact location and size depends on the delta function and, less so, on the discretization method used.

To proceed, we choose a specific preferred density for each delta function and discretization method. The exact choice is not important, as long as it falls within the preferred range. Two possible choices, which can serve as rules of thumb, are densities of 1.0 and of $1/\overline{a}$, where $\overline{a}$ is the effective radius of an immersed boundary point as explained in section 5.1. In the first case, immersed boundary points are placed one grid cell apart. In the second case, they are placed one effective radius apart. The traditional rule of thumb used in immersed boundary method computations is that points be spaced

approximately half a grid cell apart, corresponding to a density of 2.0. This density is recommended to avoid leaks in computations in which regions of fluid are bounded by thin surfaces made up of immersed boundary points. Our purpose here is quite different, and we see in figures 5.9 and 5.10 that such a large density would be inappropriate for representing a cylinder by an array of points.

In our results presented below, we use a density of 1.0 for all delta functions except δ_4^{IB} and δ_4^{D}, for which we use $1/\overline{a}$. These choices nearly minimize $\overline{\sigma}$. For a particular value of L, we choose the integer number of points, N, that best approximates the desired density.

Having chosen N, we examine the position and orientation dependence of the resistance matrix as a function of L. Figure 5.11 shows $\overline{\sigma}$ for various delta functions and discretization methods. Solid lines show results for the finite difference discretization. Dashed lines show results for the spectral discretization. For most delta functions, the spectral discretization results in somewhat smaller position and orientation dependence than the finite difference discretization.

The delta function δ_4^{IB} has the smallest $\overline{\sigma}$, below 1 percent for all L greater than 10. We find larger $\overline{\sigma}$ for δ_6^{IB}, though still below 5 percent for almost all L. When L takes its smallest values, only a few immersed boundary points are used to represent the cylinder (approximately $L+1$). Under these circumstances, it is surprising that the representation works as well as it does. We find much larger $\overline{\sigma}$ for δ_4^{M} and δ_6^{M}: over 5 percent for the entire range of

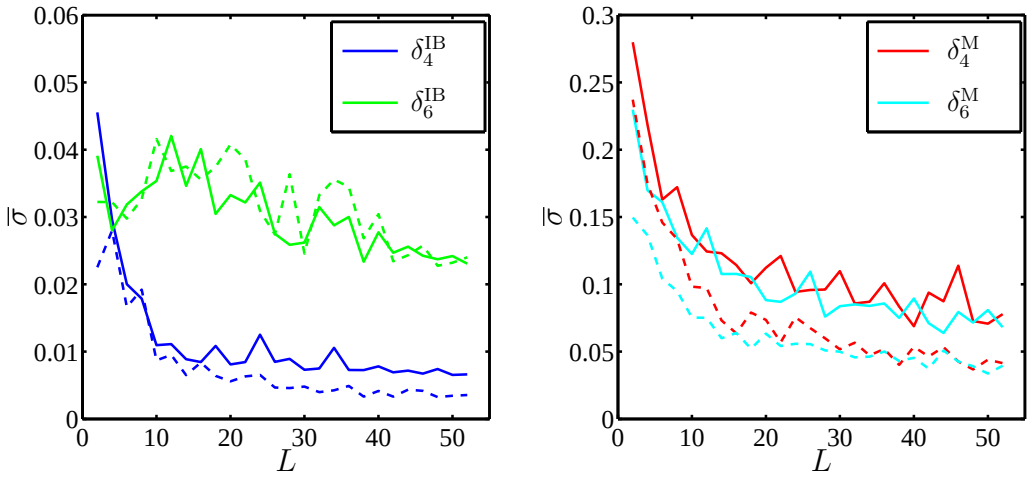


Figure 5.11: Position and orientation dependence of the pseudo-cylinder resistance matrices as a function of the length L at the preferred immersed boundary point density. Solid lines show $\overline{\sigma}$ for the finite difference discretization. Dashed lines show $\overline{\sigma}$ for the spectral discretization. Blue lines show results for δ_4^{IB}, green lines show results for δ_6^{IB}, red lines show results for δ_4^{M}, and cyan lines show results for δ_6^{M}. Note the difference in vertical scale between the plots on the left and those on the right. The delta functions traditionally used in the immersed boundary method (left) result in deviations below 5 percent for the entire range of L. Deviations obtained with the delta functions in the family δ_d^{M} are much larger.

L when using the finite difference discretization. When L is smaller than 10, $\overline{\sigma}$ is greater than 15 percent. In all cases, this is a vast improvement over the values of $\overline{\sigma}$ we obtained for very large values of ρ which were at least 25 percent, even when trimmed to exclude the worst 10 percent of trials.

5.2.3 Comparing to the results for a cylinder

We now investigate whether the mean resistance matrix of a pseudo-cylinder with the preferred choice of N is close to that of a rigid cylinder of some radius r and of length $\tilde{L}$. Unfortunately, no exact solution to the external velocity field of a translating or rotating cylinder has been found, so no exact value for the resistance matrix is available. Instead, we use an approximation from slender-body theory.

$$\begin{aligned}
\mathcal{R}_{11} &= \frac{2\pi\tilde{L}}{\log 2\tilde{L}/r - \frac{3}{2} - (1-\frac{\pi^2}{12})(\log\tilde{L}/r)^{-1}} + O\left[\tilde{L}\left(\log\tilde{L}/r\right)^{-4}\right] \\
\mathcal{R}_{22} = \mathcal{R}_{33} &= \frac{4\pi\tilde{L}}{\log 2\tilde{L}/r - \frac{1}{2} - (1-\frac{\pi^2}{12})(\log\tilde{L}/r)^{-1}} + O\left[\tilde{L}\left(\log\tilde{L}/r\right)^{-4}\right] \\
\mathcal{R}_{44} = \mathcal{R}_{55} &= \frac{\pi\tilde{L}^3/3}{\log 2\tilde{L}/r - \frac{11}{6} - (\frac{10}{9}-\frac{\pi^2}{12})(\log\tilde{L}/r)^{-1}} + O\left[\tilde{L}^3\left(\log\tilde{L}/r\right)^{-4}\right]
\end{aligned} \tag{5.6}$$

The off-diagonal components of $\mathcal{R}$ are all equal to zero. The expressions for the tangential and normal drag are derived in Keller and Rubinow [18]. The expression for rotational drag is derived in Appendix 7.3 using the method presented in their paper. The derivation of the above equations uses a fixed

point iteration to solve approximately the slender-body theory integral equation. For a cylinder, the exact solution of this integral equation may be unphysical because of endpoint problems [16, 14]. Still, equation (5.6) should be a valid approximation, and it is in good agreement with numerical solutions of the Stokes equations as well as experimental results [13]. This approximation is only valid for small $r/\tilde{L}$.

We now consider how to choose the effective radius and effective length of the pseudo-cylinder in our computations for comparison with equation (5.6). For the effective length, we would like to find a correction, $\delta L = \tilde{L} - L$, that is valid for all pseudo-cylinder lengths, L. The obvious approach would be to fit r and δL to the pseudo-cylinder data. However, the sensitivity of the slender-body theory resistance matrix to changes in these quantities is proportional to, respectively, $1/(r \log \tilde{L})$ and $1/\tilde{L}$, which become small as $\tilde{L}$ becomes large. Therefore, the fit of r and δL becomes increasingly sensitive to the pseudo-cylinder resistance matrices as $\tilde{L}$ becomes large. For this reason, we do not fit r and δL. Instead, we use heuristic arguments to arrive at guesses for their values. These guess are then justified by comparing the mean drags of the pseudo-cylinders with equation (5.6).

The first heuristic argument is geometric. Suppose that spheres of radius a are placed in a linear array such that each just touches its neighbor. Suppose now that a cylinder of radius r is of the same length as this array of spheres and also occupies the same volume. The volume of each segment of cylinder of length $2a$ must be the same as the volume of each sphere. The

radius of the cylinder must then be $\sqrt{2/3}\,a$. If L is the distance between the centers of the first and last sphere, then the cylinder will have total length $L + 2a$. We know from the previous section that an immersed boundary point acts approximately like a sphere of radius $\overline{a}$. This suggests that we use $\sqrt{2/3}\,\overline{a}$ as our guess for the effective radius r and $2\overline{a}$ as our guess for the effective length correction δL. This geometric analogy is not perfect, for we have shown that it often optimal to place the immersed boundary points closer together than $2\overline{a}$.

A second heuristic argument confirms the above guess for r. Consider a slender body in Stokes flow whose centerline position is given by $\mathbf{X}(s)$, where s, an arclength parameter, varies from 0 to $\tilde{L}$. The body is locally a cylinder, and its local radius is $r(s)$. The one-dimensional force density applied by the body to the fluid is $\mathbf{F}(s)$. Then, the velocity field can be approximated by the following integral [18, 16, 14].

$$\mathbf{u}(\mathbf{x}) = \int_0^{\tilde{L}} \left(\mathcal{S}_0 \left(\mathbf{x} - \mathbf{X}(s) \right) + \frac{r(s)^2}{2} \mathcal{D}_0 \left(\mathbf{x} - \mathbf{X}(s) \right) \right) \mathbf{F}(s) ds \tag{5.7}$$

The Stokeslet, $\mathcal{S}_0$, is defined in equation (2.10). The doublet, $\mathcal{D}_0$, is defined in equation (5.3). The far-field velocity is the sum of the local contributions of the forces. Each element of force creates a velocity equal to the force multiplied by the Stokeslet plus $r^2/2$ times a doublet, where r is the local radius. Recall from equation (5.4) that the velocity field created by a sphere of radius a is the applied force multiplied by the sum of a Stokeslet and

$a^2/3$ times a doublet. So, the velocity field created by a slender body is asymptotically the same as the sum over s of the velocity fields created by spheres placed along the centerline of the body at $\mathbf{X}(s)$, with radii $a(s) = \sqrt{3/2}\, r(s)$, to which the force density $\mathbf{F}(s)$ is applied. Our pseudo-cylinder is composed of immersed boundary points which act like spheres of radius $\overline{a}$. Therefore, the velocity field it creates will be similar to that of a cylinder of radius $r = \sqrt{2/3}\, \overline{a}$.

In summary, for the purposes of comparing the pseudo-cylinder resistance matrices with equation (5.6), we use $\sqrt{2/3}\, \overline{a}$ for the effective radius, r, and $2\overline{a}$ for the effective length correction, δL, so that $\tilde{L} = L + 2\overline{a}$. These guesses are intuitively reasonable: the effective length of a pseudo-cylinder is slightly larger than the distance between the first and last immersed boundary points by an amount on the order of the effective point radius, and the effective radius of a pseudo-cylinder is also on the order of the effective point radius.

Figure 5.12 shows the mean drags in the tangential, normal, and rotational directions for pseudo-cylinders as functions of length compared with the formulas derived from slender-body theory given in equation (5.6). The slender-body theory results are for for cylinders with lengths $\tilde{L} = L + 2\overline{a}$ and radii $r = \sqrt{2/3}\, \overline{a}$. Note, in particular, that the results shown in figure 5.12 were obtained without any additional adjustment of parameters. Agreement is nearly perfect, except at very small values of L, for which slender-body theory does not give an accurate approximation. The differences at larger values of L are on the order of the error term term for the slender-body

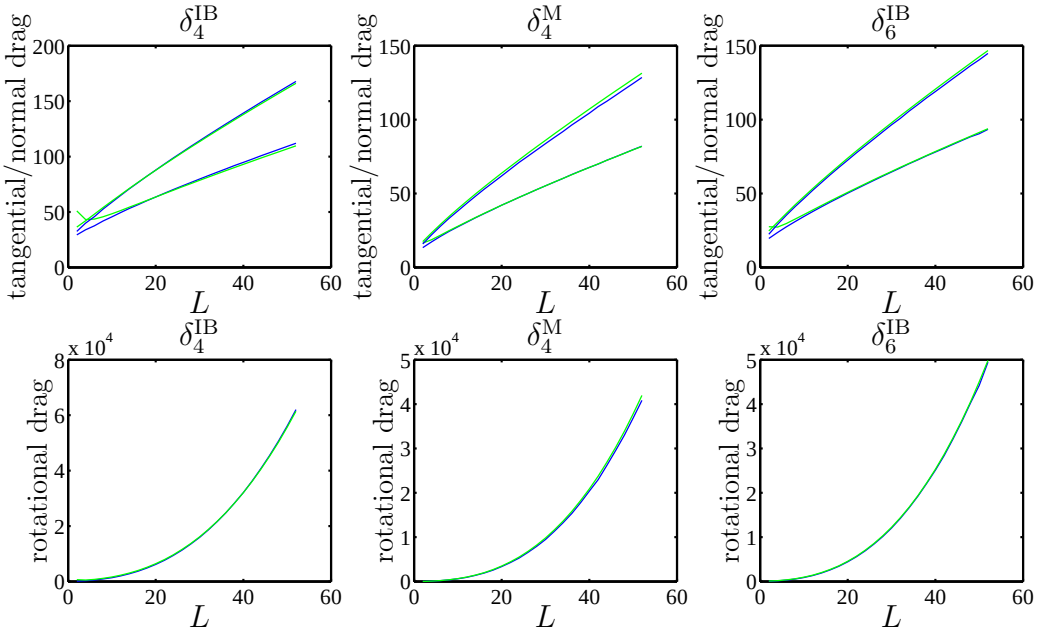


Figure 5.12: Mean drag on a pseudo-cylinder as a function of length compared to formulas from slender-body theory (equation (5.6)) for various delta functions and the finite difference discretization. The pseudo-cylinder results are shown by blue lines. The slender-body theory formulas are shown by green lines. The top row of plots shows drag in the tangential and normal directions. In all cases, normal drag is larger than tangential drag. (It is customary to say that the normal drag is twice the tangential drag, but this, in fact, is only true in the limit $\tilde{L} \to \infty$, and that limit is approached only slowly. See equation (5.6).) The bottom row shows drag in the rotational direction. Agreement is very good except at very small lengths, for which the slender-body theory formulas are not accurate.

theory approximation. Results for other delta functions and for the spectral discretization (not shown) are similar to those in figure 5.12.

To quantify the differences between $\mathcal{R}_{\text{mean}}$ and the resistance matrices implied by the slender-body theory formulas, $\mathcal{R}_{\text{sb}}$, we define $\epsilon = \|\mathcal{R}_{\text{sb}}^{-1/2}\mathcal{R}_{\text{mean}}\mathcal{R}_{\text{sb}}^{-1/2} - \mathcal{I}\|$. Figure 5.13 shows ϵ as a function of L for various delta functions and the finite difference discretization. The relative differences are under 5 percent except when L is small and slender-body theory is not valid. The differences are somewhat, but not substantially smaller for the delta functions traditionally used in the immersed boundary method as opposed to those in the family δ_d^{M}. The behavior of ϵ as $L \to \infty$ cannot be seen clearly in figure (5.13). We attempt to elucidate this behavior in section 5.2.5, in which we investigate very large values of L.

We conclude that, regardless of the delta function or discretization method, a linear array of immersed boundary points that are constrained to move as a rigid body have a mean resistance matrix very similar to that of a cylinder of length $\tilde{L} = L + 2\overline{a}$ and radius $r = \sqrt{2/3}\,\overline{a}$. This conclusion depends on our having chosen the correct density of immersed boundary points. We chose either 1.0 or $1.0/\overline{a}$, but any value in the preferred range would suffice. If we, however, had chosen a larger density, we would have gotten mean drags that were too large, as can be seen in figures 5.7, 5.8, and 5.9.

Even though the mean resistance matrix of a pseudo-cylinder is close to that of an actual cylinder for all the delta functions and discretization methods that we test, the position and orientation dependence of the resistance

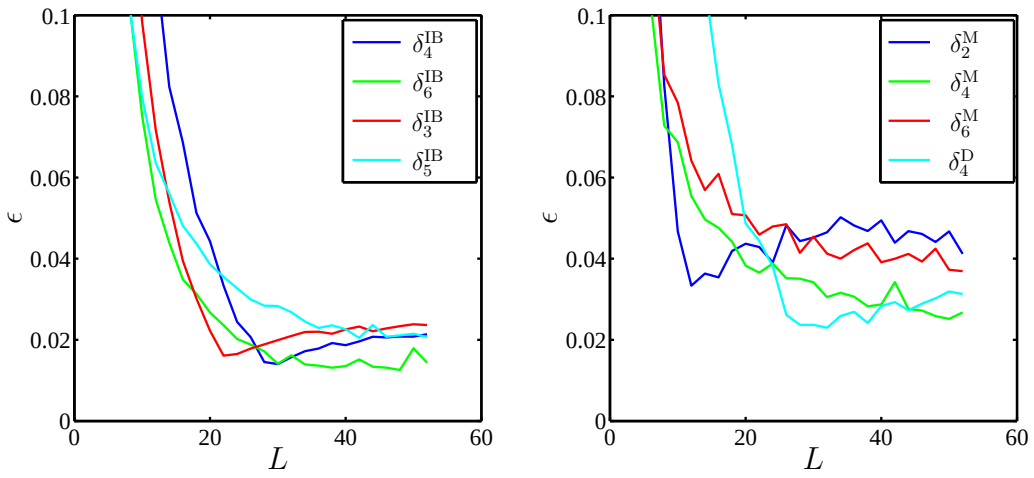


Figure 5.13: Norm of the difference between the mean resistance matrix of a pseudo-cylinder and the resistance matrix obtained from the slender-body theory formulas as a function of length for various delta functions. The difference is small for all delta functions except at small lengths where slender-body theory is invalid.

matrix is larger for those delta functions in the family δ^{M} and also for δ_4^{D}. If those delta functions traditionally used in the immersed boundary method, δ^{IB}, are employed, the resistance matrix accurately matches that of a cylinder and also is essentially independent of the position and orientation of the pseudo-cylinder, as desired.

5.2.4 Comparing velocity fields

As a final test, we examine the external velocity fields created by a pseudo-cylinder and compare with slender-body theory. We specify the velocities of the immersed boundary points, $\mathbf{U}(\mathbf{q})$, so that $\mathbf{U}$ is a standard basis element in the space of rigid body motions, V. The unique force that will produce this motion, by equation (2.32), is $\mathbf{F} = \mathcal{G}^{-1}\mathbf{U}$. The decomposition of $\mathbf{F}(\mathbf{q})$ into applied force and constraint force is arbitrary, provided that there is no net force or torque applied by the constraint force. Once we have found $\mathbf{F}(\mathbf{q})$, we may find the velocity $\mathbf{u}$ at any grid point using equations (2.24) and (2.26).

We compute $\mathbf{u}$ at every grid point in a large rectangular box surrounding a pseudo-cylinder. We perform these computations for the particular choice of $L = 30$ and, for ease of visualization, we use a pseudo-cylinder whose tangent and normal vectors are aligned with the grid. The mean position, $\mathbf{X}_0$, is chosen randomly. We report results only for the finite difference discretization and for the delta function δ_4^{IB}. For this delta function and discretization method, we use 25 immersed boundary points, which best approximates a

density of $1/\overline{a}$. Results with other delta functions and discretization methods are similar.

There is no known exact solution for the velocity field created by a cylinder undergoing rigid motion, so we compare the velocity field of a pseudo-cylinder with the approximation from slender-body theory. The slender body has the same position and orientation as the pseudo-cylinder, but extends past the endpoints of the pseudo-cylinder by a distance $\overline{a}$ on each side. We specify the velocity of the cylinder to be a rigid body motion. The force density $\mathbf{F}(s)$ is determined by approximately solving an integral equation using a fixed point iterative method as described in [18]. We then use quadrature to compute the slender-body velocities, according to equation (5.7), at the same set of grid points for which velocities are computed for the pseudo-cylinder. We denote these velocities by $\mathbf{u}^{\mathrm{SB}}$, which we compare to the pseudo-cylinder velocities $\mathbf{u}$. Equation (5.7) is only valid in the exterior of the cylinder, and we set $\mathbf{u}^{\mathrm{SB}}$ to be the exact rigid body motion velocity inside the cylinder.

Figures 5.14, 5.15, and 5.16 show two dimensional slices of $\mathbf{u}$ (top) and $\mathbf{u}^{\mathrm{SB}}$ (bottom) for cylinders moving in the the tangential, normal, and rotational directions. In each case, the velocities have been modified by subtracting a solution of the Stokes equations so that we depict the velocity field created by a fixed rigid cylinder in an incident flow from infinity. The red rectangle in these plots shows the intersection of the two-dimensional plane depicted with the surface of a cylinder of radius r and length $\tilde{L}$. The rectangle is the effective surface of the pseudo-cylinder in this plane.

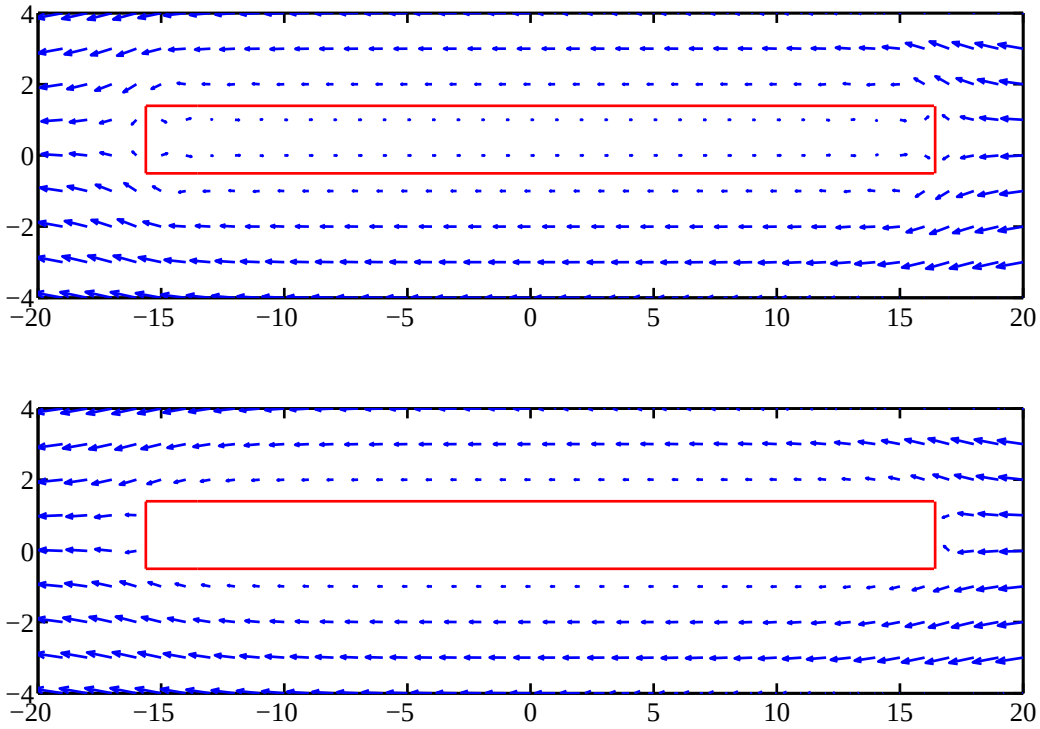


Figure 5.14: Top: two-dimensional slice of the three-dimensional velocity field created by a pseudo-cylinder moving in the tangential direction. For clarity, the velocity has been translated so that the pseudo-cylinder is fixed and there is an incoming flow at infinity along the axis of the pseudo-cylinder. The red rectangle indicates the effective surface of the pseudo-cylinder. Note that the velocity is nearly zero on the effective surface of the pseudo-cylinder as dictated by the no-slip condition, and that the velocity is small inside the effective surface. Bottom: the slender-body theory approximation to the velocity field of a cylinder of radius r and length $\tilde{L}$ moving in the tangential direction. The velocity is defined to be identically zero inside the surface of the cylinder. The velocities near the endpoints of the cylinder may not be accurate.

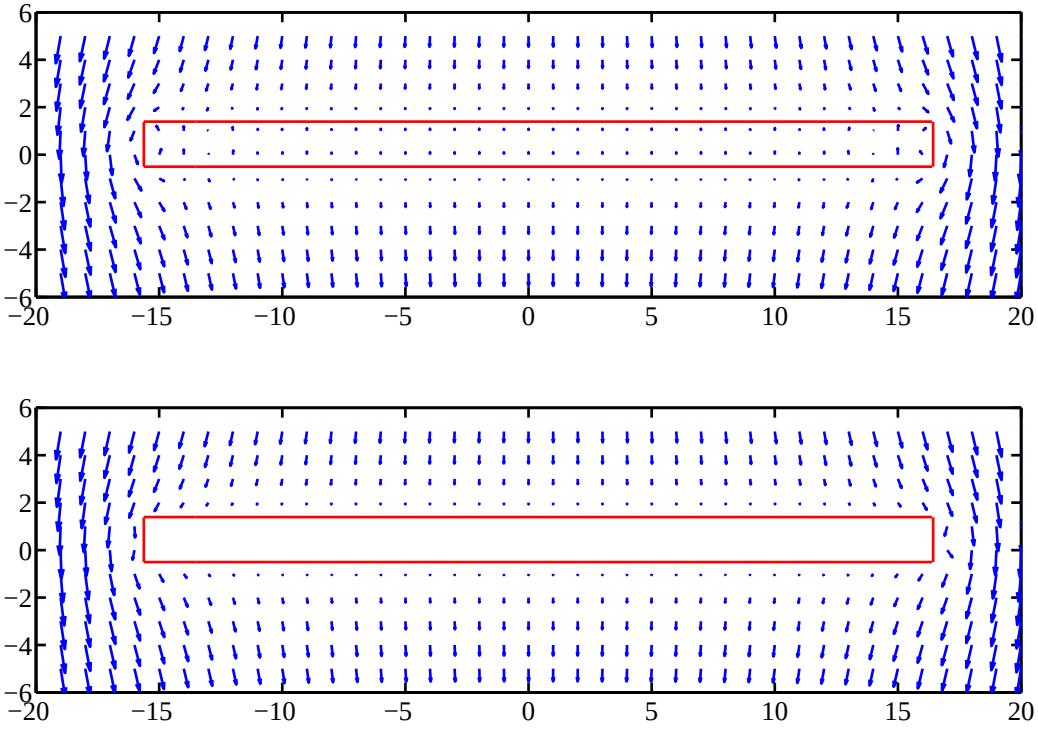


Figure 5.15: The velocity field of a pseudo-cylinder (top) and the slender-body theory approximation to the velocity field of a cylinder (bottom) held fixed with an incoming flow in the normal direction from infinity.

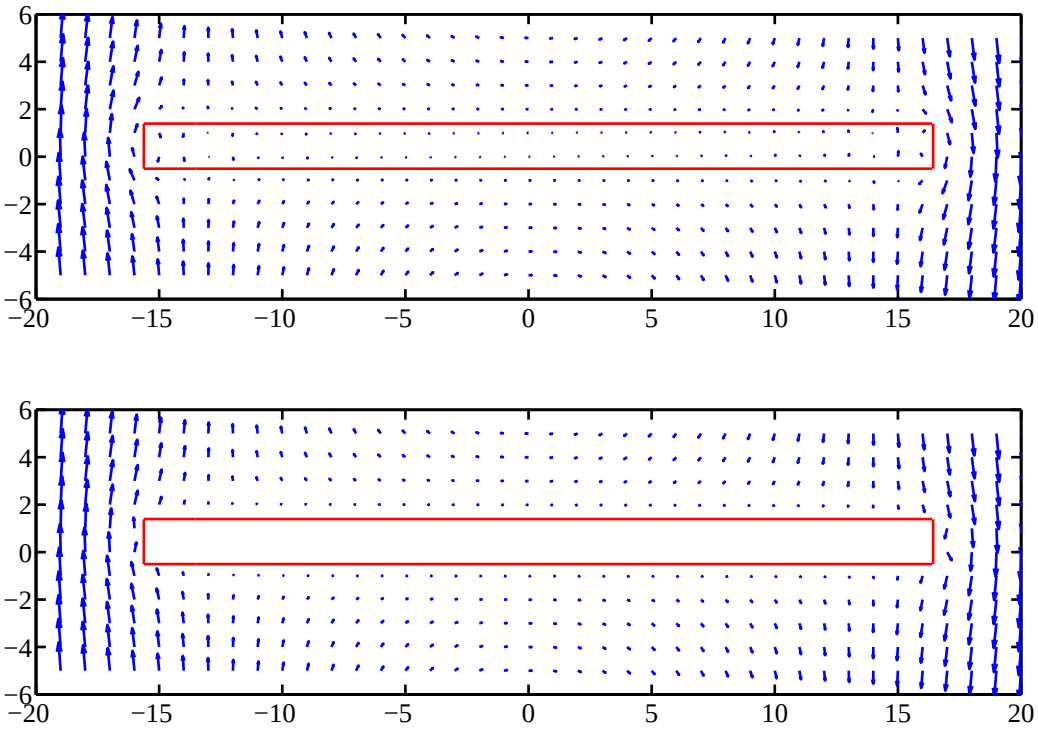


Figure 5.16: The velocity field of a pseudo-cylinder (top) and the slender-body theory approximation to the velocity field of a cylinder (bottom) held fixed with an incoming linear shear flow from infinity.

In each figure, the two velocity fields are very similar. Qualitatively, $\mathbf{u}$ appears to be close to zero on the effective surface of the pseudo-cylinder, as dictated by the no-slip condition, and to be nearly zero inside the surface. Larger, non-zero velocities appear near the endpoints of the cylinder. Pictorially, the effective length of the psuedo-cylinder $\tilde{L}$, which is the length of the red box, seems to be a good choice, as does the effective radius r. The slender-body theory approximation, $\mathbf{u}^{\mathrm{SB}}$ is identically zero inside the cylinder's surface, but appears to take several slightly unusual values near the endpoints of the cylinder. Indeed, slender-body theory is not valid near these points [16].

To compare $\mathbf{u}$ and $\mathbf{u}^{\mathrm{SB}}$ quantitatively, we want to exclude the difference that comes from the different total forces or torques being applied to the fluid in each case, which come about because of the small differences in drags described above. To exclude this source of difference between $\mathbf{u}$ and $\mathbf{u}^{\mathrm{SB}}$, we normalize each by the appropriate drag (tangential for tangential motion, etc.). For translational motion, we are comparing velocity fields that arise from the same total force applied to the fluid, and for rotational motion, we are comparing velocity fields that arise from the same total torque applied to the fluid. We calculate the relative difference $|\mathbf{u}-\mathbf{u}^{\mathrm{SB}}|/|\mathbf{u}^{\mathrm{SB}}|$ and calculate the L_2 average of this quantity on rectangular shells of grid points surrounding the cylinder. On each shell, the infimum of $\|\mathbf{x}-\mathbf{X}(s)\|_\infty$ over s is approximately constant, and we calculate the L_2 average of this quantity. Note that this is the distance of the shell from the axis of the cylinder, not

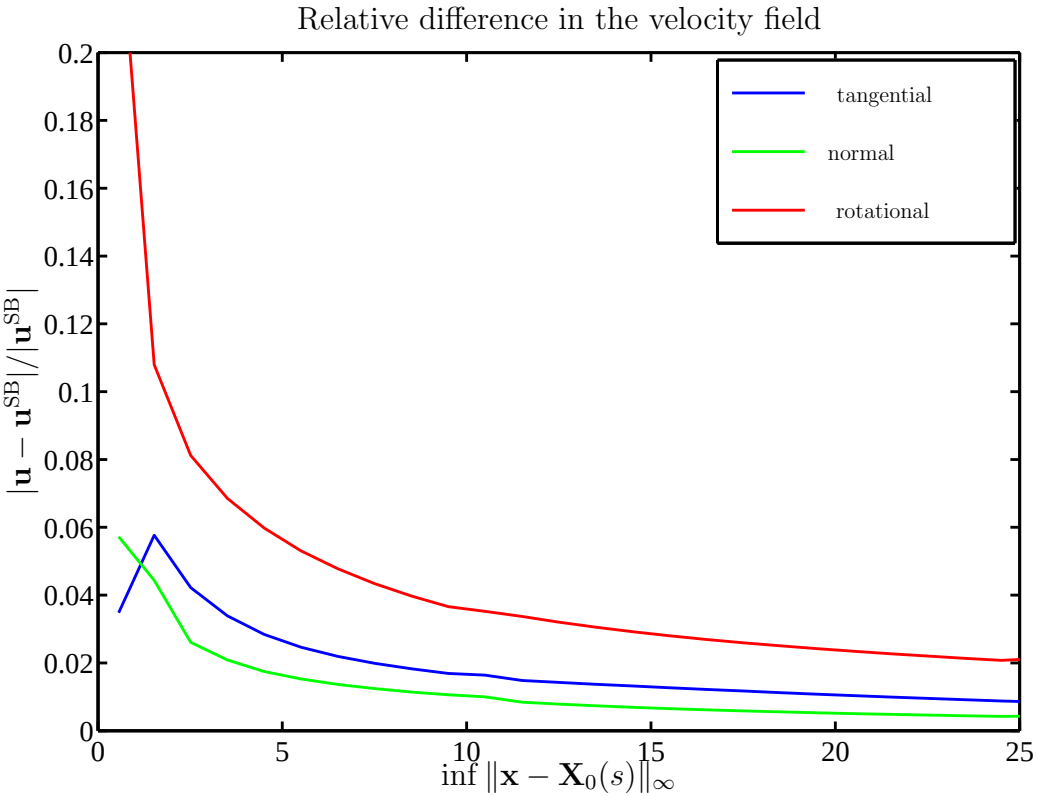


Figure 5.17: This plot compares the velocity fields created by a pseudo-cylinder in the immersed boundary method and the slender-body approximation given in equation (5.7). Motion is in the tangential (blue), normal (green), and rotational (red) directions. We have used δ_4^{IB} and the finite difference discretization. Shown is the relative difference in these fields, plotted against distance from the axis of the cylinder in the infinity norm. These quantities have been averaged in the L_2 sense over rectangular shells of grid points. Even for the worst case, which is rotational motion, the relative difference is 11 percent at a distance of 1.5 grid cells from the axis of the cylinder, and quickly decays to 2 percent at a distance of twenty-five grid cells. For the translational cases, relative difference is small even inside the surface of the cylinder.

from the cylinder's surface.

Figure 5.17 shows the average relative difference in $\mathbf{u}$ and $\mathbf{u}^{\mathrm{SB}}$ over a shell as a function of the average infinity norm distance of the shell from the axis of the cylinder. The solid line is for translational motion tangential to the cylinder's axis, the dashed line is for translational motion normal to the cylinder's axis, and the dotted line is for rotational motion. In the translational cases, the relative difference in the velocity fields is below 6 percent even up to and inside the surface of the cylinder. This difference decays rapidly as the rectangular shell of grid points gets farther from the cylinder. The relative difference in the rotational case is larger, but is still below 11 percent everywhere in the exterior of the surface of the cylinder. This difference also decays rapidly, becoming 2 percent at a distance of twenty-five grid cells.

We conclude that the velocity fields created by a pseudo-cylinder are close to the slender-body theory approximations for the velocity fields, which are presumably close to the velocity fields created by an actual cylinder. As a result, the interactions of a pseudo-cylinder with external bodies in the fluid will be similar to the interactions of a cylinder with those bodies. We saw above that the resistance matrix which describes the self-interaction of a pseudo-cylinder is close to that of an actual cylinder and is independent of the cylinder's position and orientation. We conclude that an array of immersed boundary points that is constrained to move as a rigid body is in fact a good representation of a cylinder in all possible respects.

We have shown that when h is 1, a pseudo-cylinder made up of immersed

boundary points spaced evenly over a distance L interacts with the fluid like a cylinder of radius $r = \sqrt{2/3}\,\overline{a}$ and length $\tilde{L} = L + 2\overline{a}$. When h is arbitrary, a pseudo-cylinder made up of immersed boundary points spaced evenly over a length L will interact with the fluid like a cylinder of radius $\sqrt{2/3}\,h\overline{a}$ and length $L+2h\overline{a}$. The total number of immersed boundary points will scale with h^{-1} if kept at constant density with respect to the grid. If one wishes to represent a rigid cylinder of radius r_{C} and length L_{C} by an array of immersed boundary points and one has chosen a delta function and discretization method, then one should first find the effective radius, $\overline{a}$, of a single immersed boundary point that represents a sphere as described above. A cylinder made up of these delta functions will have an effective radius of $\sqrt{2/3}\,h\overline{a}$, so one should set $h = \sqrt{3/2}\,r_{\mathrm{C}}/\overline{a}$. One should space the immersed boundary points evenly over a distance $L_{\mathrm{C}} - 2h\overline{a}$, and one should choose a density of points in the preferred range, with two possible good choices being $1.0/h$ and $1/\overline{a}h$. The total number of points will be approximately L_{C}/h or $L_{\mathrm{C}}/(h\overline{a}) = \sqrt{2/3}\,L_{\mathrm{C}}/r_{\mathrm{C}}$.

We refer to table 5.1 for a list of effective radii for various delta functions and discretization methods. We have found that $1.0/\overline{a}h$ is close to the ideal density of immersed boundary points for the delta functions δ_4^{IB} and δ_4^{D}, and that $1.0/h$ is close to the ideal density for the remaining delta functions that we tested.

5.2.5 Results for very long cylinders

Previously in this chapter, we restricted ourselves to values of L, the pseudo-cylinder length, that were less than or equal to 50. We computed the resistance matrix of a configuration of immersed boundary points by first computing $\mathcal{G}(\mathbf{X}(\mathbf{q}), \mathbf{X}(\mathbf{q}'))$ for all pairs of points. $\mathcal{G}$ was computed by the naive method described in chapter 2. For the computations, we needed values of the discrete Stokeslet, $\mathcal{S}(\mathbf{x})$, which were computed by quadrature. We were restricted to $L \leq 50$ because we had tabulated values of $\mathcal{S}(\mathbf{x})$ only for $\mathbf{x}$ having integer components with magnitudes less than or equal to 60 (recall that $h = 1$).

We would like to be able to test longer pseudo-cylinders for several reasons. We might like to simulate slender bodies with aspect ratio larger than 50, or we might like to simulate multiple bodies in which the immersed boundary points that make up the bodies are sometimes farther apart than 50 grid cells. We would also like to investigate the convergence of our results for slender cylinders as the aspect ratio of the cylinders goes to infinity.

In chapter 3, we developed asymptotic methods that allow us to efficiently compute $\mathcal{S}(\mathbf{x})$ for the spectral method when $\mathbf{x}$ has components with arbitrarily large values. We also developed methods to efficiently compute $\mathbf{G}(\mathbf{X}, \mathbf{X}')$ with $\mathbf{X} - \mathbf{X}'$ having arbitrarily large components. These methods allow us to perform computations with many more immersed boundary points, even when the discrete delta function has a larger support width. In this section, we use these methods to compute the resistance matrices of pseudo-cylinders

with much larger aspect ratios than we could use previously.

To perform computations, we repeat the procedure that we used for smaller values of L. We compute the resistance matrices of a large number (100) of pseudo-cylinders with randomly chosen positions and orientations relative to the grid. We use values of L from 50 up to 1000. The procedure for doing the asymptotic computations is described fully in chapter 3. We set tolerances so that the relative errors in the computed values of $\mathcal{G}(\mathbf{X}, \mathbf{X}')$ should be below 10^{-8}. The condition numbers of the full matrix $\mathcal{G}$ are small enough at the densities we test that the relative errors in the resistance matrices will also be small. Instead of testing all values of the immersed boundary point density, ρ, between 0 and 3, we test values of ρ equal to the preferred density as determined above as well as two and three times the preferred density. We test the same collection of delta functions as we used in the previous section. We use only the spectral discretization method, because using this method allowed us to develop our asymptotic formulas for $\mathcal{S}$ and $\mathcal{G}$ in chapter 3.

We compute σ, the measure of position and orientation dependance, as in equation (5.5) and we let $\overline{\sigma}$ be the maximum of σ over the many trials. We, as before, let the effective radius r be $\sqrt{2/3}\overline{a}$ where $\overline{a}$ is the effective radius of a sphere for the particular choice of delta function. We let the effective length correction δL be $2\overline{a}$. We compute the resistance matrix implied by the slender-body formulas, equation (5.6), using these parameters. We let ϵ be the relative difference between the slender-body theory resistance matrix

and the mean resistance matrix found in our trials.

We first examine the dependence of the computed drags on the position and orientation of the pseudo-cylinders with respect to the grid. Figure 5.18 shows $\overline{\sigma}$ for various delta functions as a function of the pseudo-cyliinder length. Those delta functions traditionally used in the immersed boundary method are shown on the left. Higher moment order delta functions as well as the dilated function δ_4^{D} are shown on the right. The errors are smallest for the 3 and 4 point (meaning support width 3 and 4) delta functions traditionally used in the immersed boundary method. The errors are somewhat larger for the 5 and 6 point delta functions traditionally used in the immersed boundary method. The errors are a bit larger still for the 4 and 6 point delta functions with maximal interpolation order, and the errors are largest for the 2 point delta function.

Because figure 5.18 is somewhat messy for the delta function of maximum moment order, we also show the mean value of σ obtained over our many trials in figure 5.19. We conclude similarly that the 3 and 4 point delta functions traditionally used in the immersed boundary method show extremely small position and orientation dependence. The other delta functions have approximately the same position and orientation dependence when the mean of σ is considered. We saw above that when the maximum of σ is considered, the delta functions traditionally used in the immersed boundary method perform somewhat better.

In the previous section, we showed that there exists an ideal range of

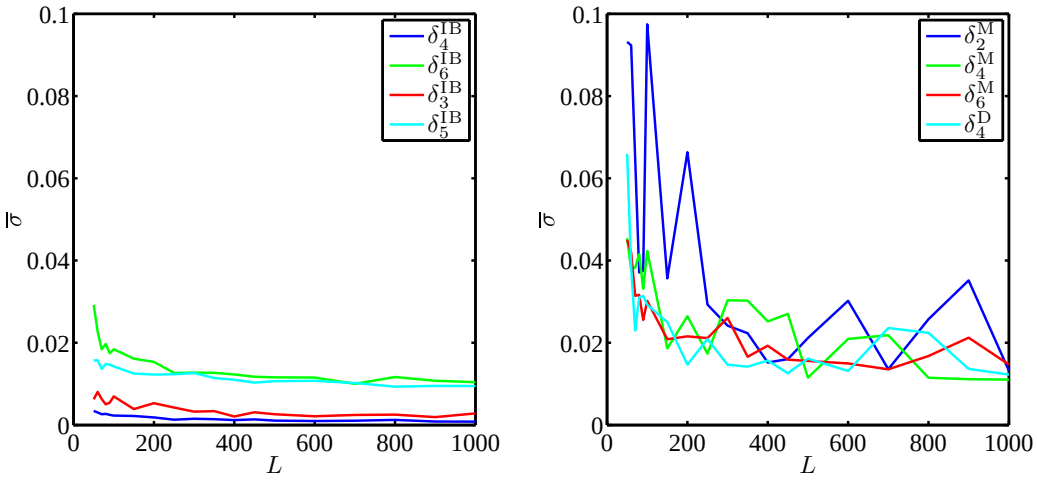


Figure 5.18: Position and orientation dependence of the pseudo-cylinder resistance matrices as a function of the length L at the preferred immersed boundary point density for very large values of L. The quantity $\overline{\sigma}$ is a measure of maximum relative deviation (see equation (5.5)). Results are shown for various delta functions and for the spectral discretization method. Those delta functions traditionally used in the immersed boundary method, shown on the left, generally perform better than those with maximum interpolation order, shown on the right.

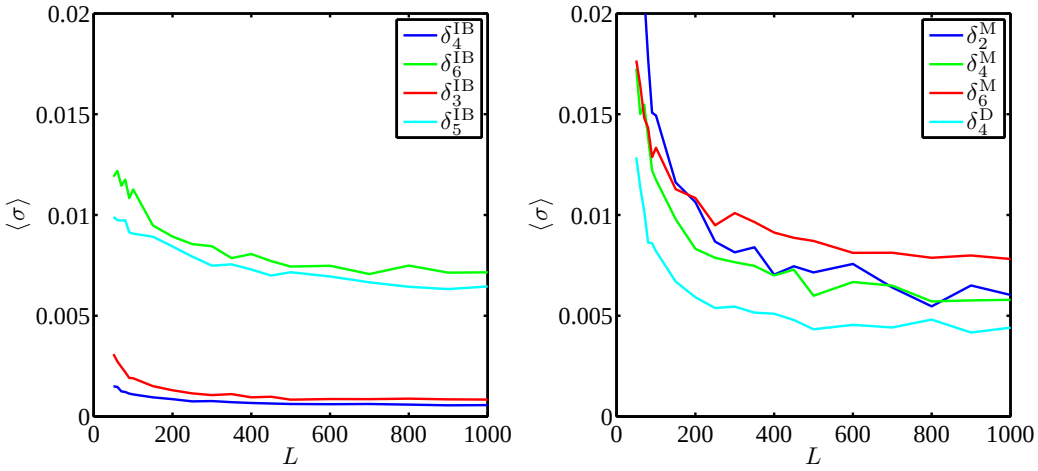


Figure 5.19: Same as the plot above, except the mean value of σ, the measure of position and orientation dependance, is shown instead of the maximum. Again, those delta functions traditionally used in the immersed boundary method, shown on the left, generally perform better than those with maximum interpolation order, shown on the right.

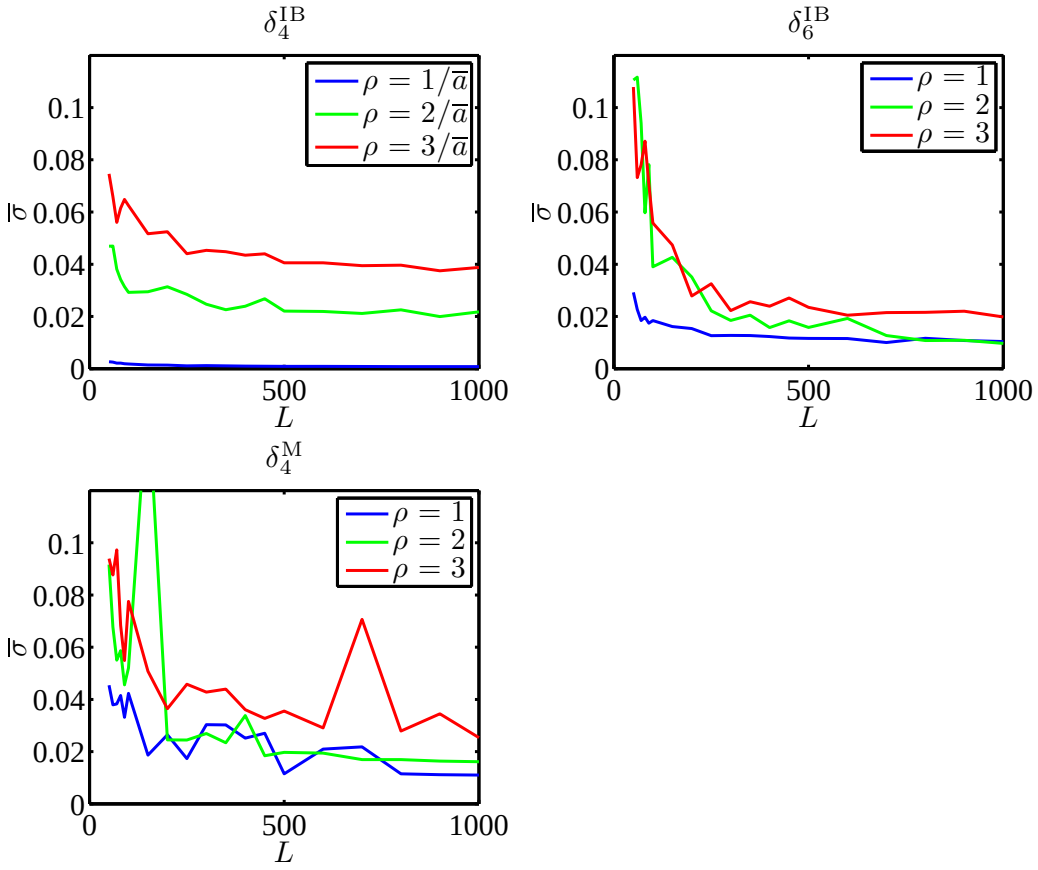


Figure 5.20: Position and orientation dependence of the pseudo-cylinder resistance matrices as a function of the length L for very large values of L. This plot compares $\overline{\sigma}$ for the preferred immersed boundary point density, with $\overline{\sigma}$ for double and triple the preferred density for various delta functions. Using a higher density of immersed boundary points results in greater position and orientation dependence. For the delta function δ_4^{IB}, σ was so large for some trials that we plot the maximum of σ excluding the largest 5 percent of trials.

densities of immersed boundary points in a pseudo-cylinder. Too many points resulted in greater position and orientation dependence of the drag coefficients. Figure 5.20 confirms that this conclusion continues to hold for pseudo-cylinders of very large aspect ratios. Shown are values of $\overline{\sigma}$ computed for various pseudo-cylinder lengths, L, using various delta functions, and using 3 different values for the density of immersed boundary points: the density suggested in the previous section (shown in blue), twice that density (shown in green), and three times that density (shown in red). For the delta function, δ_4^{IB}, we found very large values of $\overline{\sigma}$ at higher densities, so we actually plot the maximum of σ trimmed of the largest 5 percent of trials. Still, for this delta function in particular, higher densities of immersed boundary points resulted in larger position and orientation dependencies. The same conclusion holds, for the other two delta functions shown, though not as dramatically.

We now compare the average resistance matrices found for the pseudo-cylinders with results from slender-body theory. Figure 5.21 shows the mean drag coefficients in the tangential, normal, and rotational direction that we compute for pseudo-cylinders of various lengths and using various delta functions. These are shown by the blue lines and are compared with the slender-body theory formulas for these drag coefficients shown by green lines. In the figures showing normal and tangential drag, the normal drag is always greater. The immersed boundary method and slender body theory give nearly identical results in all cases.

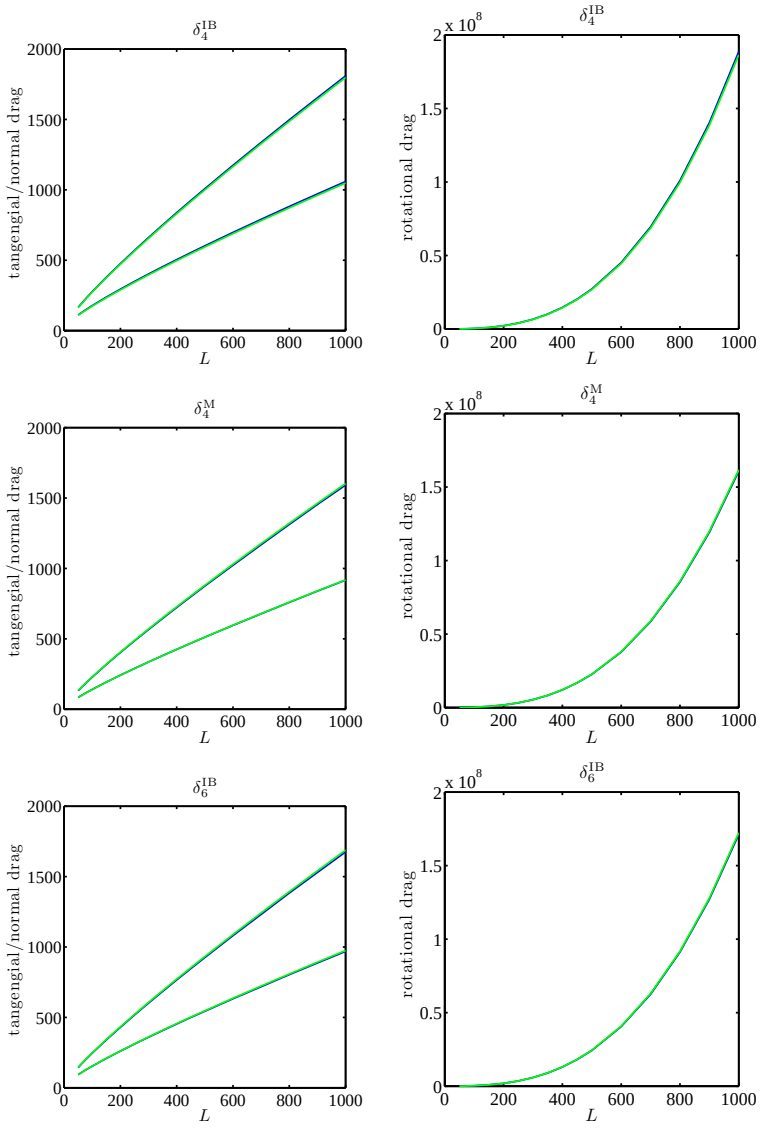


Figure 5.21: Results for large values of L computed by asymptotic methods. Mean drag on a pseudo-cylinder as a function of length compared to formulas from slender-body theory (equation (5.6)) for various delta functions and the spectral discretization. The pseudo-cylinder results are shown by blue lines. The slender-body theory formulas are shown by green lines. The left column of plots shows drag in the tangential and normal directions. In all cases, normal drag is larger than tangential drag. The right column shows drag in the rotational direction.

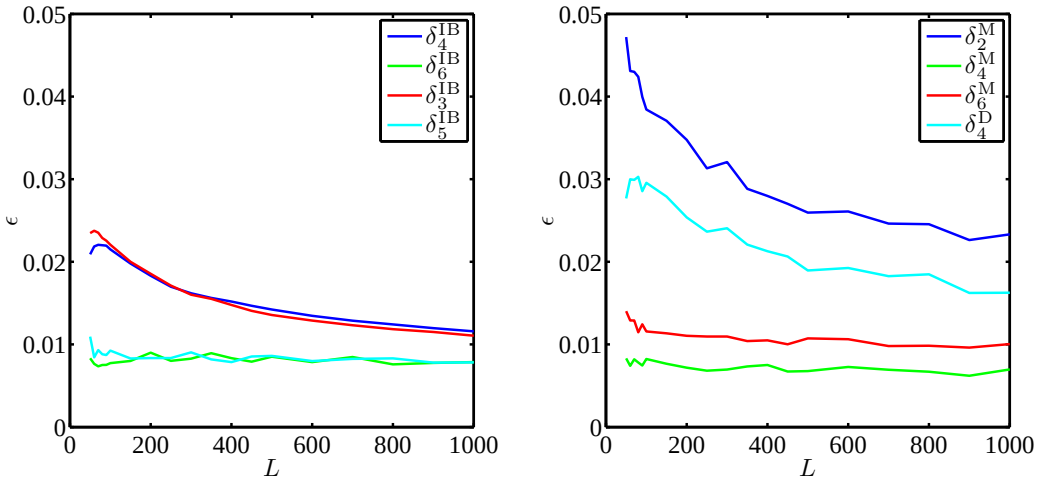


Figure 5.22: Norm of the difference between the mean resistance matrix of a pseudo-cylinder and the resistance matrix obtained from the slender-body theory formulas, ϵ, as a function of length for various delta functions and for very large values of L.

Figure 5.22 shows the relative difference between the mean resistance matrices found for the pseudo-cylinders and the resistance matrices obtained by the slender-body theory formulas. For all delta functions, the errors are small. In some cases, they appear to be decaying as L becomes large. In others, it is not clear whether they will decay to 0 as $L \to \infty$. If these errors were to decay to 0, we expect decay rates no faster than $1/\log L$, which is not necessarily inconsistent with this figure.

Previously, we chose not to fit the parameters r and δL to the computed resistance matrices because the sensitivities of these fits grows unboundedly as L becomes large. Instead, we chose r and δL based on heuristic, geometric arguments, and we found values that work quite well. Here, we test our earlier approach by fitting r and δL so as to minimize ϵ, the relative error in the computed average resistance matrix of the pseudo-cylinders compared with the slender-body theory formulas. Figure 5.23 shows the fit values of r and δL as a function of L for various delta functions. The previously used values of r and δL for the delta function δ_4^{IB} are respectively 1.07 and 2.63; the values for the delta function δ_6^{IB} are 0.69 and 1.68; the values for the delta function δ_4^{M} are 0.47 and 1.14. In all three plots in this figure, we see that the radius r does not vary much and is close to the value we used previously. However, the values of δL do not seem to converge as L becomes very large. For the delta function δ_4^{M}, the optimal δL actually becomes negative, which is unphysical.

Figure 5.24 shows the minimized value of ϵ obtained by optimizing r and

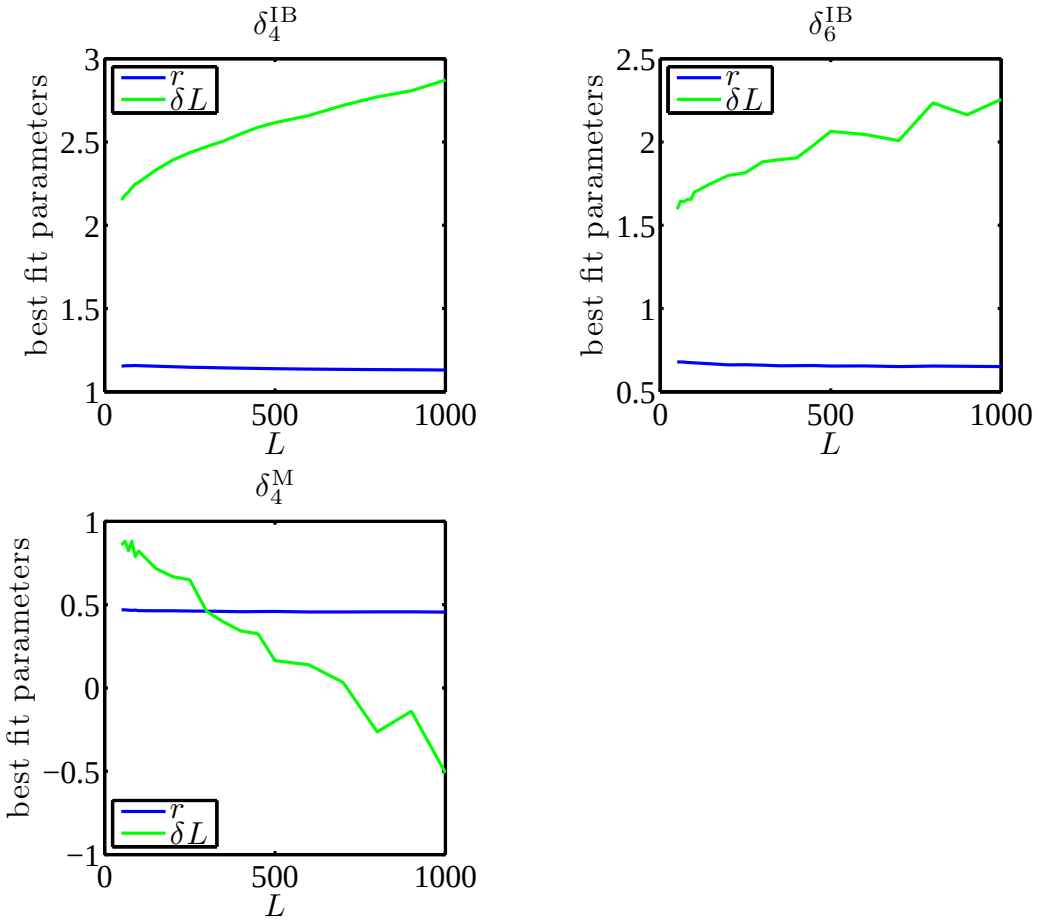


Figure 5.23: Best fit values of the pseduo-cylinder radius, r, and effective length correction, δL, for very large values of L and for various delta functions.

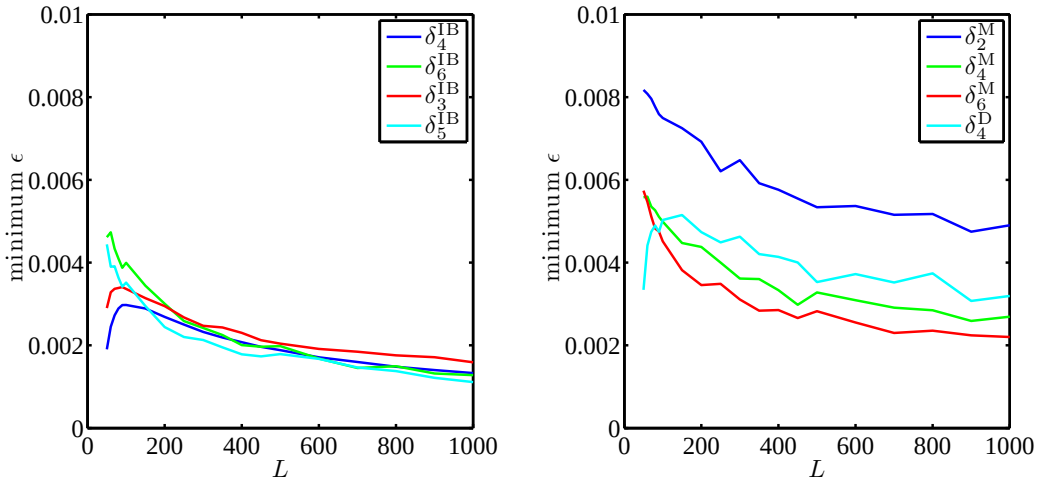


Figure 5.24: Norm of the difference between the mean resistance matrix of a pseudo-cylinder and the resistance matrix obtained from the slender-body theory formulas, ϵ, when the best fit values of r and δL are used as the parameters in the slender-body theory formulas. By best fit, we mean those values which minimize ϵ. The minimized value of ϵ is shown as a function of L for very large values of L.

δL for a variety of delta functions. This minimum does appear to converge to zero as $L \to \infty$, which we may take as a sign that as the aspect ratio of the pseudo-cylinders becomes very large, the resistance matrix converges to the resistance matrix of some slender cylinder. However, we do not have evidence that δL will also converge, so the optimal cylinder that the pseudo-cylinder is converging to has a length which depends in a more complicated fashion on L than simply $L + \delta L$ for some fixed δL. It does appear that the optimum effective radius r converges.

These optimized values of ϵ are smaller by a factor of 5 to 10 than the values of ϵ found by using the parameters r and δL found from heuristic, geometric arguments. While this is an improvement, it is not extremely significant, and the fact that δL does not converge and is negative for some delta functions casts doubt on our approach. For practical reasons, we would like a simple relationship to hold between the distance between the endpoints of a pseudo-cylinder, L, and its effective length. We would also like a simple, L independent, characterization of the effective radius of a pseudo-cylinder. Simple formulas for r and δL do not need to be retested for every new length of pseudo-cylinder we want to represent or every new delta function we wish to use. Also, simple characterizations of r and δL are more likely to be robust when non-rigid slender bodies are modeled.

We would like claims that for the heuristic values of r and δL, $\epsilon \to 0$ as $L \to \infty$. If, in fact, ϵ does converge to zero, then the pseudo-cylinder will, asymptotically, have the same mean resistance matrix as a cylinder. This is

because the slender-body theory resistance matrix is asymptotically that of a cylinder. If the position and orientation dependence, $\overline{\sigma}$, also converges to zero as figure 5.18 seems to indicate, then the pseudo-cylinder will asymptotically have the same resistance matrix as a cylinder, regardless of its position and orientation relative to the grid. As in slender-body theory, the asymptotic convergence is in the limit of the aspect ratio $r/\tilde{L}$ decreasing to zero. In particular, this asymptotic convergence will occur for a pseudo-cylinder of fixed length in the limit as the grid spacing decreases to zero. Unless we have chosen the effective radius r exactly correctly, the best convergence rate that we can obtain for the relative error in the resistance matrix is $O([\log(L/r)]^{-1})$. This rate seems consistent with the results in figure 5.22, but the results are not conclusive.

We have found in this section that our conclusions for pseudo-cylinders with shorter aspect ratios hold also for pseudo-cylinders with very large aspect ratios. If the appropriate density of immersed boundary points is used, the drag coefficients of the cylinders show little dependence on the position and orientation of the cylinders relative to the Cartesian fluid grid. If too large of a density of points is used, we observe significantly greater position and orientation dependence of the drag coefficients. We choose the effective radius and length of the pseudo-cylinders based on geometric arguments, and the computed drag coefficients of the pseudo-cylinders are very close to those predicted by slender body theory for rigid cylinders with the chosen effective lengths and radii. These conclusions hold for all delta functions that we

test, though the position and orientation dependence is generally smaller for those delta functions traditionally used in the immersed boundary method than for those with maximal interpolation order. We conclude that an array of immersed boundary points constrained to move as a rigid body is an accurate way to represent a rigid cylinder in the immersed boundary method of a particular radius and length if parameters are chosen appropriately. We show how to choose parameters and specify the dimensions of the cylinder represented. Our results should therefore be useful to practitioners who wish to represent slender bodies or fibers in their immersed boundary method simulations.

Chapter 6

Conclusion

6.1 Conclusion

We have developed a numerical method for immersed boundaries in Stokes flow on an infinite domain that solves the discretized equations using their Green's function. This method allows us to calculate the resistance matrix of a rigid body comprised of an arbitrary configuration of immersed boundary points, as well as the fluid velocity field created by a moving body.

We have applied this method to two simple configurations of immersed boundary points that are commonly used, a single point that is meant to represent a spherical particle, and a linear array of points that is meant to represent a slender cylinder. We have found, in both cases, that with the appropriate choice of parameters, these representations are accurate, and their interactions with the fluid are independent of position and, in the case

of the cylinder, independent of orientation with respect to the Eulerian grid.

Our results should be useful to those who perform computations involving spheres and slender bodies in the immersed boundary method, not only because we validate the approach of using a simple, efficient representation, but also because we prescribe specific choices of parameters. The Eulerian grid spacing must be proportional to the physical radius of the spheres or slender bodies simulated and we specify the constants of proportionality for a variety of delta functions in Table 5.1. The immersed boundary points in an array should have spacing approximately equal to one grid space. If too few or too many points are used, significant dependencies on position and orientation with respect to the Eulerian grid result. Finally, we do not detect a qualitative difference between using a finite difference and a spectral discretization for the the fluid equations, but we have shown that errors are much smaller if the approximate delta functions traditionally used in the immersed boundary method are employed as opposed to higher order delta functions with the same support.

We conjecture that the relative error associated with the representation of a cylinder by an array of immersed boundary points approaches zero in the limit as the aspect ratio, the ratio of the cylinder's length to its radius, goes to infinity. If this turns out to be the case, then the simple representation of a cylinder in the immersed boundary method will be asymptotically accurate in the same way that slender-body theory is asymptotically accurate.

Our numerical method may be used to perform dynamic simulations of

rigid or elastic bodies in Stokes flow in an unbounded domain. Used in this way, the method is similar to the method of regularized Stokeslets introduced by Cortez [6, 7]. Other methods can perform such simulations for particular types of bodies, such as the Stokesian dynamics method for particles [5] and slender-body theory based methods for rigid or elastic ellipsoids [29, 34]. The immersed boundary method can be used for arbitrarily shaped bodies. The computational complexity of our method is proportional to the square of the number of immersed boundary points, which restricts its usefulness. Also the constant of proportionality is large compared to that of the method of regularized Stokeslets, although we can significantly reduce this constant by asymptotic methods that are in current development. A fast algorithm may be possible and is a subject of continuing research. In contrast, the standard immersed boundary method for a finite domain is trivially linear in the number of immersed boundary points.

We conjecture that our results are applicable to representations of spheres and slender bodies in the immersed boundary method at moderate Reynolds number (perhaps as high as ten). Testing this prediction is the subject of future work. The Navier-Stokes equations are nonlinear, and so the relationship of the bodies' velocities to the applied force distribution can be complicated, it is non-trivial to find the constraint force for a rigid body, and we cannot eliminate the fluid variables. Expensive three-dimensional computations are required, and using an unbounded domain is no longer possible. Still, we can study, for instance, numerical solutions of steady Navier-Stokes flow around

a single immersed boundary point in a large periodic domain. We can measure the drag on the immersed boundary point as functions of its position in a grid box and its Reynolds number and compare with results for steady flow around a sphere. We conjecture that, at moderate Reynolds number, an immersed boundary point's interactions with the fluid approximate those of a sphere of radius $\overline{a}$, independent of the point's location with respect to the grid.

In any computation using the immersed boundary method, one might question whether the results depend on the position and orientation of the Lagrangian mesh of immersed boundary points relative to the Eulerian fluid grid. Our results show that even for a single immersed boundary point or for a one-dimensional array of points in three dimensions with the proper spacing, such grid effects are small. It seems probable that a more complicated elastic body composed of many immersed boundary points would have even less grid dependence because of averaging. Our results would then indicate that grid dependent effects in the immersed boundary method for the Stokes equations are smaller than may be suspected.

Chapter 7

Appendices

7.1 Approximate delta functions

All delta functions we use are of the following form.

$$\delta_h(\mathbf{x}) = \frac{1}{h^3}\phi(x/h)\phi(y/h)\phi(z/h) \tag{7.1}$$

The delta function is a product of one-dimensional functions, scaled with the grid spacing so that it is supported on a fixed number of grid points and so that its integral is constant. We impose conditions on the one-dimensional function ϕ so that it is uniquely specified. These conditions are inherited by the three-dimensional delta function.

We always require that ϕ be continuous, so that the interpolation velocity at a Lagrangian point or the force spread from a Lagrangian point are

continuous functions of the point's position. We also, for practical reasons, require that ϕ have a finite support d, where d is a small positive integer. The two interaction equations, (2.23) and (2.24), show that the values $\delta_1(\mathbf{X} - \mathbf{x})$ for $\mathbf{x} \in \mathbb{Z}^3$ are needed to spread force to the grid and interpolate velocity from the grid. These values are the tensor product of the vectors $\phi(X - j)$, $\phi(Y - j)$, and $\phi(Z - j)$ for $j \in \mathbb{Z}$. These vectors each have at most d nonzero values. Other than continuity, the conditions we impose on ϕ will be relations between the components of these vectors that must be satisfied for each value of X. We expect that d such conditions will determine a unique ϕ.

The first set of conditions that we impose on ϕ concerns the accuracy of velocity interpolation and force spreading. We say that ϕ satisfies m moment conditions if

$$\sum_{j \in \mathbb{Z}} \phi(x - j) = 1 \quad \forall x \in \mathbb{R} \tag{7.2}$$

$$\sum_{j \in \mathbb{Z}} (x - j)^k \phi(x - j) = 0 \quad \forall x \in \mathbb{R}, \quad 1 \leq k \leq m - 1. \tag{7.3}$$

If ϕ satisfies m moment conditions, then it has interpolation order m. This implies that the first $m - 1$ moments of $\mathbf{F}$ and $\mathbf{f}$ will agree. It also implies that if $\mathbf{u}$ is a velocity field defined on all of $\mathbb{R}^3$ and is a polynomial of degree at most $m - 1$, and if we define an interpolated velocity field $\mathbf{U}$ on all of $\mathbb{R}^3$ using equation (2.23), then these two velocity fields will agree exactly. Derivations of these facts can be found in [33].

Any reasonable ϕ should have an interpolation order of at least one, oth-

erwise the total forces in the Eulerian and Lagrangian variables will differ and a constant velocity field will not be interpolated correctly. An interpolation order of two guarantees that the total torque in the Eulerian and Lagrangian variables agree as well. We find that we must always impose an even number of moment conditions, otherwise the ϕ that we construct cannot be continuous.

A second condition that we sometimes impose on ϕ is that the Euclidian norm of the vector $\phi(x-j)$ for $j \in \mathbb{Z}$ be independent of x.

$$\sum_{j \in \mathbb{Z}} \left(\phi(x-j)\right)^2 = C \quad \forall x \in \mathbb{R} \tag{7.4}$$

We call this condition the sum of squares condition. It is traditionally satisfied by delta functions used in the immersed boundary method. Sums of this form arise when force is spread from a Lagrangian point to the grid, then interpolated back to find a velocity at the Lagrangian point. The sum of squares condition says that this self-interaction should be independent of the point's position with respect to the grid. The sum of squares condition also implies, via the Schwarz inequality, that the interaction between any two distinct Lagrangian points is weaker than the interaction of a point with itself. An extensive discussion of these facts is given in [26].

A third type of condition that we sometimes impose on ϕ is that, for each

x, half of the weight of $\phi(x-j)$ falls on the even j and half on the odd j.

$$\sum_{j \text{ even}} \phi(x-j) = \sum_{j \text{ odd}} \phi(x-j) \quad \forall x \in \mathbb{R} \tag{7.5}$$

If ϕ satisfies at least one moment condition, each of these sums will be one half. We call this condition the balanced condition. Some numerical discretizations of the fluid equations for the immersed boundary method at higher Reynolds number suffer from spurious oscillations in the pressure and velocity caused by a decoupling of the eight grids composed of all even or all odd numbered grid points in the three directions. Using a ϕ that satisfies the balanced condition has been shown to reduce these oscillations. Though these oscillations do not arise when solving the Stokes equations, the balanced condition is used to construct well-known ϕ that are often used in the immersed boundary method, so we will test these ϕ along with those that do not satisfy the balanced condition.

Using these conditions, we define three families of ϕ. A function ϕ in the first family [33] has support width d equal to an even integer, at least two. This function satisfies d moment conditions, the maximum number. The moment conditions are d linear equations in the d unknown nonzero components of $\phi(x-j)$ for $x \in \mathbb{R}$. A unique solution can be found. The result is a ϕ that is continuous but not C^1, and is a piecewise polynomial of degree $d-1$. We denote a ϕ in this family with support width d by ϕ_d^{M}. In this appendix, we compute results for the first three such functions. Their

formulas are:

$$\phi_2^{\mathrm{M}}(x) = \begin{cases} 1 - |x| & 0 \le |x| \le 1 \\ 0 & 1 < |x| \end{cases} \tag{7.6}$$

$$\phi_4^{\mathrm{M}}(x) = \begin{cases} 1 - \frac{1}{2}|x| - |x|^2 + \frac{1}{2}|x|^3 & 0 \le |x| \le 1 \\ 1 - \frac{11}{6}|x| + |x|^2 - \frac{1}{6}|x|^3 & 1 < |x| \le 2 \\ 0 & 2 < |x| \end{cases} \tag{7.7}$$

$$\phi_6^{\mathrm{M}}(x) = \begin{cases} 1 - \frac{1}{3}|x| - \frac{5}{4}|x|^2 + \frac{5}{12}|x|^3 + \frac{1}{4}|x|^4 - \frac{1}{12}|x|^5 & 0 \le |x| \le 1 \\ 1 - \frac{13}{12}|x| - \frac{5}{8}|x|^2 + \frac{25}{24}|x|^3 - \frac{3}{8}|x|^4 + \frac{1}{24}|x|^5 & 1 < |x| \le 2 \\ 1 - \frac{137}{60}|x| + \frac{15}{8}|x|^2 - \frac{17}{24}|x|^3 + \frac{1}{8}|x|^4 - \frac{1}{120}|x|^5 & 2 < |x| \le 3 \\ 0 & 3 < |x| \end{cases} \tag{7.8}$$

Plots of these functions are shown in figure 7.1. They are even about the origin, as are all ϕ we construct, though this is not a condition that we impose *a priori*.

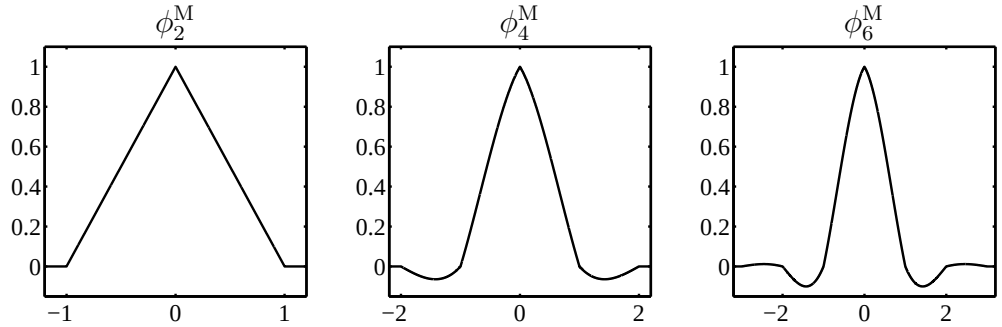


Figure 7.1: Plot of ϕ with maximum moment order.

The derivations of functions in the second and third families of ϕ are

closely related. The delta in the second family of support width three was first used in [28]. Higher order versions of these functions were first introduced in [32]. Details of the derivations are given in [26]. A ϕ in the second family has support width d equal to an odd integer, at least three. This function satisfies $d-1$ moment conditions as well as the sum of squares condition. A ϕ in the third family has support width d equal to an even integer, at least four. This function satisfies $d-2$ moment conditions, the sum of squares condition, and the balanced condition. The moment conditions and, for even d, the balanced condition are $d-1$ linear equations in d unknowns. So, all components of $\phi(x-j)$ for $x \in \mathbb{R}$ can be expressed in terms of a single component. The continuity of ϕ at the endpoints of its support allows us to calculate C in the sum of squares condition. This condition then becomes a quadratic equation in the final component of $\phi(x-j)$ that can be solved with the quadratic formula. Continuity dictates which root of the equation is appropriate. The result is a ϕ that is C^1, although this is not imposed explicitly, and is a piecewise sum of a polynomial and the square root of a second polynomial. We denote a ϕ in one of these two families with support width d by ϕ_d^{IB}, since these are the ϕ that are conventionally used in the immersed boundary method. When d is odd, ϕ is in the second family. When d is even, ϕ is in the third family and satisfies the balanced condition. In this appendix, we

compute results for the first two such ϕ in each family. Their formulas are:

$$\phi_3^{\mathrm{IB}}(x) = \begin{cases} 1 + \sqrt{1 - 3|x|^2} & 0 \le |x| \le \frac{1}{2} \\ 5 - 3|x| - \sqrt{-2 + 6|x| - 3|x|^2} & \frac{1}{2} < |x| \le \frac{3}{2} \\ 0 & \frac{3}{2} < |x| \end{cases} \tag{7.9}$$

$$\phi_5^{\mathrm{IB}}(x) = \begin{cases} \frac{17}{35} - \frac{1}{7}|x|^2 + \sqrt{\frac{3123}{39200} - \frac{311}{980}|x|^2 + \frac{101}{490}|x|^4 - \frac{1}{28}|x|^6} & 0 \le |x| \le \frac{1}{2} \\ 1 + \frac{1}{6}|x| - \frac{2}{3}|x|^2 + \frac{1}{6}|x|^3 - \frac{2}{3}\phi_5^{\mathrm{IB}}(|x| - 1) & \frac{1}{2} < |x| \le \frac{3}{2} \\ 1 - \frac{19}{12}|x| + \frac{2}{3}|x|^2 - \frac{1}{12}|x|^3 + \frac{1}{6}\phi_5^{\mathrm{IB}}(|x| - 2) & \frac{3}{2} < |x| \le \frac{5}{2} \\ 0 & \frac{5}{2} < |x| \end{cases} \tag{7.10}$$

$$\phi_4^{\mathrm{IB}}(x) = \begin{cases} \frac{1}{8}(3 - 2|x| + \sqrt{1 + 4|x| - 4|x|^2}\,) & 0 \le |x| \le 1 \\ \frac{1}{8}(5 - 2|x| - \sqrt{-7 + 12|x| - 4|x|^2}\,) & 1 < |x| \le 2 \\ 0 & 2 < |x| \end{cases} \tag{7.11}$$

$$\phi_6^{\mathrm{IB}}(x) = \begin{cases} \frac{61}{112} - \frac{11}{42}|x| - \frac{11}{56}|x|^2 + \frac{1}{12}|x|^3 + \frac{\sqrt{3}}{336}\,(243 + 1584|x| & \\ \quad - 748|x|^2 - 1560|x|^3 + 500|x|^4 + 336|x|^5 - 112|x|^6)^{\frac{1}{2}} & 0 \le |x| \le 1 \\ \frac{21}{16} + \frac{7}{12}|x| - \frac{7}{8}|x|^2 + \frac{1}{6}|x|^3 - \frac{3}{2}\phi_6^{\mathrm{IB}}(|x| - 1) & 1 < |x| \le 2 \\ \frac{9}{8} - \frac{23}{12}|x| + \frac{3}{4}|x|^2 - \frac{1}{12}|x|^3 + \frac{1}{2}\phi_6^{\mathrm{IB}}(|x| - 2) & 2 < |x| \le 3 \\ 0 & 3 < |x| \end{cases} \tag{7.12}$$

Plots of these functions are shown in figure 7.2.

Any ϕ can be dilated and scaled by a positive integer λ to make a new function ϕ' as $\lambda\phi'(\lambda x) = \phi(x)$. The new ϕ' satisfies the same conditions as ϕ. To investigate the effect of dilating ϕ, we compute results for ϕ_2^{M} dilated

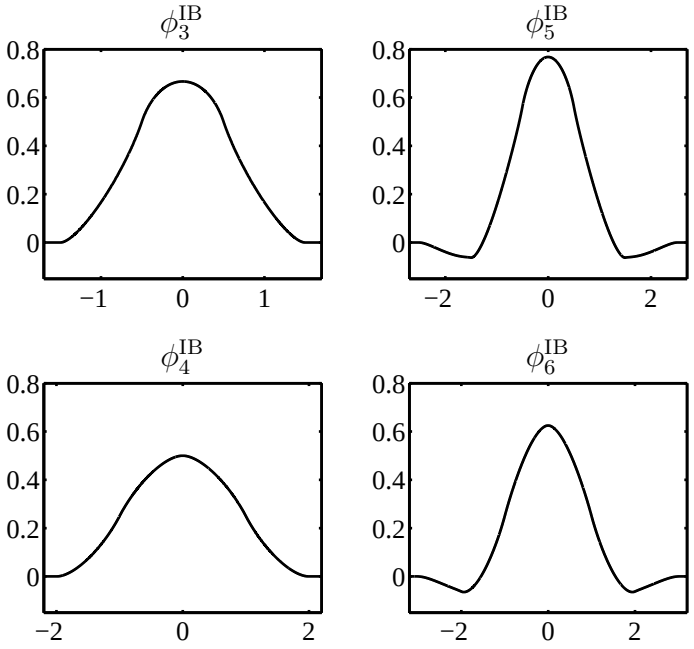


Figure 7.2: Plot of ϕ traditionally used in the immersed boundary method.

by two. We call this function ϕ_4^{Md}.

7.2 Quadrature method for the discrete stokeslet

To compute the discrete Stokeslet, we need to evaluate the integrals

$$\mathcal{S}_1 = \int_{[-\frac{1}{2},\frac{1}{2}]^3} \frac{1}{\alpha(\mathbf{k})}(\mathcal{I} - \hat{\mathbf{g}}(\mathbf{k})\hat{\mathbf{g}}(\mathbf{k})^{\mathrm{T}})e^{2\pi i\mathbf{k}\cdot\mathbf{x}}\mathbf{dk} \tag{7.13}$$

where $\mathbf{x}$ has integer components taking values between $-M$ and M. In practice, we use $M = 60$. The functions α and $\mathbf{g}$ depend on which discretization (finite difference or spectral) is used. Equation (2.28) gives their values for the finite difference discretization. Equation (2.29) gives their values for the spectral discretization. We describe here the procedure by which we evaluate these integrals.

We first take advantage of symmetries of $\mathcal{S}_1$ to reduce the amount of computation needed. If we note that, for both discretization methods, α is an even function of each component of $\mathbf{k}$ and $\mathbf{g}_i$ is an odd function of $\mathbf{k}_i$ for $i = 1, 2, 3$, we see that we need only calculate $\mathcal{S}_1(\mathbf{x})$ when the components of $\mathbf{x}$ are nonnegative integers. For, if s_1, s_2, and s_3 are ± 1, then the $(i,j)^{\mathrm{th}}$ component of $\mathcal{S}_1(s_1x, s_2y, s_3z)$ equals the $(i,j)^{\mathrm{th}}$ component of $s_is_j\mathcal{S}_1(x,y,z)$. Next, we see that we need only calculate $\mathcal{S}_1(\mathbf{x})$ when the components of $\mathbf{x}$ are non-increasing, meaning that $x \geq y \geq z$. This is because $\mathcal{S}_1$ has symmetries when the components of $\mathbf{x}$ are permuted. If s_1, s_2, and s_3 are

now a permutation of the numbers 1, 2, and 3, and if $\mathbf{x}_s$ is the vector whose i^{th} component is $\mathbf{x}_{s_i}$, then the $(i,j)^{\text{th}}$ component of $\mathcal{S}_1(\mathbf{x}_s)$ is the $(s_i, s_j)^{\text{th}}$ component of $\mathcal{S}_1(\mathbf{x})$. Finally, because $\mathcal{S}_1(\mathbf{x})$ is a symmetric matrix for all $\mathbf{x}$, we need only calculate 6 of its components. In total, we need to compute on the order of $M^3/6$ integrals, with each integral having 6 components.

We next use symmetries of the integrand in equation (7.13) to reduce the integration domain. We note that the diagonal components of $\alpha^{-1}(\mathcal{I} - \hat{\mathbf{g}}\hat{\mathbf{g}}^{\mathrm{T}})$ are even with respect to all components of $\mathbf{k}$. The off diagonal components are odd with respect to two components and even with respect to the third. We expand $\exp(2\pi i \mathbf{k}\cdot\mathbf{x})$ into a sum of products of sines and cosines. Using the oddness or evenness of these terms, we find a simpler expression for $\mathcal{S}_1$. For any diagonal component

$$(\mathcal{S}_1(\mathbf{x}))_{ii} = 8\int_{[0,\frac{1}{2}]^3} \frac{1}{\alpha(\mathbf{k})}(1-\hat{\mathbf{g}}(\mathbf{k}))_i\hat{\mathbf{g}}(\mathbf{k})_i^{\mathrm{T}})\cos(2\pi\mathbf{k}_1\mathbf{x}_1)\cos(2\pi\mathbf{k}_2\mathbf{x}_2)\cos(2\pi\mathbf{k}_3\mathbf{x}_3)\mathbf{dk}. \tag{7.14}$$

For an off-diagonal component, in particular the $(i,j)^{\text{th}}$ component with $i \neq j$ and where l is the remaining index

$$(\mathcal{S}_1(\mathbf{x}))_{ij} = 8\int_{[0,\frac{1}{2}]^3} \frac{1}{\alpha(\mathbf{k})}(1-\hat{\mathbf{g}}(\mathbf{k})_i\hat{\mathbf{g}}(\mathbf{k})_j^{\mathrm{T}})\sin(2\pi\mathbf{k}_i\mathbf{x}_i)\sin(2\pi\mathbf{k}_j\mathbf{x}_j)\cos(2\pi\mathbf{k}_l\mathbf{x}_l)\mathbf{dk}. \tag{7.15}$$

We have reduced the domain of integration to an eighth of its original size and eliminated the need to use complex numbers.

The integrand has a singularity at the origin that behaves like $|\mathbf{k}|^{-2}$. For

the finite difference discretization, there is also a discontinuity singularity at the other seven corners of the integration domain. We use a partition of unity to isolate the singularities. The partition employs a cutoff function, ψ.

$$\psi(x) = \begin{cases} 0 & x < 0 \\ \int_0^x t^8(1-t)^8 dt \,/\, \int_0^1 t^8(1-t)^8 dt & 0 \le x < 1 \\ 1 & 1 \le x \end{cases} \tag{7.16}$$

The function ψ is a piecewise polynomal, and can be easily evaluated. It is constructed to have eight continuous derivatives. Number the singularities and index them by i, so that the i^{th} singularity is located at $\mathbf{x}_i$. For each singularity, we define a partition function, χ_i.

$$\chi_i(\mathbf{x}) = \psi\left(\frac{r_{\max} - |\mathbf{x} - \mathbf{x}_i|}{r_{\max} - r_{\min}}\right) \tag{7.17}$$

The i^{th} partition function is identically one inside a sphere of radius $r_{\min}$ about the i singularity and is identically zero outside a sphere of radius $r_{\max}$. It varies smoothly between the two spheres. In practice, we find that we obtain good results when $r_{\min} = 1/25$ and $r_{\max} = 1/5$. This choice of $r_{\max}$ make the supports of the χ_i disjoint.

For each i, we multiply the integrands in equations (7.14) and (7.15) by χ_i and transform to spherical coordinates (r, θ, ϕ), centered at $\mathbf{x}_i$ and oriented so the integration domain is in the first octant. In spherical coordinates, the integrands are smooth functions up to a radius $r_{\max}$ from the origin,

so we may use standard quadrature techniques. The integration domain is: $0 \leq r \leq r_{max}$, $0 \leq \theta < \pi/2$, and $0 \leq \phi < \pi/2$. We divide this domain into N_q^3 "boxes" with equal lengths in each of the r, θ, and ϕ directions. In each box we use standard eighth-order Gauss-Legendre quadrature and sum over all boxes. In practice, we use $N_q = 32$ for the singularity at the origin and $N_q = 16$ for the discontinuity singularities.

What remains is to compute the integrals of the integrands in equations (7.14) and (7.15) multiplied by $1 - \sum \chi_i$. Assuming $r_{\max} < 1/2 - r_{\min}$, these will be identically zero inside spheres of radius $r_{\min}$ about all singularities and C^8 everywhere. For large $\mathbf{x}$, however, the integrands will be highly oscillatory and a large number of function evaluations will be needed to obtain high accuracy. To overcome this, we used a method of Ixaru and Paternoster to select a set of quadrature weights and abscissae that are specially designed to integrate functions of the form $f(\mathbf{k}) = g(\mathbf{k}) \exp(\pm 2\pi i \boldsymbol{\omega} \cdot \mathbf{k})$ for specific choices of $\boldsymbol{\omega}$ and where $g(\mathbf{k})$ is slowly varying [15].

We first approximate a one-dimensional integral of a function $f(k) = g(k) \exp(\pm 2\pi i \omega k)$ on $[-1, 1]$ by

$$\int_{-1}^{1} f(k) dk \approx \sum_{i=1}^{4} f(k_i) w_i. \tag{7.18}$$

We require that this approximation is exact when $g(x) = k^n$, $n = 0$, 1, 2, and 3. The result is a system of eight nonlinear equations in the eight unknowns, k_i and w_i, that we solve with Newton's method. The weights

and abscissae approach those of the four-point Gauss-Legendre method as ω approaches zero. The nonlinear system has multiple solutions, so care is needed in selecting the initial guess to make k_i and w_i continuous functions of ω.

To integrate a three-dimensional function of the form $f(\mathbf{k}) = g(\mathbf{k}) \exp(\pm 2\pi i \boldsymbol{\omega} \cdot \mathbf{k})$ on the cube $[-1, 1]^3$, we generate a set of quadrature weights and abscissae for each component of $\boldsymbol{\omega}$. Those corresponding to $\boldsymbol{\omega}_j$ are k_i^j and w_i^j. Then, we use the approximation

$$\int_{[-1,1]^3} f(\mathbf{k}) \mathbf{dk} \approx \sum_{i=1}^{4} \sum_{j=1}^{4} \sum_{l=1}^{4} f(k_i^1, k_j^2, k_l^3) w_i^1 w_j^2 w_l^3. \tag{7.19}$$

We are ready to calculate the remaining integral needed to obtain $\mathcal{S}_1$. We divide the domain $[0, 1/2]^3$ into N_q^3 identical cubes. We approximate the integral on each cube using equation (7.19), where the integrand is scaled and translated. The vector $\boldsymbol{\omega} = \mathbf{x}/N_q$, so we must calculate new quadrature weights and abscissae for each value of $\mathbf{x}$. Doing this is of negligible cost compared with calculating the integrals. In practice, we use $N_q = 32$.

To approximate the error in our calculations, we halved and doubled all values of N_q and calculated $\mathcal{S}_1$ for a subset of the values of $\mathbf{x}$. We let $\mathcal{S}_1^1$ be the result when we use the standard N_q, $\mathcal{S}_1^{1/2}$ be the result when we halve N_q, and $\mathcal{S}_1^2$ be the result when we double N_q. We calculate these for $\mathbf{x}_1$ between 0 and M and $\mathbf{x}_2$ and $\mathbf{x}_3$ between 0 and 6. We define two measures of relative

error.

$$\epsilon_1(\mathbf{x}) = \frac{\|\mathcal{S}_1^{1/2}(\mathbf{x}) - \mathcal{S}_1^1(\mathbf{x})\|}{\|\mathcal{S}_1^2(\mathbf{x})\|} \tag{7.20}$$

$$\epsilon_2(\mathbf{x}) = \frac{\|\mathcal{S}_1^1(\mathbf{x}) - \mathcal{S}_1^2(\mathbf{x})\|}{\|\mathcal{S}_1^2(\mathbf{x})\|} \tag{7.21}$$

The double bars indicate the Euclidean matrix operator norm. Figure 7.3 shows a plot of ϵ_1 and ϵ_2 averaged over the $\mathbf{x}_2$ and $\mathbf{x}_3$ directions, so the result is a function of $\mathbf{x}_1$. We see that the error increases exponentially as $\mathbf{x}_1$ increases. At distances of up to 20 grid points, our quadrature method, when we use the standard N_q, has converged to ten digits. At the maximum distance of 60 grid points, we still have six digits of accuracy. The base two logarithm of the ratio ϵ_1/ϵ_2 should approximate the convergence order of the quadrature method. Using this approximation, we find the order to be between 6.0 and 17.1 with a spatial mean of 10.5.

7.3 Slender-body theory results

Consider a slender body whose centerline position is given by $\mathbf{X}(s)$ where s is an arclength parameter that varies from 0 to $\tilde{L}$. The body is locally a cylinder whose local radius is $r(s)$. The body moves at velocity $\mathbf{U}(s)$ and imparts a force density $\mathbf{F}(s)$ to the fluid. Slender-body theory derives an integral equation that gives the approximate relationship between $\mathbf{U}$ and $\mathbf{F}$ [18, 16, 14]. The unit tangent vector $\hat{\mathbf{s}}(s)$ is given by $\mathbf{X}_s(s)/|\mathbf{X}_s(s)|$, the

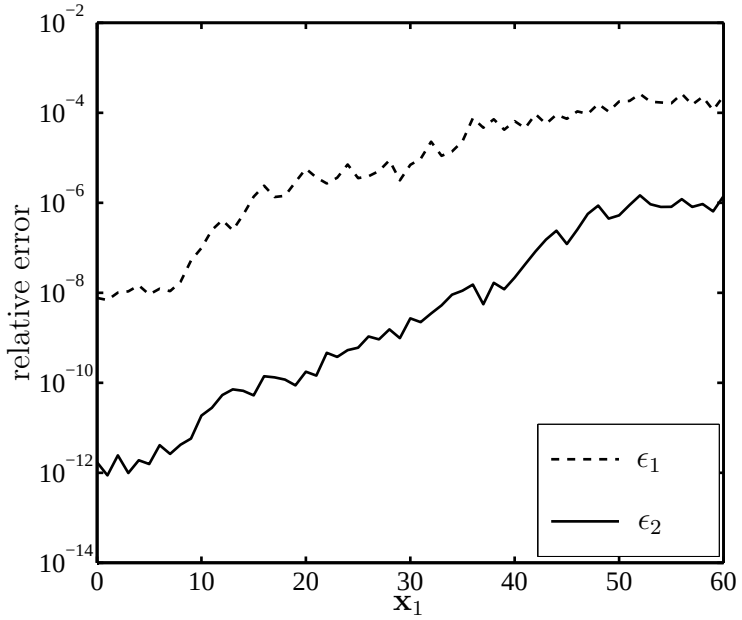


Figure 7.3: Relative errors in the quadrature method to compute $\mathcal{S}_1(\mathbf{x})$. The dashed line shows ϵ_1, the error obtained using a number of quadrature points characterized by $N_q = 16$ relative to $N_q = 64$. The solid line shows ϵ_2, the error obtained using $N_q = 32$ relative to $N_q = 64$. These errors are functions of $\mathbf{x}_1$, the distance from the origin in the x direction, and they are averaged over $\mathbf{x}_2$ and $\mathbf{x}_3$, the distances in the y and z directions. The vertical axis shows a logarithmic scale. The computations in this appendix were performed using $N_q = 32$, so the solid line shows the relative error in $\mathcal{S}_1(\mathbf{x})$ for these computations. The errors increase exponentially as $\mathbf{x}_1$ increases, but we still obtain six digits of accuracy at $\mathbf{x}_1 = 60$.

vector $\mathbf{R}(s,s')$ denotes $\mathbf{X}(s)-\mathbf{X}(s')$, and $\hat{\mathbf{R}}$ denotes $\mathbf{R}/|\mathbf{R}|$. The integral equation of slender-body theory is

$$8\pi\mu\mathbf{U}(s)=\Lambda(s)\mathbf{F}(s)+K\left[\mathbf{F}\right](s) \tag{7.22}$$

where

$$\Lambda(s)=-\left(1+\log\frac{r(s)^2}{4s(\tilde{L}-s)}\right)\left(\mathcal{I}+\hat{\mathbf{s}}(s)\hat{\mathbf{s}}(s)^{\mathrm{T}}\right)+2\left(\mathcal{I}-\hat{\mathbf{s}}(s)\hat{\mathbf{s}}(s)^{\mathrm{T}}\right) \tag{7.23}$$

$$K\left[\mathbf{F}\right](s)=\int_0^{\tilde{L}}\left(\frac{\mathcal{I}+\hat{\mathbf{R}}(s,s')\hat{\mathbf{R}}(s,s')^{\mathrm{T}}}{|\mathbf{R}(s,s')|}\mathbf{F}(s')-\frac{\mathcal{I}+\hat{\mathbf{s}}(s)\hat{\mathbf{s}}(s)^{\mathrm{T}}}{|s-s'|}\mathbf{F}(s)\right)ds'. \tag{7.24}$$

In the case that $\mathbf{X}(s)$ is a straight line, this equation simplifies. Let $U^{\mathrm{t}}(s)$ and $F^{\mathrm{t}}(s)$ be the velocities and forces in the tangential direction and $U^{\mathrm{n}}(s)$ and $F^{\mathrm{n}}(s)$ be the velocities and forces in an arbitrary normal direction. The integral equation then decomposes as follows.

$$8\pi\mu U^{\mathrm{t}}=-2\left(1+\log\frac{r(s)^2}{4s(\tilde{L}-s)}\right)F^{\mathrm{t}}(s)+2\int_0^{\tilde{L}}\frac{F^{\mathrm{t}}(s')-F^{\mathrm{t}}(s)}{|s-s'|}ds' \tag{7.25}$$

$$8\pi\mu U^{\mathrm{n}}=\left(1-\log\frac{r(s)^2}{4s(\tilde{L}-s)}\right)F^{\mathrm{n}}(s)+\int_0^{\tilde{L}}\frac{F^{\mathrm{n}}(s')-F^{\mathrm{n}}(s)}{|s-s'|}ds \tag{7.26}$$

Given $\mathbf{U}$, these equations may be solved to find $\mathbf{F}$. The fluid velocity may then be found by equation (5.7). This is a uniformly valid approximation to the velocity in the exterior of the slender body and is second order accurate in $r/\tilde{L}$ provided $\log r(s)^2/(4s(\tilde{L}-s))$ is uniformly bounded in s. We consider

a body with constant radius r, which does not satisfy this property. Errors in the velocity field are introduced at the endpoints of the slender body that may be seen in figures 5.14, 5.15, and 5.16.

Keller and Rubinow [18] propose a fixed-point iterative method to solve the above equations. After two iterations, they find an analytic expression for $\mathbf{F}$ when $\mathbf{U}$ is a constant function of s, which corresponds to a translating cylinder. Let $\epsilon = r/\tilde{L}$, and let $g(s) = \log[4s(\tilde{L} - s)/\tilde{L}^2]$. Define an integral operator J which acts on Lipschitz continuous functions f by

$$J[f](s) = \int_0^{\tilde{L}} \frac{f(s') - f(s)}{|s' - s|} ds'. \tag{7.27}$$

Note that f need not be uniformly Lipschitz, so $J[g]$ is well defined, despite the logarithmic singularities in g as $s = 0$ and $s = \tilde{L}$. Then, the Keller-Rubinow approximate forces for translational motion are

$$F^{\mathrm{t}}(s) = \frac{2\pi\mu U^{\mathrm{t}}}{\log 1/\epsilon}\left(1 + \frac{g(s) - 1}{2\log\epsilon} + \left[\frac{g(s) - 1}{2\log\epsilon}\right]^2 + \frac{1}{(2\log\epsilon)^2} J[g](s)\right) \tag{7.28}$$

$$F^{\mathrm{n}}(s) = \frac{4\pi\mu U^{\mathrm{n}}}{\log 1/\epsilon}\left(1 + \frac{g(s) + 1}{2\log\epsilon} + \left[\frac{g(s) + 1}{2\log\epsilon}\right]^2 + \frac{1}{(2\log\epsilon)^2} J[g](s)\right). \tag{7.29}$$

The errors of these approximations are $O((\log\epsilon)^{-4})$. These are the expressions for the force applied to the fluid by a rigidly translating cylinder that we use in equation (5.7) to compute the velocity fields for comparison with the velocities produced by an array of immersed boundary points. The total force applied to the fluid is the integral of $\mathbf{F}$ with respect to s. For any

function f, $\int_0^{\tilde{L}} J[f](s)ds = 0$, so the terms involving $J[g]$ do not contribute to the total force. The expressions for $F^{\mathrm{t}}(s)$ and $F^{\mathrm{n}}(s)$ may then be integrated analytically to yield the slender-body theory approximations to the tangential and normal drag of a cylinder given in equation (5.6).

We perform a similar procedure for the case of a cylinder that rotates about a line perpendicular to its axis. Now, $U^{\mathrm{n}}(s) = (s - \tilde{L}/2)\Omega$ for some angular velocity Ω. After two iterations of the Keller-Rubinow iterative method, we find an expression for the force density which we call F^{r}.

$$F^{\mathrm{r}}(s) = \frac{4\pi\mu\Omega(s-\tilde{L}/2)}{\log 1/\epsilon}\left(1 + \frac{g(s)-1}{2\log\epsilon} + \frac{g(s)^2+1}{(2\log\epsilon)^2} + \frac{(s-\tilde{L}/2)^{-1}}{(2\log\epsilon)^2}J[(s-\tilde{L}/2)g](s)\right) \tag{7.30}$$

This is the expression for the force applied by a rotating cylinder that we use in equation (5.7) to compute velocity fields for comparison with the velocities produced by an array of immersed boundary points. Integrating $(s - \tilde{L}/2)F^{\mathrm{r}}(s)$ gives the total torque applied to the fluid.

This integral can be computed analytically by using properties of the operator J. First, J is self adjoint, meaning for arbitrary functions $p(s)$ and $q(s)$,

$$\int_0^{\tilde{L}} p(s)\int_0^{\tilde{L}} \frac{q(s')-q(s)}{|s'-s|}ds'ds = \int_0^{\tilde{L}} q(s)\int_0^{\tilde{L}} \frac{p(s')-p(s)}{|s'-s|}ds'ds. \tag{7.31}$$

To see why this is true, subtract the right side of this equation from the left. The resulting integrand is antisymmetric in s and s', but these two integration

variables may be interchanged without changing the integral. Thus, the integral must be zero. In inner-product notation, $(p, J[q]) = (J[p], q)$, where the L_2 inner product is implied.

Second, it may be easily seen that $J[s^k]$ is a polynomial in s of degree at most k. Every polynomial space is thus an invariant subspace of J, so for each $k \geq 0$ there must be an eigenfunction of J that is a polynomial of degree k. These eigenfunctions must be orthogonal in L_2, so they must be the Legendre polynomials on the interval $[0, \tilde{L}]$. The eigenvalue of the k^{th} Legendre polynomial may be easily computed by finding the coefficient that multiplies s^k in $J[s^k]$. This eigenvalue is $-2\sum_{j=1}^{k} 1/j$ for $k > 0$ and 0 for $k = 0$. Alternate proofs of these facts can be found in [14].

We can now compute the total torque, the integral of $(s - \tilde{L}/2)F^{\text{r}}(s)$. All the terms in this integral are computable by standard methods, except for the term involving J. We need to be able to compute the integral of $(s - \tilde{L}/2)J[(s - \tilde{L}/2g](s)$, which is

$$\Big(s - \tilde{L}/2, J[(s - \tilde{L}/2)g]\Big) = \Big(J[s - \tilde{L}/2], (s - \tilde{L}/2)g(s)\Big) = -2\int_0^{\tilde{L}} (s - \tilde{L}/2)^2 g(s) ds. \tag{7.32}$$

The final integral can be computed by standard methods. We have used the self-adjointness of J and that $s - \tilde{L}/2$ is the Legendre polynomial of degree one in the interval $[0, \tilde{L}]$. The total torque can then be computed analytically to yield the slender-body theory approximation to the rotational drag in equation (5.6).

Bibliography

[1] M. Abramowitz and I.A. Stegun. *Handbook of Mathematical Functions*. Courier Dover Publications, 1965.

[2] P. J. Atzberger, P. R. Kramer, and C. S. Peskin. A stochastic immersed boundary method for biological fluid dynamics at microscopic length scales. *J. Comput. Phys.*, 224(2):1255–1292, 2007.

[3] G. K. Batchelor. *An Introduction to Fluid Dynamics*. Cambridge University Press, Cambridge, 2000.

[4] D.C. Bottino and L.J. Fauci. A computational model of ameboid deformation and locomotion. *Eur. Biophys. J.*, 27(5):532–539, 1998.

[5] J.F. Brady and G. Bossis. Stokesian dynamics. *Annu. Rev. Fluid Mech.*, 20(1):111–157, 1988.

[6] R. Cortez. The method of regularized stokeslets. *SIAM J. Sci. Comput.*, 23(4):1204–1225, 2002.

[7] R. Cortez, L. Fauci, and A. Medovikov. The method of regularized Stokeslets in three dimensions: analysis, validation, and application to helical swimming. *Phys. Fluids*, 17(3):31504–31504, 2005.

[8] R. Dillon and L. J. Fauci. An integrative model of internal axoneme mechanics and external fluid dynamics in ciliary beating. *J. Theor. Biol*, 207:415–430, 2000.

[9] R. Dillon, L. J. Fauci, and D. Gaver. A microscale model of bacterial swimming, chemotaxis and substrate transport. *J. Theor. Biol.*, 177(4):325–40, 1995.

[10] Z. H. Duan and R. Krasny. An adaptive treecode for computing nonbonded potential energy in classical molecular systems. *Journal of Computational Chemistry*, 22:184–195, 2001.

[11] L. J. Fauci and C. S. Peskin. A computational model of aquatic animal locomotion. *J. Comput. Phys.*, 77(1):85–108, 1988.

[12] A. L. Fogelson and C. S. Peskin. A fast numerical method for solving the three-dimensional Stokes equations in the presence of suspended particles. *J. Comput. Phys.*, 79(1):50–69, 1988.

[13] J. Garcia de la Torre and V. A. Bloomfield. Hydrodynamic properties of complex, rigid, biological macromolecules: theory and applications. *Q. Rev. Biophys.*, 14(1):81–139, 1981.

[14] T. Götz. *Interactions of fibers and flow: asymptotics, theory and numerics*. PhD thesis, University of Kaiserslautern, 2000.

[15] L. G. Ixaru and B. Paternoster. A Gauss quadrature rule for oscillatory integrands. *Comput. Phys. Commun.*, 133(2):177–188, 2001.

[16] R. E. Johnson. An improved slender-body theory for Stokes flow. *J. Fluid Mech.*, 99:411–431, July 1980.

[17] E. Jung and C. S. Peskin. Two-dimensional simulations of valveless pumping using the immersed boundary method. *SIAM J. Sci. Comput.*, 23(1):19–45, 2001.

[18] J. B. Keller and S. I. Rubinow. Slender-body theory for slow viscous flow. *J. Fluid Mech.*, 75:705–714, 1976.

[19] Y. Kim and C.S. Peskin. Penalty immersed boundary method for an elastic boundary with mass. *Physics of Fluids*, 19:Article Number 053103, 2007.

[20] M.-C. Lai and C. S. Peskin. An immersed boundary method with formal second-order accuracy and reduced numerical viscosity. *J. Comput. Phys.*, 160(2):705–719, 2000.

[21] C. Lanczos. *The Variational Principles of Mechanics*. Courier Dover Publications, fourth edition, 1986.

[22] S. Lim and C. S. Peskin. Simulations of the whirling instability by the immersed boundary method. *SIAM J. Sci. Comput.*, 25(6):2066–2083, 2004.

[23] K. Lindsay and R. Krasny. A particle method and adaptive treecode for vortex sheet motion in three-dimensional flow. *J. Comput. Phys.*, 172:879–907, 2001.

[24] D. M. McQueen and C. S. Peskin. A three-dimensional computer model of the human heart for studying cardiac fluid dynamics. *Comput. Graphics*, 34(1):56–60, 2000.

[25] L. A. Miller and C. S. Peskin. A computational fluid dynamics of 'clap and fling' in the smallest insects. *J. Exp. Biol.*, 208(2):195–212, 2005.

[26] C. S. Peskin. The immersed boundary method. *Acta Numer.*, 11:479–517, 2002.

[27] C. S. Peskin and D. M. McQueen. Fluid dynamics of the heart and its valves. In H. G. Othmer, F. R. Adler, M. A. Lewis, and J. C. Dallon, editors, *Case Studies in Mathematical Modeling: Ecology, Physiology, and Cell Biology*, pages 309—337. Prentice-Hall, Englewood Cliffs, NJ, 1996.

[28] A. M. Roma, C. S. Peskin, and M. J. Berger. An adaptive version of the immersed boundary method. *J. Comput. Phys.*, 153(2):509–534, 1999.

[29] M. J. Shelley and T. Ueda. The Stokesian hydrodynamics of flexing, stretching filaments. *Physica D*, 146(1-4):221–245, 2000.

[30] J. M. Stockie and S. I. Green. Simulating the motion of flexible pulp fibres using the immersed boundary method. *J. Comput. Phys.*, 147:147–165, 1998.

[31] J. M. Stockie and B. R. Wetton. Stability analysis for the immersed fiber problem. *SIAM J. Appl. Math.*, 55(6):1577–1591, 1995.

[32] J.M. Stockie. *Analysis and computation of immersed boundaries, with application to pulp fibres*. PhD thesis, University of British Columbia, 1998.

[33] A.-K. Tornberg and B. Engquist. Numerical approximations of singular source terms in differential equations. *J. Comput. Phys.*, 200(2):462–488, 2004.

[34] A.-K. Tornberg and M. J. Shelley. Simulating the dynamics and interactions of flexible fibers in Stokes flows. *J. Comput. Phys.*, 196(1):8–40, 2004.

[35] L. Zhu and C. S. Peskin. Simulation of a flapping flexible filament in a flowing soap film by the immersed boundary method. *J. Comput. Phys.*, 179(2):452–468, 2002.